JAERI-M
6359

ANNUAL REPORT OF THE DIVISION OF THERMONUCLEAR FUSION RESEARCH, JAERI

covering the period of April 1, 1974 to March 31, 1975

January 1976

Division of Thermonuclear Fusion Research

日本原子力研究所
Japan Atomic Energy Research Institute

JAERI-M 6359

Annual Report of the Division of Thermonuclear Fusion Research, JAERI

covering the period of April 1, 1974 to March 31, 1975

Division of Thermonuclear Fusion Research, Tokai, JAERI

(Received December 16, 1975)

Works performed in the Division of Thermonuclear Fusion Research for the period of April 1974 to March 1975 are described.

(1) In JFT-2, power-up work of the generator to increase the toroidal magnetic field from 10 kG to 18 kG was completed in October 1974, and the JFT-2 phase-II experiment started.

(2) A JFT-2a tokamak of a tear-drop cross-section with axisymmetric divertor was put into operation in August 1974, as scheduled. Initial experiments confirmed that the plasma enclosed inside a separatrix magnetic surface was stably produced.

(3) In the diagnostics, a data processing system and a multi-channel particle analyzer were fabricated and put into operation.

(4) A test stand (ITS-1) for the development of neutral beam injectors was assembled, and the preliminary experiment on an ion source started in February 1975.

(5) In design study of a large tokamak device JT-60, the preliminary design was completed under contract with the industry. Physical studies on the plasma confinement in JT-60 and refinement and improvement of the design continued.

(6) Theoretical and computational works continued in neutral injection heating, impurity transport, relaxation of radial electric field and mhd stability.

(7) The design of a 2000 MW fusion power reactor which started in the previous year was further improved. The concept and design criteria of an experimental power reactor were studied.

---

note: Thermonuclear Fusion Laboratory was reorganized into Division of Thermonuclear Fusion Research in April 1975.

JAERI－M 6359

核融合研究部年報（昭和49年度）

日本原子力研究所東海研究所核融合研究部

（1975年12月16日受理）

核融合研究部における昭和49年度の研究進行状況をまとめたものである。その概要は次のとおりである。

(1) JFT－2では，トロイダル磁場を10 kGから18 kGに上昇させるための電源増力工事を49年10月に完成し，第2期実験を開始した。

(2) ダイバータ付涙滴断面トカマクJFT－2aは，49年8月に予定どうり運転を開始した。最初の実験において，セパラトリックス磁気面によって囲まれたプラズマが安定につくられていることを確認した。

(3) プラズマ診断については，データ処理装置およびマルチチャンネル粒子分析装置が完成した。

(4) 中性粒子入射源を開発するためのテストスタンドITS－1を完成し，50年2月から初期実験を開始した。

(5) 臨界プラズマ試験装置JT－60の設計研究については，予備設計を完結した。さらに，JT－60のプラズマ閉込めに関する物理的検討と，より詳細な設計を進めている。

(6) 理論的研究では，中性粒子入射加熱，不純物輸送，経方向電場の減衰，MHD安定性などの研究をつづけている。

(7) 昨年開始した2000 MW核融合実用炉の設計を発展させた。さらに核融合実験炉の炉概念と設計条件についての検討を行った。

CONTENTS

PREFACE

The fiscal year covered by this annual report is the last of a six-year plan which has been pursued as the Special Integrated Research of Atomic Energy. During the years, JFT-1, 2 and 2a became operating and theoretical and computational research and designs of JT-60 and a tokamak reactor were performed. In a review of the plan[1], the Steering Committee for Nuclear Fusion Research notes that we have succeeded in "take-off" for a further advanced stage of r&d on fusion power; the stage is the next to the six-year plan and could be symbolized by JT-60. The Nuclear Fusion Research and Development Committee, an ad hoc panel for the next plan, submitted a report to AEC on 26 July 1974, after having received a report of the Technology Subcommittee of the Committee and carefully analyzed the state of the art of domestic and foreign CTR activities and related social factors. In 31 July 1975, AEC decided to promote a second stage plan as a "national project", in accordance with the submitted report.

A brief summary of activities in this period[2], ending March 1975 is as follows.

A new generator for JFT-2 of 21 MW peak was installed and the toroidal field was increased to 18 kG from 10 kG. JFT-2 was not productive in this period; no discharge from April to October in order to install the generator and also from February to April 1975 to repair a trouble with the toroidal coil supports. Just before the trouble, the electron temperature was 1 keV at plasma current of 170 kA by a laser scattering measurement.

A tokamak with tear-drop cross-section and an axisymmetric diverter, JFT-2a, became operating in August 1974, just on schedule. Equilibrium of plasma in a magnetic limiter configuration was shown. The typical parameters were 200 eV in electron temperature, 1×10^{13} cm^{-3} in density and 20 kA in discharge current (ion temperature is 80 - 100 eV by a measurement in June 1975). An extensive study on a divertor is going on.

In February 1975, a test stand for neutral beam injectors, ITS-1, was assembled as the first step of its development at JAERI. A beam of 6 A at 25 keV was obtained in the next month by a DuoPIGatron ion source.

A preliminary design study of a tokamak confining a reactor grade plasma was approved formally for the fiscal year. The tokamak is called JT-60[3], named after the volume of the plasma in cubic meters. The

major parameters, such as aspect ratio, minor radius and toroidal field strength, were optimized for magnetic energy, to attain T_i: 5-10 keV and n_T: $2\text{-}6 \times 10^{13} cm^{-3} s$. In the persent design, the major radius is 3 m, the minor radius 1 m and the toroidal field on the axis of the plasma 50 kG. An analysis of radiation loss by impurities indicates the necessity of impurity control. Thus JT-60 is to be equipped with a magnetic limiter and a liner of specially treated Mo or low Z material. By the end of the period, a preliminary design was finished; no fatal factor in manufacture was found and targets for the component development were elucidated. In designing, Japanese industrial activities relevant to it were mobilized, to which our appreciation is addressed.

An extensive theoretical study was performed, of which a theory on the disruptive instability connected with disturbance of magnetic surfaces was noteworthy.

A design of a tokamak reactor was completed to its first step; a gas cooled 2000 MWt reactor with solid (Li_2O) fertile material and cold gas blanket around the reactor core plasma.

It is our highest honour to report that their Majesties, the Emperor and the Empress visited the Thermonuclear Fusion Laboratory on 21 October 1974.

(S. Mori)

(1) For the detail, see a report of the plan, compiled by the Liaison Committee under the Steering Committee, July 1975, 297 pages in Japanese. The report contains the activities on research and development on toroidal confinement at JAERI, related technical development at the Institute of Physical and Chemical Research, a high beta study at the Electro-Technical Laboratory, fusion reactor engineering studies at JAERI and the National Research Institute for Metals, and appendices about budgets, personnel, major installations, publications etc.

(2) The preceeding reports are JAERI-M 4564, 5029, 5564 and 5888.

(3) The direct translation of the formal Japanese name of JT-60 is a critical plasma testing facility; "critical" means that input power to the plasma is just balanced to the D-T fusion output. JT-60 is

expected to demonstrate the "critical" condition in hydrogen or deuterium plasma.

I. TOROIDAL CONFINEMENT EXPERIMENTS

1. JFT-2

N. Fujisawa, M. Maeno, N. Suzuki,
T. Takeda, K. Toi*

1.1 Introduction

The JFT-2 phase-I experiment was terminated at the end of April, 1974. The phase-II experiment with the increased toroidal field 18 kG from 10 kG was started in December, 1974. But, in February, 1975, the experiment was stopped due to a trouble of the toroidal field coils. In the following subsections we will discuss plasma confinement and dynamic limiter experiments with the toroidal field of 10 kG, and numerical analyses.

(N. Fujisawa)

1.2 Experimental Studies

1) Plasma confinement experiment

The experimental conditions under which plasma confinement was studied are listed in Tab. I.1-1. The direction of the toroidal magnetic field is counterclockwise as viewed from above, and the plasma current flows in the direction opposite to the toroidal magnetic field.

Since discharge behaviors fluctuate considerably at the initial stage of the operation, 2000 - 3000 shots of discharges were intentionally made for the purpose of conditioning. The ultimate pressure of 1.2×10^{-7} Torr was obtained. Purified hydrogen is continuously introduced into the vacuum vessel through a palladium film as the working gas, the pressure of which is adjusted to 3.3×10^{-4} Torr. At filling pressures above 3.5×10^{-4} Torr the plasma has the tendency to show the so-called disruptive instabilities. At filling pressures below 3.3×10^{-4} Torr, hard X-ray radiation which seems to be caused by runaway electrons gradually increases with the decrease of the pressure.

---

* Present address: Institute of Plasma Physics, Nagoya University, Nagoya, Japan.

Electron temperatures obtained from Thomson scattering measurement rise with increasing plasma current from 50 kA to 80 kA, but they remain constant after 80 kA. This confinement experiment was carried out at the maximum plasma current of 75 kA, which corresponds to $q_a = 4.3$, where q_a is the value of q calculated at the limiter.

The time behaviors of various parameters under the above mentioned conditions are shown in Fig. I.1-1.

The condenser banks for ohmic heating consist of two kinds of banks as shown in Tab. I.1-1, the first bank is fired at 6 ms. After the second bank being fired at 26 ms, the plasma current reaches its peak value of 75 kA at 60 ms as shown in Fig. I.1-1a.

The displacement of the plasma axis from the shell axis is determined with magnetic probes. The time behavior of the horizontal and vertical displacements is shown in Fig. I.1-1b. The former is 1 - 2 cm inwards in the time interval from 30 ms to 100 ms. The latter is well centered within 1 cm. The vertical displacement can be adjusted by an external horizontal field which compensates an error field generated by the toroidal coils.

The electron densities are measured with a 4 mm microwave interferometer. The density at R = 90 cm averaged over the microwave path parallel to the major axis is shown in Fig. I.1-1c. The density from 10 ms to 20 ms was not able to be measured because of large fluctuations in the plasma. The density in the time interval from 20 ms to 35 ms increases, but after 35 ms it decreases monotonically.

Figure I.1-1d shows temperatures of the plasma. The ion temperatures are determined from the energy spectrum of the charge exchanged neutral particles, which presumably give the ion temperature in the hot region of the plasma. The electron temperatures at the center of the vacuum vessel deduced from the Thomson scattered light show a large spread, although the discharges are reproducible from shot to shot in all macroscopic quantities such as the plasma current and the loop voltage. The electron temperatures are also determined from the energy spectrum of soft X-ray radiation. The electron conductivity temperature is calculated by using the plasma current, the loop voltage, the plasma displacement and the diamagnetic signal, assuming that the effective charge is 1.0. It should be noted that the time of the maximum electron conductivity temperature coincides with that of the maximum plasma current.

Figure I.1-1e shows details of the time behavior of the carbon and

oxygen light intensities. The intensities of these lines were measured witha 50 cm normal incidence VUV monochrometer on a horizontal midplane of the torus at the dynamic limiter box. The time behavior of these light intensities is consistent with the electron temperatures above mentioned.

The time evolution of the mode number of the low frequency oscillations is measured by using magnetic pick-up coils, and is shown in Fig. I.1-1f. The low frequency oscillations are characterized by magnetic field perturbations having mode structures $\exp[i(m\theta-n\phi)]$ with m ranging from 6 to 2 and $n = 1$. It may be noted that $m = 2$ modes appear even at $q_a = 5$, and that the $m = 2$ modes seem to be associated with the decrease of the electron density. The direction of the mode rotation is in the electron diamagnetic direction, and its frequency is 1 - 5 kHz.

The horn of the 4 mm microwave interferometer is able to be moved horizontally at intervals of 6 cm. Figure I.1-2 shows the time evolutions of the electron density profiles obtained by inverse transformation of the electron line density on the assumption of zero density at the surface of the liner. The peak of the density profile is shifted by 2 - 4 cm inwards from the vacuum vessel center. It should be noted that this displacement of the density profile agrees with that of the plasma axis determined from the magnetic probes. It should be emphasized that the density profile is rather peaked. The profile at 30 ms coinsides with that of

$$n(\xi) = n(0)\ (1 - \xi^2)\ ;\quad \xi = r/a_{liner},$$

and after 40 ms the profiles fit

$$n(\xi) = n(0)\ (1 - \xi^2)^2\ .$$

Figure I.1-3 shows the electron temperature profile determined from the Thomson scattering measurement at 30 ms. The reproducibility of the electron temperature is not good as previously mentioned. The temperature profile can be expressed as

$$T_e(\xi) = T_e(0)\ (1 - \xi^2)^2\ .$$

In order to determine the ionization rate, the vertical distribution of H_α photon flux was measured. This H_α photon flux was measured with both the 25 cm visible monochrometer and the spectrometer of the Thomson scattering apparatus. The measurement with the former was subject to the strong influence of the dynamic limiter which was composed of two rails

separated vertically by 51 cm. In this paper, the H_α photon flux obtained from the latter is assumed to be as the uniform component along the torus. Figure I.1-4 shows the radial profile of the neutral particle density as a function of time, which is calculated from the collisional-radiative theory and the radial profile of the H_α photon flux obtained by inverse transformation. It should be emphasized that the neutral particle density increases with time, while the radial profile remains almost constant.

The particle confinement time τ_p, defined as

$$\frac{dN}{dt} = \Sigma(\text{ionization rates}) - \frac{N}{\tau_p} \; ; \; N = \text{total electron number},$$

is shown in Fig. I.1-5. The particle confinement time monotonically drops from 10 ms at 30 ms to 3 ms at 100 ms.

The electron particle flux Γ can be calculated from the radial profile of the ionization rate. The diffusion coefficient D, defined as

$$\Gamma = -D\nabla n + (\text{Ware Pinch}),$$

is shown in Fig. I.1-6. The radial profile of the diffusion coefficients is similar to the Phirsh-Schlüter type, and their absolute values increase from $100 \times D^{ps}$ at 30 ms to $400 \times D^{ps}$ at 100 ms, where D^{ps} is the Phirsh-Schlüter diffusion coefficient for $Z_{eff} = 1$.

To interpret the energy confinement, a numerical model is used. The input data of the model are the total plasma current, the time behaviors of the radial profiles of the electron density and the neutral particle density. The transport coefficients are adjusted so that the simulation results are in good agreement with the measured temperatures and the loop voltage. However, the model above mentioned can not explain the measured ion temperature, because the charge exchange loss and the thermal convection loss cool the ion temperature. In order to decrease the ion energy loss, the computations have been carried out assuming that the photon flux of the H_α line is one third of the measured photon flux.

The best fitting of the simulation with the experimental results can be obtained with the following transport coefficients: the thermal conductivity of electrons κ_e = (100 at 30 ms → 400 at 100 ms) × (Phirsh-Schlüter), the thermal conductivity of ions κ_i = (Neoclassical), the electrical resistivity η = (Spitzer), and $Z_{eff} = 3$. The runaway current is also introduced into the model in consideration of the time evolution of

the measured conductivity temperature and the detected hard X-ray radiation. The ratio of the runaway current to the total plasma current is chosen to increase from 0 at 30 ms to 0.3 at 80 ms.

The results of the simulation are represented in Figs. I.1-1a and I.1-1d. The gross energy confinement time τ_E is shown in Fig. I.1-5. Figure I.1-7 shows the radial variations of the electron and ion local power balances at 60 ms. The electron power balance shows that the thermal conduction loss is the dominant electron loss process in the center, and the convection loss is the main loss process near the edge. The ion power balance indicates that the dominant loss processes are the convection loss and the charge exchange loss.

2) Dynamic limiter experiment

The dynamic rail limiter is composed of two molybdenum plates which are set parallel to each other inside the dynamic limiter box, and can be driven upwards and downwards pneumatically with the average and maximum speeds of 5 m/s and 9 m/s, respectively. The experiments were carried out for three operation modes of the dynamic limiter; the open, closed and dynamic modes. In the open and closed operation modes, the two molybdenum plates are fixed at their distances of 51 cm and 25 cm, respectively. In the dynamic operation mode the dynamic limiter plates were triggered to move at 50 ms as shown in Fig. I.1-8. The experimental conditions are as follows; the toroidal magnetic field is 10 kG, the vertical magnetic field is 35 G and the filling pressure is 2.5×10^{-4} Torr H_2.

The time behaviors of the various parameters for the above-mentioned three operation modes are shown in Fig. I.1-9. The value of q_a for the closed operation mode is chosen above 3. Figure I.1-9c indicates that the horizontal displacement of the plasma axis for the dynamic operation mode coincides with that of the closed operation mode before the dynamic limiter is triggered ($t < 50$ ms) and that of the open operation mode after the dynamic limiter is almost fully open ($t > 70$ ms).

Temperatures of the electrons and the ions are determined from the Thomson scattering and the charge exchanged neutral particle measurement, respectively. It should be noted that both temperatures have large error bars. The time evolutions of the mode number of the low frequency oscillations are shown in Fig. I.1-9e for three operation modes. The $m = 2$ modes appear in all operation modes.

Figure I.1-10 shows the electron density profiles for the three operation modes. The displacements of the peak of the density profile coincide with those of the plasma axis determined from the magnetic probes. In case of the dynamic operation mode the density profile approaches to that of the open operation mode after the dynamic limiter is triggered, and it is probable that the density near the plasma boundary diffuses with the dynamic limiter.

The radial profiles of the H_α photon flux for the three operation modes are shown in Fig. I.1-11. It is reasonable that the plasma column for the closed operation mode is limited by the dynamic limiter, while it may be understood from Fig. I.1-11a that the radius of the hot core of the plasma for the open operation mode is within 10 cm. The cooling by the neutral particles seems to be one of the probable explanations. Figure I.1-11c represents that the peak of the H_α photon flux moves outwards with the dynamic limiter. It is very difficult to conclude from this figure whether the region of the hot core of the plasma expands with the dynamic limiter, or not. The Thomson scattering measurement suggests that the region of the hot core does not expand. It is likely that the displacement of the peak of the H_α photon flux originates in the diffusion of the density at the plasma boundary.

3) Soft X ray measurement

Preliminary experiments have shown that a liquid nitrogen cooled Si(Li) detector with a 0.33 mil thick Be window can be used for measuring low energy X rays (below $\sim$500 eV). The maximum count rate of the pulse-height-analyser was $\sim$30 k.c.p.s. The conventional coincidence method using a gate signal proved unsatisfactory because it requires a number of discharges to obtain time behaviour of the spectrum.

We improved the data handling system so as to allow measurements of X ray spectra over a whole plasma duration time in one discharge. We used a ND 50/50 4096 channel pulse-height-analyser as a two-dimensional analyser. The 4096 channels are divided into eight groups, each of which consists of 512 channels. A plasma duration time is divided into eight intervals to each of which is allocated each of the eight groups. Each group consisting of 512 channels can record X ray spectrum during the prescribed time interval. Thus this arrangement allows a successive measurement of X ray spectra over a whole plasma duration of the discharge.

A typical spectrum obtained for one of the time intervals is shown in Fig. I.1-12. The electron temperature was determined from the slope of the X ray energy spectrum, the Maxwell distribution being assumed. Figure I.1-13 shows the time dependence of the electron temperatures. The energy spectrum has a good exponential dependence. It is noted that these data were obtained by summing up the measurements for only three discharges.

1.3 Numerical Analysis

1) Numerical method to obtain an optimum configuration of external magnetic field coils in a tokamak device by nonlinear programming[1)]

In a large tokamak device in the next stage of the fusion research, it seems that the equilibrium of the toroidal plasma is maintained essentially by control loops excited by an external power supply instead of a currently used conducting casing. To design the control loops for the maintaining magnetic field which confines the tokamak plasma in equilibrium, a method based on the optimization procedure using an algorithm of the nonlinear programming was devised. The method searches the optimum configuration of the control loops subject to the physical and technical requirements. It has been concluded that the method is effective for the design of control loops and also that of the primary windings in a practical tokamak. Moreover, the equilibrium configurations of the tokamak plasma without the conducting casing can be easily obtained by using the nonlinear optimization procedure with the virtual casing principle proposed by Shafranov and Zakharov[2)].

In the method described here the optimum design of the external magnetic field coils is obtained by minimizing an objective function (F), a surface integral of the "length" of difference vector between the magnetic fields produced by the coils ($\hat{B}$) and the desired magnetic field (B), which is expressed as

$$F = \int_S |\hat{B} - B|^2 ds \cong \sum_{m=1}^{M} w_m |\hat{B}_m - B_m|^2 \ .$$

Utilization of the nonlinear programming codes is very advantageous in this kind of problems because an arbitrary set of parameters can be chosen as

unknown variables and constraining conditions on the limits of the parameters are easily introduced. In our case the positions of the coils were chosen as unknown variables.

Two examples of the results are presented in Figs. I.1-14 and I.1-15. In Fig. I.1-14 the positions of the vertical magnetic field coils are determined by fitting the magnetic field to the desired one[3] which is given on the median plane of the plasma column. Figure I.1-15 shows an example of the primary coils which is obtained by minimizing the magnetic field energy on the plasma surface.

(K. Toi and T. Takeda)

2) Numerical method for solution of the integral equation of the first kind —— Application to analysis of plasma density profile ——

A numerical method based on nonlinear programming is applied to the solution of an integral equation of the first kind. Instead of determining the values of the dependent variable at the prescribed values of the independent variable, this method solves the equation by determining values of the independent variable, with some appropriate constraining conditions. By this method, unphysical oscillations likely to appear in the solution of the integral equation of the first kind are eliminated, and various nonlinear integral equations of the first kind appearing in the analyses of experimental data can be solved with comparative ease.

To demonstrate the usefulness of this method, a data set of line densities of a plasma column, integrated along paths across a region of interest, was inversely transformed, and a density profile of the plasma column was successfully obtained. In this case the line densities along the microwave path parallel to the vertical axis (y-axis) are measured at $x = x_m$ (m=1, 2, ...M), where x- and y- coordinates are chosen in a plasma crosssection. The objective function (F) of the nonlinear programming is expressed as

$$F = \sum_{m=1}^{M} w_m \, (\hat{\phi}_m - \phi_m)^2$$

where w_m, $\hat{\phi}_m$ and ϕ_m are the weighting factor, the calculated and measured values of the line density at $x = x_m$, respectively. If the contours of the density profile are expressed by several parameters, the calculated line density ϕ_m is written by these parameters. In our analysis a contour

is assumed to be a circle. The radius of the circle and the displacement of the circle along the x-axis are chosen as the parameters which describe the shape and position of the contour, and the relative density of each contour is prescribed beforehand. Thus the number of the unknown parameters which describe a profile made of N contours is 2N+1, i.e., $r_1, r_2, \ldots r_N, d_1, d_2, \ldots d_N, S$, where r_j, d_j and S are the radius and position of the j-th contour circle and the value of the maximum density, respectively. As an example of the analysis a data set of the microwave phase shift (line density) in Fig. I.1-16 was prepared which is obtained from a prescribed density profile (Fig. I.1-17, broken line). The result of the analysis is shown in Fig. I.1-17 by a solid line. Very good agreement is seen between the prescribed and calculated profiles.

(T. Takeda)

3) Magnetic island formation due to error field in the JFT-2 tokamak[4]

Formation of islands in magnetic surfaces due to the error field in resonance with the rotational transform of magnetic lines of force in tokamak devices was studied.

The width of islands had been obtained analytically by M. N. Rosenbluth et al. and is shown to be proportional to the square root of the intensity ratio of the error field to the azimuthal field and also inversely proportional to the square root of the shear. We obtained the same result from a simpler analysis which gives a clearer physical picture.

To confirm the validity of this theoretical expression, islands which may appear due to the resonant components of the pulsed vertical field provided in the JFT-2 tokamak were numerically calculated by following the magnetic lines of force using R.K.G. method. The theoretical value is in good agreement with the width of islands thus obtained. Figure I.1-18 shows an example.

(S. Matsuda, M. Yoshikawa)

References

1) K. Toi and T. Takeda: JAERI-M 6018, (1975).

2) V. D. Shafranov and L. E. Zakharov: Nuclear Fusion, 12 (1972) 599.

3) V. S. Mukhovatov and V. D. Shafranov: Nuclear Fusion, 11 (1971) 605.
4) S. Matsuda and M. Yoshikawa: Japan. J. appl. Phys., 14 (1975) 87.

Table I.1-1 Experimental Conditions

Toroidal Field	9	kG
Vertical Field	65	G
Horizontal Field	8	G
Filling Pressure	3.3×10^{-4}	Torr H_2
Ohmic Heating Energy	400 + 10400	μF
	10 + 1.7	kV
ECRH Preionization	1	kW
Limiter Radius	25	cm
Plasma Current	75	kA

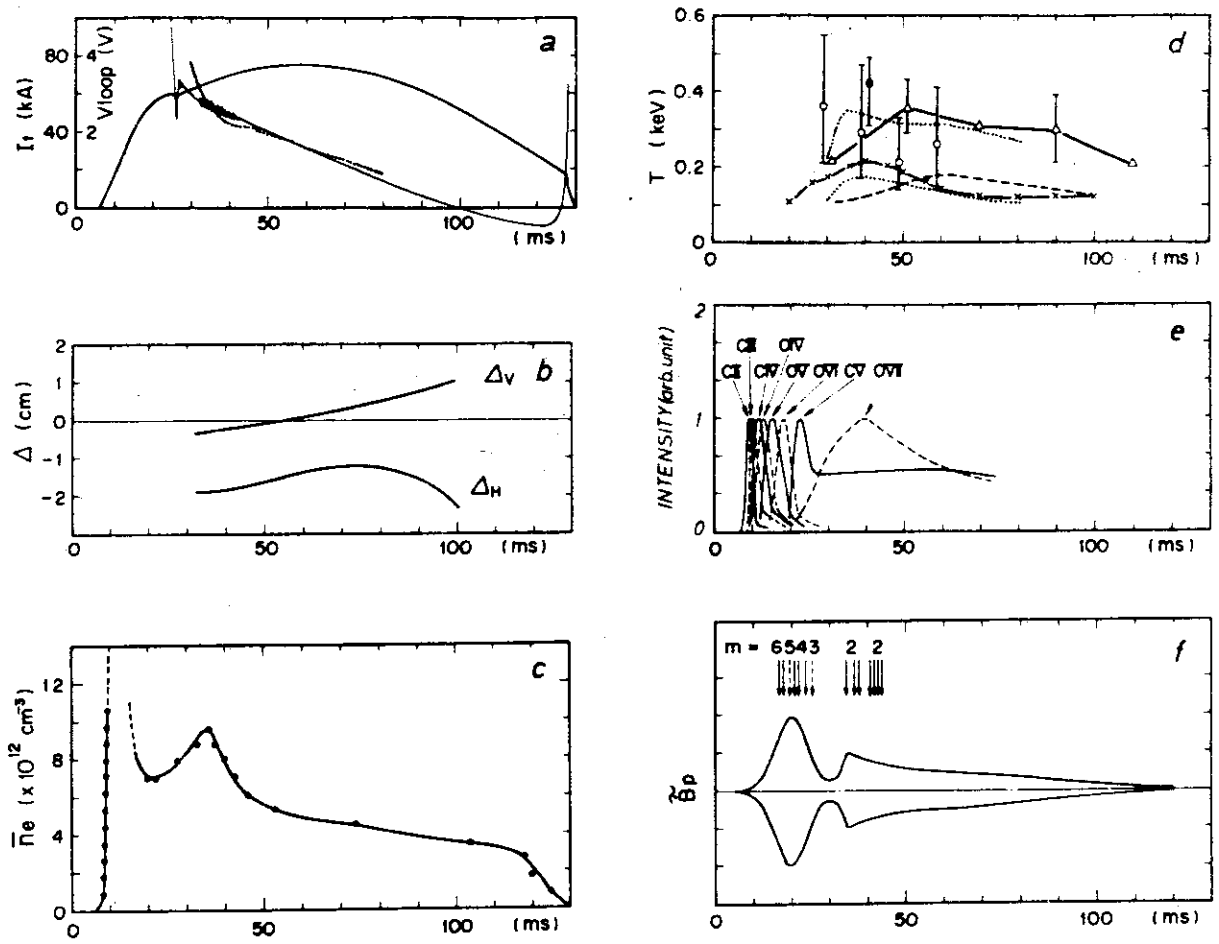

Fig.I.1-1 Time behaviors of a discharge in hydrogen under conditions presented in Tab.II. (a) I_t; ohmic heating current including the liner current (>1 kA; t<25 ms). V_{loop}; loop voltage measured on the inner surface of the aluminum shell, and loop voltage obtained by the simulation (.....). (b) Vertical and horizontal displacements of the plasma from pick-up coils. (c) Electron line density from a 4 mm microwave interferometer. (d) Temperatures; ion temperature(×) measured from energy spectrum of charge exchanged neutral particles, electron temperature(o) from Thomson scattering measurement, electron temperature(Δ) from energy spectrum of soft X-ray radiation, conductivity temperature(---), and electron and ion temperatures obtained by the simulation(....). (e) Time behaviors of carbon and oxygen ion light emissions measured with the 50 cm normal incidence VUV monochrometer. (f) Magnetic field oscillations and mode number m.

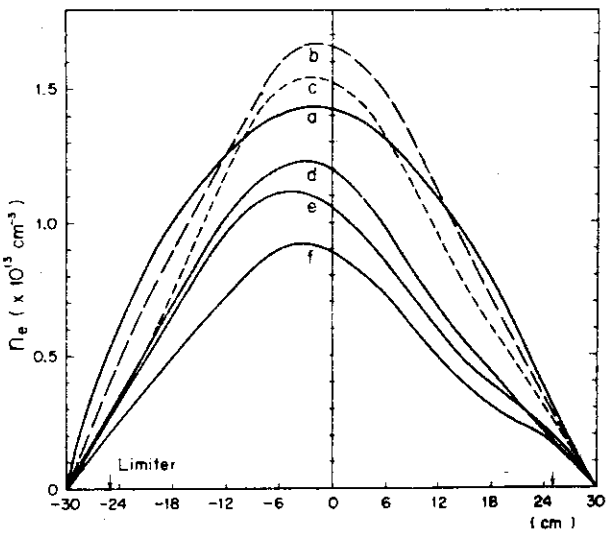

Fig.I.1-2 Time evolutions of radial profiles of electron densities from a 4 mm microwave interferometer.
(a) 30 ms, (b) 40 ms, (c) 50 ms, (d) 60 ms, (e) 70 ms, (f) 100 ms.

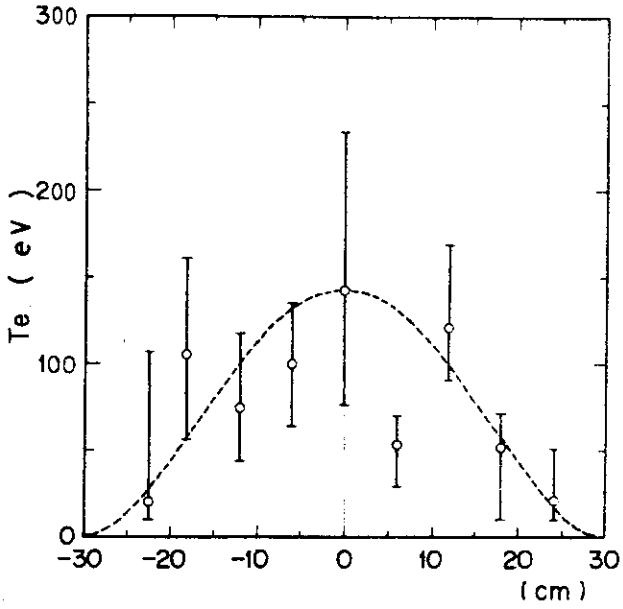

Fig.I.1-3 Vertical profile of electron temperatures at R=90 cm measured from Thomson scattered light at 30 ms. Broken line indicates the profile of $(1-\xi^2)^2$.

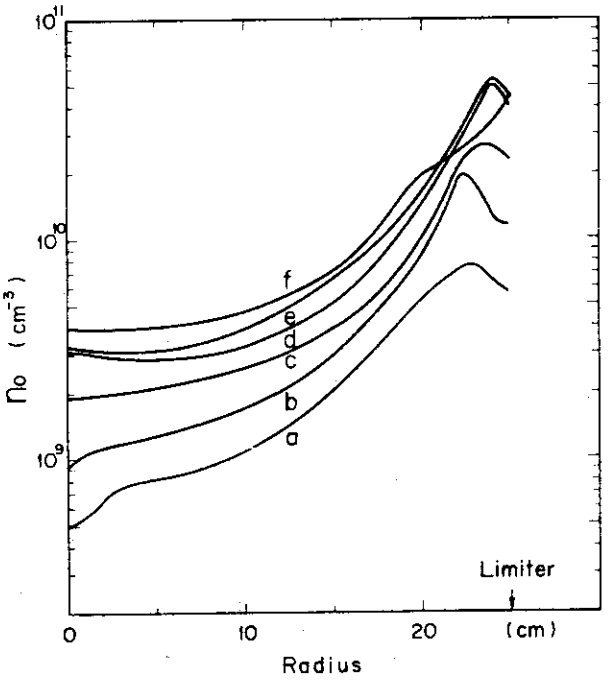

Fig.I.1-4 Time evolutions of radial profiles of neutral particle density from H_α photon flux.
(a) 30 ms, (b) 40 ms, (c) 50 ms, (d) 60 ms, (e) 70 ms, (f) 100 ms.

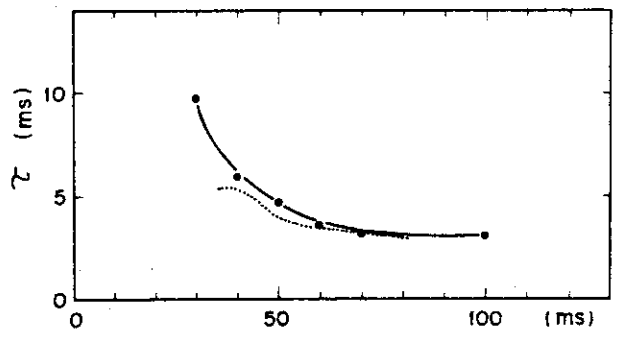

Fig.I.1-5 Particle confinement time from H_α photon flux and electron density(——) and gross energy confinement time obtained by the simulation(....).

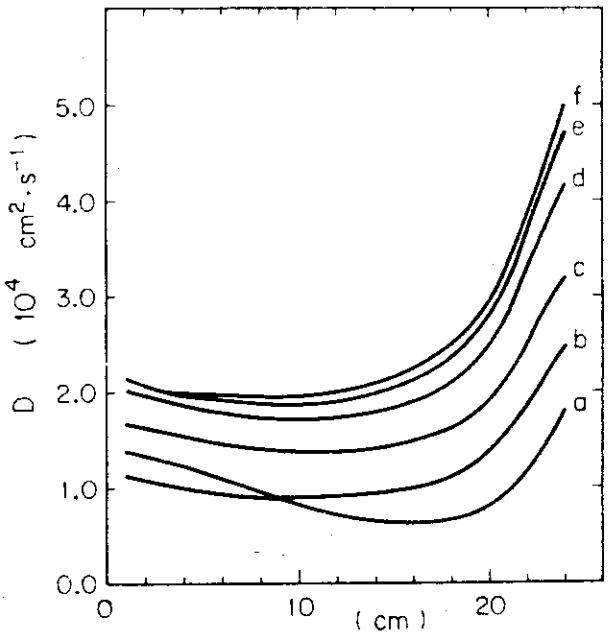

Fig.I.1-6 Time evolutions of radial profiles of diffusion coefficients calculated from electron density profiles and ionization rates.
(a) 30 ms, (b) 40 ms, (c) 50 ms, (d) 60 ms, (e) 70 ms, (f) 80 ms.

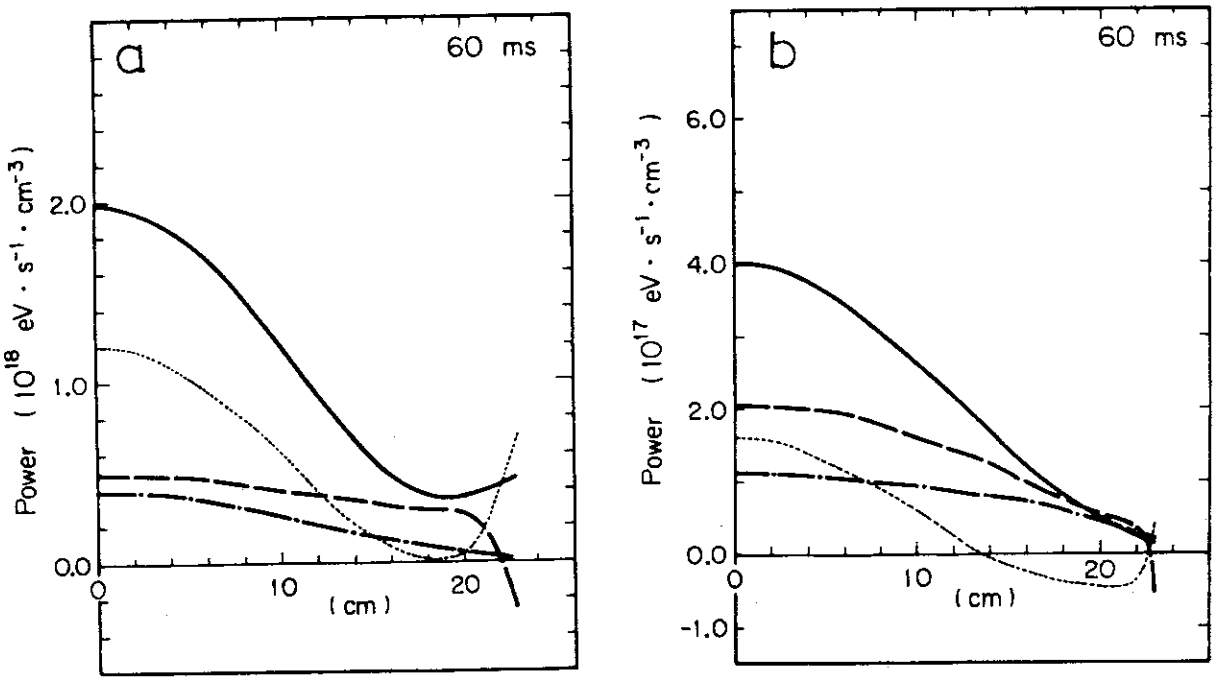

Fig.I.1-7 Local power balance at 60 ms obtained by the simulation.
(a) Radial profile of electron power balance; Ohmic heating(——), thermal conduction loss(....), convection loss(----), and power transfer to ions(— - —). (b) Radial profile of ion power balance; power transfer from electrons(——), thermal conduction loss(...), convection loss(----), charge exchange loss(— - —).

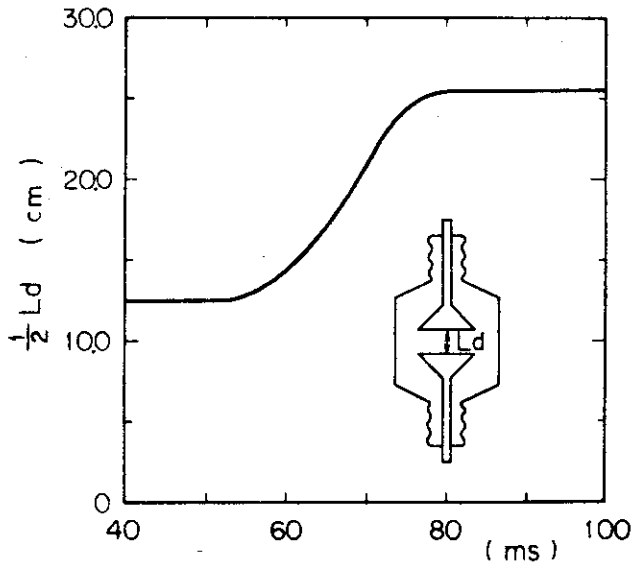

Fig.I.1-8 Half distance between limiter plates after the dynamic limiter is triggered at 50 ms.

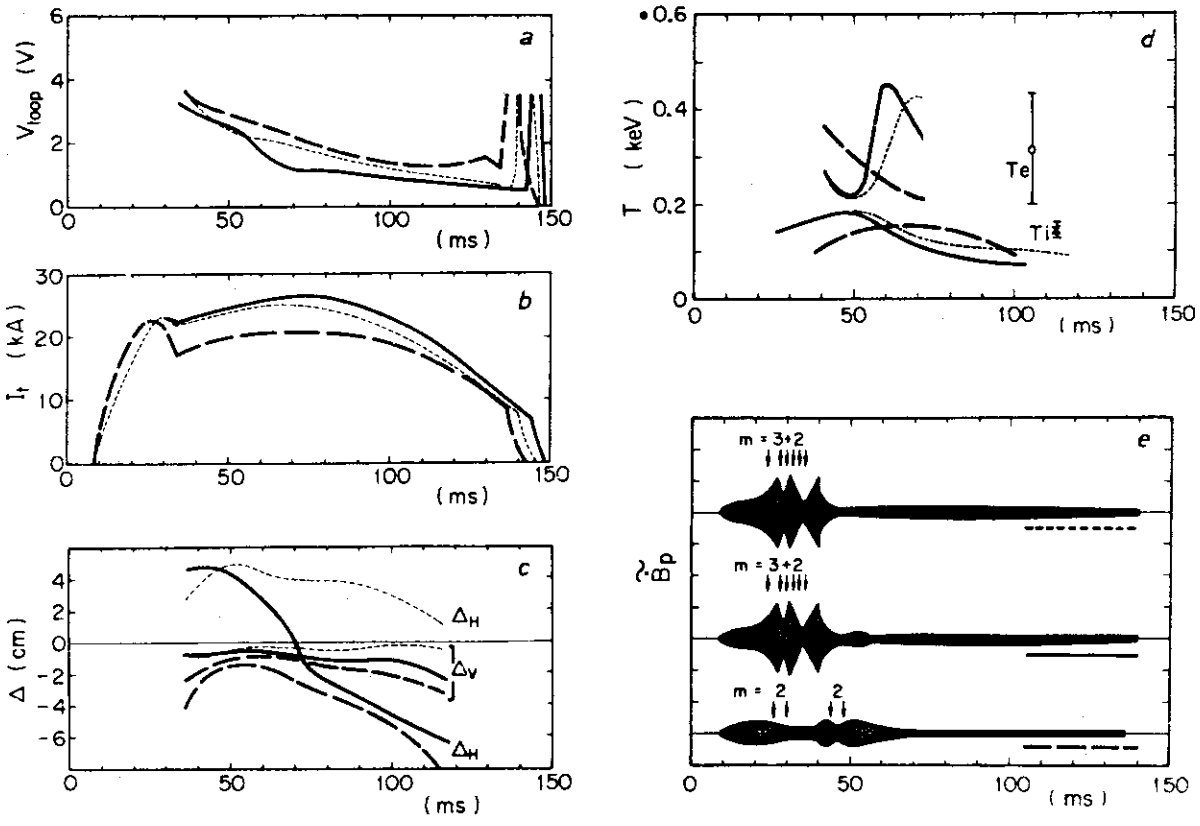

Fig.I.1-9 Time behaviors of discharges for three operation modes of dynamic limiter experiment. (a) Loop voltages. (b) Plasma currents. (c) Plasma displacements. (d) Temperature. (e) Magnetic field perturbations. Solid line, broken line and dotted line indicate dynamic operation mode, open operation mode and closed operation mode, respectively.

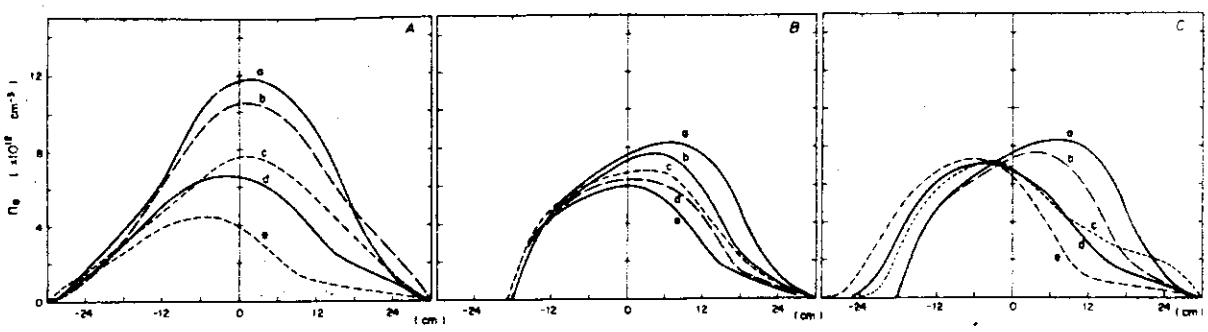

Fig.I.1-10 Time evolutions of density profiles for three operation modes of the dynamic limiter experiment. (A) Open operation mode. (B) Closed operation mode. (C) Dynamic operation mode. (a) 50 ms, (b) 60 ms, (c) 70 ms, (d) 80 ms, (e) 100 ms.

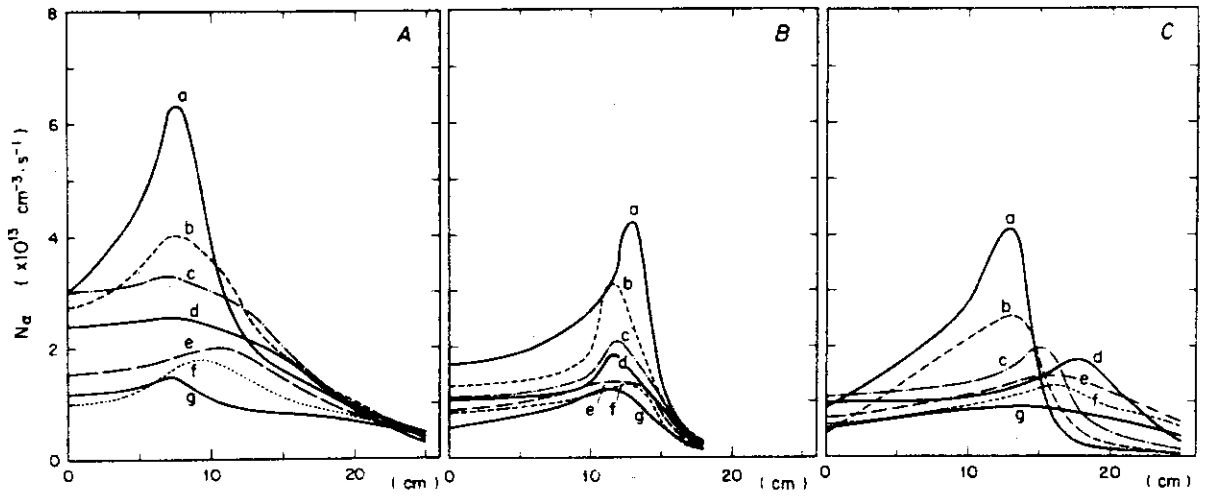

Fig.I.1-11 Time evolutions of H_α photon flux profiles for three operation modes of the dynamic limiter experiment. (A) Open operation mode. (B) Closed operation mode. (C) Dynamic operation mode. (a) 40 ms, (b) 50 ms, (c) 60 ms, (d) 70 ms, (e) 80 ms, (f) 90 ms, (g) 100 ms.

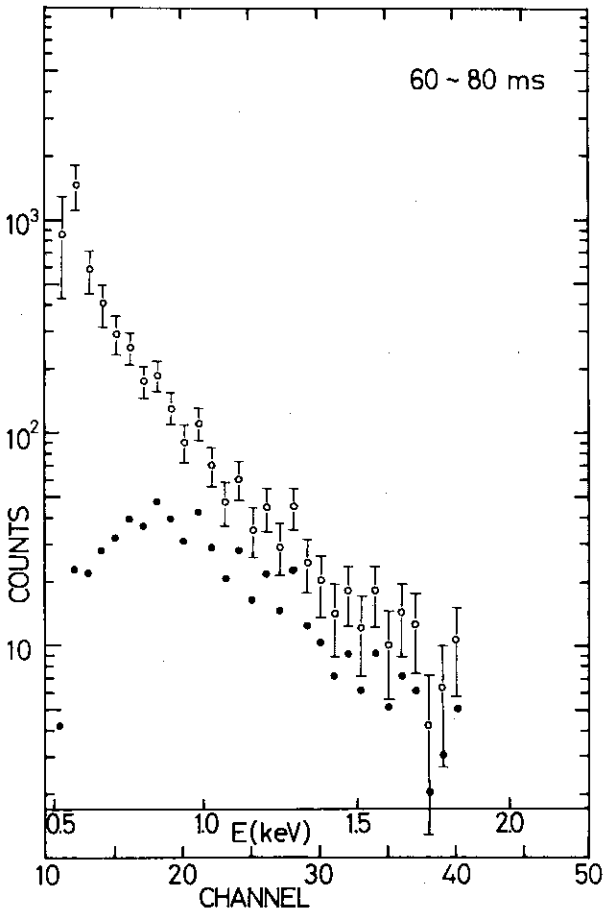

Fig.I.1-12

The dark dots show the pulse height distribution (sum of 3 discharges) obtained in the period of 60~80 ms after the discharge started. The circles show the X ray energy spectrum obtained after corrections for the absorption of the 0.33 mil thick Be window. The error bars show the standard deviation of the counts.

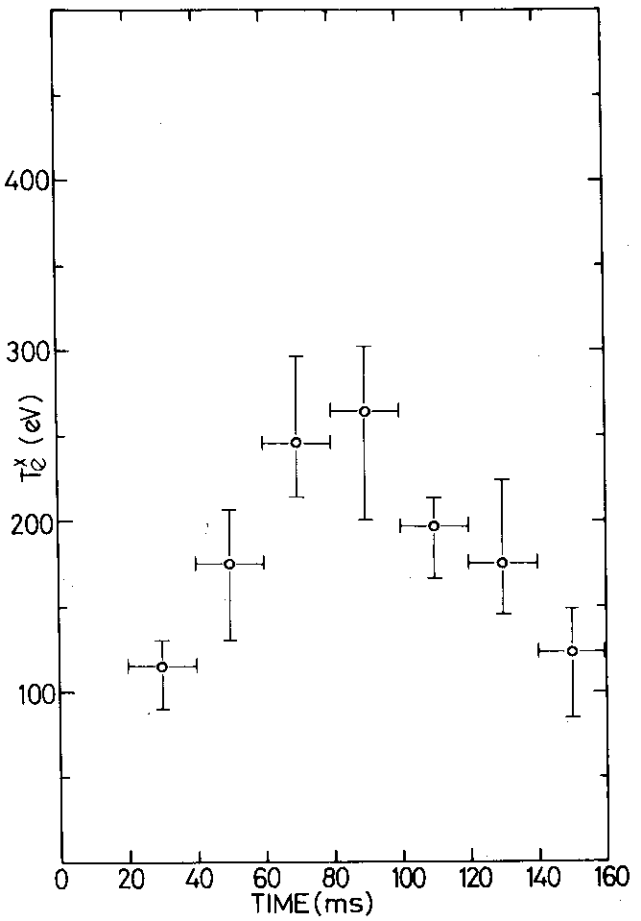

Fig.I.1-13

The time behavior of the electron temperature obtained from the slope of the soft X ray energy spectrum. Experimental conditions;

B_t = 18 kG, Max I_p = 75 kA and P_f = 3.5×10^{-4} torr H_2 .

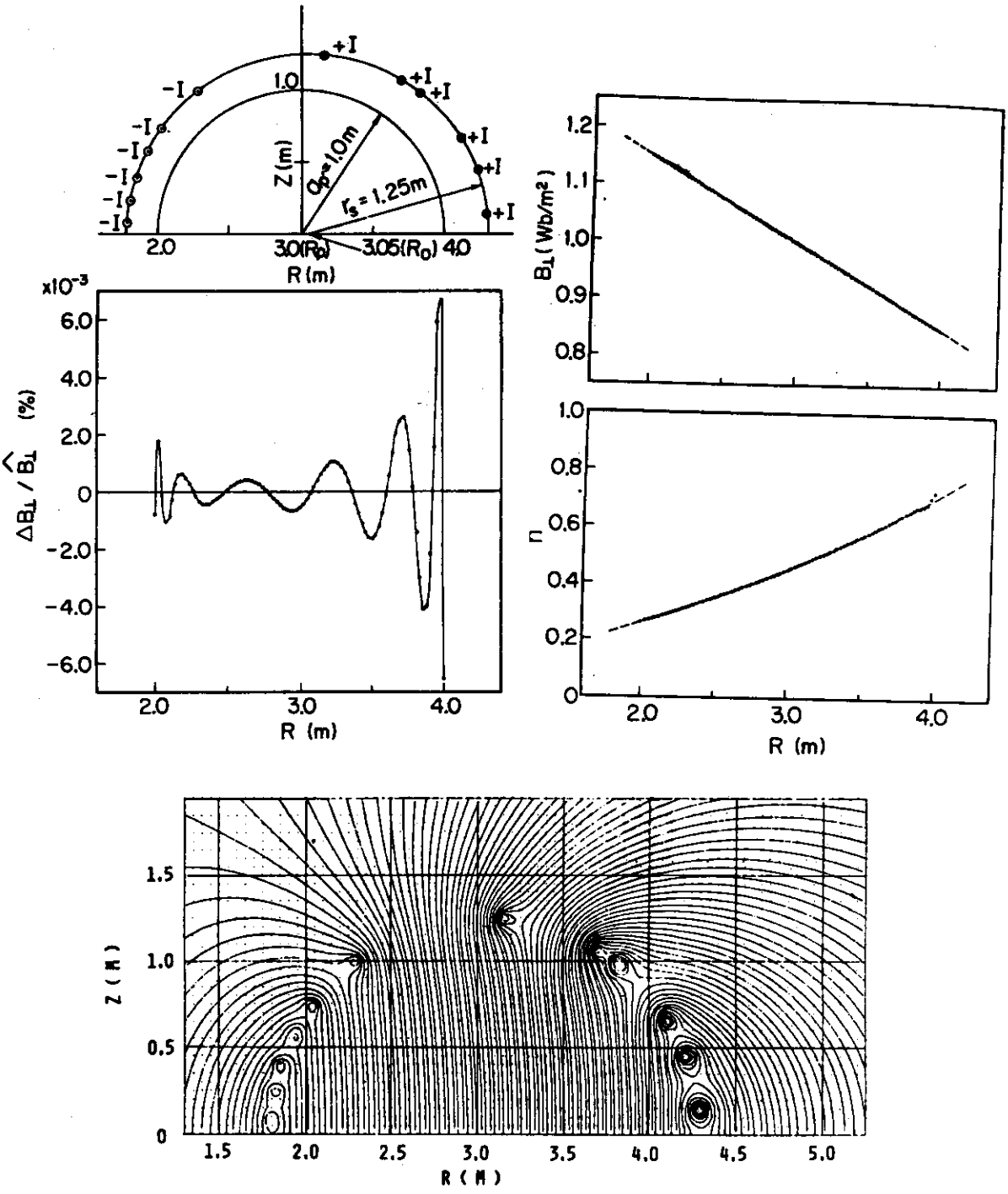

Fig.I.1-14 The optimum positions of the vertical magnetic field coils. fhe distribution of the deviation of the designed magnetic field from the desired one is shown for N=12 (N is the number of coils in the upper half plane). The designed magnetic field, the decay index and the two-dimensional pattern of the magnetic lines of force are also shown.

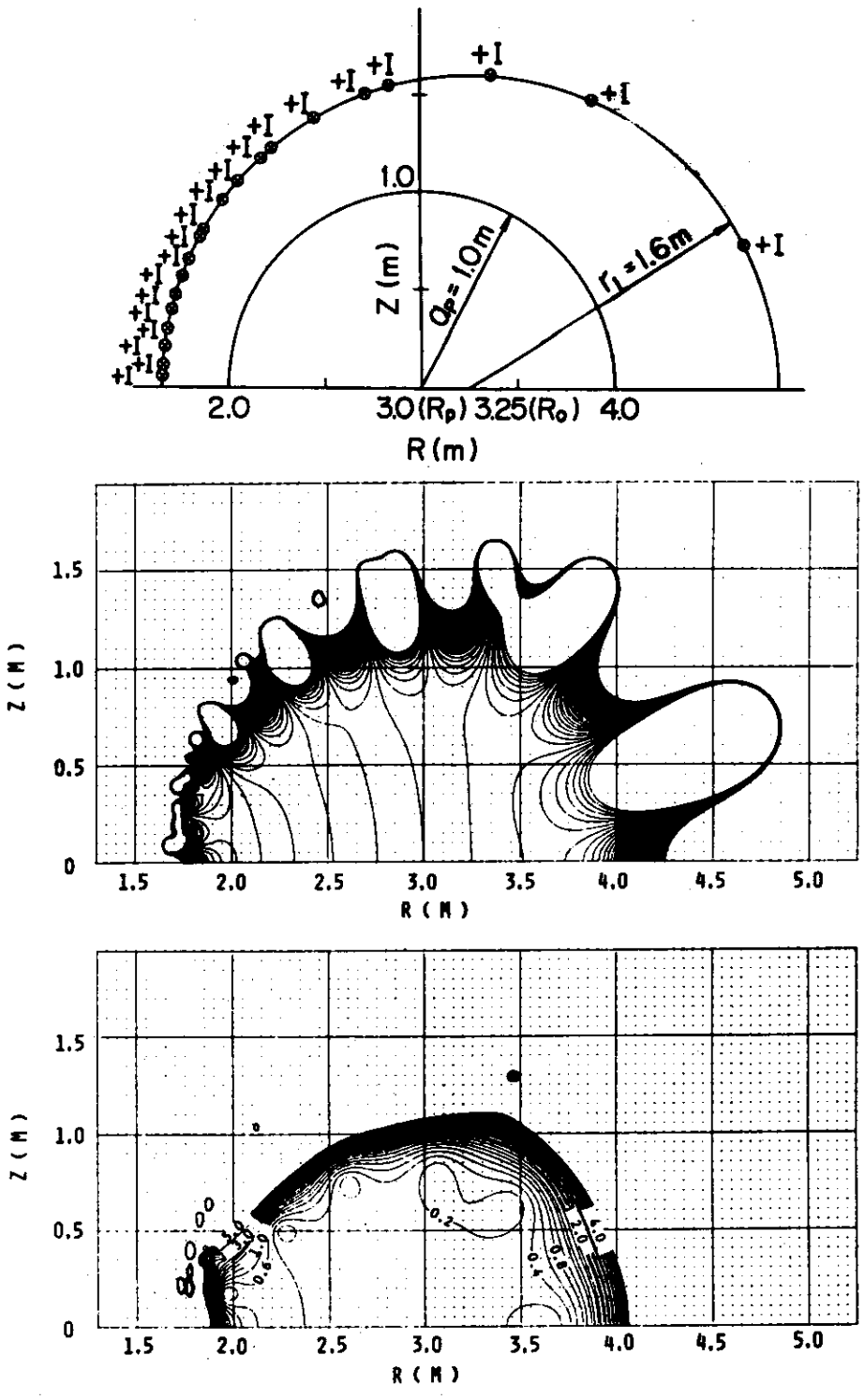

Fig.I.1-15 The optimum configuration of the primary windings (N = 20). The two-dimensional pattern of the magnetic lines of force and the magnitude of the magnetic field (gauss) for the total ampere-turn of 1 MAT.

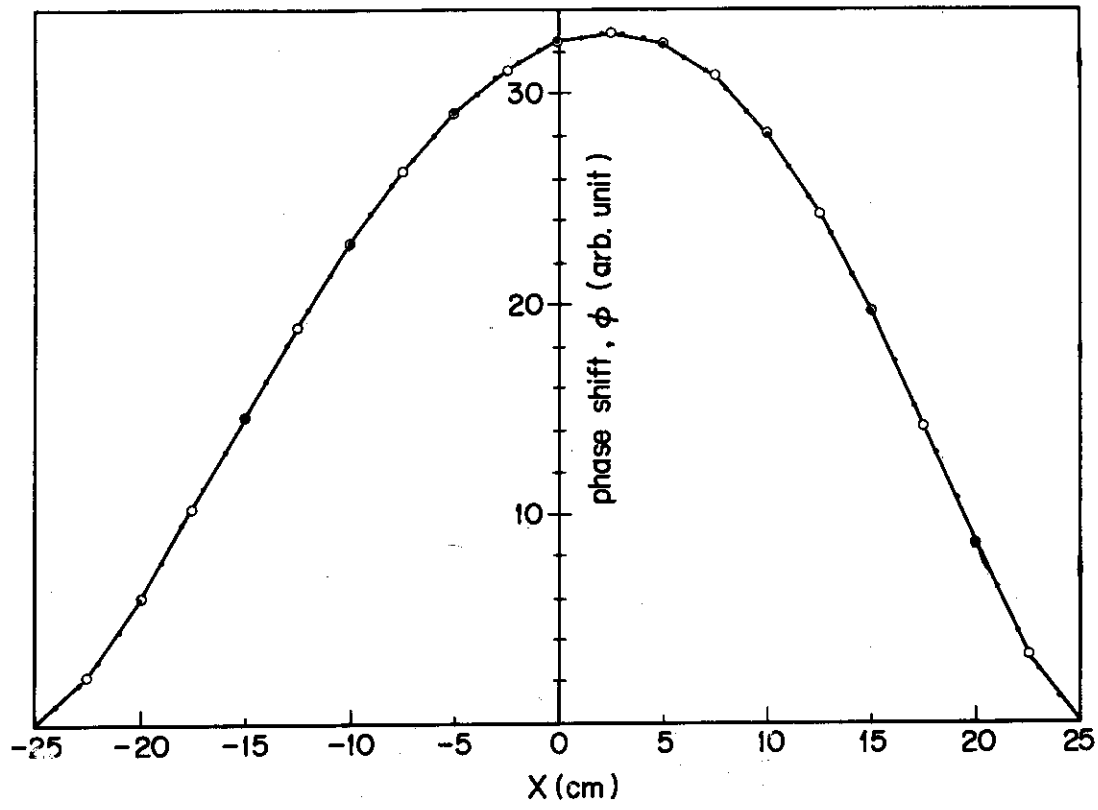

Fig.I.1-16 The microwave phase shift (line density) obtained for the profile (Fig.I.1-17, broken line).

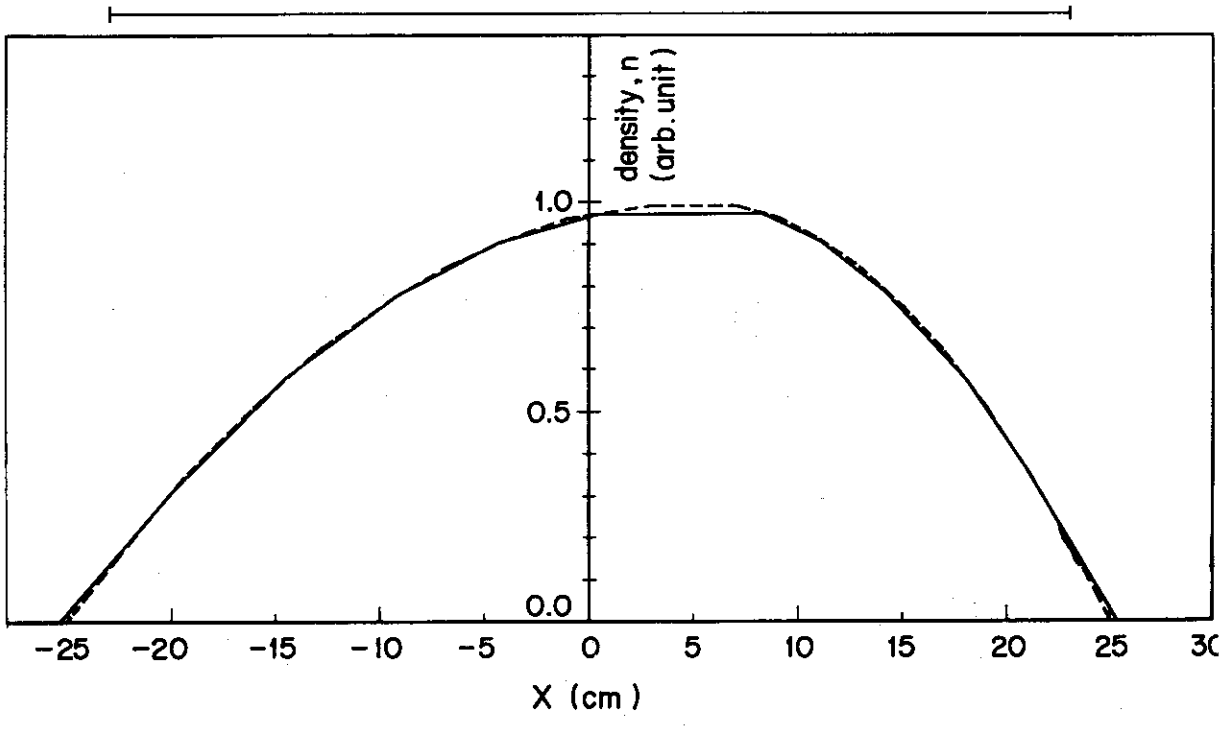

Fig.I.1-17 The density profile on the median plane of a plasma column. The prescribed test profile and the one calculated from the phase shift data (Fig. I.1-16) are shown by broken and solid lines, respectively.

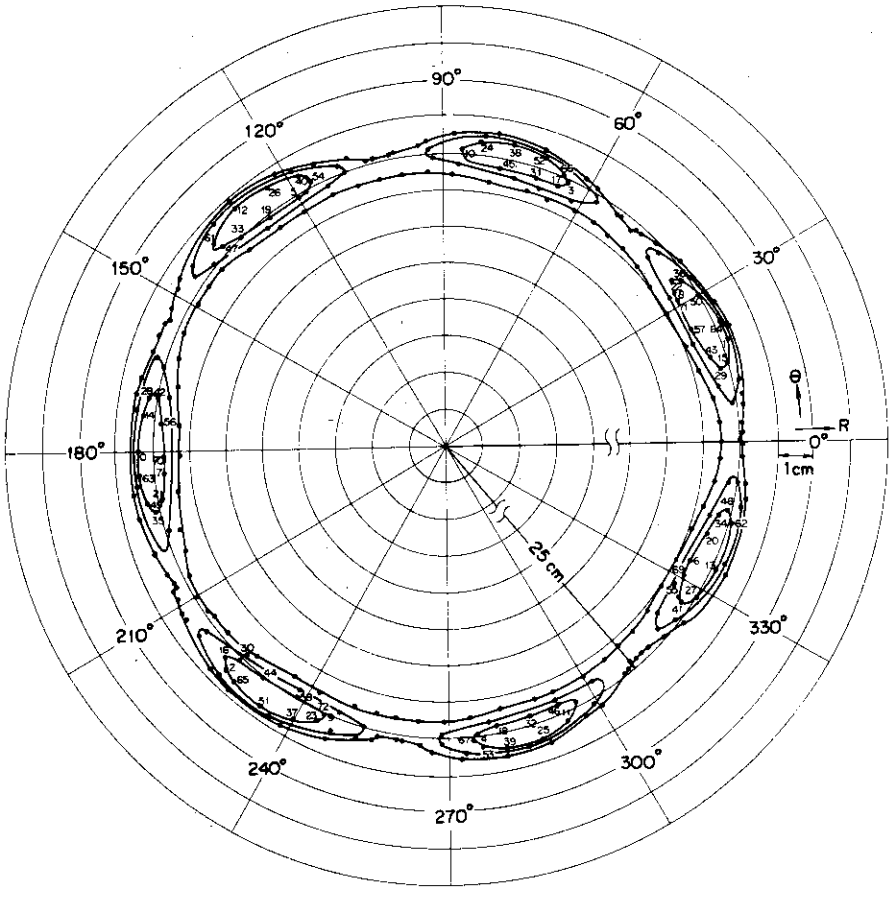

Fig.I.1-18 An example of islands formed by the resonance with the pulsed vertical field in the JFT-2 tokamak at r=25cm. The plasma current distribution is assumed to be parabolic with other parameters q=7/4, Ip=200kA, B_t=10kG, $\langle B_{pv} \rangle$=108G.

2. JFT-2a

A. Kitsunezaki, H. Maeda, M. Nagami,
T. Nagashima, H. Ohtsuka, Y. Shimomura

2.1 Introduction

JFT-2a (DIVA) is a Tokamak device with teardrop-like cross-section and is equipped with an axisymmetric divertor[1)2)3)]. The design of the device was made in 1972[4)] and some engineering tests in 1972 and 1973[5)]. The detailed engineering design was completed in 1973 and the construction started in August 1973. The device was put into operation in September 1974[6)].

The cross-sectional view of JFT-2a is shown in Fig. I.2-1 and detailed description of the device is given in refs. 6 and 7.

The research objectives are summarized as follows.

(1) Plasma production and confinement in a Tokamak with a teardrop-like cross-section with[3)7)] and without a separatrix magnetic surface.

(2) Characteristics of a divertor or a magnetic limiter[2)].

A series of preliminary experiments concerning 1) plasma behavior during discharge cleaning, 2) discharge characteristics with and without a magnetic limiter and 3) plasma density and neutral particle density are reported in the following sections.

(Y. Shimomura)

2.2 Experimental Results

The experimental results described in this section were obtained under the following conditions. The toroidal field is fixed at 1 T and no vertical field is applied. The horizontal field is adjusted so as to locate a plasma on the median plane with the exception of the first 2300 discharges. The divertor hoop current is varied up to 90 % of a plasma current. The movable shell is in open position, the limiters extend 1 cm from the shell, and no titanium is flushed. The base pressure is $(0.3 - 1.5) \times 10^{-7}$ Torr. Hydrogen gas of $(0.4 - 2) \times 10^{-4}$ Torr is

introduced through a variable leak valve or four fast acting valves.

More than 10,000 discharges have been performed in which preliminary measurements were made. The plasma current I_P, the one turn voltage V_D, the divertor hoop current I_D, the vertical plasma displacement Δy, the poloidal field distribution and its fluctuations along the inner shell surface, the electron density from a single channel zebra-stripe 4 mm microwave interferometer and electrostatic probes, the neutral particle density outside the shell, the visible and VUV radiations and the hard X-ray radiation were measured. The other measurements including laser scattering, neutral particle energy analysis, soft X-ray analysis, multi-channel microwave interferometory and thermocouple measurements are under preparation.

1) Plasma behavior during discharge cleaning

Early discharges are macroscopically unstable and/or are characterized by runaway electrons presumably because of the uncleanness of the shell and limiter surface which had been treated with insufficient care and the horizontal error field of about 10^{-3} T due to toroidal coil misalignment. The error field was compensated by the horizontal coils so as to locate the plasma on the median plane. After several hundreds of discharges, the surface of the limiter and the surface of the shell near the limiter were found to be locally contaminated in stripes by black material. The black increased as the shot number increased up to about two thousand and then decreased. After about four thousand discharges, this black material became unrecognizable, and stable and reproducible discharges were obtained.

Before starting measurement, 30-60 discharges of 20 kA current pulses of 20-40 ms duration for 1 $\sim$ 2 hours are needed to obtain stable and reproducible discharges. Fig. I.2-2 shows oscillograms of these preparatory discharges. It is seen that large negative spikes intermittently appear in the loop voltage in the first discharge of a day accompanied by the density and the H_α line fluctuations which decrease with increasing number of discharges. It can be seen that the second peak of the electron line density at R = 63 cm decreases with the shot number. The height of the second peak approaches a constant value after 30 - 50 discharges as shown in Fig. I.2-3.

After venting the vacuum vessel for a day or less, it is necessary to perform about 200 shots of such discharges to obtain stable and

reproducible discharges.

The variation of the characteristics of the early discharges after the vacuum vessel having been exposed to the atmosphere for a month or so is shown in Figs. I.2-4 and I.2-5. The pressure outside the shell increases above the filling pressure and the plasma resistivity is extremely high during the first 20 - 30 discharges. After more shots are fired, we obtain those discharges in which the pressure outside the shell decreases greatly during a discharge, and find that the resistivity and the negative spikes reduce. About one thousand discharges are required to obtain stable and reproducible discharges.

2) Discharge characteristics with and without a separatrix magnetic surface

In this subsection, experimental results with and without exciting the divertor hoop, and some discussions concerning a separatrix magnetic surface and a magnetic limiter are presented. Discharges are obtained with the continuous gas admission.

(i) Typical discharges at 20 kA

Fig. I.2-6 shows oscillograms of typical discharges at about 20 kA, which gives the q value of about 4 in a circular cross-section Tokamak with a major radius of 60 cm and a minor radius of 10 cm. On the left-hand side oscillograms without a divertor hoop current (Case A) are shown and on the right-hand side we see oscillograms with a divertor hoop current of 90 % of a plasma current (Case B). Their gross behavior is rather similar, except that the discharge with a divertor hoop current lasts longer because a plasma column shifts outward without a divertor hoop current and a vertical field. The resistivity temperature is about 70 eV at 13 ms assuming $\bar{Z} = 2$, and the average density measured by a zebrastripe 4 mm microwave interferometer is about 1.4×10^{13} cm ^{3} at R = 63 cm. The pressure measured by a fast ionization gauge placed 10 cm from the plasma in the gap between neighboring shell sectors shows a drop of the filling pressure from 1.3×10^{-4} Torr to a plateau of 2.5×10^{-5} Torr. Negative spikes intermittently appear in the loop voltage during the discharge accompanied by a sudden increase of the L_{α} line and C IV line intensity (1548.2A), and by density fluctuations.

The density distribution was measured by single-channel 4 mm microwave

interferometer for the bulk of the plasma (Fig. I.2-7). Typical photographs of a plasma column are shown in Fig. I.2-8. It is clear that a plasma of Case A shifts outward and a plasma of Case B locates at the center of the shell except at the end of the discharge. Except the positions of plasmas, the characteristics of density distribution and time variations of Case A and Case B are similar during the initial 15 ms. Fig. I.2-9 shows the magnetic field distribution measured by magnetic probes placed on the inner shell surface. For comparison, also shown in the figure are the calculated poloidal field distributions for a uniform current distribution of two values of β_p. It is noted that the measured magnetic field distribution agrees with the calculated one in the case of $\beta_p = 0.1$ whose equilibrium configuration is shown in Fig. I.2-10. However, the agreement does not necessarily exclude other current distributions and other values of β_p.

The density distribution in the outskirt of the plasma is measured with double probles. Fig. I.2-11 shows typical waveforms of ion saturation currents near the divertor hoop (R = 40 cm and Z = -3.75 cm) and near the inner shell surface (R = 68 cm and Z = -6.2 cm). The ion saturation current of Case B near the divertor hoop is about 10^3 times as large as that of Case A except at the beginning of the discharges. The density profile near the divertor hoop obtained by scanning a double probe (Fig. I.2-12) shows a peak at Z = -3 cm, suggesting the presence of plasma extending towards the divertor near the separatrix magnetic surface. The electron temperature is about 10 eV and the maximum plasma density is about 1×10^{12} cm^{-3} at 13 ms. The density profile near the inner shell surface obtained by scanning a double probe (Fig. I.2-13) shows that the ion saturation current of a plasma with a separatrix magnetic surface is less than that without a separatrix magnetic surface only at the beginning of a discharge.

The full profile of the ion saturation current near the divertor hoop is shown in Fig. I.2-14 for Case B. It is clearly seen that the profile has asymmetry as to the median plane. The larger peak always locates at 3 cm from the median plane in the direction of electron drift even when the direction of toroidal field and/or plasma current are varied. It is considered that the radial and/or toroidal electric field and toroidal magnetic field cause this asymmetry.

Fig. I.2-15 shows oscillograms of typical discharges with a divertor hoop current of 45 % of a plasma current (Case C). In this case, the gross

behavior of a main plasma is similar to that of Case B but the ion saturation current near the divertor hoop is about 10^{-2} of that of Case B except at the beginning of a discharge. In Fig. I.2-15, the ion saturation current at R = 40 cm and Z = -2 cm is shown. This is similar to those in other positions (R=40 cm and Z=-3∿+3 cm).

(ii) Typical discharges at higher and lower currents

Fig. I.2-16 shows oscillograms of discharges of 20 kA, 25 kA and 30 kA with a divertor hoop current of 90 % of a plasma current. The plasma is unstable with a plasma current of more than 20 kA and the current does not increase any more than 30 kA. Fig. I.2-16 shows negative spikes occurring in the discharge of 25 kA together with the corresponding fluctuations of the poloidal magnetic field. It is observed that the fluctuations of poloidal field at frequency of about 20 kHz are excited, and the amplitude of the fluctuations increases until a negative spike apears as shown in Fig. I.2-17. In discharges at a current lower than about 15 kA, distruptive fluctuations in the one turn voltage, electron density and line radiation greatly reduce.

(iii) Discussions

It is interesting to know whether a plasma enclosed inside a separatrix magnetic surface is produced or not in this device. In the case of I_D/I_p = 0.9 (Case B), a plasma of the density of 1×10^{12} cm^{-3} is observed and, in the case of I_D/I_p = 0.45 (Case C), very thin plasma is observed except at the beginning of a discharge. These experimental results are consistent with calculated results. In Case B, it is clear that a plasma enclosed inside a separatrix magnetic field is produced and the plasma extends into the divertor region approximately along the magnetic surfaces. At the beginning of a discharge in all cases, plasma may be produced near the divertor hoop because of the high pressure, large one turn voltage and small rotational transform, and rather large ion saturation currents are observed near the divertor hoop as shown in Figs. I.2-11, I.2-12 and I.2-15.

The experimental results described above indicate that, there are no significant difference is the gross behavior between the plasmas with and without a separatrix magnetic surface. It is also indicated that the MHD behavior of a plasma with a teardrop-like cross-section with a separatrix magnetic surface is similar to that of a conventional Tokamak. Numerical

calculation of localized mode also shows that the current density limit of this device with a large aspect ratio is not largely different from that of a conventional Tokamak. Detailed investigation of this behavior is further needed. But it can be said that no adverse effects of the separatrix magnetic surface on the plasma confinement are observed. This result encourages an attempt to reduce impurity content in a confined plasma by means of an axisymmetric divertor.

Preliminary results suggest that the plasma flow into the divertor region is not dominant in these discharges because there is no significant difference between the plasmas with and without a separatrix magnetic surface. In ref. (2), the particle flux into the divertor was estimated assuming a mirror loss in which the particle flux is determined by the collisional frequency and not by the flow velocity of each particle. In the discharges described above, the collisional time is less than 10 μs assuming that the ion temperature is lower than the electron temperature, and the flow time of the plasma along the magnetic field from the confinement region into the divertor region is 50 μs or more assuming that the flow velocity is 0.5 × (sound velocity). Therefore, the estimation shown in ref. (2) is not reasonable in these discharges. Another estimate applicable to cases where the flow velocity along magnetic field lines is slow and particle diffusion across magnetic field lines is large are described below. If the following equation is satisfied, most of the particles lost from the confinement region reach the divertor region.

$$x_b >> \sqrt{\tau_f D} \equiv x_D,$$

where x_b is the distance between the confined plasma and the wall, D is the particle diffusion coefficient and τ_f is expressed by the following equation.

$$\tau_f \simeq \pi R\bar{q}/V_f,$$

where V_f is the flow velocity along the magnetic field lines. Assuming V_f = 0.5 × (sound velocity) and D = (anomally factor) × (neoclassical diffusion coefficient), x_D for a hydrogen plasma with $\bar{q} \simeq 4$ and R = 60 cm is expressed by the following equation

$$x_D \simeq 4 \times 10^{8}\sqrt{\gamma \bar{q}^3 [n(cm^{-3})][T_e(eV)]^{-1}}/B_T(T) \text{ cm} .$$

For Case B at 13 ms, $x_D \simeq 0.2\sqrt{\gamma}$ cm and $x_b < 1$ cm. Assuming $\gamma \gtrsim 100$, a larger part of the particles lost from the confinement reaches not to the divertor region but to the wall. Assuming that the flow velocity is 0.5 × (sound velocity), the experimental particle flow into the divertor region is about 3.5×10^{16} (particles/ms) at 13 ms in Case B and the particle loss flux from the confinement is $1.5 \times 10^{18}/\tau_n$ at the same time where τ_n is particle confinement time. τ_n has not been measured but must be smaller than 10 ms. From these estimations, it can be said that most of the particles lost from the confinement reach not to the divertor region but to the wall in these discharges.

In order to realize an effective magnetic limiter and/or divertor, it is necessary to increase the particle flow F_D to the divertor and to decrease the particle flow F_W to the wall. It is considered to be resonable that F_D/F_W is small in JFT-2a which is of small dimensions and has a weak toroidal field. F_D/F_W may be increased effectively by increasing the intentisty of the toroidal field but the maximum intensity of the toroidal field is 1 T is JFT-2a. Another possibility of increasing F_D/F_W is to increase rotational transform or plasma current. However, experimental results show that the plasma becames unstable when a plasma current is more than 20 kA, and it can be said that it is impossible to increase largely F_D/F_W by largely increasing rotational transform in a stable discharge.

The flow velocity into the divertor region and particle confinement time may increase as increasing plasma temperature and as decreasing plasma density. It is under preparation to investigate these possibilities by reducing a greater part of neutral particles around a plasma by using fast acting valves and flushing titanium.

It is being prepared to increase the distance from confined plasma to the wall by increasing a divertor hoop current.

Further detailed investigation is needed concerning the particle and heat flux into the divertor region, the particle and energy confinement time, the electron and ion temperature and the impurity contents.

3) Plasma density and neutral particle density

To start discharges as soon as possible after hydrogen gas being

admitted by four fast acting gas valves of various plenum pressures, a large one turn voltage in the early phase of discharge is required that is obtained by using two condenser banks. These two condenser banks are discharged one after the other and supply a large one turn voltage of about 100 V in the early phase of discharge and sustain a plasma current at a constant value for several milliseconds. Four fast acting gas valves are axisymmetrically located and supply hydrogen gas directly into the shell. In this subsection, discharge characteristics of plasma and neutral particle density under various discharge conditions are described.

(i) Experimental data

Fig. I.2-18 shows oscillograms of typical discharges using two condenser banks. The discharge starts at 0.8 ms after the four fast acting valves are driven. A plasma current reaches the maximum value at 1.2 ms after the start of discharge, and the one turn voltage and the plasma current are sustained at constant values for 7 ms. The resistivity temperature is about 100 eV for this period assuming $\bar{Z} = 2$ and uniform distribution. Plasma density reaches the first peak value at about 1.5 ms. In Fig. I.2-18, neutral particle density outside the shell (R=50 cm and Z=20 cm) is also shown. The discharge starts at the time when the pressure at R = 50 cm and Z = 20 cm reaches one third of the mean filling pressure in the vacuum chamber. The neutral particle density at this position reduces during the discharge and reaches a value less than one tenth of the mean filling pressure at the end of the discharge.

The time variations of the electron line density distribution and total electron number are shown in Fig. I.2-19 under various discharge conditions; fast acting gas valves and $I_D/I_P = 0.9$ (Case (FB)), continuous leak valve and $I_D/I_P = 0.9$ (Case (CB)), fast acting gas valves and $I_D = 0.0$ (Case (FA)). It can be seen that there are no significant differences between those cases shown in Fig. I.2-19 except that the position of the density peak shifts outward in Case (FA) without exciting the divertor hoop as described in 2.2.2. In all of those cases, the density distribution becomes sharp, then negative spikes appears and the plasma column spreads. In the cases with $I_D/I_P = 0.9$, the total number of electrons at the first density peak is equal to the total number of atoms admitted in the shell. The value of the first density peak is constant even if a plasma current varies from 12 kA to 27 kA.

In Fig. I.2-20, the time variations of the total number of electrons and neutral particles are shown. The total number of neutral atoms is calculated from the pressure at R = 50 cm and Z = 20 cm assuming that the density of neutral particles is uniform outside the shell. It is shown that the sum of atoms and electrons reduces after 10 ms and is only one twenty-fifth of the number of the atoms admitted. The total number of atoms in the vacuum chamber increases in the time constant of several seconds after discharge.

Fig. I.2-21 shows the relation between the line electron density at the first peak and filling pressure and it is shown that a plasma with various density can be obtained.

(ii) Discussion

By using fast acting gas valves and applying a large one turn voltage, most of the particles admitted are ionized and trapped at about 2.3 ms after the fast acting gas valves are driven, and the number of the remaining neutral particles outside the shell is about one sixth of the of admitted gas at the same time if we assume that the neutral particle density is uniform outside the shell. The total number of electrons at the first density peak is equal to the total number of atoms admitted in the shell but the total number of electrons at the second peak varies with discharge conditions in which the filling pressure remained constant as shown in 2.2.1. It may be noted here that the interaction between the walls and a plasma plays a dominent role in the latter part of discharge.

Not only the total number of neutral particles but also the sum of neutral particles and electrons reduces after 10 ms and it is clear that the atoms admitted in the vacuum chamber are absorbed into the wall during the discharge. These absorbed particles are released long after the discharge and the desorbing time constant is several seconds. It has not been investigated that which surface plays an important role in this phenomenon.

It is interesting that the total number of electrons is roughly constant for several milliseconds, but it is not clear what kind of particle recycling process plays an important role. Particle influx from the outside of the shell is estimated to be less than 3×10^{16} (particles/ms) at 10 msec assuming that hydrogen molecules spread into the shell with thermal velocity of 300 °K. Particle flux due to the thermal desorption

is estimated to be less than 10^{15} (particles/ms) at the same time from Fig. I.2-20. Sum of these flux is much less than the total particle loss flux of plasma which is 1.5×10^{17} (particles/ms) even if we assume that particle confinement time is 10 ms. For this reason it is reasonable to consider that other recycling process is important in this device.

4) Conclusion

Preliminary measurements indicate that a plasma enclosed inside a separatrix magnetic surface is obtained and no adverse effects of the separatrix magnetic surface are observed. This experimental result encourages the attempt to reduce impurity content in a plasma by using an axisymmetric divertor in a future large Tokamak. However, the plasma particle flux into the divertor region is not considered to be dominant part of the loss flux from the confined plasma in JFT-2a which is of the small dimentions and a weak toroidal field. It is also shown that electric field is important to the plasma behavior near the separatrix magnetic surface.

By using four fast acting gas valves, a greater part of admitting gas are ionized and confined at about 2 ms after the admission and it is shown that the particle influx into a plasma from thermal desorption is not dominant in the device. The typical plasma parameters are summarized below.

Plasma current	I_p = 20 kA
Divertor hool current	$I_D = 0.9 \times I$
Pulse length	T_D = 30 ms
Mean electron density in the shell	$\bar{n}_{es} = 1.2 \times 10^{13}$ cm^{-3}
Conductivity temperature (assuming $\bar{Z}$=2 and uniform distribution)	T_e = 100 eV

Further detailed measurements including laser scattering and neutral particle energy analysis are under preparation.

Further experiment is required especially concerning the particle and heat flux into the divertor region with and without flushing titanium.

(A. Kitsunezaki, H. Maeda, M. Nagami,
T. Nagashima, H. Ohtsuka, Y. Shimomura)

References

1) Yoshikawa, M. et al., Fifth Conference on Plasma Physics and Controlled Nuclear Fusion Research (Tokyo, 1974) Paper CN-33/A1-2.
2) Yoshikawa, M., Shimomura, Y., Maeda, H., and Kitsunezaki, A., Sixth European Conference on Controlled Fusion and Plasma Physics (Moscow, 1973) 173.
3) Kitsunezaki, A., Maeda, H., Shimomura, Y. and Yoshikawa, M., Third International Symposium on Toroidal Plasma Confinement (Garching, 1973) Paper G-2.
4) Annual Report of JAERI Thermonuclear Fusion Laboratory (for period ending March 31, 1972) JAERI-M 5029 (1972) 54.
5) Annual Report of JAERI Thermonuclear Fusion Laboratory (covering the period April 1, 1972 - March 31, 1973) JAERI-M 5564 (1973) 50.
6) Annual Report of JAERI Thermonuclear Fusion Laboratory (covering the period April 1, 1973 - March 31, 1974) JAERI-M 5888 (1974) 23.
7) Shimomura, Y., et al., JAERI-M 6102 (1975).

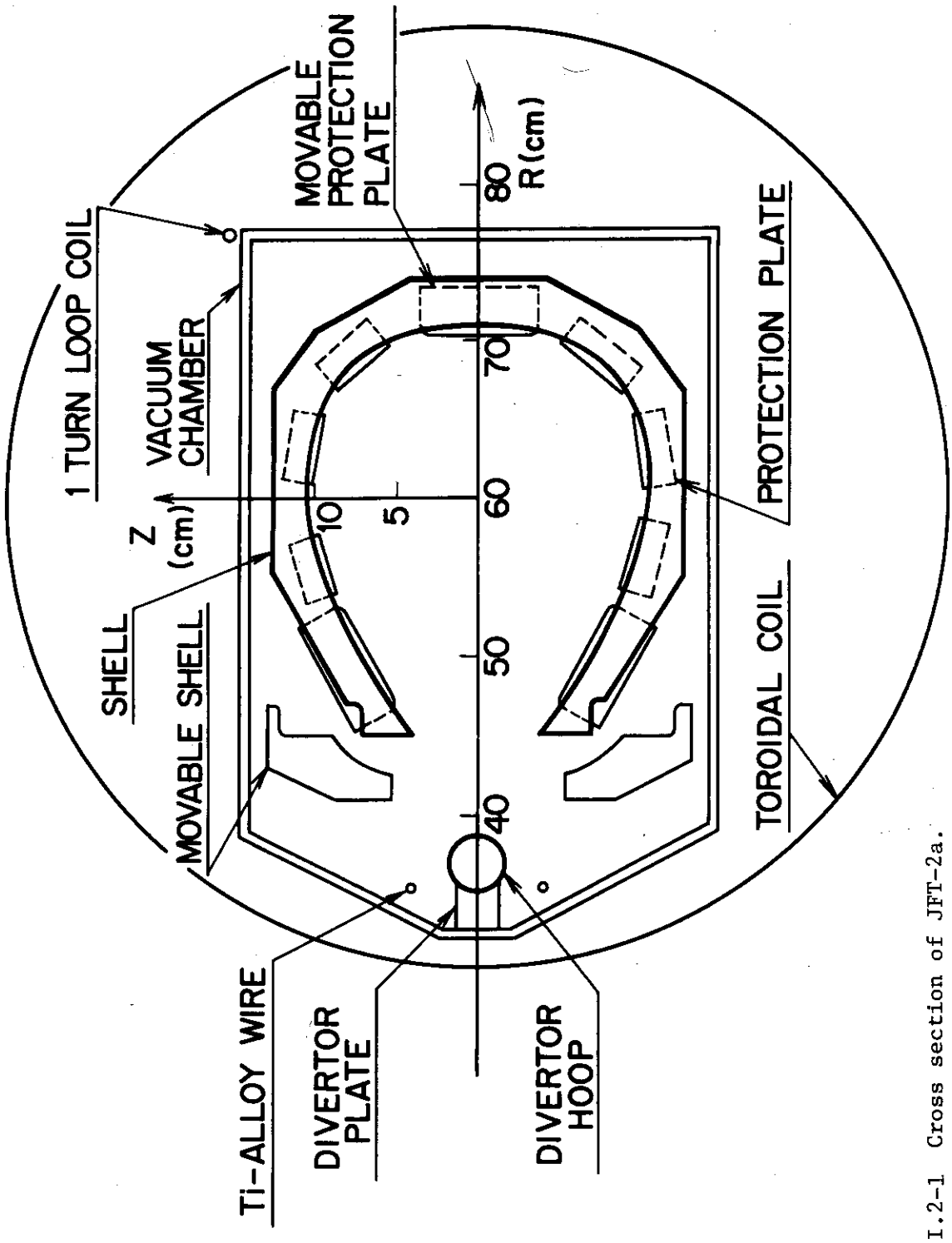

Fig.I.2-1 Cross section of JFT-2a.

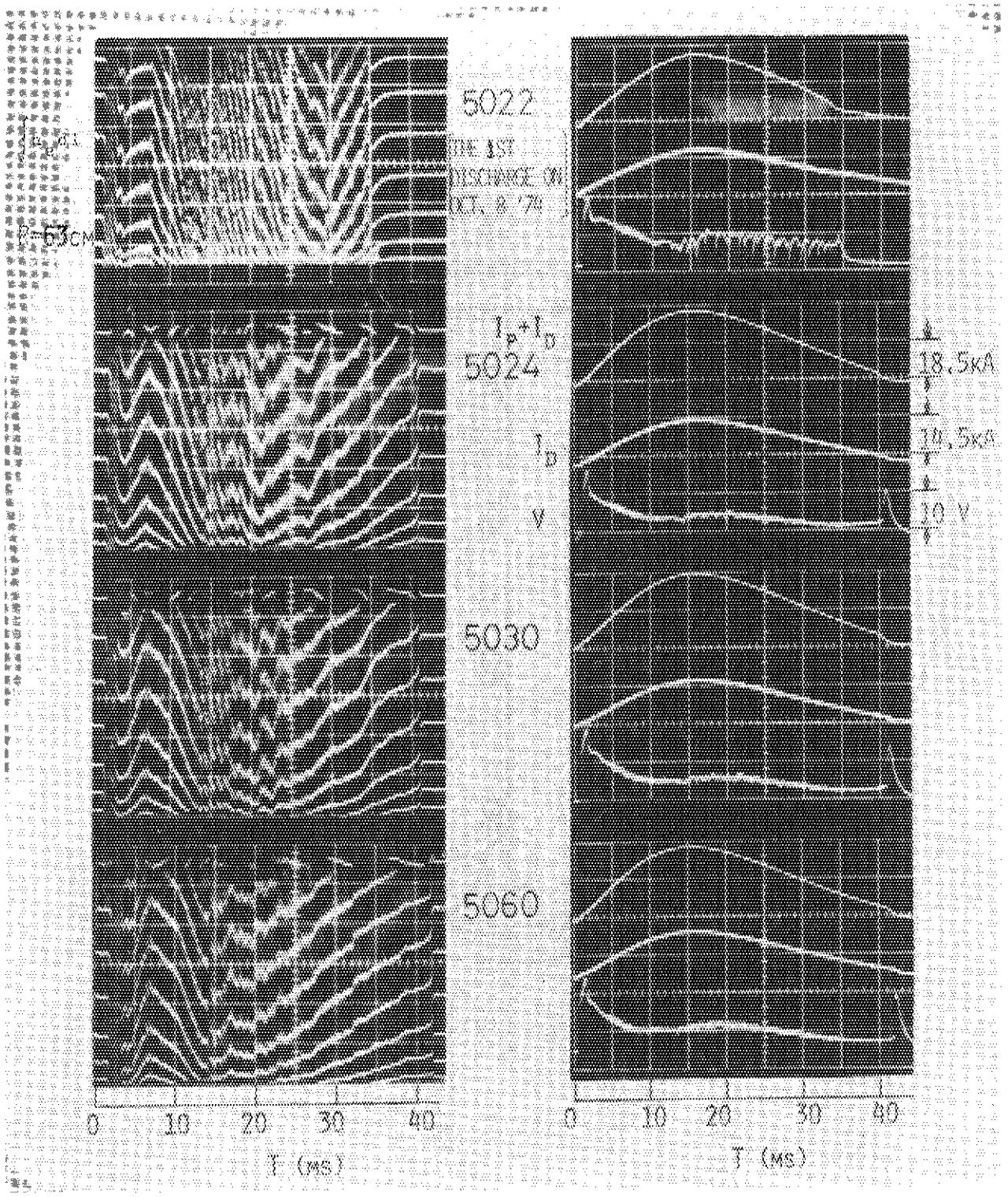

Fig.I.2-2 Oscillograms of sum of plasma current I_P and divertor hoop current I_D, I_P, loop voltage V, electron line density, and light intensity of H_α line. The operation condition is I_D/I_P = 0.9, B_V = 0 and the continuous filling pressure = $\sim 1.4 \times 10^{-4}$ Torr.

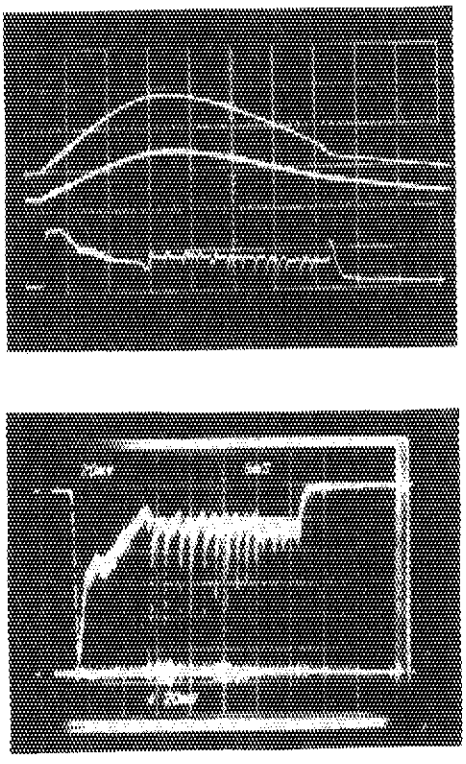

Fig.I.2-2

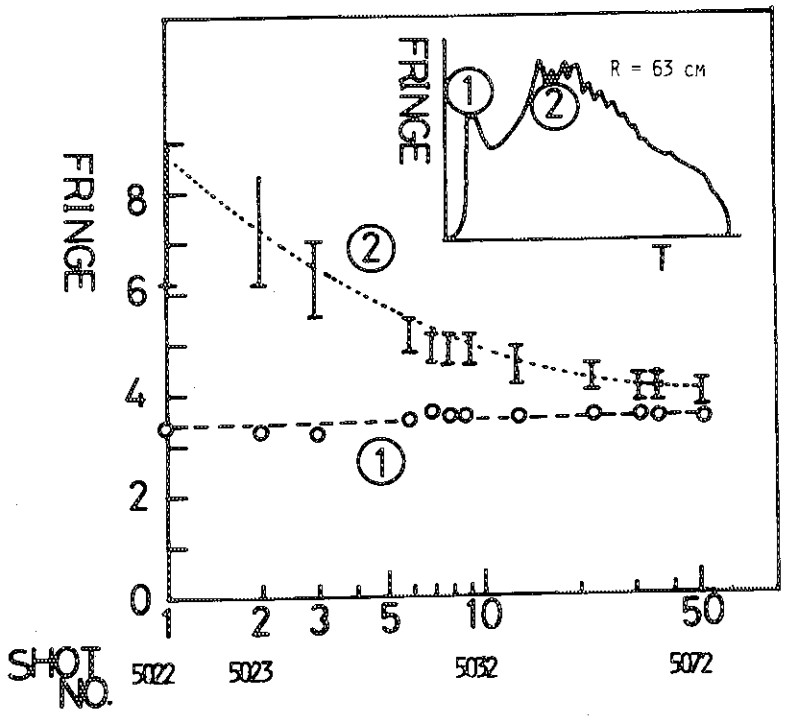

Fig.I.2-3 Electron line density vs. shot-number where the discharge of No.5022 is the first shot on a day. The operation condition is the same as in Fig.I.2-2.

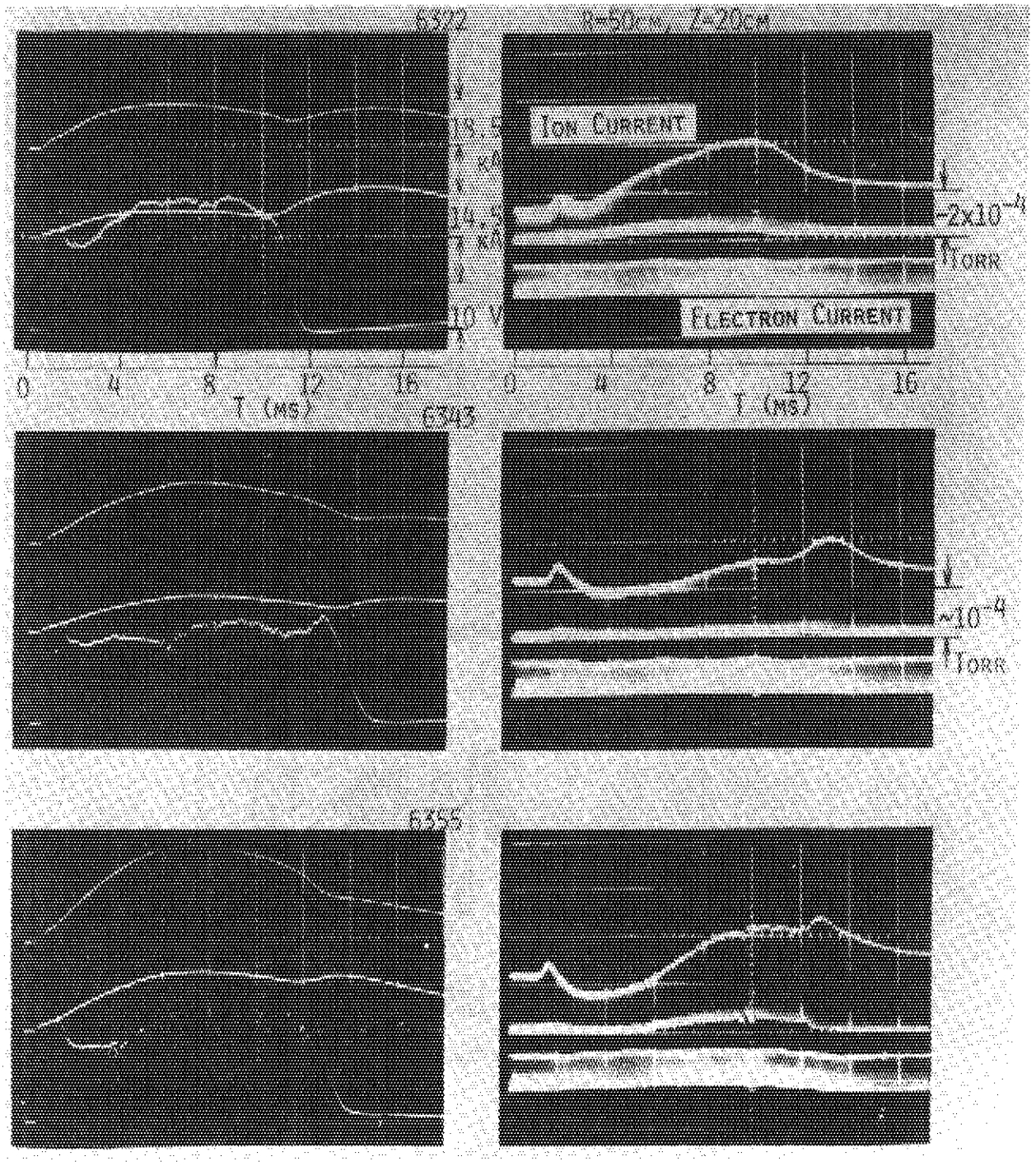

Fig.I.2-4 Oscillograms of sum of plasma current I_P and divertor hoop current I_D, I_D, loop voltage V, and ion and electron currents of fast ionization gauge. The discharge of No.6322 is the third discharge after opening the vacuum vessel to the atmosphere for about a month. The operation condition is the same as in Fig.I.2-2.

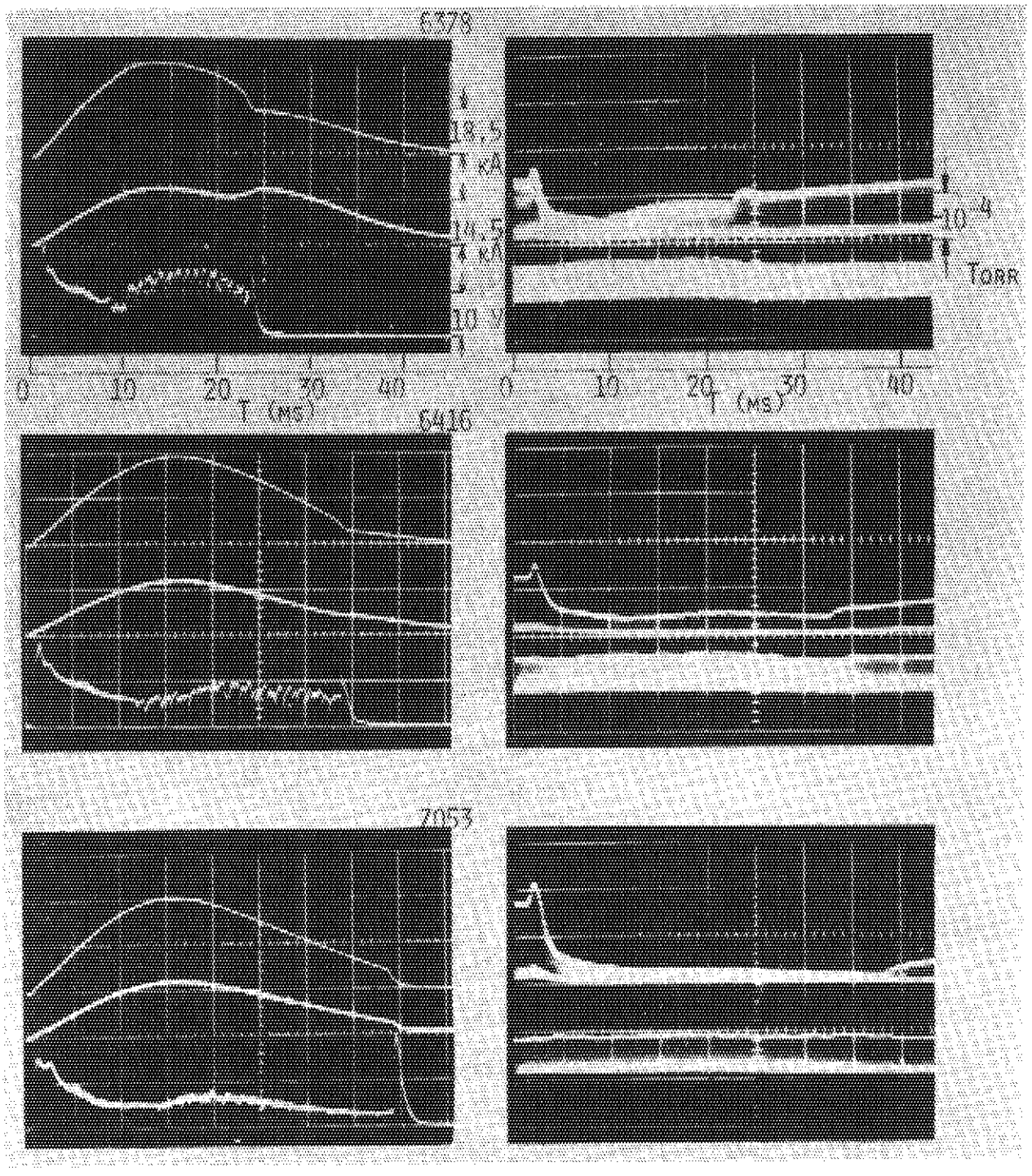

Fig. I.2-4

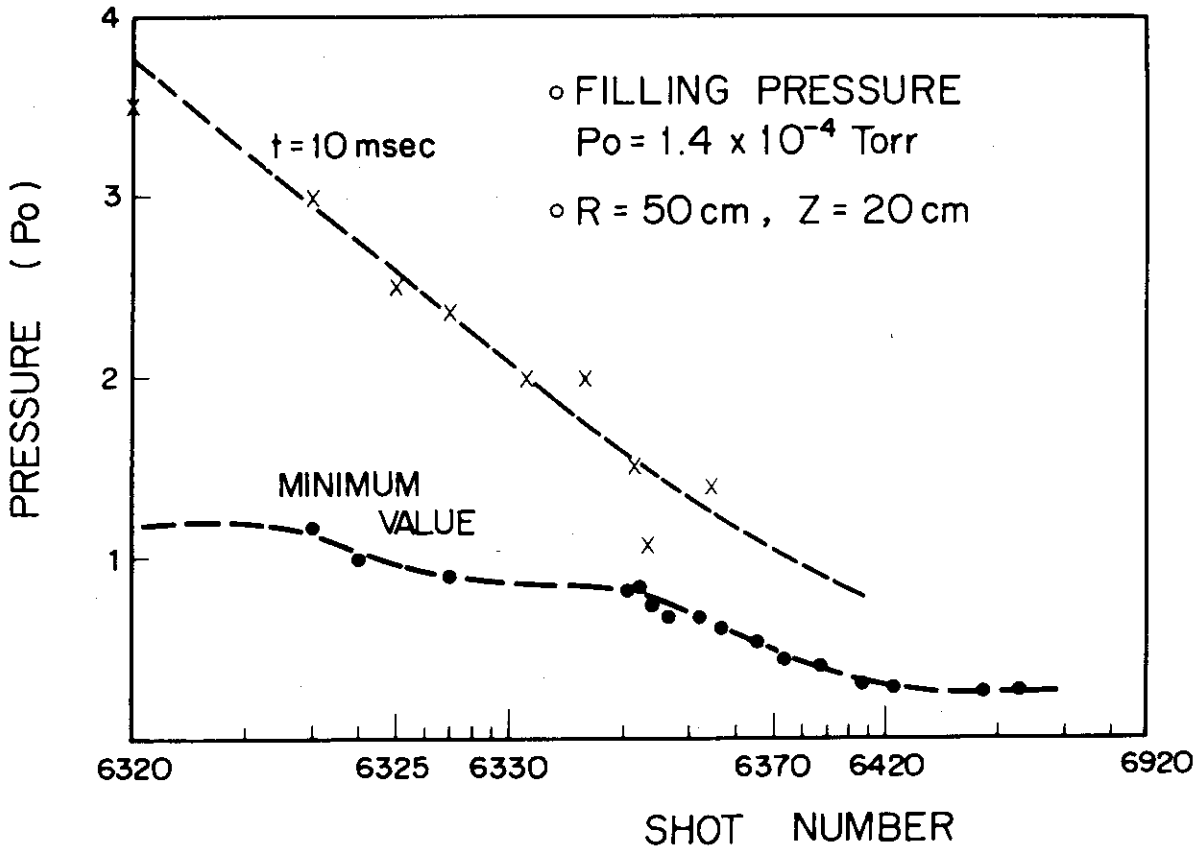

Fig.I.2-5 Neutral particle pressure vs. shot-number. The discharge of No.6320 is the first discharge after opening the vacuum vessel to the atmosphere for about a month. The operation condition is the same as in Fig.I.2-2.

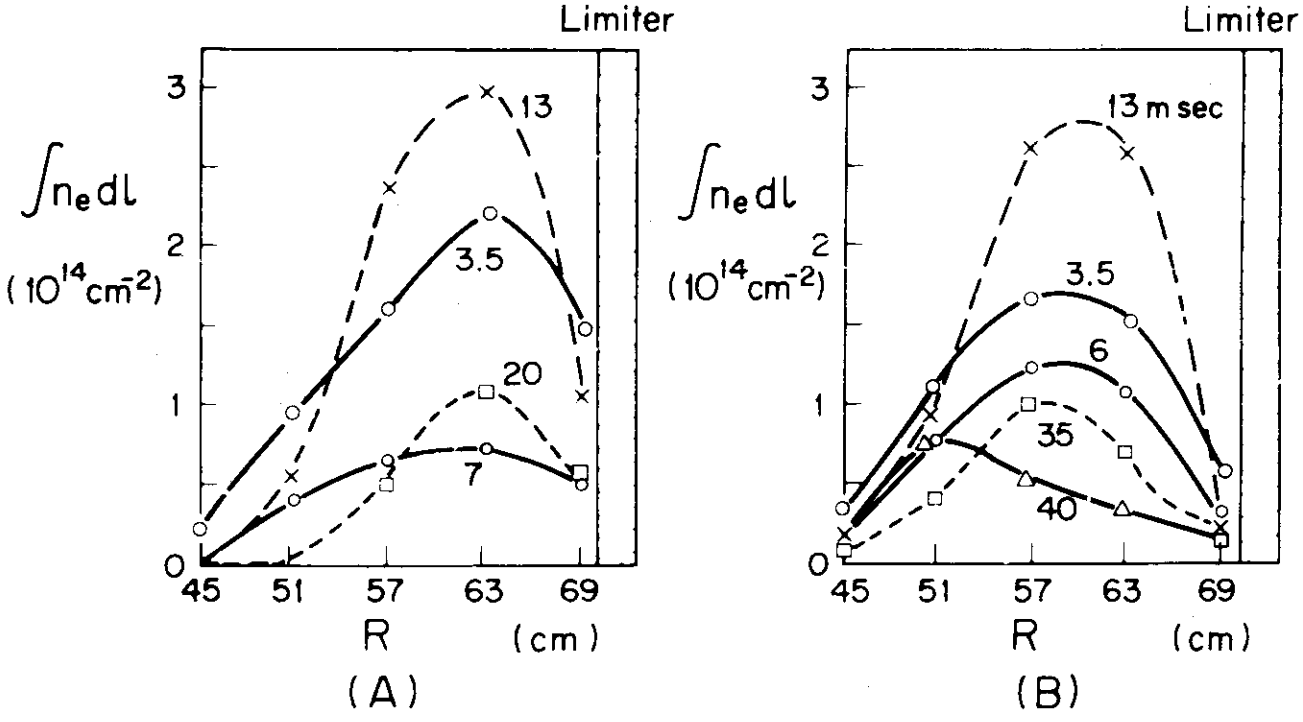

Fig.I.2-7 Time variation of electron line density distribution. The operation condition is the same as in Fig. I.2-6.

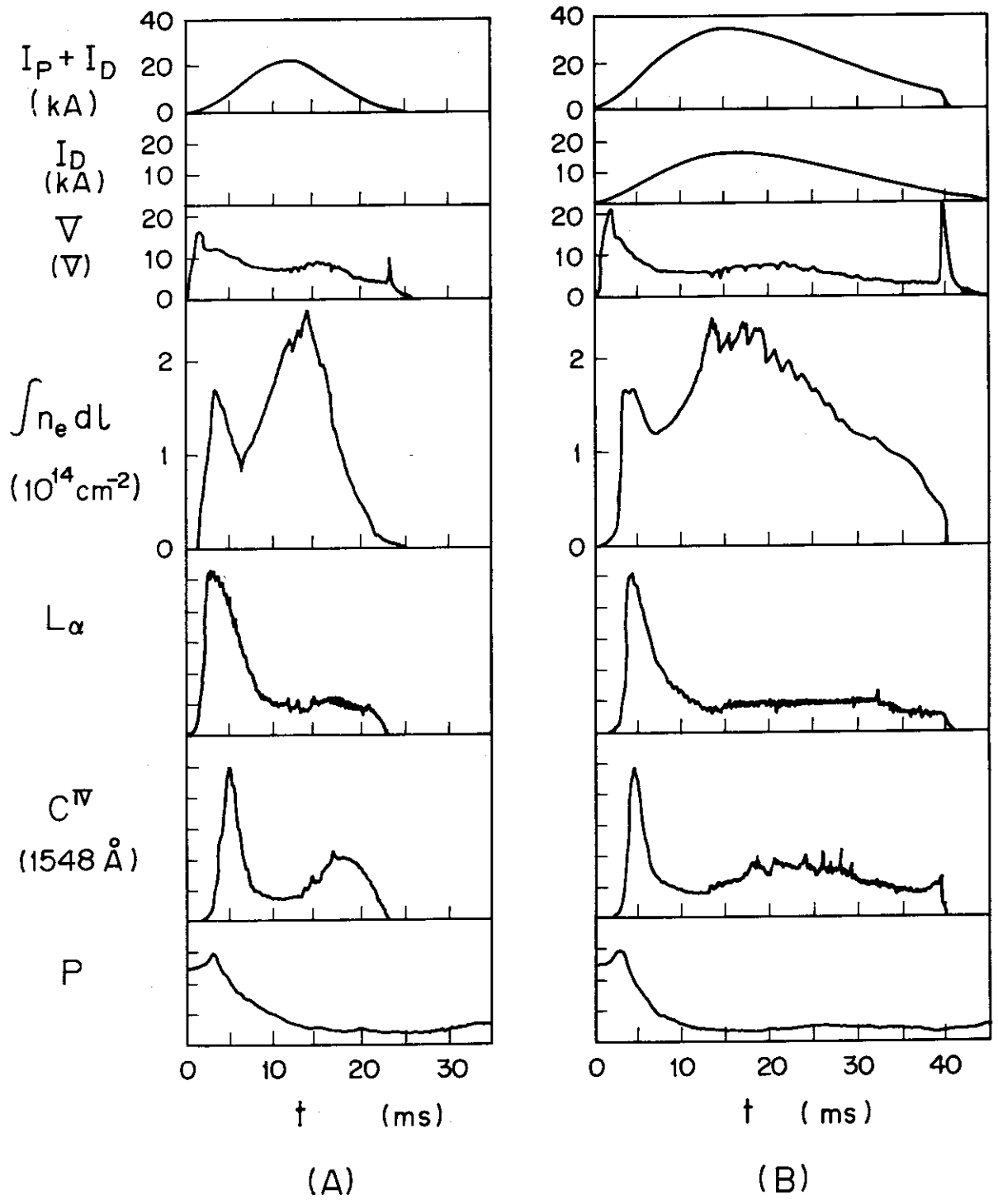

Fig.I.2-6 Oscillograms of sum of plasma current I_P and divertor hoop current I_D, I_D, electron line density, light intensities of L_α and CIV lines, and neutral particle pressure P_o at the gap of neighboring shell sections. Case A is for $I_D/I_P=0$ and Case B for $I_D/I_P=0.9$. The operation condition is $B_V=0$ and the continuous filling pressure 1.3×10^{-4} Torr.

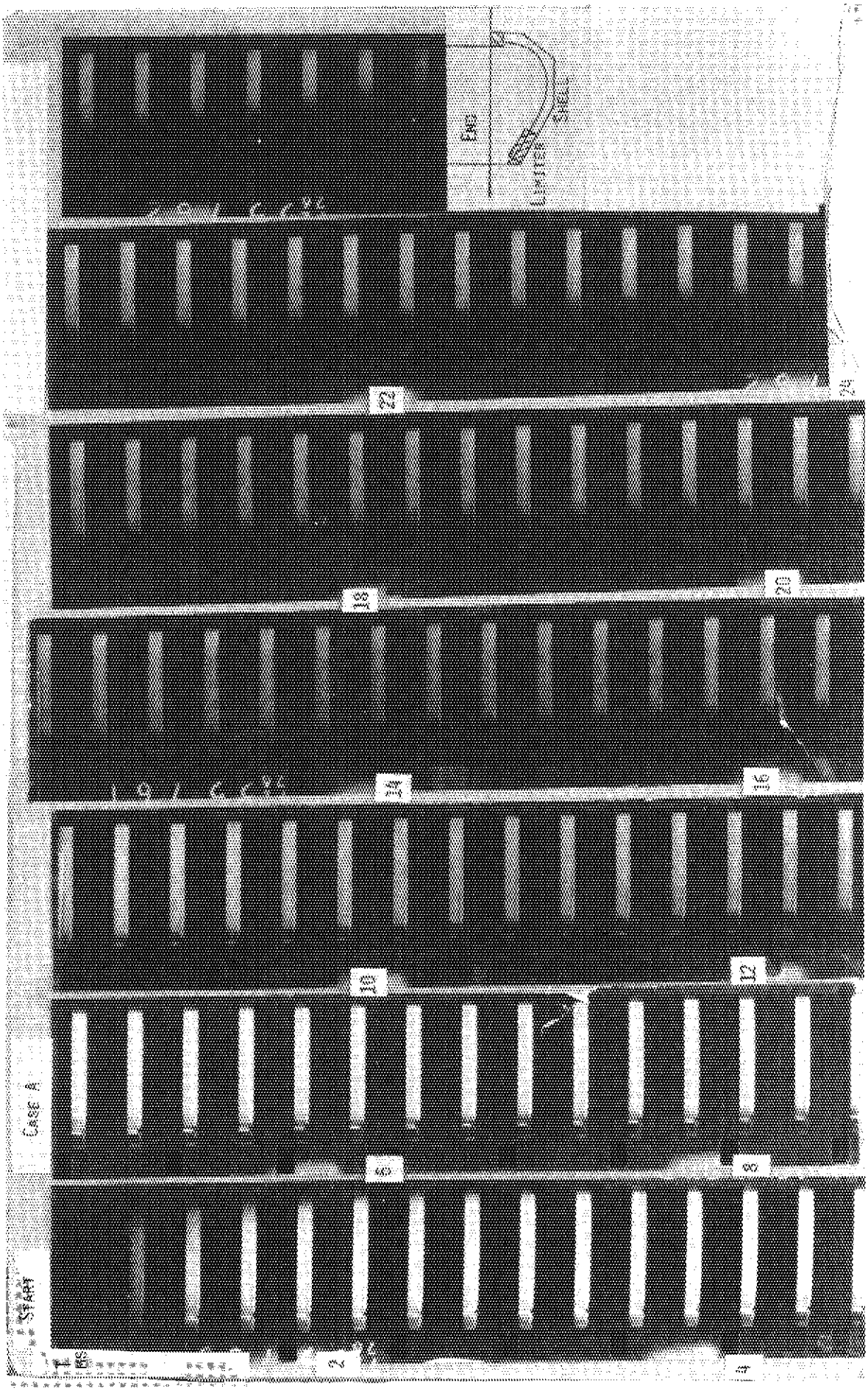

Fig.I.2-8-a Photographs of plasma column. The operation condition is the same as in Fig.I.2-6.

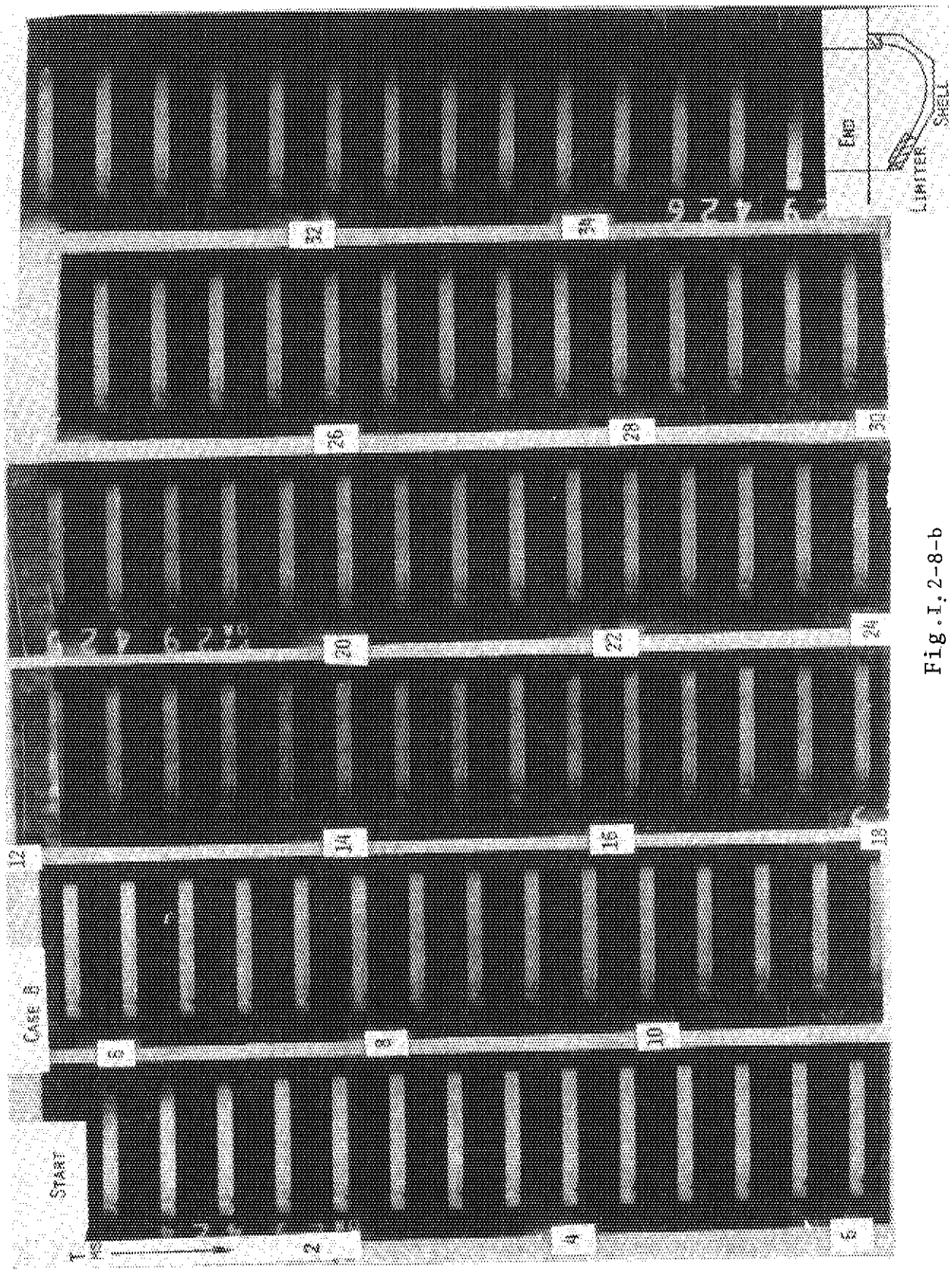

Fig. I. 2-8-b

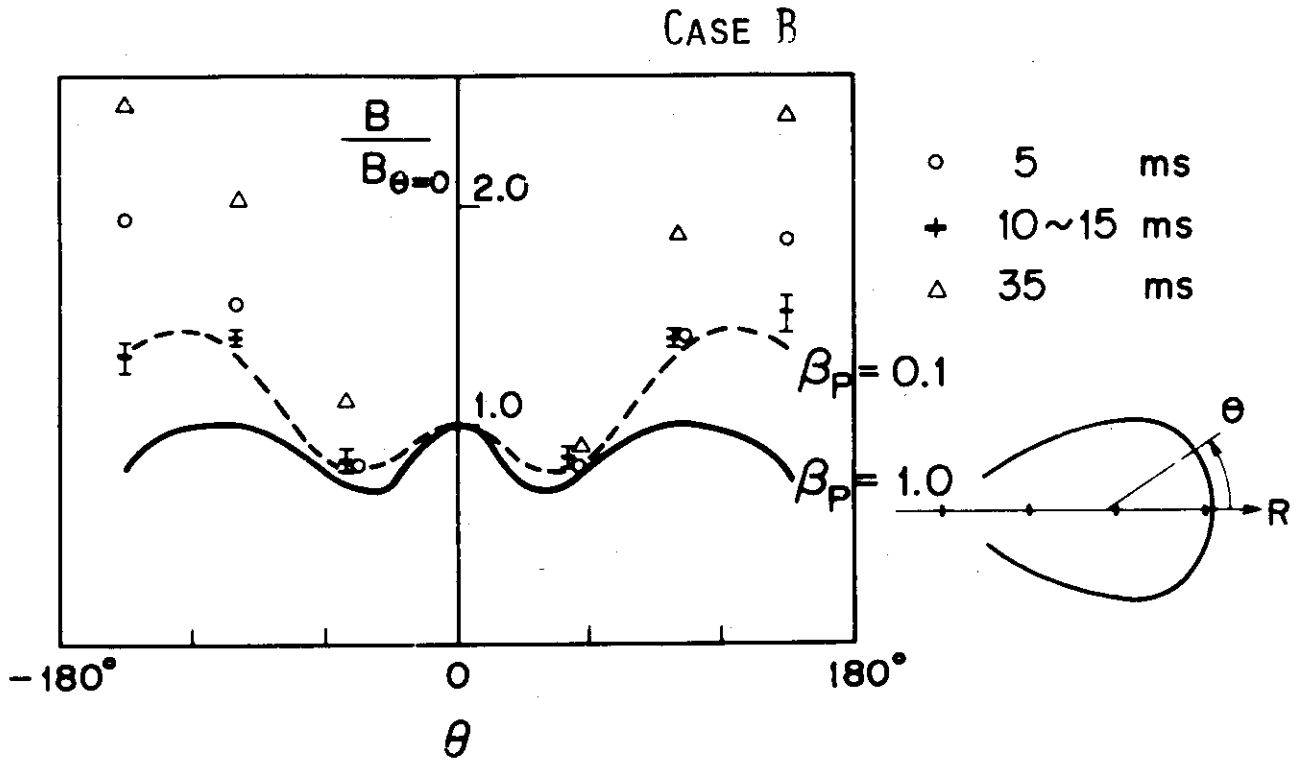

Fig.I.2-9 Poloidal magnetic field distribution on the inner surface of the shell measured by magnetic probes for Case B. Curves show calculated results for a uniform current distribution with βp=1 and 0.1. The operation condition is the same as in Fig.I.2-6.

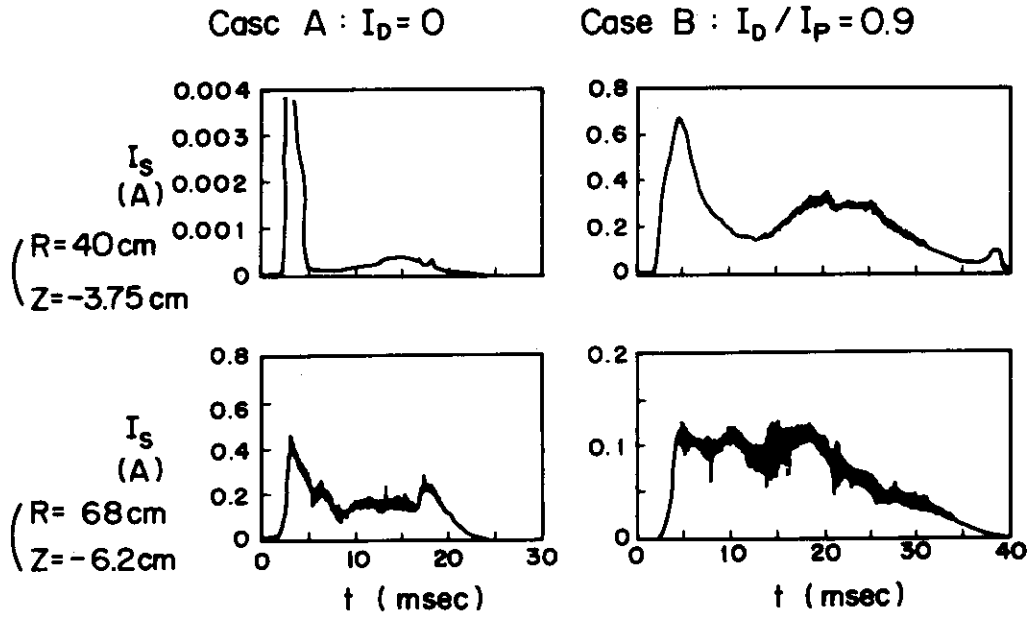

Fig.I.2-11 Oscillograms of double probe current near the divertor hoop (R=40cm, Z=-3.75cm) and near the inner surface of the shell (R=68cm, Z=-6.2cm). The operation condition is the same as in Fig.I.2-6.

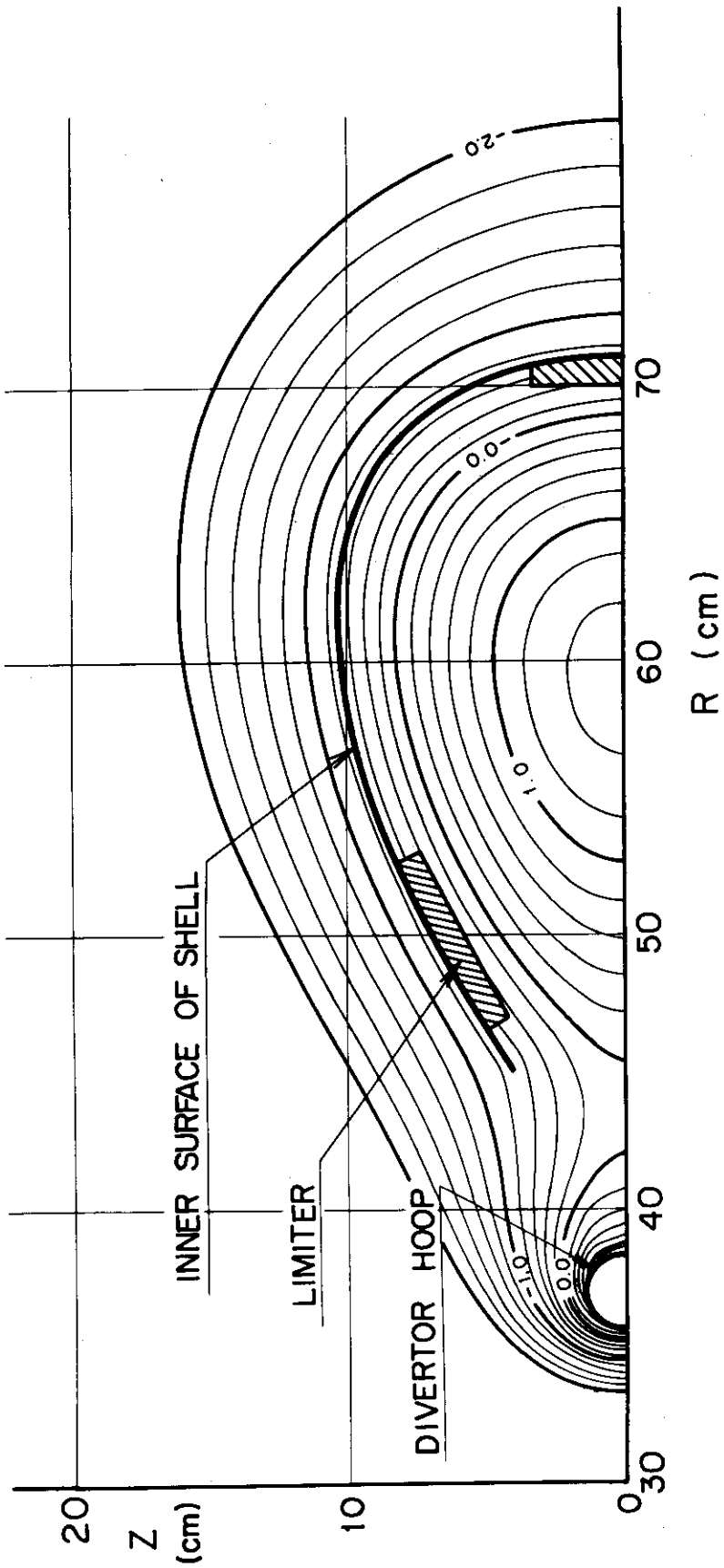

Fig.I.2-10 An example for an equilibrium configuration of uniform current distribution, β_p=0.1 and I_D/I_p=0.9, obtained by numerical calculation.

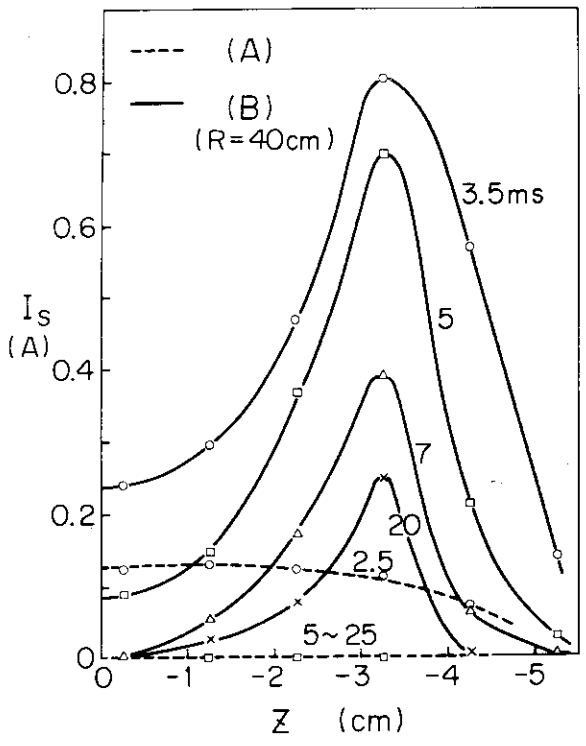

Fig.I.2-12

Double probe current near the divertor hoop vs. vertical distance from the median plane. Direction of electron drift is antiparallel to Z axis. The operation condition is the same as in Fig.I.2-6.

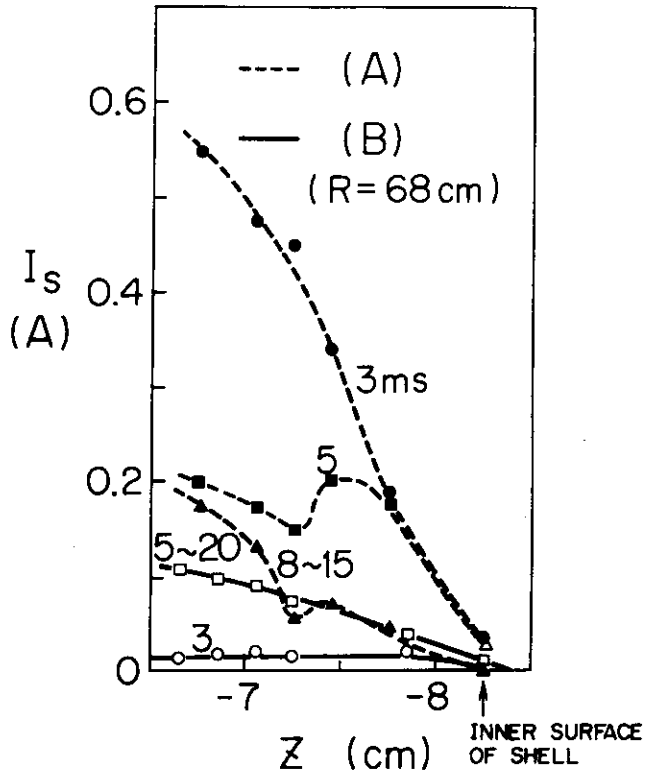

Fig.I.2-13

Double probe current near the inner surface of the shell vs. vertical distance from median plane. Direction of electron drift is antiparallel to Z axis. The operation condition is the smae as in Fig.I.2-6.

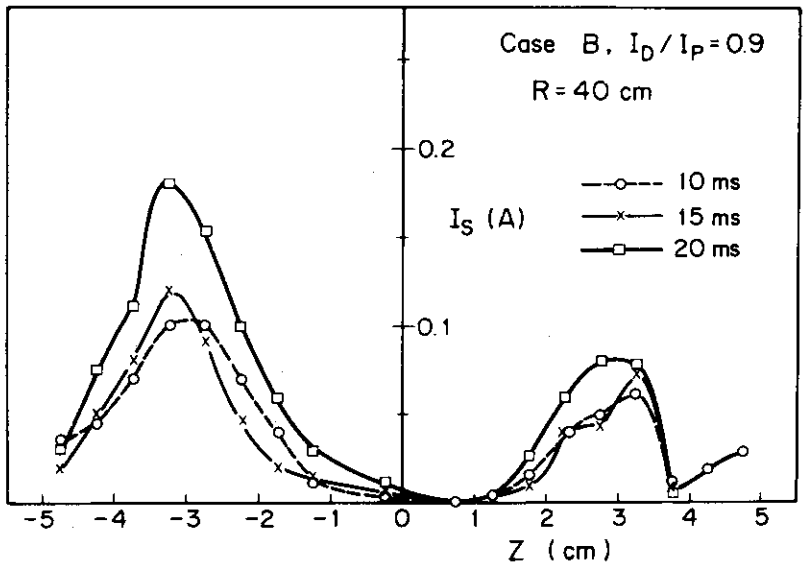

Fig.I.2-14 Double probe current near the divertor hoop vs. vertical distance from the median plane. Direction of electron drift is antiparallel to Z axis. The operation condition is similar to that shown in Fig.I.2-6.

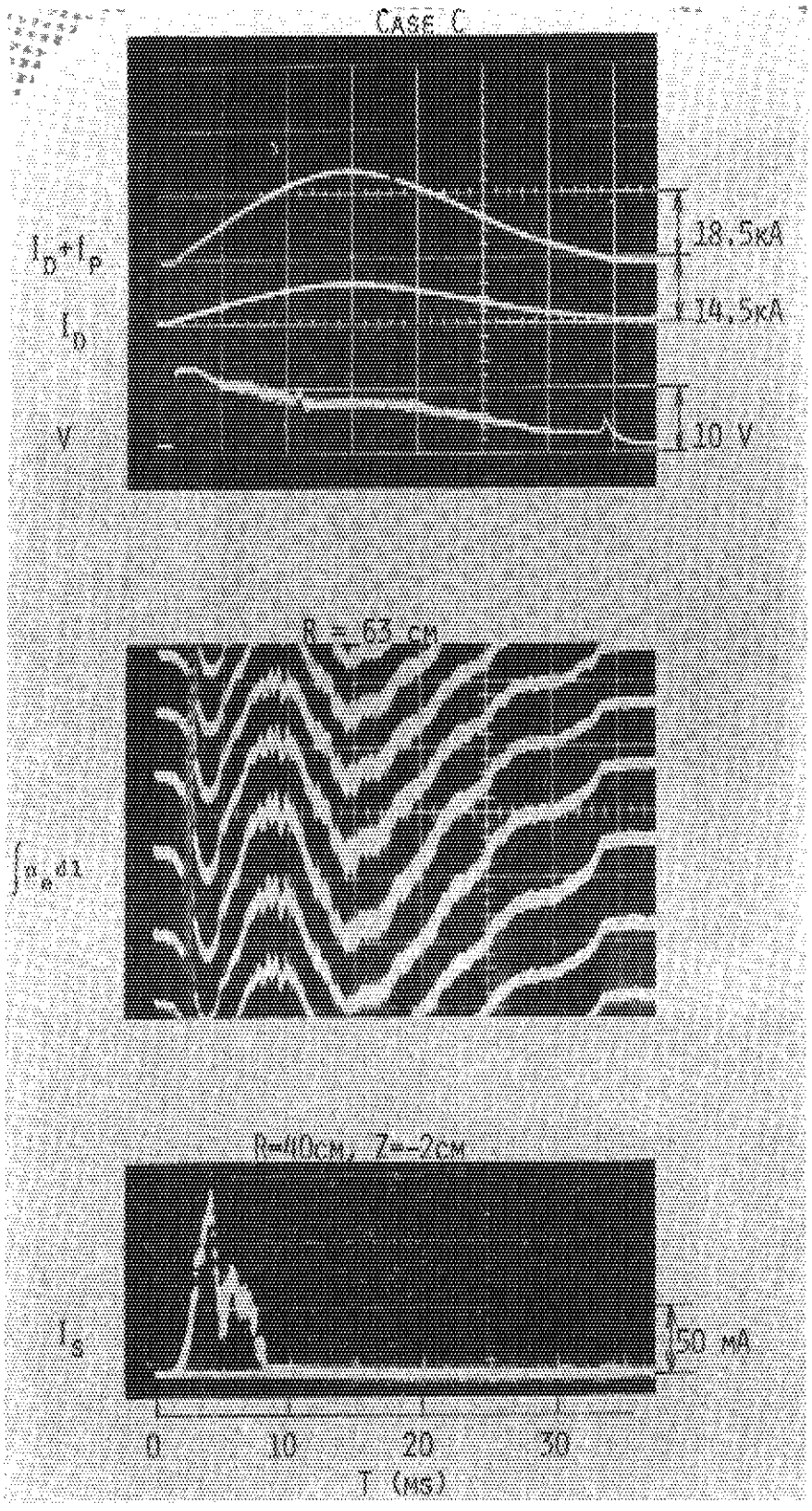

Fig.I.2-15 Oscillograms of sum of plasma current I_P and divertor hoop current I_D, I_D, loop voltage V, electron line density, and double probe current near the divertor hoop. The operation condition is I_D/I_P=0.45, B_V=0 and the continuous filling pressure = 1.3×10^{-4} Torr.

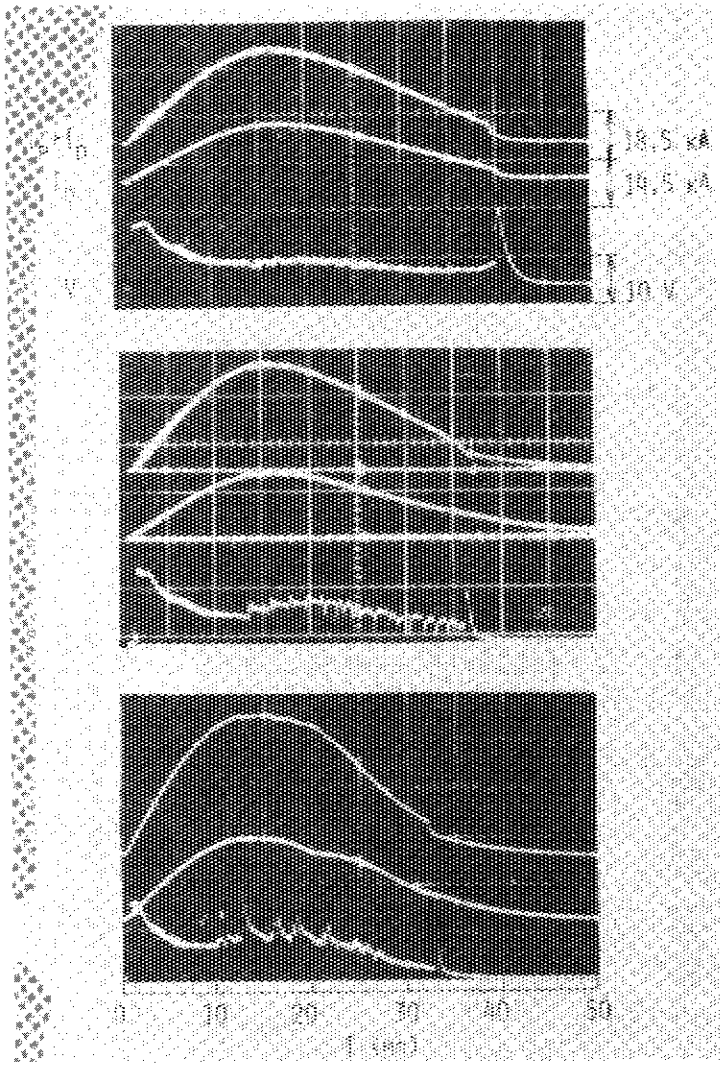

Fig.I.2-16 Oscillograms of sum of plasma current I_P and divertor hoop current I_D, and loop voltage V. The operation condition is I_D/I_P=0.9, B_V=0 and continuous filling pressure = 1.3×10^{-4} Torr.

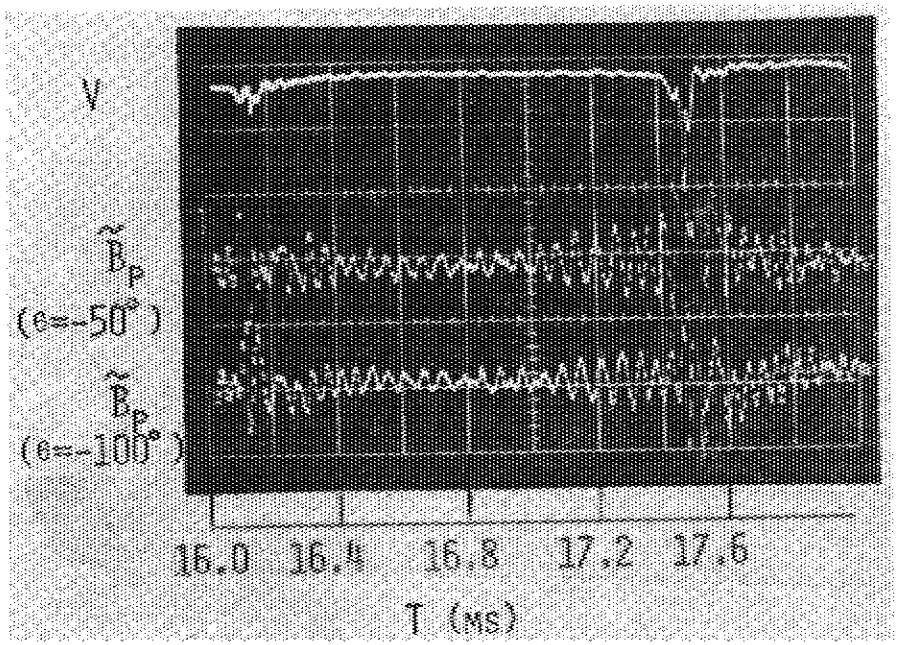

Fig.I.2-17 Oscillograms of fluctuations of loop voltage V and poloidal field $\tilde{B}_P$. The operation condition is similar to that shown in Fig.I.2-6 and the maximum plasma current is about 25 kA.

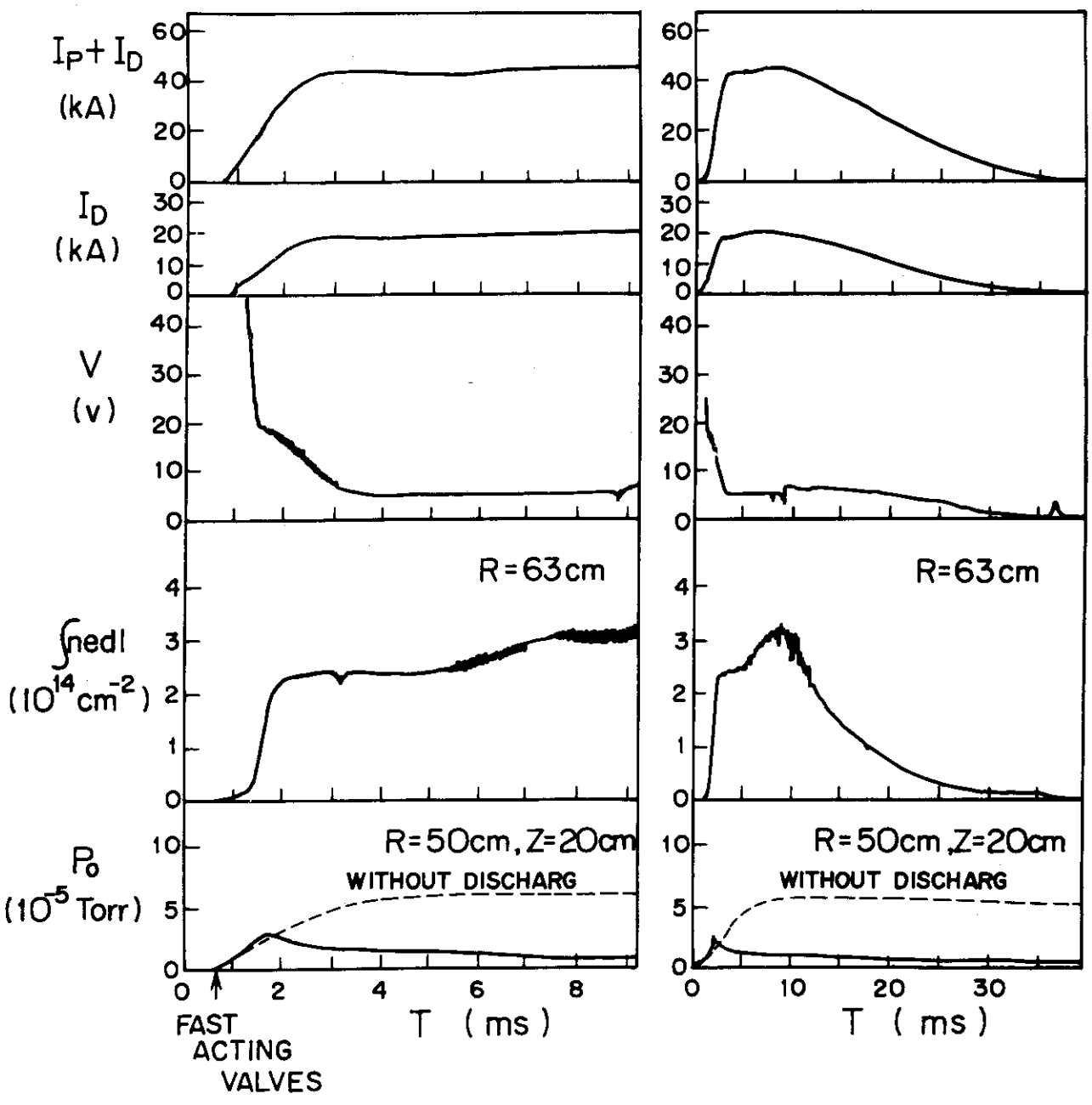

Fig.I.2-18 Oscillograms of sum of plasma current I_P and divertor hoop current I_D, I_D, loop voltage V, electron line density, and neutral particle pressure P_o. The operation condition is $I_D/I_P=0.9$, $B_V=0$ and the working gas admitted by four fast acting gas valves.

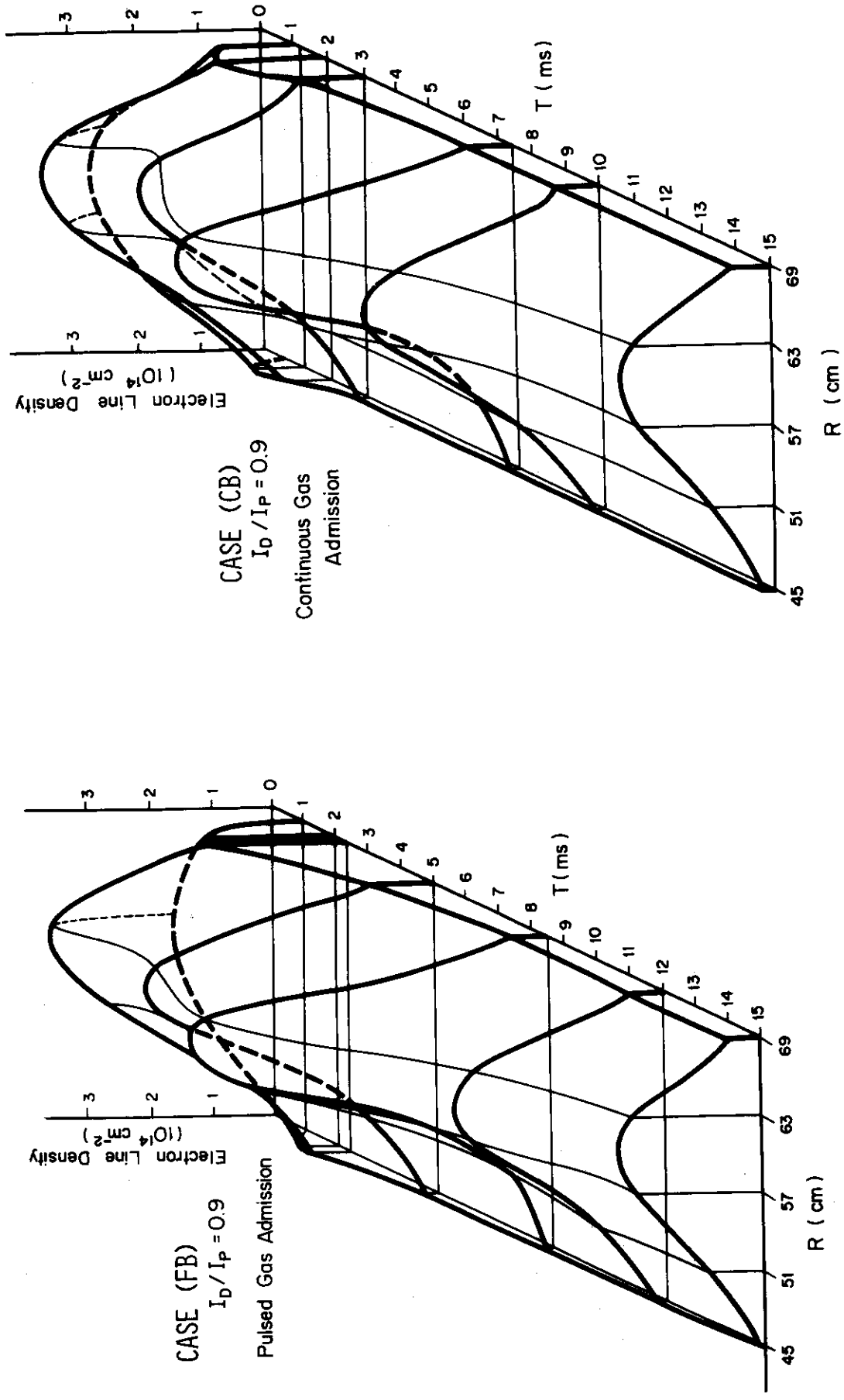

Fig.I.2-19 Electron line density distribution and total number of electrons. The maximum plasma current is about 20 kA.

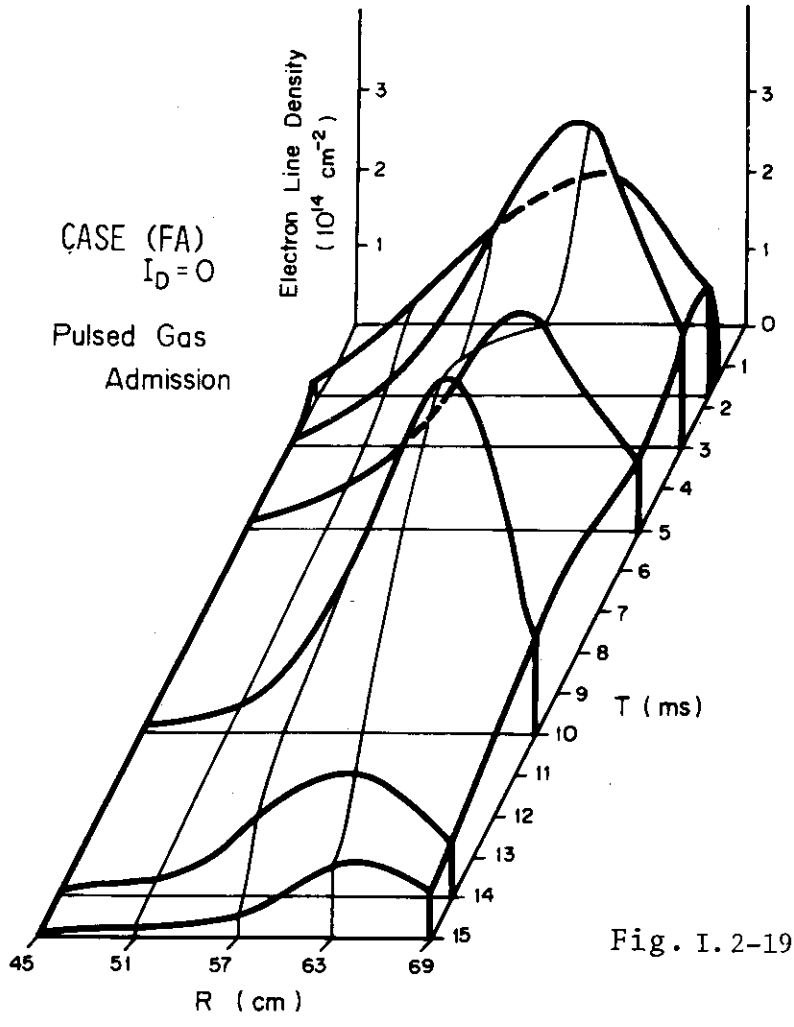

Fig. I.2-19

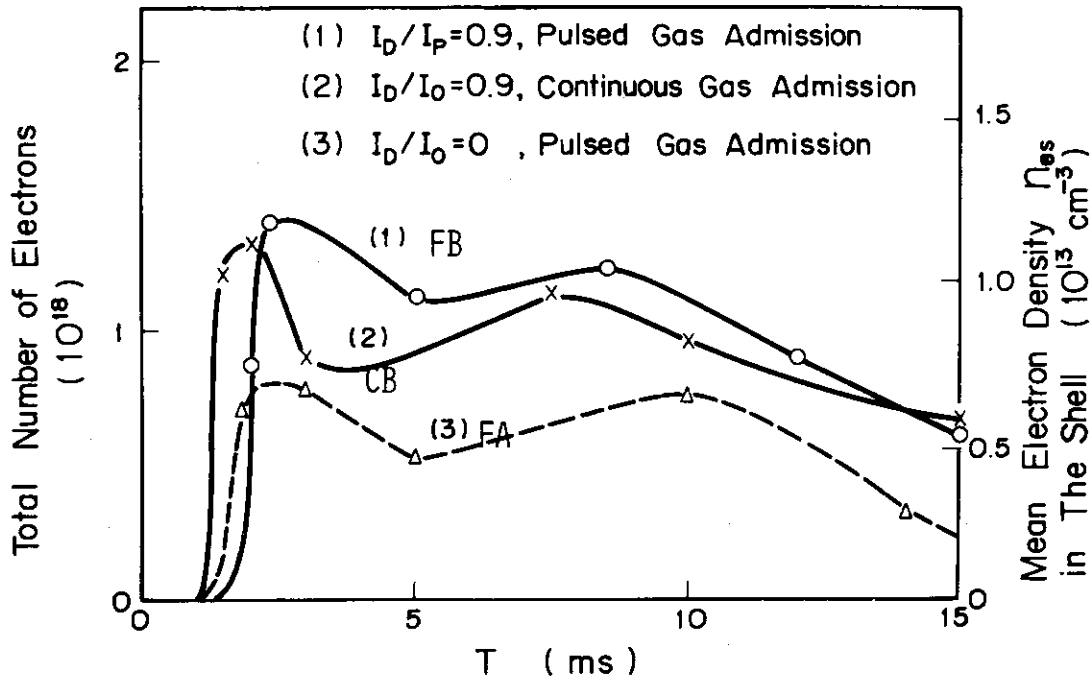

Fig. I.2-19

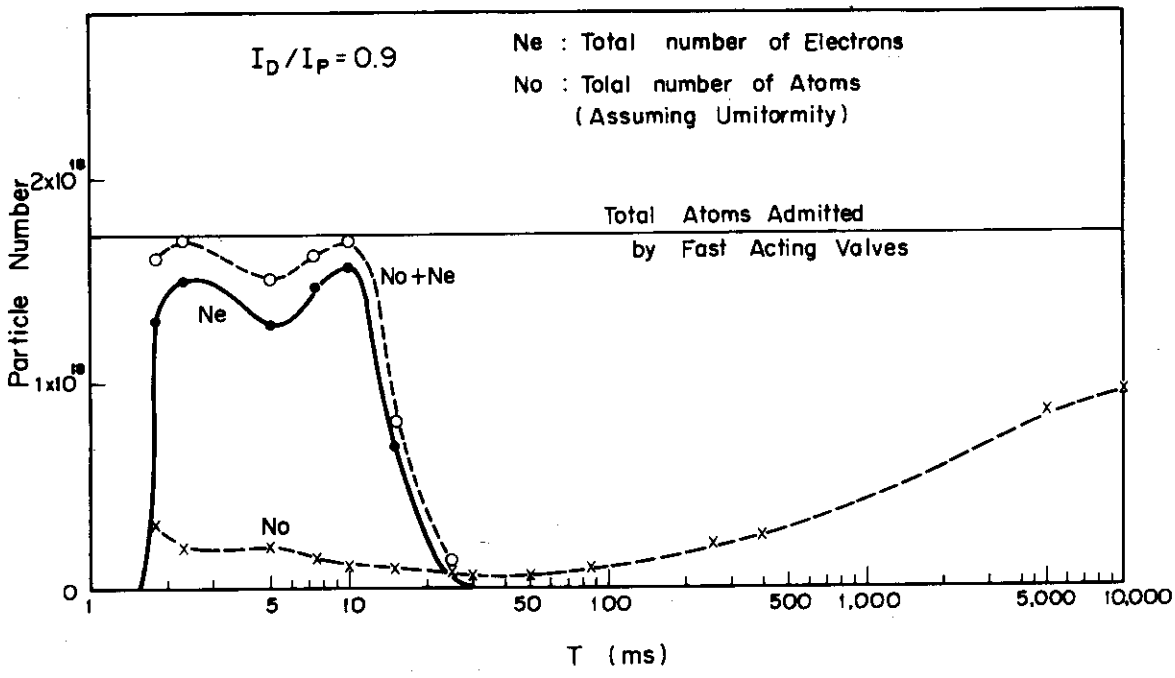

Fig.I.2-20 Total number of electrons and neutral particles. The discharge condition is the same as in Fig.I.2-18.

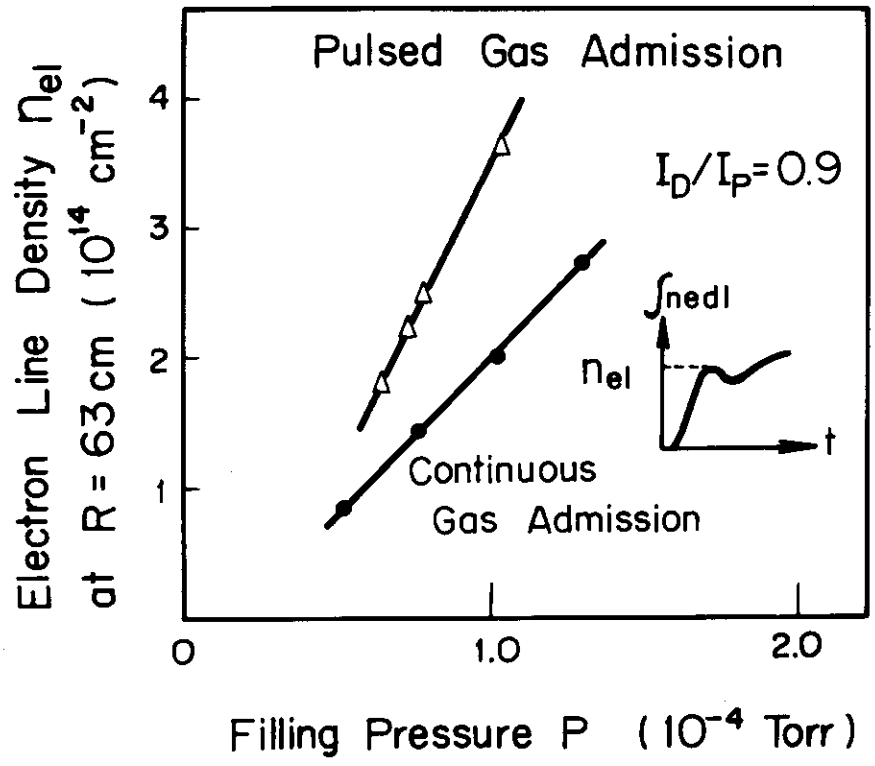

Fig.I.2-21 Electron line density vs. filling pressure. The maximum plasma current is about 20 kA and the operation condition is $I_D/I_P=0.9$ and $B_V=0$.

3. Diagnostics

A. Funahashi, S. Kasai, T. Kawakami, K. Kumagai,
T. Matoba, T. Shoji, K. Takahashi, H. Takeuchi

3.1 Introduction

The diagnostics group is mainly engaged in (1) measurement of the fundamental quantities of tokamak-plasmas, (2) design of new diagnostic apparatus and (3) development of advanced diagnostic techniques.

In this reporting period, considerable efforts were devoted to measurement of the fundamental quantities necessary to study the particle and energy balance in JFT-2 plasmas and to construction of various diagnostic instruments for JFT-2a plasmas such as mm-wave interferometers and a spectrometer for the Doppler temperature. A data processing system and a multi-channel particle analyser for tokamak experiments were completed and put into operation.

(A. Funahashi)

3.2 Microwave Interferometric Measurement

A 75-GHz fringe-shift (1 ch.) and a conventional (2 ch.) interferometer were manufactured for measurement of the electron densities in JFT-2a. The fringe-shift interferometer[1] was designed to produce five fringe-stripes and is capable of detecting down to one-tenth of one fringe-shift. It consists of a KA701A klystron (output 400 mW), 75-GHz microwave circuits, delay lines (total length 17 m), collecting lenses, shutters to prevent the lenses from becoming opaque due to plasma-sputtering, and electronic circuits for producing zebra-stripes. The fringe-shift interferometer has been used for diagnosis of the JFT-2a plasma since September 1974.

Fig.I.3-1 shows a typical example of observed zebra-stripes. Fig. I.3-2 shows the time variation of the average electron density obtained from Fig. I.3-1 and those of the plasma current and loop voltage and the experimental conditions.

Some early results on JFT-2a obtained from measurement with the 75-GHz interferometer are described in Section I-2 and reported in ref. 2.

(A. Funahashi, K. Takahashi)

3.3 Thomson Scattering Measurements

The following two improvements were made for the Thomson scattering apparatus. Magnetic shield cases of photomultipliers were replaced with coaxial double-layer permalloy cases with the result that the sensitivity changes of photomultipliers caused by the plasma current were vanished. In order to improve the S/N ratio of the electronic circuits, a pre-amplifier was installed between the photomultiplier and the high speed gate circuit. A block diagram of the improved electronic circuits is shown in Fig. I.3-3.

The electron temperatures and densities of JFT-2 plasmas produced at an intensified toroidal magnetic field (18 kG) were measured from December 1974 to February 1975. The Rayleigh scattering intensity of nitrogen gas was used for one of the absolute corrections of the scattered light intensity (Fig. I.3-4). The measured Rayleigh scattering curve coincides, within a factor of 2, with the theoretical curve corrected for the laser power and the sensitivity of the photomultiplier. This factor may be mainly caused by uncertainty of the laser power correction. In Fig. I.3-5, intensities of individual channel signals in a logarithmic scale are plotted as a function of the square of the wavelength shift for a typical discharge at B_t = 18 kG. The time variation of the electron temperature and density at the same plasma parameters is shown in Fig. I.3-6.

A new observation port was manufactured for the Thomson scattering measurements in JFT-2a. The laser oscillator, the optical system and the photodetector system which are presently in use for study of JFT-2 plasmas will be used for JFT-2a as well. The observation port of JFT-2a is shown in Fig. I.3-7. The viewing dump is set up below the equatorial plane for the reason that the divertor hoop is placed on the equatorial plane. Therefore the scattering angles are chosen 75°, 82° and 90° for three different scattered light paths. Scattering measurements in JFT-2a are scheduled to start from March 1975.

(T. Matoba, K. Kumagai, A. Funahashi)

3.4 Charge-exchanged Particle Measurement

A multi-channel neutral particle energy analyser for measuring ion temperatures of plasmas was constructed that enables us to measure

simultaneously several points on the particle energy distribution in a single shot and thus to reduce the errors inherent in the measurement with a single channel analyser.

The system of this analyser consists of the following subsystems:

(1) Energy analysis

Parallel plate electrostatic energy analyser:

channel number ---------- 10

energy resolution ---------- 50% (ch.1) 6% (ch.10)

(2) Neutral particle detection

Ionizor ---------- gas stripping reaction

Ion detector --------- channel type electron multiplier (ceratron EMW1081)

(3) Vacuum system

Differential pumping -- 1000 l/sec sputter ion pump

Drift tube pumping ---- 80 l/sec sputter ion pump + Ti getter pump

(4) Data acquisition system

Pulse counting method -- pre-amp + linear amp + discriminator + counter

Fig. I.3-8 shows the energy analyser, Fig. I.3-9 the data acquisition system and Fig. I.3-10 the whole system of the multi-channel analyser apparatus.

The energy calibration of the electrostatic energy analyser was performed with electron beams, and the transmission efficiency calibration was performed with proton beams. As a result of energy calibration experiments, it was shown that the difference between the designed and measured values was 1% $\sim$ 5%. The transmission efficiency was about 50%, because a shadow mask was installed at the exit of each channel to prevent the electrostatic field from being disturbed by the high electric field of the ceratron. The stripping cell efficiency for H_2 gas was also measured by using a neutral beam source shown in Fig. I.3-11. The neutral beam source consists of an RF ion source and a charge exchange cell. The experimental value of the stripping cell efficiency was in agreement with that calculated from the charge-stripping and the electron capture cross sections.

The first measurements with this apparatus were performed on JFT-2a.

To reduce the back ground noise due to hard X rays of plasmas, the analyser was shielded with 10 cm thick lead, and consequently the hard X ray noise was negligible. In order to prevent the particle orbits in the analyser from being disturbed by a poloidal magnetic field due to plasma current, we also shielded the energy analyser and the stripping cell with high μ permalloy. The magnetic disturbance in the analyser was reduced to at most 1/100 of the external poloidal field and is believed to be negligible for the present measurement.

The data were obtained by measuring the particle signal and the back ground signal due to optical radiations from plasmas. We obtained the energy spectrum of neutral particles by subtracting the averaged back ground signal from the apparent particle signal in each shot. Fig. I.3-12 shows typical results obtained for JFT-2a plasmas at a plasma current of 15.2 kA and a toroidal field of 10 kG.

(H. Takeuchi, K. Takahashi, H. Shirakata, A. Funahashi)

3.5 Spectroscopic Measurements of Impurities

We investigated the spatial distribution of spectral line intensity of impurities in JFT-2 plasmas by using a 50 cm VUV monochrometer [3]. Observed impurities are mainly oxygen and carbon ions. The experimental conditions are as follows; the toroidal magnetic field strength $B_t \simeq 9$ kG, the maximum plasma current $I_{p\ max} \simeq 76$ kA, the filling pressure of hydrogen gas $P_f \simeq 3.2 \times 10^{-4}$ Torr.

Fig. I.3-13(a) shows the intensities of a CV(2270.9 Å) line at 30 msec after the discharge started. In the figure the solid curve is the integrated intensity of this impurity line viewed along a major radius on the equatorial plane of the torus. The error bars include a factor of a change with time of a quantum efficiency of sodium salicylate which is sprayed on a quartz plate placed in front of the photomultiplier of the monochrometer. This integrated intensity can be transformed into a radial intensity distribution by Abel's inversion. The radial intensity distribution, which is shown by the dotted curve in Fig. I.3-13(a), has a maximum intensity at $r = 10 \pm 3$ cm (r is a distance from the center of a plasma) and a shell type profile.

The spatial distribution of a OVII(1623.3 A) line at 30 msec (Fig. I.3-13(b)) differs from that of the CV line and has a profile with a peak

in a central region of the plasma. However, at 40 msec the OVII line profile is similar to the CV line profile at 30 msec. It has a maximum intensity at r = 9 ± 3 cm (Fig. I.3-14).

(S. Kasai, A. Funahashi)

3.6 Data Processing System

A data processing system for tokamak experiments of JFT-2 was brought to completion in August 1974 except a pulse stretcher of the laser scattering signal, which was completed in October 1974. Further modification of the system was made so as to make it available to JFT-2a as well.

An outline of this system was already described in a previous annual report (JAERI-M 5888). The main characteristics of the input ports are indicated in Tab. I.3-1. The characteristics of the high speed pulse stretcher for a laser scattering signal (pulse width 10 ns) are shown in Fig. I.3-15.

A few examples of data processed from magnetic probe signals are shown in Fig. I.3-16. In order to decrease various errors induced electro-magnetically, the noises of blank operation without plasma currents are stored in memories and eliminated from the signals. The experimental conditions for these data are: B_t = 18 kG, $P_f = 3.5 \times 10^{-4}$ Torr. The conductivity temperature (Z_{eff} = 3) is in good agreement with the temperature from the laser scattering measurements.

(T. Shoji, T. Kawakami, A Funahashi)

References

1) A. Funahashi et al.: Fringe-Shift Interferometric Apparatus for Tokamak-Plasma Diagnostics, JAERI-M 6166 (July 1975) (in Japanese).
2) Y. Shimomura et al.: The First Results on JFT-2a, JAERI-M 6102 (April 1975) (in Japanese)
3) A. Funahashi, S. Kasai, T. Matoba and N. Fujisawa: JAERI-M 5961 (1975).

	PORT NAME	CHAN-NEL	INPUT LEVEL	FILTER	SAMP. START	SAMP. TIME	SAMP. POINTS	EXPERIMENTAL SIGNALS
			mV	kHz	mS	μS	1CH	
ANALOG	PM 1	10	±20 ~500	0.2 ~10	M.P. + 0~1200	50 ~4000	400	Probes (Ip, Vp, A, q, B, w, Tσ)
	PM 2	10	〃	〃	〃	〃	〃	Correlations (m, n)
	PM 3	2	〃	50	〃	2	6000	Oscillations
	PM 4	10	±10 ~2000	20	M.P.	1000 ~4000	400	Correlator, Doppler (Ti)
	SS 1	2	±10 ~500	1 ~10	M.P. + 0~1200	50 ~4000	500	Spectroscopics (n_n, n_i)
	MD 1	8	〃	50	M.P.	20 ~4000 (soft)	2000	Microwaves ($n_e(r)$)
	MD 2	2	〃	1	〃	200 ~4000	500	〃
	MX	2	〃	0.2 ~10	〃	200 ~4000	500	Medium Xray (Te)
PULSE	HX	1	2 ~2000	GATEW. 1~20mS	M.P. + 0~1200	1 pulse /5μS	500	Hard Xray (runaway)
	SX	1	〃	〃	〃	〃	〃	Soft Xray (f(E))
	ACD	2	~1V	〃	M.P.	1 pulse /50μS	600	α-particle (j(r))
	LTE	13 12	50 ~1000		M.P. + 0~1200	pulse w. 10 nS 1 μS	1	Laser (Te, n_e)

Table.I.3-1 Main characteristics of the input ports of the data processing system.

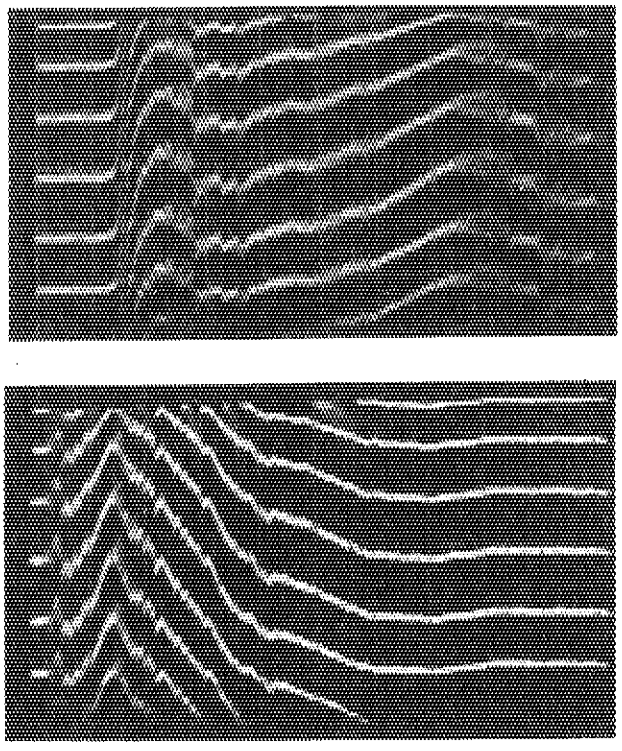

Fig.I.3-1 A typical example of zebra stripes observed along R = 60 cm in JFT-2a (upper trace: 1 ms/div, and lower trace: 5 ms/div)

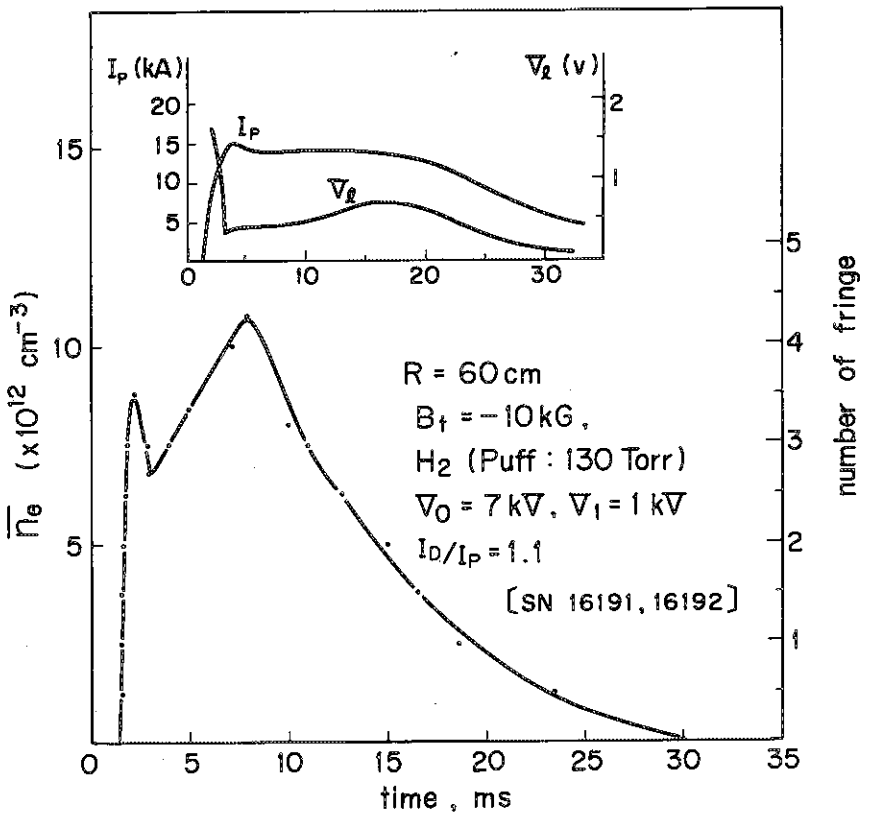

Fig.I.3-2 The average electron density in JFT-2a.

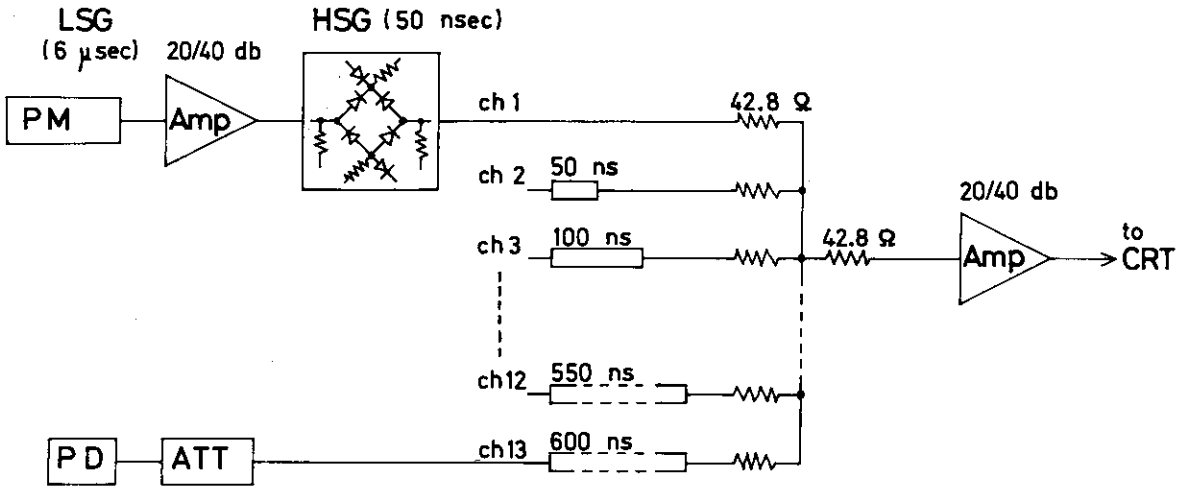

Fig.I.3-3 Block diagram of the electronic circuits.

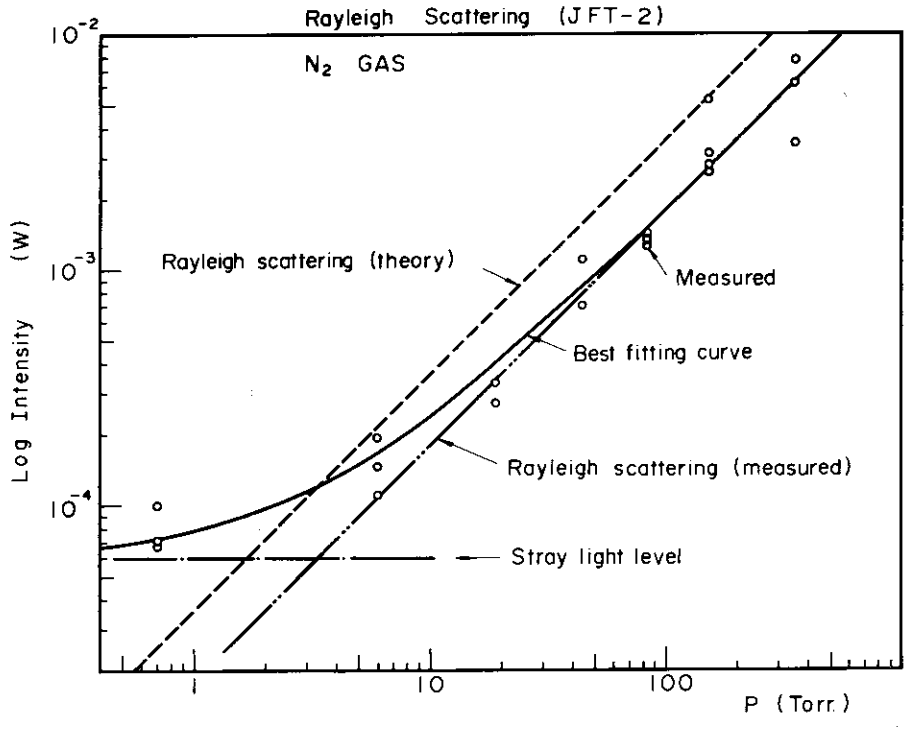

Fig.I.3-4 Intensity of the Rayleigh scattering light.

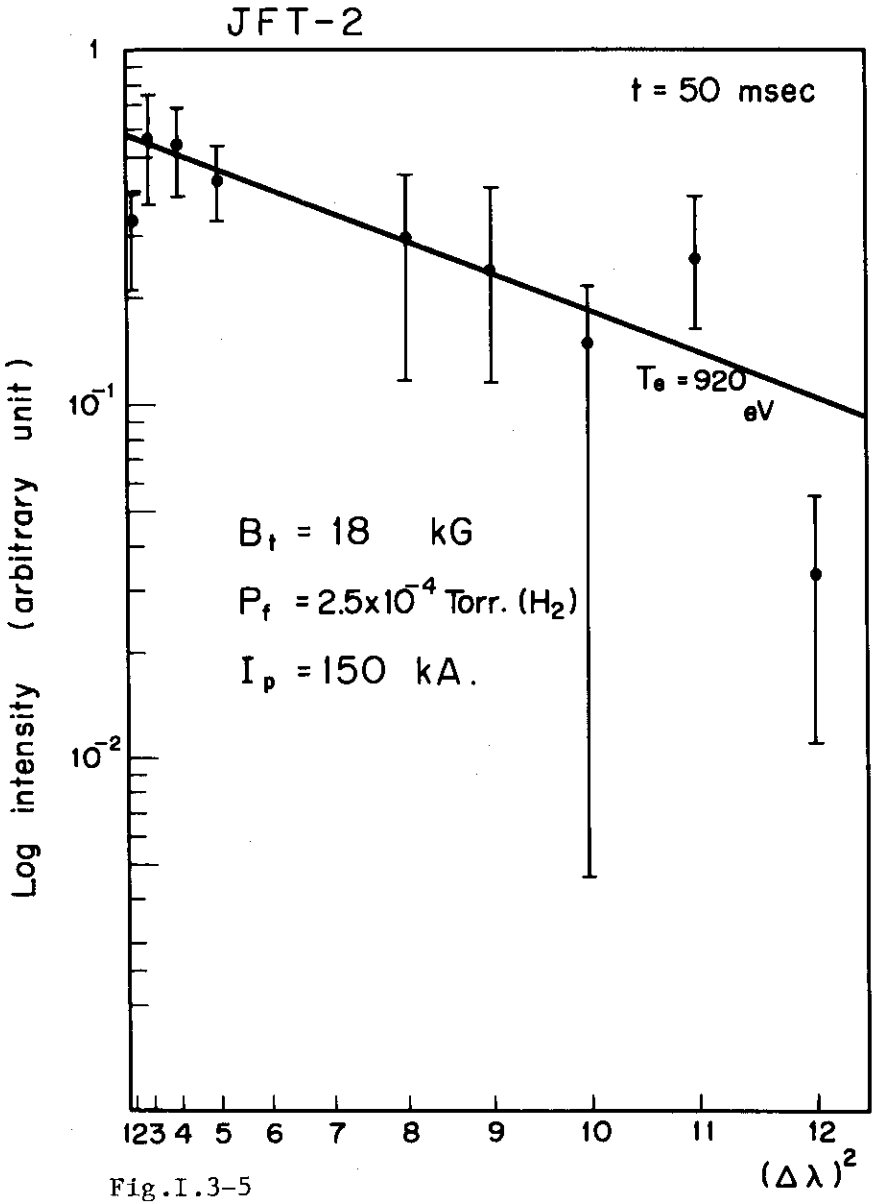

Fig.I.3-5

Logarithm of the scattered intensity as a function of the square of the wave length shift, $(\Delta\lambda)^2$.

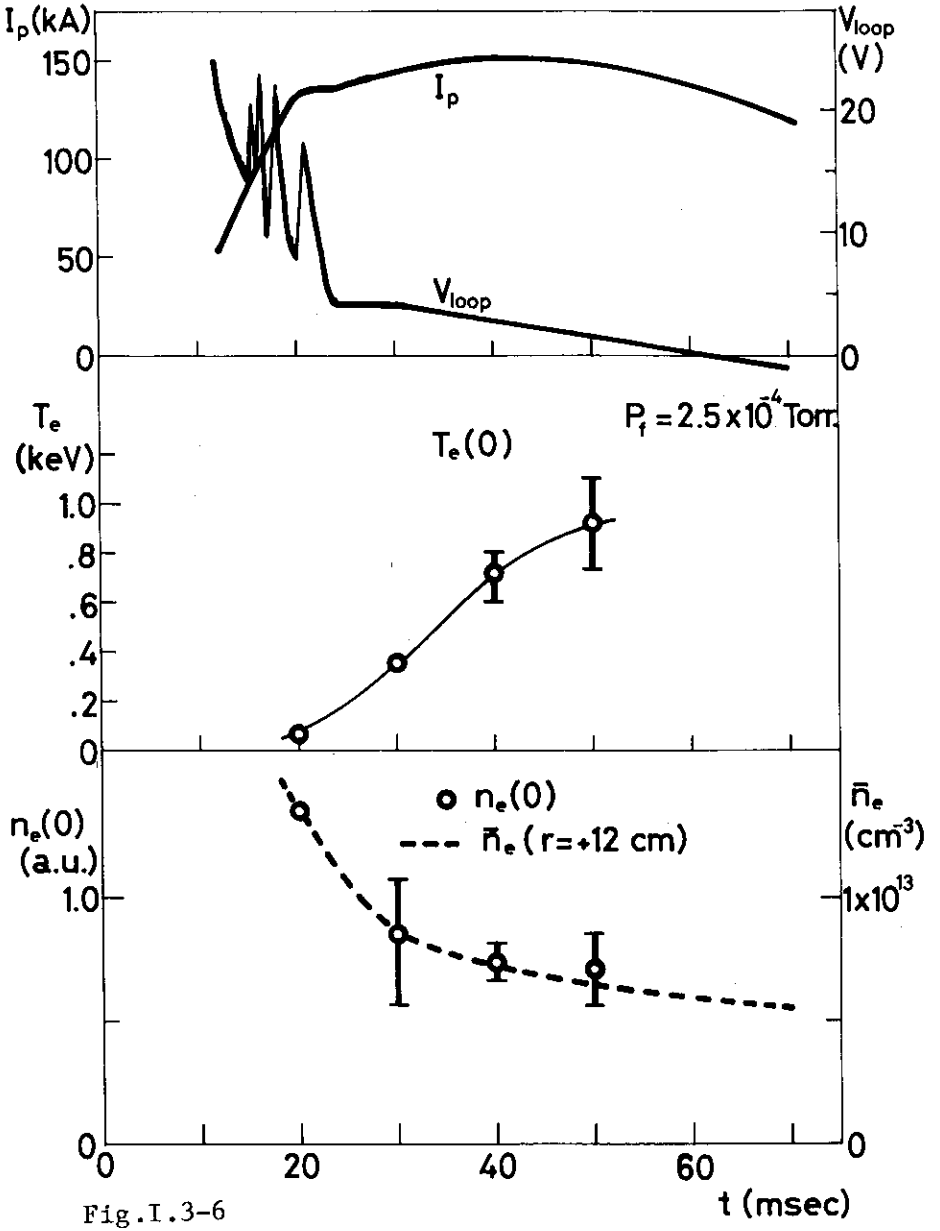

Fig.I.3-6

Electron temperature and density at the ceneter as a function of time.

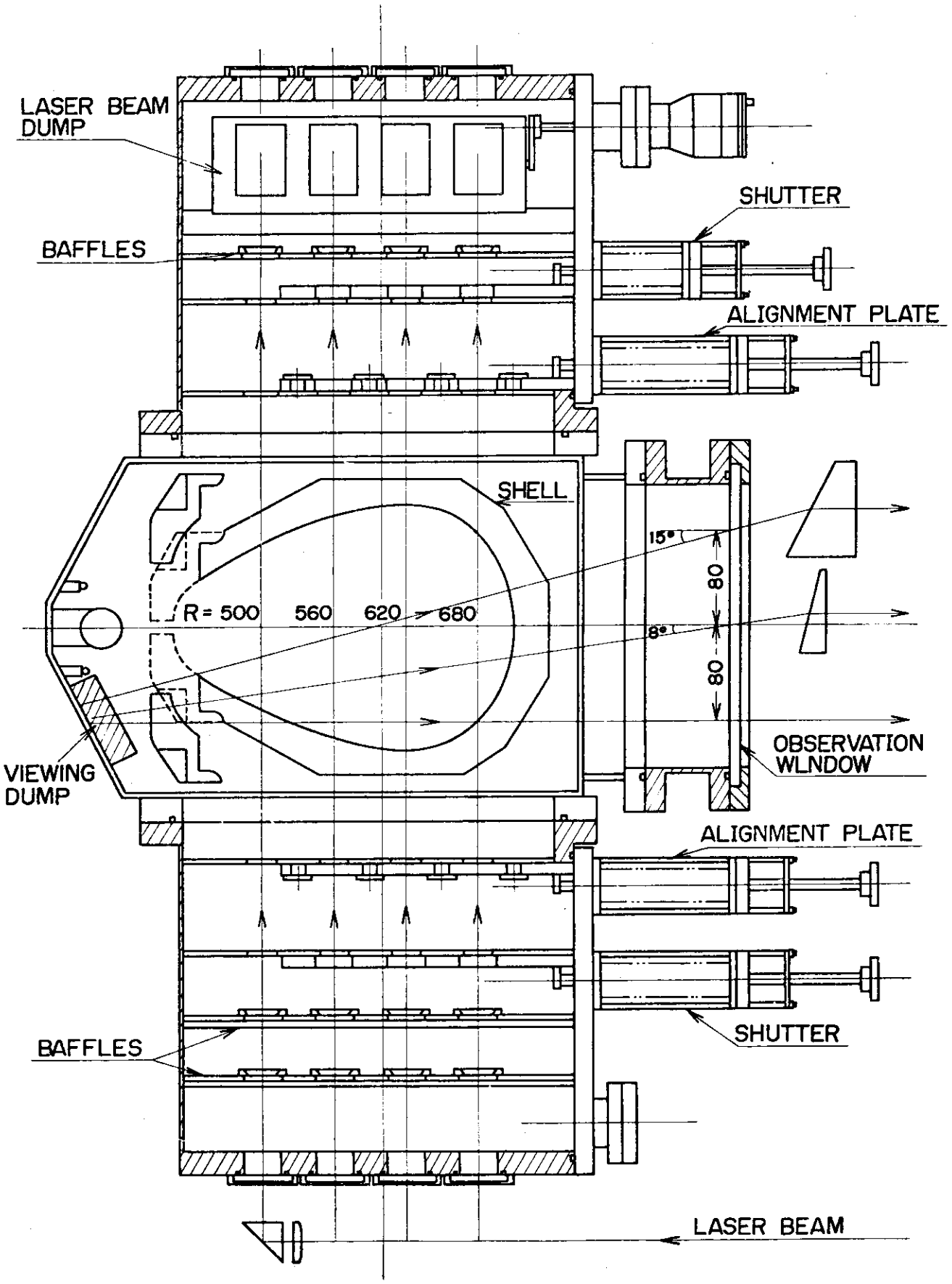

Fig.I-3-7 Observation port of JFT-2a.

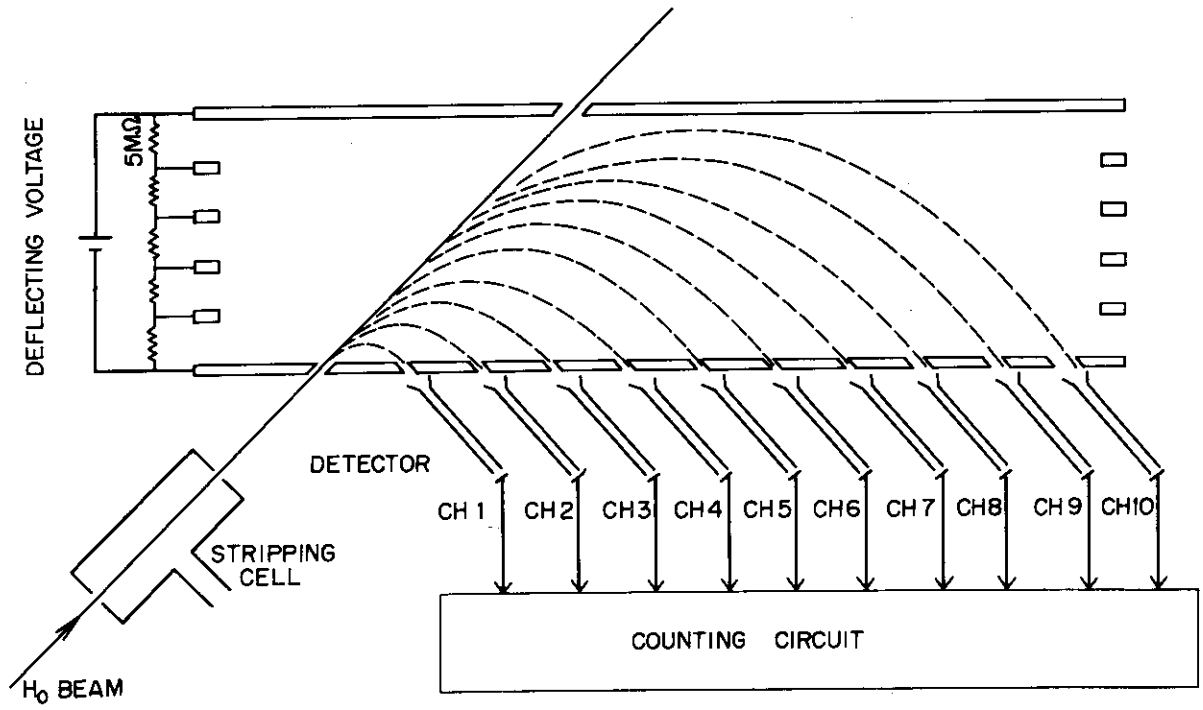

Fig.I-3-8 Schematic diagram of multi-channel (10ch) neutral particle energy analyser.

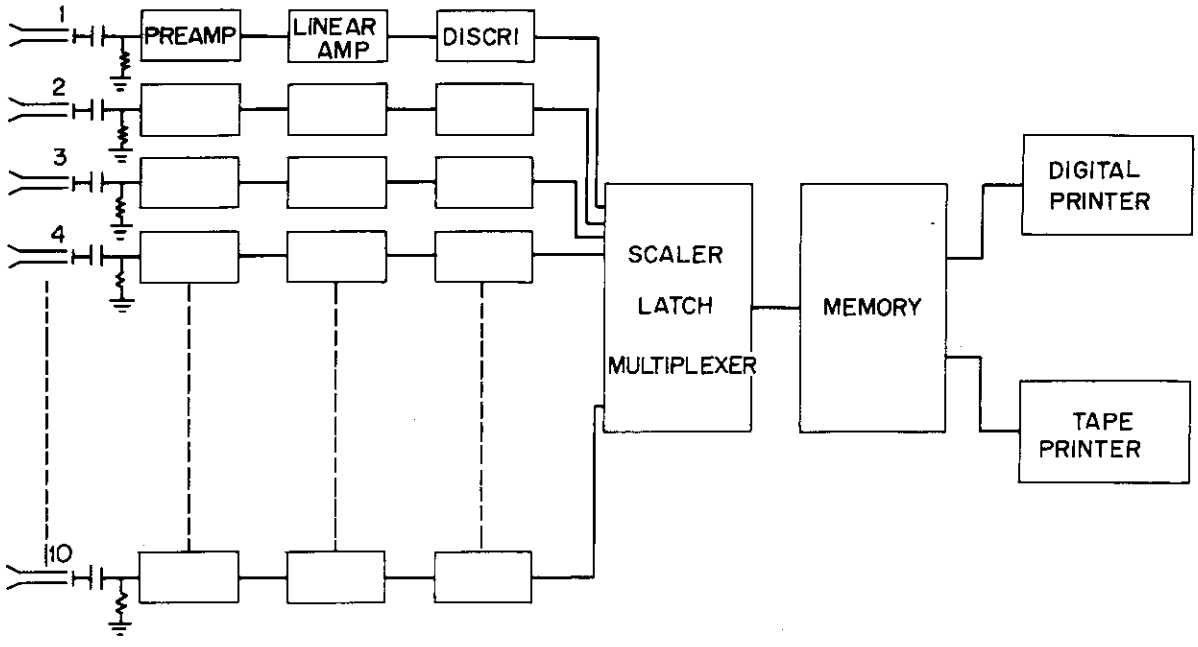

Fig.I.3-9 Data acquisition system for charge-exchanged particle measurement.

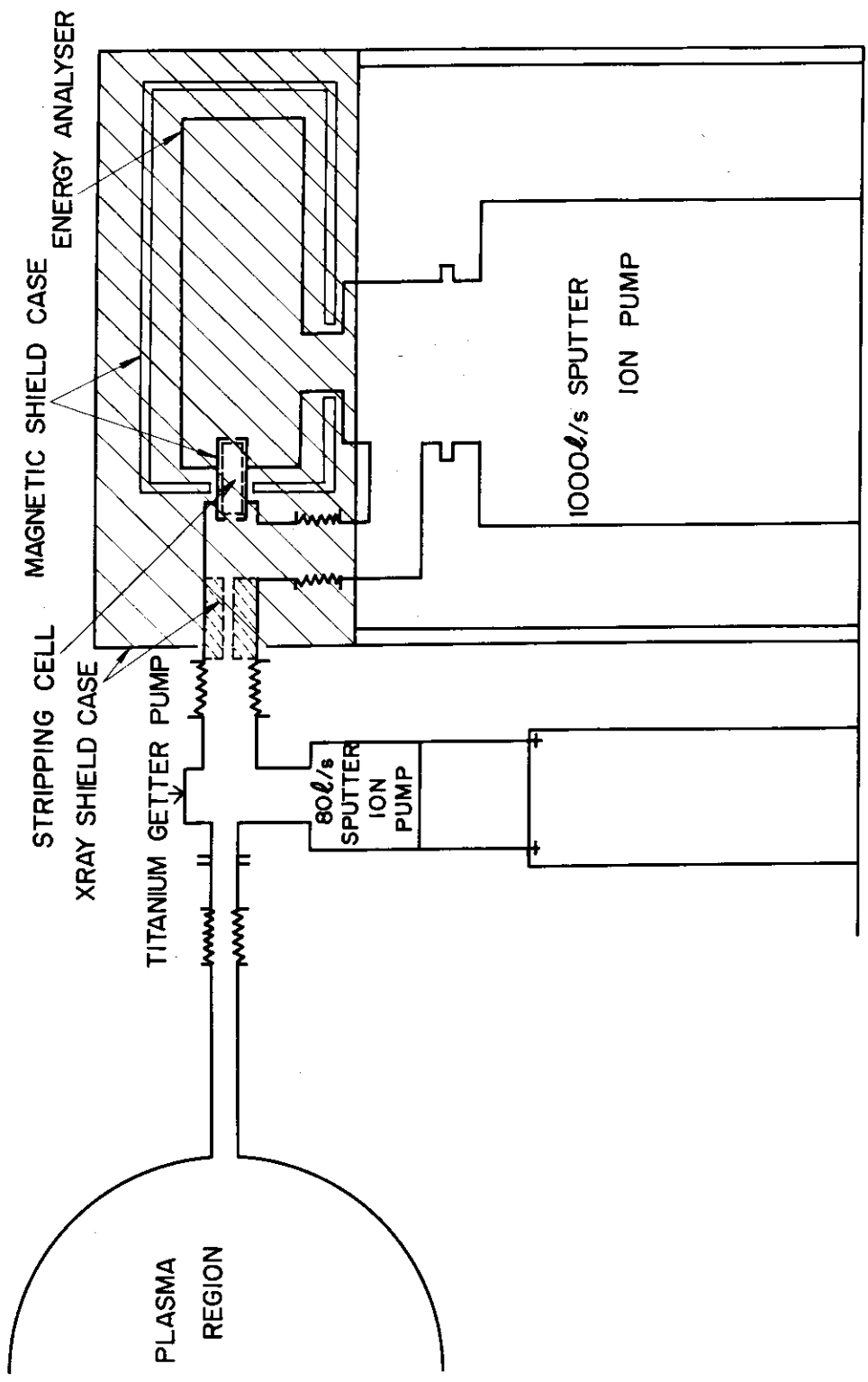

Fig.I.3-10 Multi-channel neutral particle energy analyser apparatus connected to a plasma device

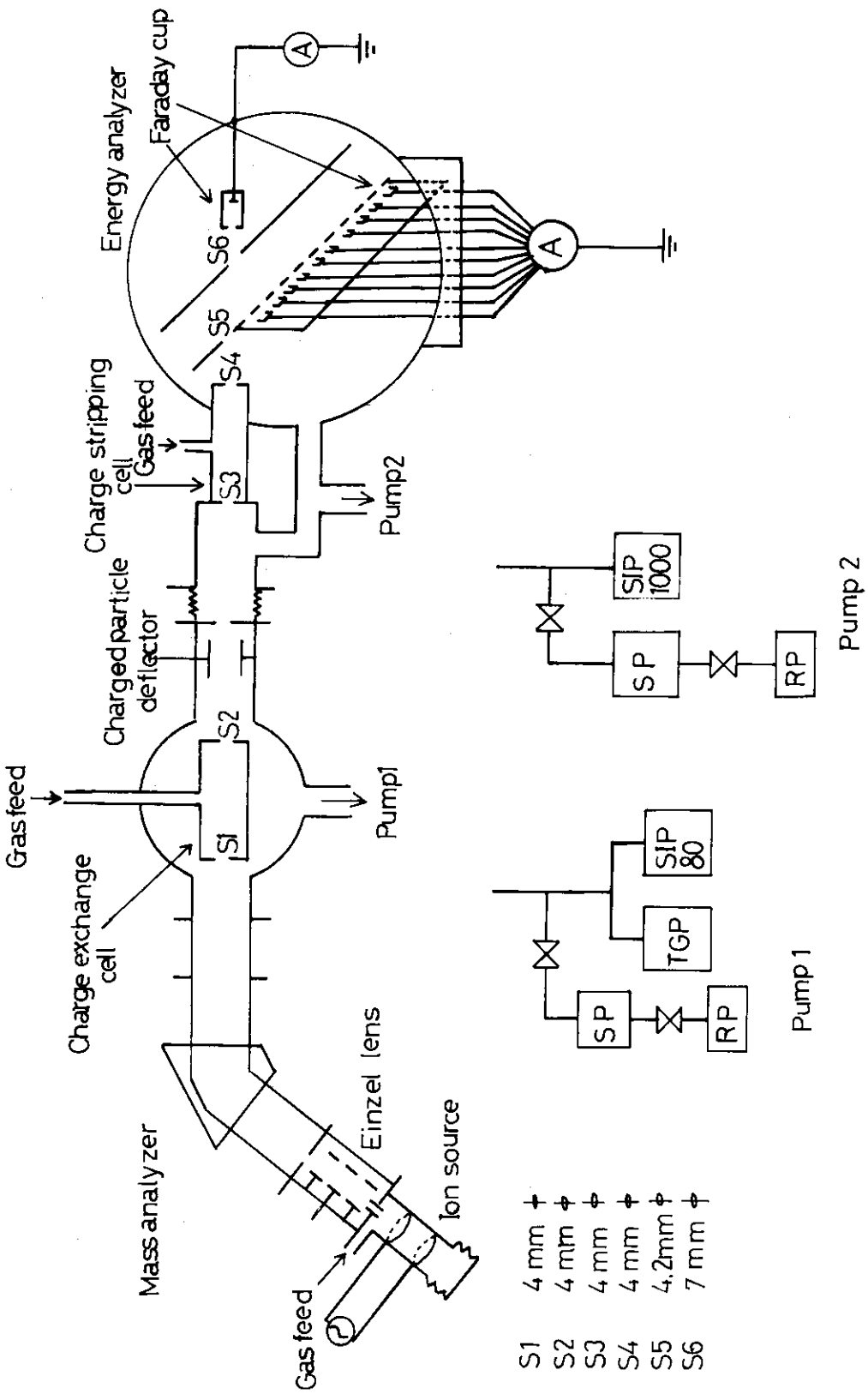

Fig.I.3-11 Neutral beam source for measuring the stipping cell efficiency.

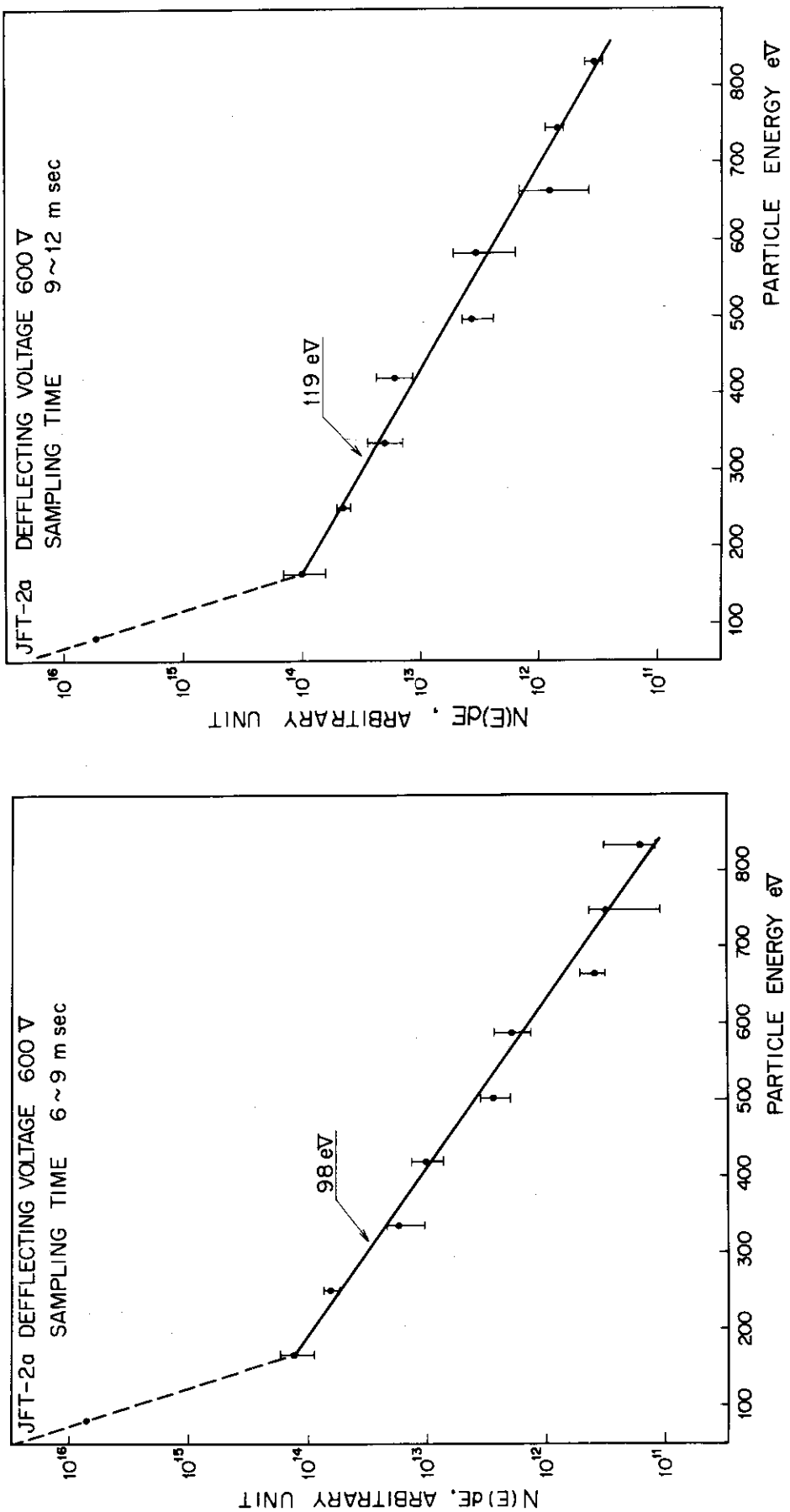

Fig.I.3-12 Ion energy spectrum measured over the particle energy range 83 to 833 eV on JFT-2a (Bt: 10kG, Ip: 15.2kA)

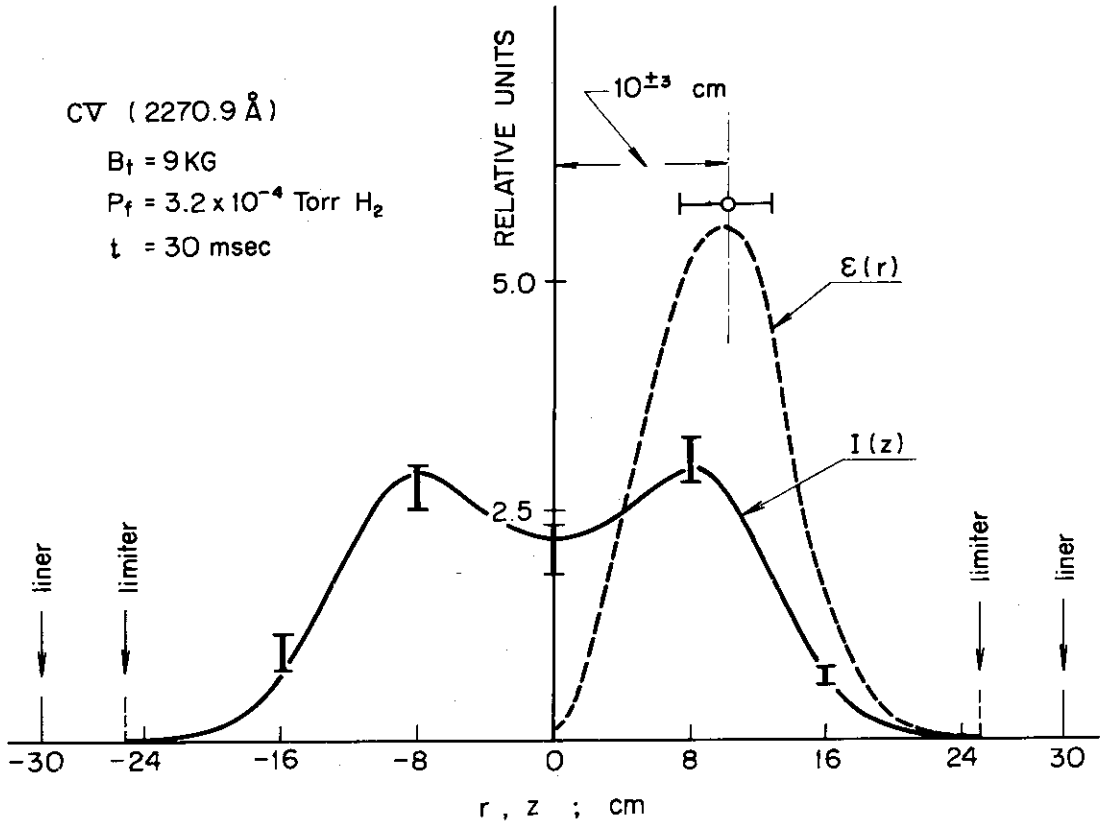

Fig.I.3-13(a) Spatial distributions of CV line obtained at 30 msec.

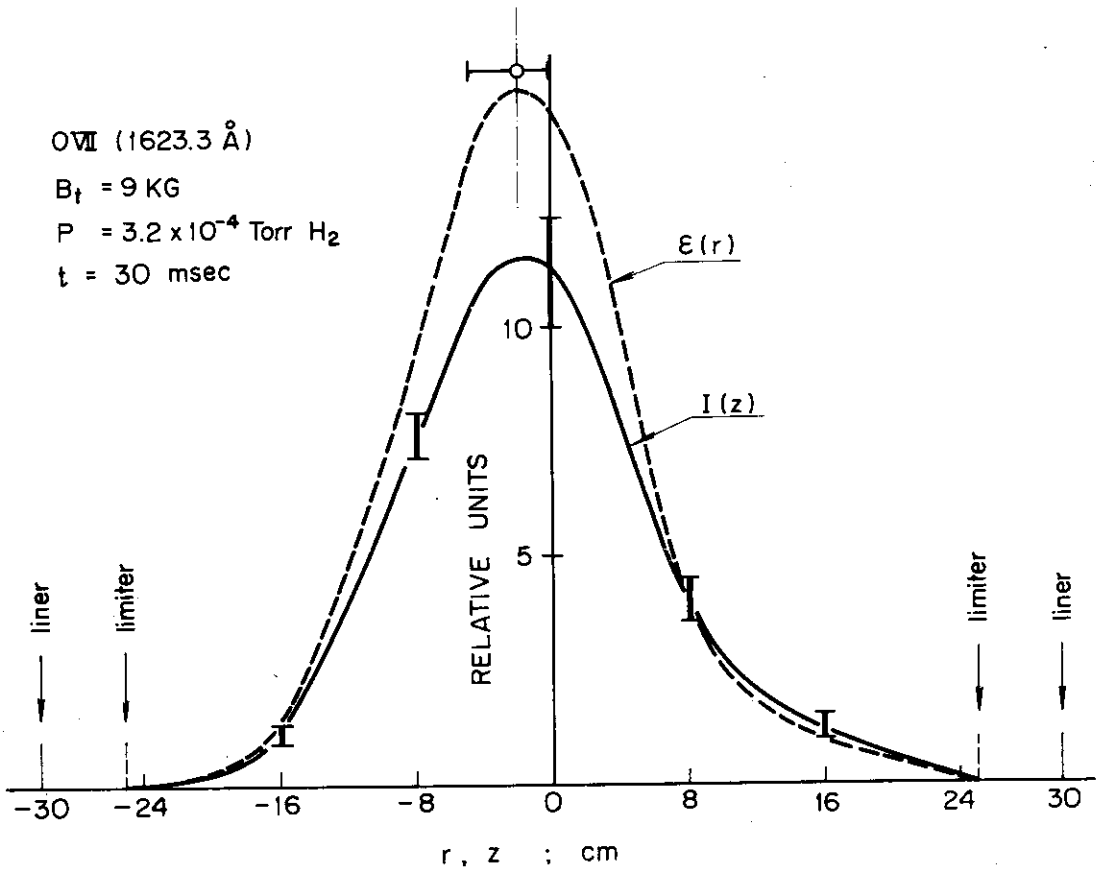

Fig.I.3-13(b) Spatial distributions of OVII line obtained at 30 msec.

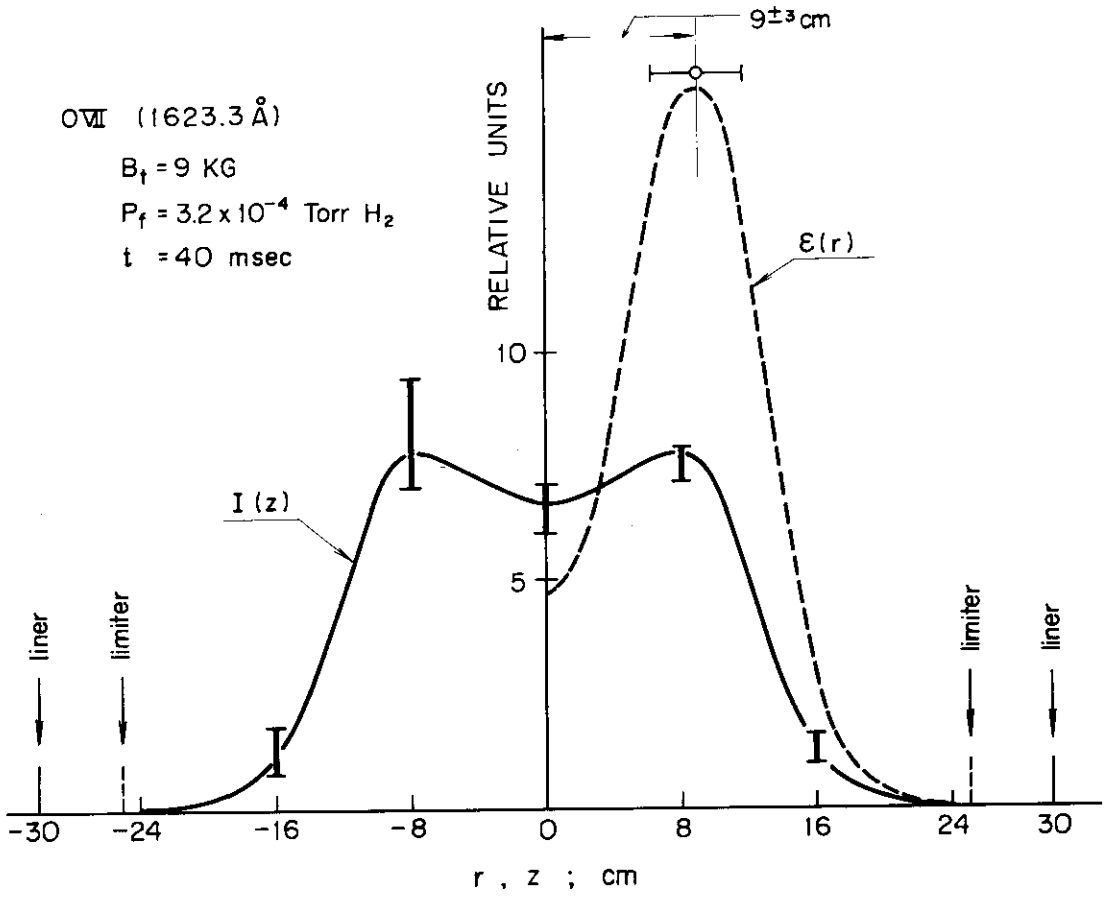

Fig.I.3-14 Spatial distribution of an OVII line at 30 msec.

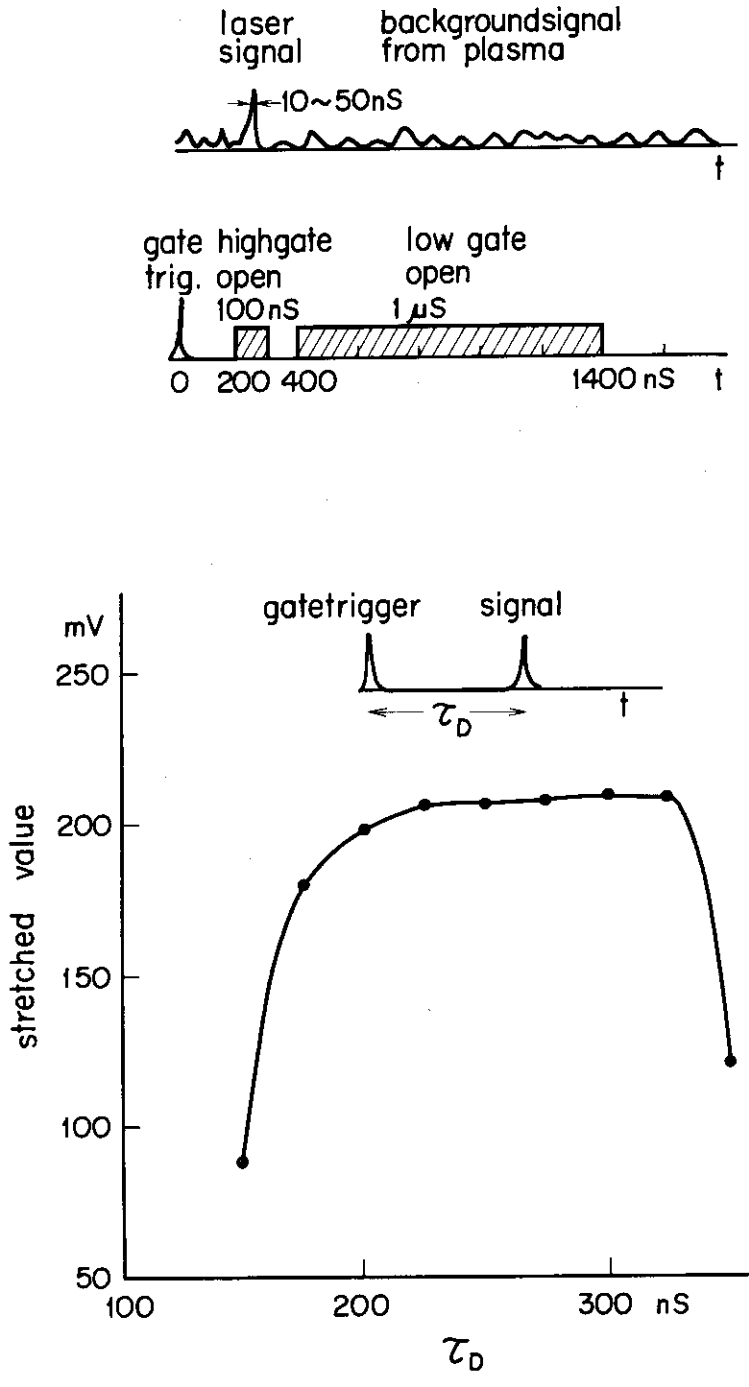

Fig.I.3-15 Characteristics of the high speed pulse stretcher.

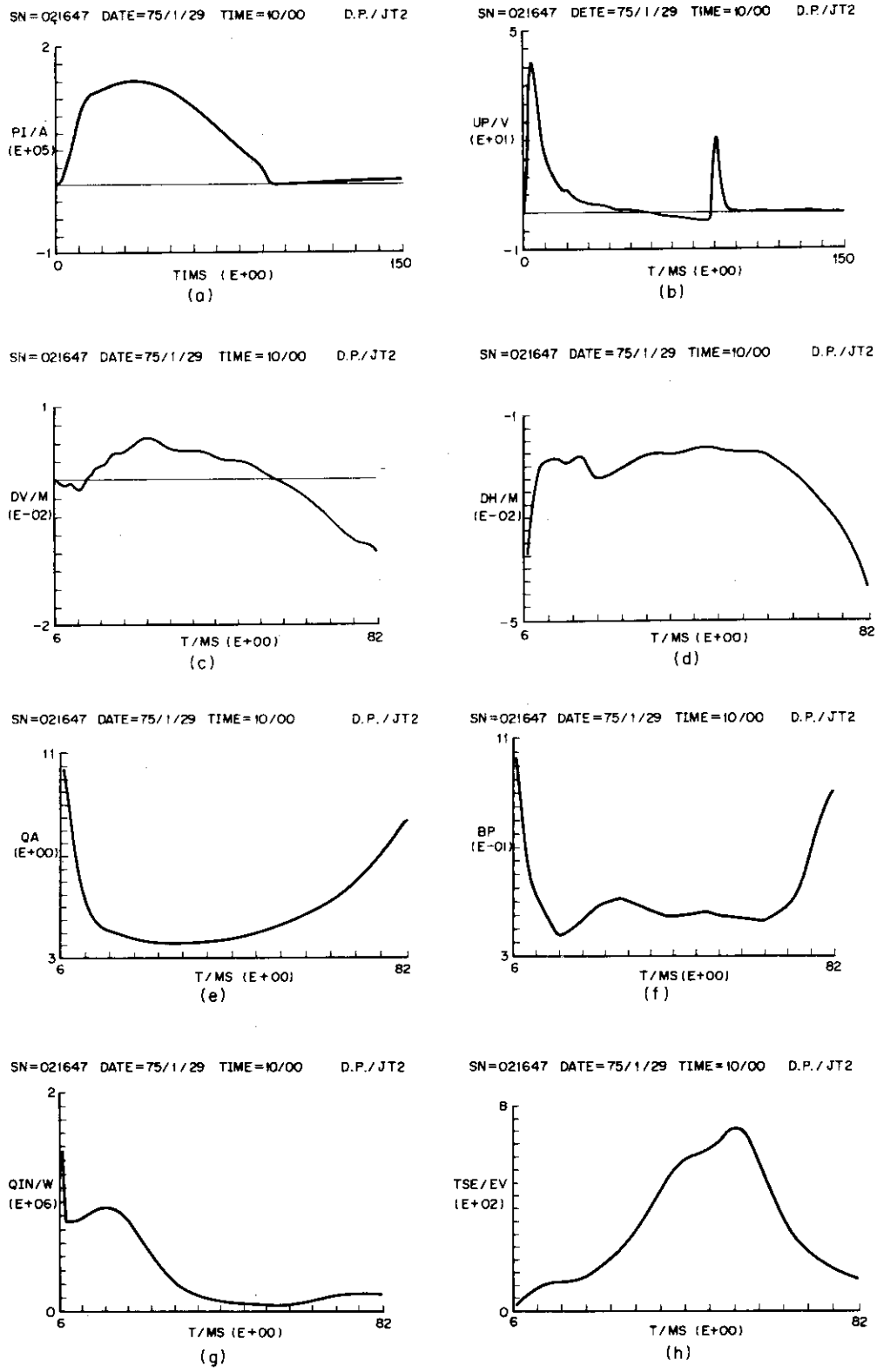

Fig.I.3-16 Processed data from magnetic probe signals; B_t=18kG, P_f=3.5×10^{-4}Torr, B_{vd}=140G, (a) plasma current, (b) one turn voltage, (c) vertical shit, (d) horizontal shift, (e) safety factor, (f) poloidal beta, (g) input energy, and (h) conductivity temperature (Z_{eff}=3).

4. Operation and Engineering

K. Anno, T. Arai, M. Isaka, K. Kodama, S. Kunieda, T. Ohga,
T. Shiina, T. Tani, T. Tokutake, N. Toyoshima, K. Yokokura

4.1 Introduction

The Group of Facility Operation and Engineering was formed in May 1973 to assume responsibility for operation and maintenance of the JFT-2 and JFT-2a devices, and associated engineering work.

In the 1974 fiscal year, the group was being mainly engaged in (1) power-up work of the generator to increase the toroidal field strength of JFT-2 from 10 kG to 18 kG, (2) manufacturing of a new pre-ionization equipment and a fast action gas valve for JFT-2, and (3) was also responsible for installation of JFT-2a.

In the 1975 fiscal year, the following engineering work is planned.

JFT-2; extension of the vacuum pumping system, increase of condenser capacity in the power supply for the primary winding of the iron core, construction of a cooling system of the turbo molecular pump (which is now cooled by the cooling system for the toroidal field coils) and improvement of the piping system of liquid nitrogen.

JFT-2a; construction of a power supply for modulation of the divertor current.

Fig. I.4-1 shows the major engineering works on JFT-2 and JFT-2a during this reporting period. Fig. I.4-2 shows a plan view of the building and arrangement of JFT-2 and JFT-2a.

(S. Kunieda)

4.2 JFT-2 Device

1) Power-up of the toroidal field supply system

The JFT-2 device was shutdown on April 24, 1974 to set out upgrading work of the toroidal field from 10 kG to 18 kG.

The required maximum magnetomotive force of the toroidal field coil is 8.1×10^3 kAT with a current duration of 3 sec. The required d.c. voltage and current are 1,700 V and 12,100 A respectively. These loads

are provided to the toroidal field coils by means of two motor-driven flywheel-generator sets as is shown schematically in Fig. I.4-3.

The motor-generator No.1 consists of:

induction motor	----------	1,000 kW
motor-driven flywheel	------	280 ℑ - m^2
d.c. generator	----------	9,680 kWP

The motor-generator No.2 consists of:

induction motor	----------	1,500 kW
motor-driven flywheel	-----	330 ℑ - m^2
d.c. generator	----------	2 × 6,030 kWP (each operated at 5,445 kWP)

The rated speed is 500 r.p.m.

The M-G No.1 was installed in the existing power room and No.2 in a new building (30 m × 10 m × 8 m) (Fig. I.4-2).

During the same period, the liner (0.6 mm thick) was replaced with a new one 1.2 mm thick. The d.c. vertical magnetic field coils of 300 V/T were replaced with coils of 1,500 V/T. The horizontal magnetic field coils were also replaced with those of 1,500 V/T.

The reconstruction work was completed on November 5. Discharge cleaning had been continued for about one month and experiment was resumed in December. Fig. I.4-4 shows the total gas inlet rate ($Q_T = Q_{leak} + Q_{outgas}$) in the vacuum vessel.

On February 11, 1975 the toroidal field coil support was broken and its repair was finished on March 30.

2) Development of equipment

A ECRH type pre-ionization apparatus (pulse width 2 msec, maximum output 1 kW at 28 GHz) had been used before the reconstruction of JFT-2. To meet the requirements of the increased toroidal field of 18 kG, a Z-pinch system was assembled. Its power supply consists of four condensers of 10 kV, 50 μF and the maximum charging voltage is 20 kV.

A fast acting gas valve that is part of a gas admitting system was constructed in cooperation with the Experimental Group. Its cross section is shown in Fig. I.4-5 and its performance curve in Fig. I.4-6.

4.3 JFT-2a Device

The installation of JFT-2a in the same building as for JFT-2 was started in April, 1974 and completed in August. Reconstruction of the building was required to reinforce the foundations and to lay on cable pits.

Test operation indicated the necessity of shortening the build-up time of plasma currents. To do this, the power supply for the primary winding of the main current transformer was modified to a system of two banks instead of one bank. This work was completed in January, 1975. Fig. I.4-7 shows the total gas inlet rate ($Q_T = Q_{leak} + Q_{outgas}$) in the vacuum vessel.

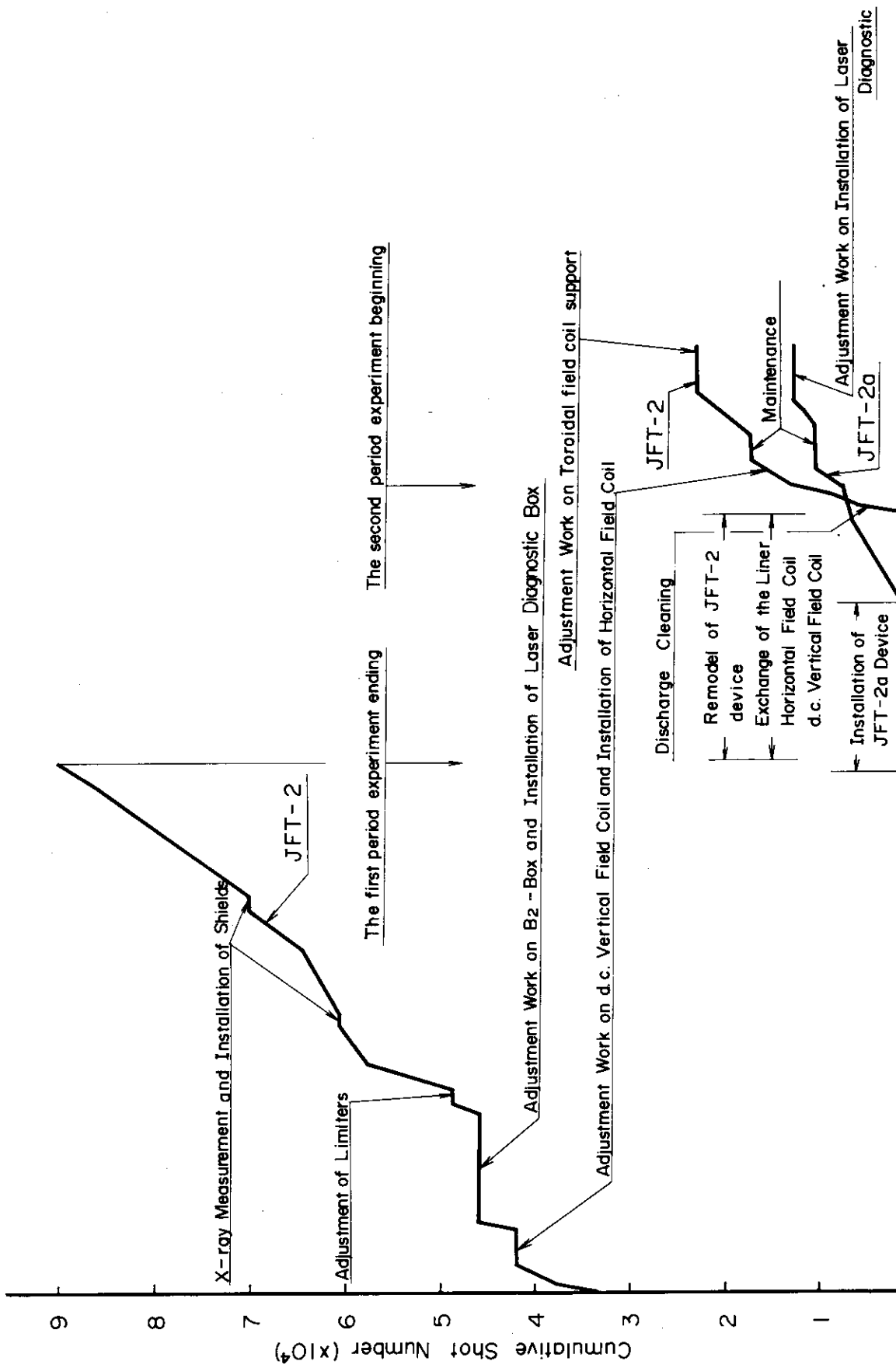

Fig. I.4-1 Operation log of JFT-2 device and JFT-2a device

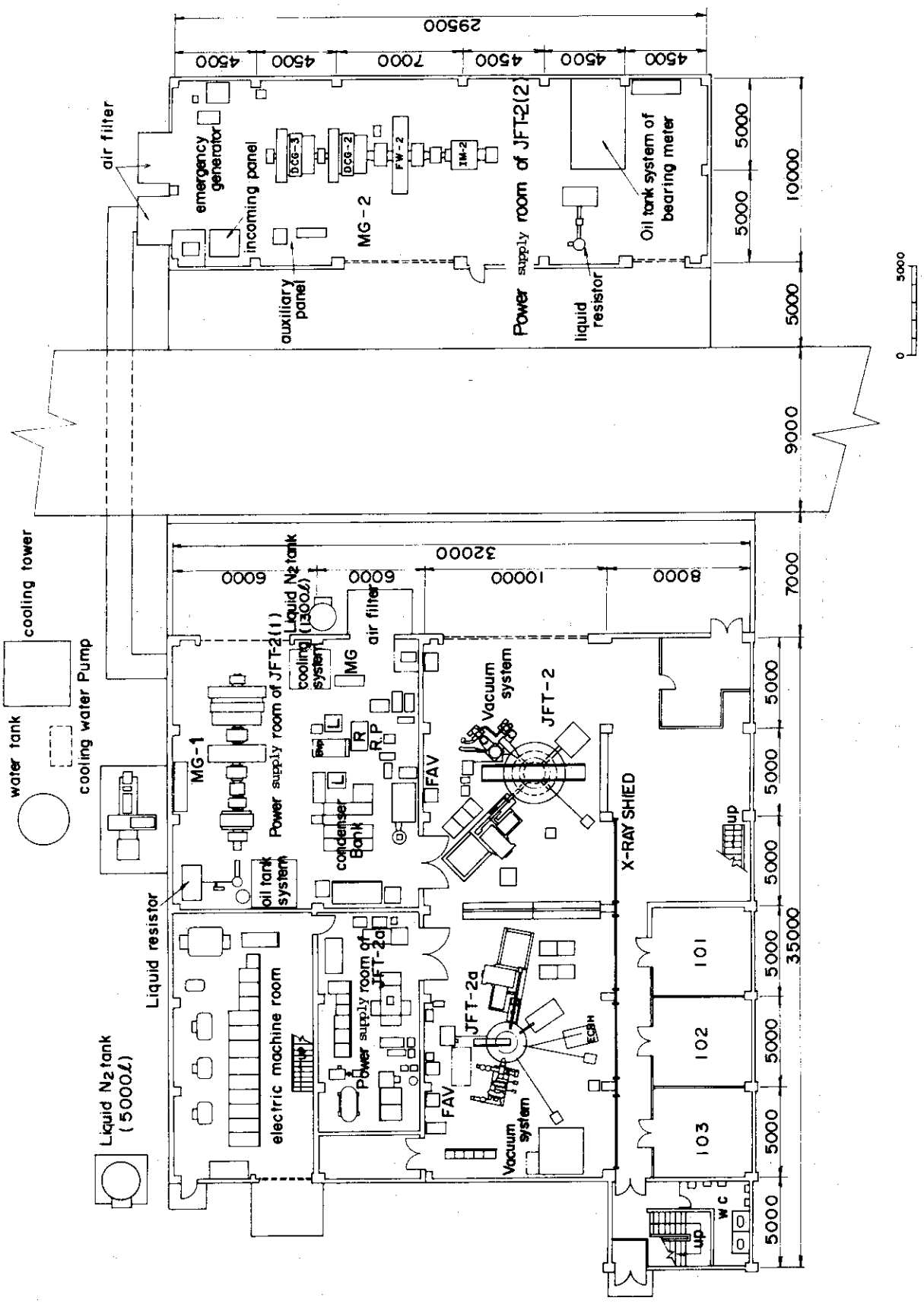

Fig. I.4-2 Plan view of the building for JFT-2 and JFT-2a

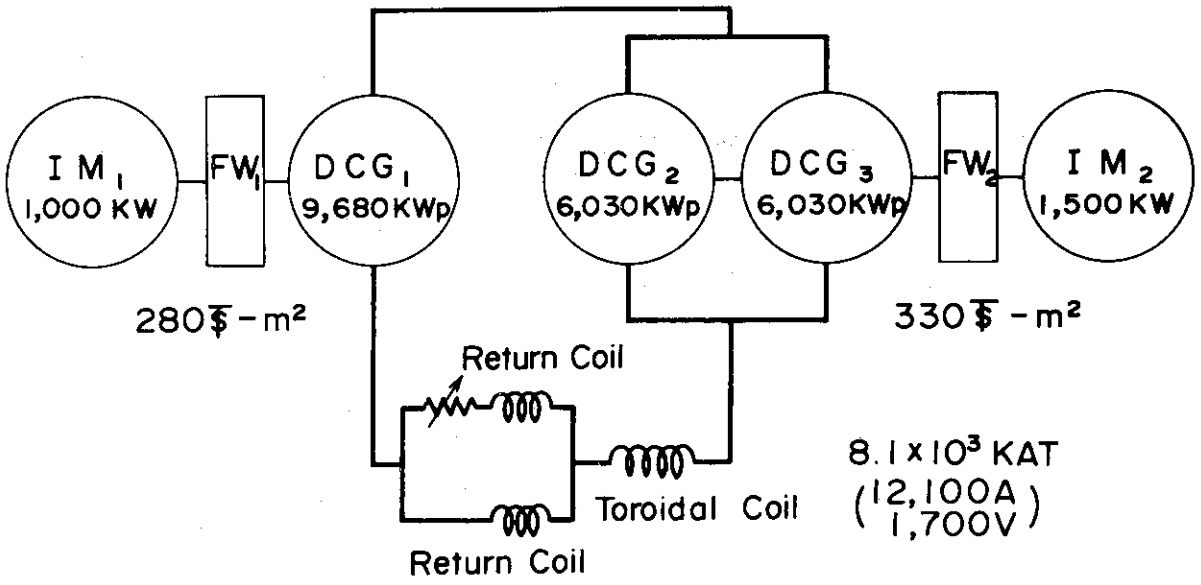

Fig. I.4-3 Block diagram of the power supply for JFT-2

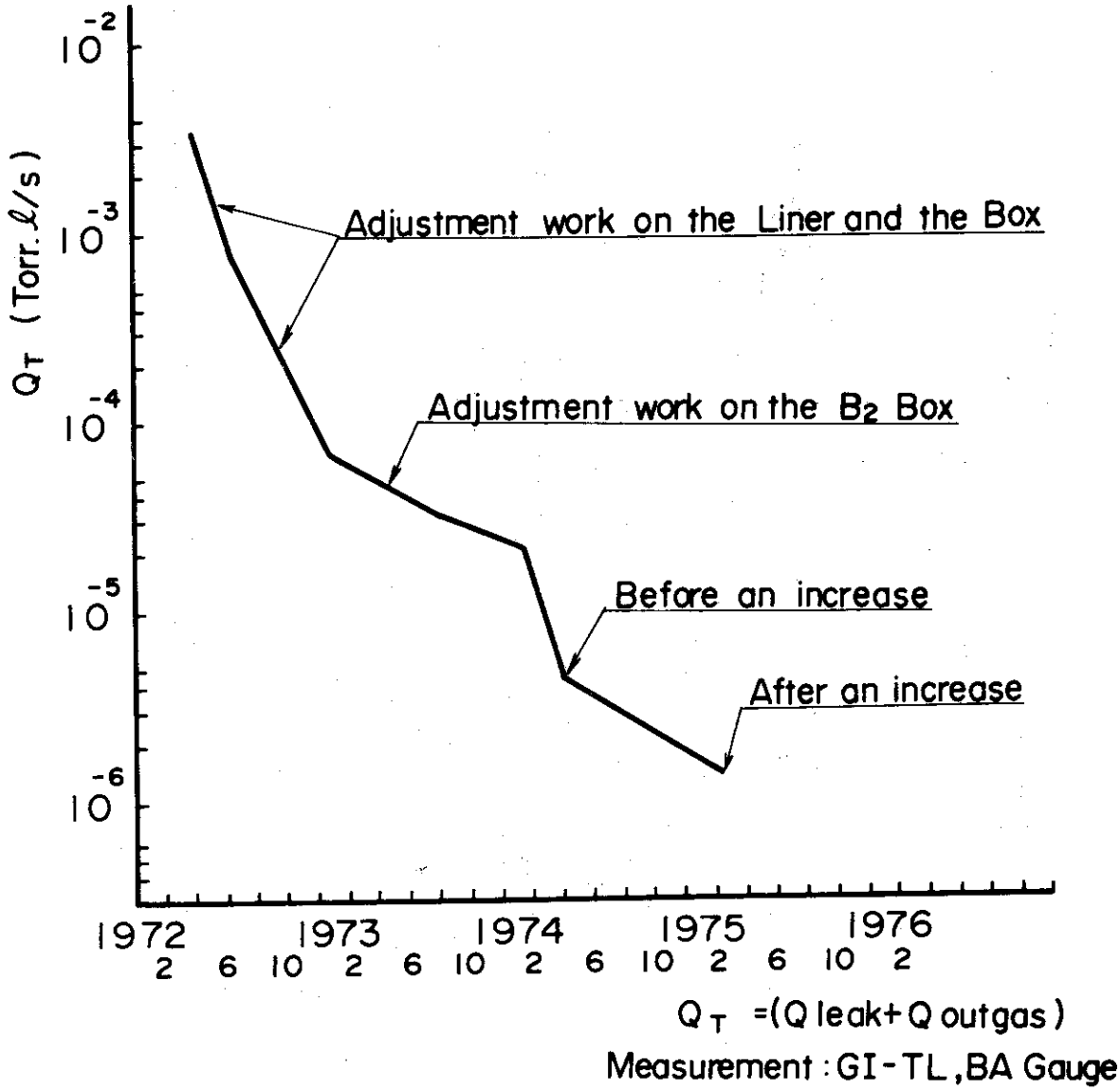

Fig. I.4-4 Total gas inlet rate in the vacuum vessel of JFT-2

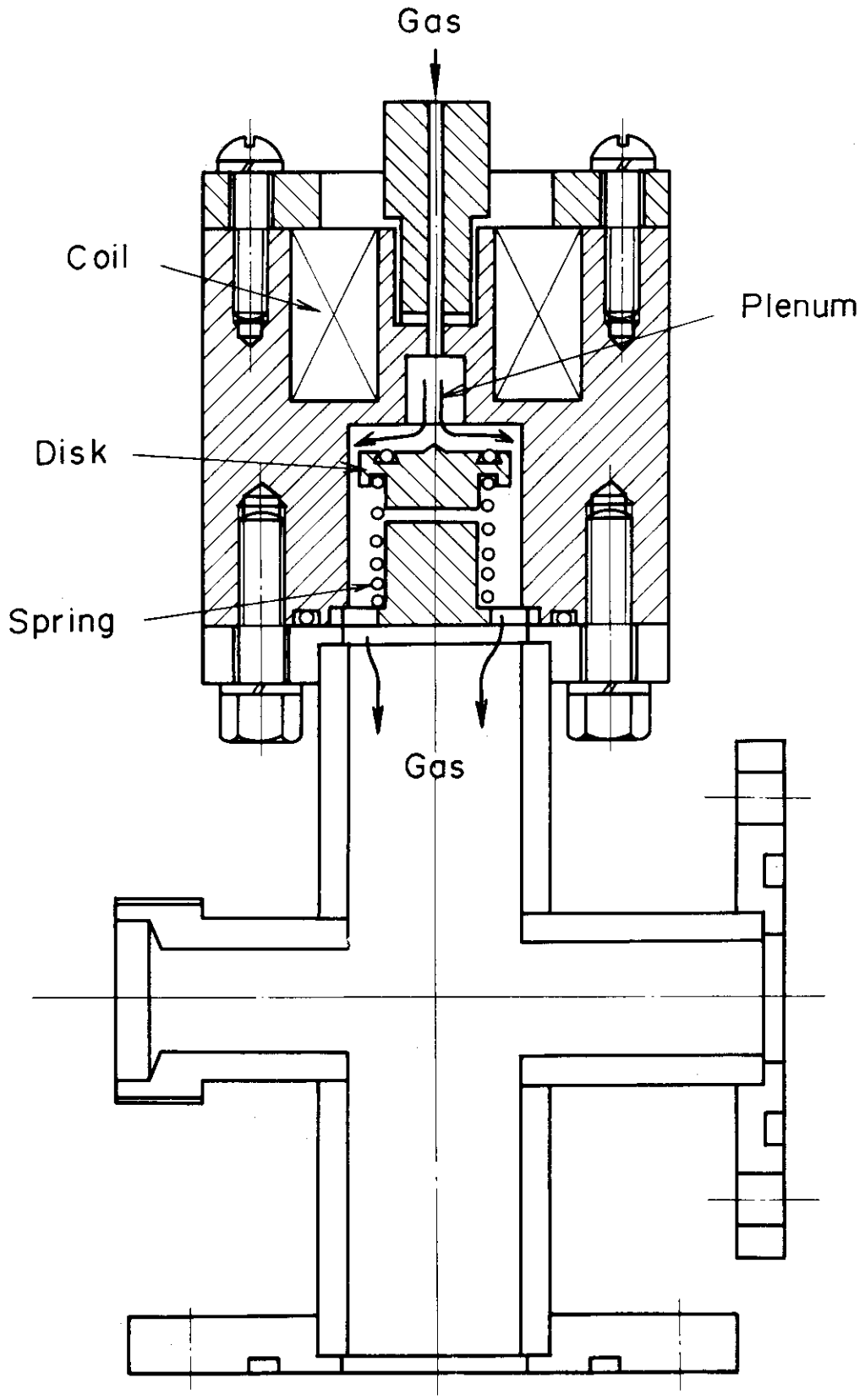

Fig. I.4-5 Cross section of fast acting gas valve

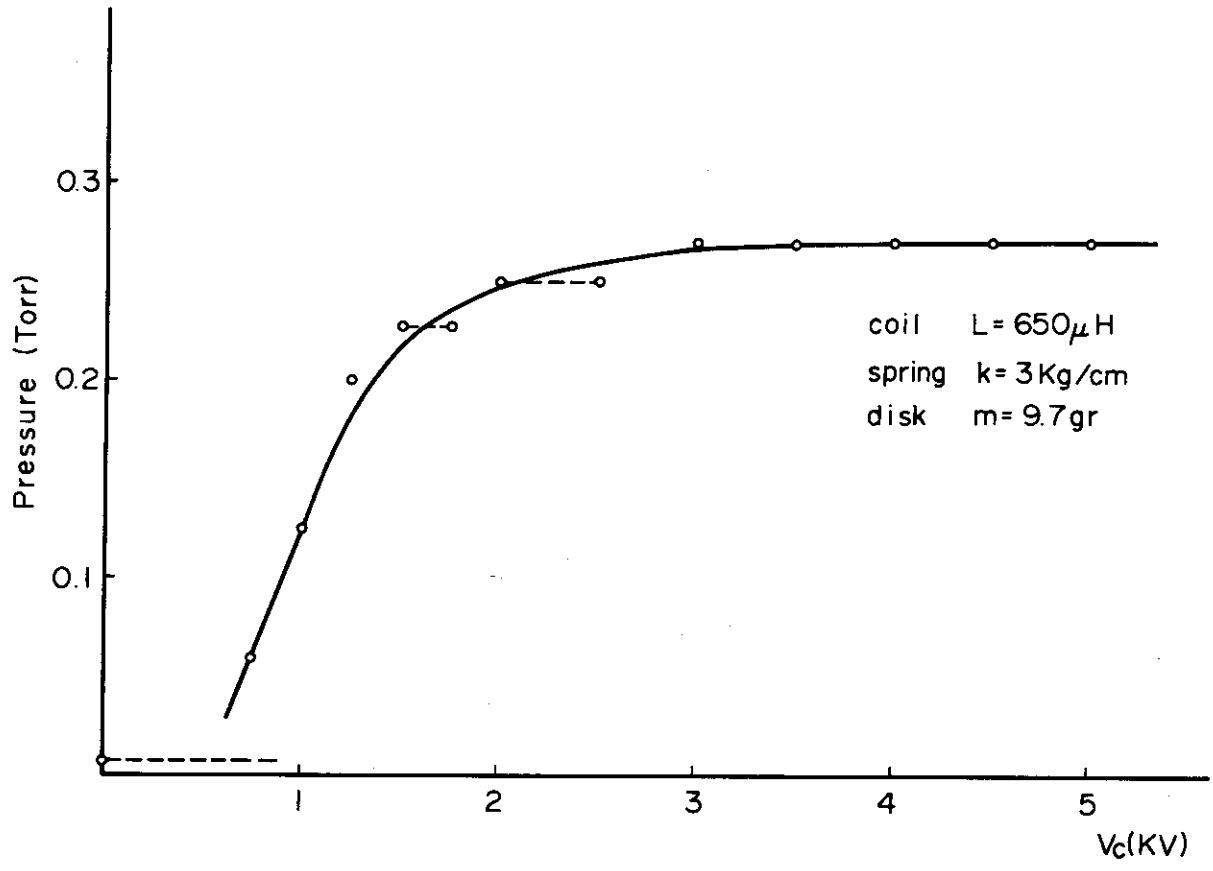

Fig. I.4-6 Performance curve of fast acting gas valve

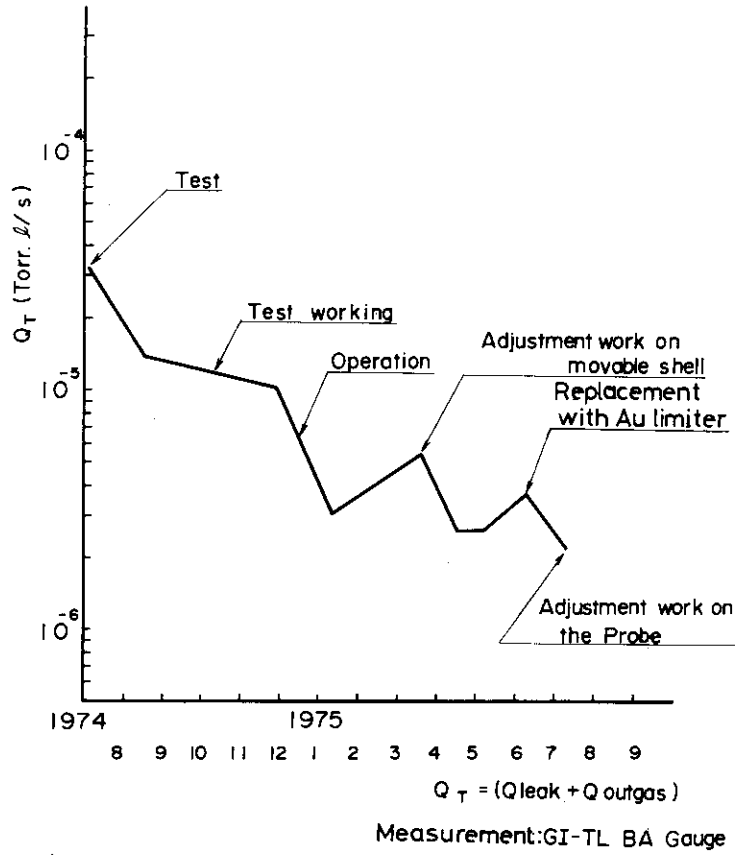

Fig. I.4-7 Total gas inlet rate in the vacuum vessel of JFT-2a

5. Development of Neutral Injection System

S. Matsuda, Y. Ohara, H. Shirakata, T. Sugawara*

5.1 Introduction

In order to develop neutral injection systems for supplementary heating in JFT-2 and JT-60, we started the development of an intense ion source in 1974. The injector test stand No.1 (ITS-1) was constructed, and preliminary experiment on the duoPIGatron ion source was started at the beginning of 1975. In the mean-time, an effect of the finite size electrode on the beam divergence was investigated, and a computational calculation on a two stage ion extractor assembly was made. A preliminary study was also made to clarify the technical problems related to the development of the neutral injection system for heating the JT-60 plasma.

(H. Shirakata)

5.2 Preliminary Experiments on the ITS-1

The injector test stand No.1(ITS-1) was completed and preliminary experiments started in February 1975.

The purposes of this test stand are

(1) To develop an ion source which may meet the requirements for the JFT-2 injection experiments.

(2) To develop higher current ion sources for future injectors.

Our first ion source is geometrically similar to the Oak Ridge "8 A" source with a few differences (Fig. I.5-1). All the insulation materials are made of aluminum oxide Al_2O_3 and the accel-decel electrodes are composed of parallel plates. Up to date we could extract ion beams of up to 6 A at 25 keV with typical beam divergences of 2.5° - 4° (e-folding distance). The electrode spacing is 6 mm in these cases. We have operated in a continuous gas feed mode under a relatively high operation pressure (about 80 μHg in the filament region).

The power supply system withstands a maximum 500 ms pulsed load with a duty cycle of 10% at a maximum output power of 12 A, 30 kV. The accel

---

* On leave from Research and Development Center, Tokyo Shibaura Electric Co. Ltd., Kawasaki, Japan

power supply has an SCR switch in an AC power line which can open the line within 10-20 ms in the case of breakdown. A series reactance (1.6 H) can absorb short breakdowns whose duration is up to 0.5 msec.

After preliminary measurements are completed on the present ion source, we will then turn our efforts to modification of this source and construction of a scaled up version. The programs for the next fiscal year are listed below.

1) Smaller aperture accel-decel electrode system (693 apertures in the 7 cm diam. electrode).
2) Source plasma production with a larger anode chamber to obtain a uniform illumination of the target cathode.
3) Construction of a 10 cm diam. electrode ion source with a coaxial zwischen.
4) Relation between materials and impurity contents in the beam line.
5) To regulate the power supply by using vacuum tubes; to shorten the current turn off/on time in the case of breakdown and to regulate the voltage drop.
6) Electrode cooling efficiency experiments.

(S. Matsuda, Y. Ohara, H. Shirakata, T. Sugawara)

5.3 Effect of the Finite Size Electrode on the Beam Divergence[1)]

Neutral beam injection heating of toroidal plasmas would require a low-divergent intense ion source. In such a system, the area of the extraction electrode with multi-aperture alignment is, unlike other sources, generally quite large. The total beam divergence is determined by a couple of factors, i.e. the divergence of the beam element and the size of the extraction electrode. We calculated the beam profile as a function of distance from the source on the assumption of Gaussian distribution of each beam element in the case of parallel electrodes (Fig. I.5-2). One may reduce the total beam divergence by modification of the electrode configuration. For instance, a properly designed curved electrode or a displaced aperture electrode can focus all the beam elements on the focal point and thus the total beam divergence can be reduced to the divergence of the beam element. This method is significant in the present injector system where the beam drift length is relatively short. However, it will not effective in the future injectors which may require a long drift length

due to the evacuation difficulties. Thus, more effort should be required to devise the means to reduce the divergence of the beam element.

(S. Matsuda)

5.4 Two Stage Extractor Assembly[2)]

A large-sized tokamak demands more beam energy and a longer pulse duration time. When the ion source has a configuration of one stage acceleration, the beam power flux density decreases with the increase of acceleration energy due to the electrical breakdown. This problem is solved by employing a multiple stage source. A longer pulse duration requires the reduction of heat loading on grids. Incident particles are primary ions, charge-exchanged and ionized slow ions, and secondary emitted and ionized electrons. The primary ion incidence on grids is independent of background neutral gas pressure. When the heat load due to the pressure dependent process is dominant, the acceleration gap should be devided into many stages and each aperture of a grid must have a corresponding aperture in the next stage grid. In the pressure independent case, the peripheral length of aperture per unit beam current should be short and a single hole should contain the beamlets from many apertures of the forestage grid. The beam divergence of the latter case was numerically analysed. The extractor studied is of two stages as shown in Fig. I.5-3, where the second curved electrode has many apertures. In the calculation the second electrode was assumed to be a homogeneous emitting surface of ion beam with a finite velocity. Effect of the first stage divergence was calculated on the following model. The beam is emitted in three directions from the second electrode, namely, the direction normal to the electrode and the divergent and convergent directions at an angle of ω_f. The parameters a_N and ψ are optimized to yield a low divergence beam of a given perveance G for $\omega_f = 0$, $t_N/a_N = 2/3$, and $z_N/z_s = 1/5$ (Fig. I.5-4). The initial divergence effect was examined for the above combination of parameters. The beam divergence are expressed by $\omega = \omega_* + \omega_f$ in the range of $\omega_f < 1$ degree, where ω_* is the divergence angle for $\omega_f = 0$. This behaviour is presumed to result from the relatively large convergence angle of the second electrode(ψ). The numerical calculation shows that the simple model assembly of two stage extractor provides a good focusing below the perveance per exit hole of about 0.1 micropervs for protons.

(Y. Ohara and T. Sugawara)

5.5 Preliminary Study on the JT-60 Neutral Injection System.

A preliminary study was made to assess the technological areas necessary for the development of the JT-60 neutral injection system. Basic requirements for the injection system are summarised as follows.

Neutral beam injection power;	10 - 20 MW
Neutral beam energy;	50 - 100 keV
Neutral injection pulse length;	2 - 10 sec
Limitation on the input cold gas flux;	$<10^{20}$ (H°/sec)

It has become clear that the developments are necessary of an ion source to produce several MW of beam power at 50 to 100 keV with up to 10 sec pulse length, and of a dry vacuum pumping system with large pumping speed.

(S. Matsuda, Y. Ohara, H. Shirakata, T. Sugawara)

Reference

1) S. Matsuda: Japan J. appl. Phys., 13 (1974) 1630.
2) T. Sugawara and Y. Ohara: Japan J. appl. Phys., 14 (1975) 1029.

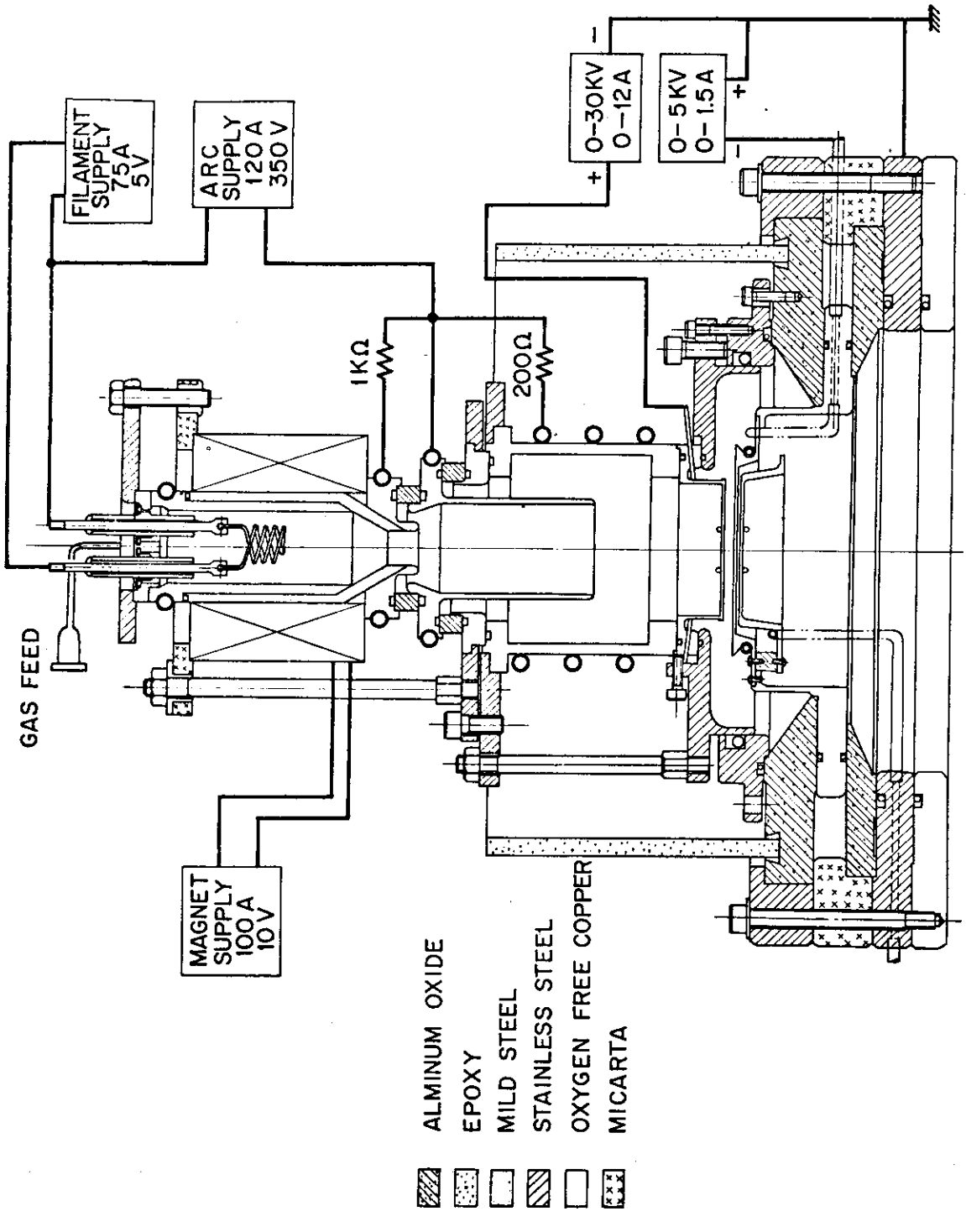

Fig. I.5-1 JAERI duoPIGatron

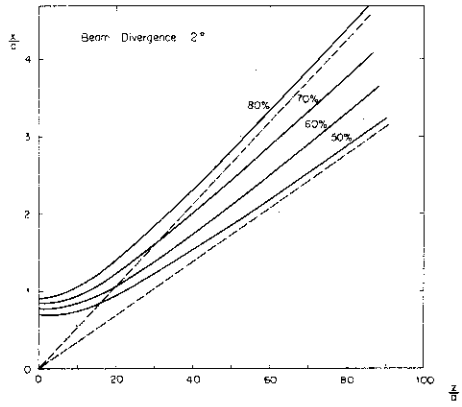

(a)

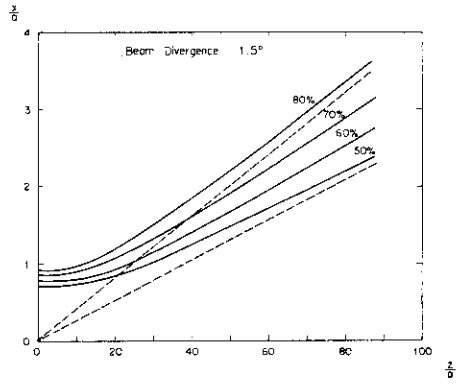

(b)

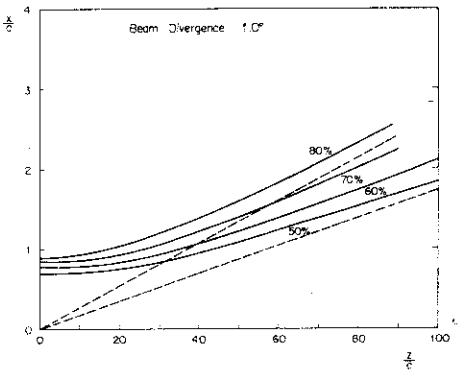

(c)

Fig.I.5-2 Radius of the target into which fraction of the total beam is injected as a function of distance from the extraction electrode. Divergences of the beam element determined by the half width of the half height are assumed to be (a) 2.0°, (b) 1.5° and (c) 1.0° respectively. The broken lines indicate the lowest limit of the total beam divergence by improving the finite size effect.

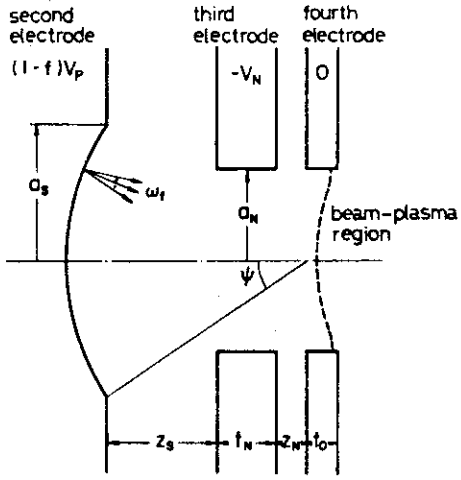

Fig. I.5-3 The second stage configuration. The beam-plasma boundary is indicated by the broken line.

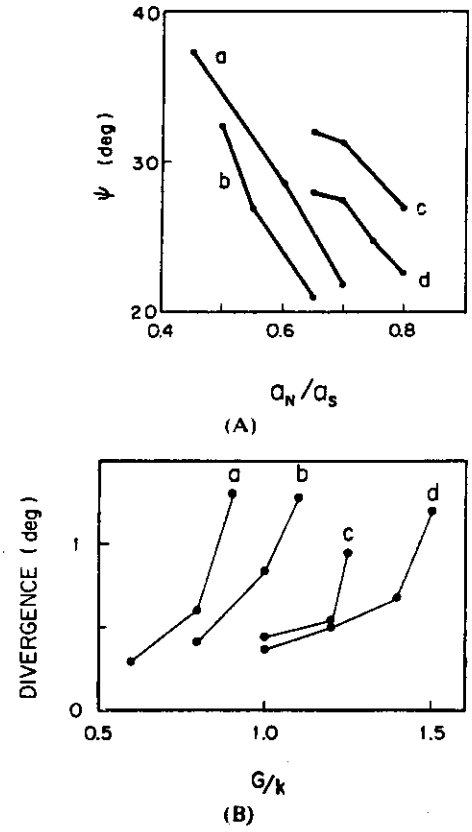

Fig.I.5-4 Optimum values of convergence angle and exit hole radius(A), and the relation between the beam divergence and the perveance(B). The larger ψ dots in (A) correspond to the higher G dots in (B). (a) $S=2/3$, $f=1/3$, (b) $S=2/3$, $f=1/2$, (c) $S=1$, $f=1/3$, (d) $S=1$, $f=1/2$.

II. JT-60

N. Asami*, Y. Gomay**, A. Kameari*, T. Kobayashi***,
M. Morita, H. Ninomiya, M. Ohkubo, M. Ohta, H. Suzuki,
Y. Suzuki, S. Tamura, K. Tani, T. Tazima, M. Yamamoto,
H. Yamato**, M. Yoshikawa

1. Introductory Remarks

1.1 Introduction

JT-60 (Fig. II.1-1) is a large Tokamak device now under design at Japan Atomic Energy Research Institute (JAERI). Its basic aim is to produce and confine a plasma of temperatures in a multi-keV range and of confinement times comparable to a second, and to study its plasma-physical properties as well as engineering problems associated with them.

In this respect it bears a similarity to large Tokamak devices under design elsewhere in the world. In comparison, emphasis in the JT-60 design is placed less on the break-even capability in DT plasmas and more on the achievement of equivalent T-$n\tau$ values in hydrogen and/or deuterium plasmas and the study of plasma-engineering-oriented aspects of the near-reactor plasmas. The freedom in deisgn options arising from its non-DT character is to be utilized to its maximum in securing flexibility in plasma-physical as well as plasma-engineering and technological considerations. For example, a magnetic limiter and expanding limiters are incorporated in the device and used, when needed, to control impurity concentration of the plasma and the current distribution in the plasma.

The preliminary design of the device is completed in 1974-5. The detail design and required engineering development are started in 1975. The construction is expected to begin in 1976 and the completion in 1980. Both dates are subject to the approval and funding by the Government.

---

* On leave from Engineering and Development Division, Mitsubishi Atomic Power Industries Inc.
** On leave from Research and Development Center, Tokyo Shibaura Electric Co., Ltd.
*** On leave from Atomic Energy Research Laboratory, Hitachi, Ltd.

1.2 Basic Assignments

The basic assignments to the JT-60 may be summarized as follows:

(1) to produce and confine plasmas that can physically simulate reactor conditions and

(2) to gather information necessary to optimize the type and design parameters of the next installation

(3) to the extent that non-DT experiments allow.

Numerically the target plasma parameters to achieve its assignments are:

(1) $T = (5\text{-}10)\ 10^7$ K

(2) $n\tau = (2\text{-}6)\ 10^{13}\ cm^{-3}$ sec,

Under the above condition the plasma is typically in the ion-trapped regime where the ion trapped mode may become dominant in determining the confinement times.

(3) The duration of the discharges should be about ten seconds to allow the study of long-time effects on the plasma confinement.

1.3 Objectives

As mentioned in the previous sections information vital to further advancement of nuclear fusion research is to be obtained in JT-60. It constitutes objectives of JT-60 programs:

(1) Scaling laws of plasma confinement times in the near-reactor regime,

(2) Dependence of magnetohydrodynamic properties on plasma parameters in the near-reactor regime,

(3) Wall-plasma interaction, especially impurity behaviors and methods to control them,

(4) Effectiveness of supplementary heating, and

(5) Plasma equilibrium and methods to control it.

It is necessary in the design of JT-60 to evaluate each of the above objectives and to determine machine parameters, characteristics, and provisions for the device so that the basic assignments described in

Sec. 1 be met to the best knowledge available at present.

1.4 Plasma-Physical Options in the Design

There are a number of options both plasma-physical and technological in the design of a large Tokamak device. In this section the choices made in the plasma-physical design are described.

1) Choice of Tokamak Confinement Laws

In determining the machine parameters to achieve the target plasma parameters, choices have to be made on the values of q and β and the scaling low of $n\tau$.

(1) Values of q and β

The value of $q_{al} = B_t a/B_p R$ is chosen to be 2.5, which typically corresponds to the real value of q_a of 3.5. β_p is chosen to be unity.

(2) Scaling laws of $n\tau$

Four kinds of the scaling laws of $n\tau$ are considered in the determination of the machine parameters: the pseudoclassical, the empirical ($\propto a^2 B_p$), the neo-Bohm (200-300 times Bohm), and the trapped particle instability-induced.

2) Basic Choice of Machine Characteristics

(1) Circular Cross-section

A circular cross-section is chosen for the device. When the magnetic limiter is in operation, the cross-section necessarily becomes a non-circular. However, the deformation from the circular cross-section is to be minimized and localized.

The reasons behind the decision is partially the conservatism in the plasma-physical and the engineering considerations, and partially the existence of a parallel program JT-4, a smaller vertically-elongated Tokamak.

(2) Basic parameters: $R \sim 3$ m, $a \sim 1$ m, and $B \sim 3$ T.

The choice is a compromise of two conflicting trends in optimization:

(a) Maximization of $n\tau$

A crude optimization study was made in whicn $n\tau$ is maximized for a

fixed total (toroidal and transformer) magnetic energy considering the limits of mechanical stresses and temperature rises in the coils. The analysis shows that the above choice is close to the optimum for the trapped ion instability-induced scaling and that lower values of R/a and B_t are favored for other scaling laws of $n\tau$, such as $R \sim 3.4$ m, $a \sim 1.4$ m and $B_t \sim 3.9$ T.

(b) Alleviation of Demanding Engineering Problems

When R/a and B_t are reduced, the magnetic energy stored in the transformer and hence the capacity of the current breaker in its power supply have to be increased. The power of the supplementary heating systems is also required to be made higher. The increase is substantial for both and, for an example mentioned in (a), is by factor of 1.5. Since it further burdens the requirements on the technologically critical components, choosing a fat, low-field device based on the argument in (a) may not be as wise as it seems.

(3) Comparative Study of Impurity Control with an without Magnetic Limiters

One of the pivotal questions in fusion reactor designs is whether or not to use a magnetic limiter or a divertor. In the JT-60 design a magnetic limiter is incorporated in addition to axisymmetric limiters to examine its relevance in reducing the heat loading on the limiters and in reducing high-Z impurity by a divertor action. A comparative study can be made in both cases, with and without the magnetic limiter.

(4) Comparative Study of Expanding Limiters

In order to control the current density and to reduce impurity production at the current build-up stage an expanding magnetic limiter is used. For an operation without the magnetic limiter a fast movable limiter is also installed.

(5) Comparative Study of Methods to Control Current Distributions

(a) Expanding limiters. See (4)

(b) Multi-stage transformer power supply with variable time intervals and rise times

The staged rise of plasma current which reduces the requirements on the transformer coil and the breakers can be used to control the plasma

current distribution.

(c) Localized supplementary heating

Neutral injector heating at various injection energies and RF heating may be effective in controlling the current distribution.

(d) Preionization by using the fast movable limiter

The electron emission or plasma injection from the movable limiter and the RF power applied to it may be effective in shaping the current distribution.

(e) Feeding of Cold Gases

The temperature distribution may be varied by external feeding of gases.

It may be advantageous to combine two or more of these methods, since they each affect the current distribution in a different way. Careful programming of these methods may provide a most satisfactory result in establishing and maintaining a favorable current distribution.

(6) Comparative Study of Liner and Limiter Materials

The dismantling of those components should be made convenient for the ease in their replacement. It allows the comparison of different materials, structures, and surface conditions in an experimental search for the best in reducing wall-plasma interaction.

(7) Feed-back Control up to the Quadrupole Component

In maintaining the plasma equilibrium, control is made not only on the vertical and the horizontal position, but also on the ellipticity of the cross-section.

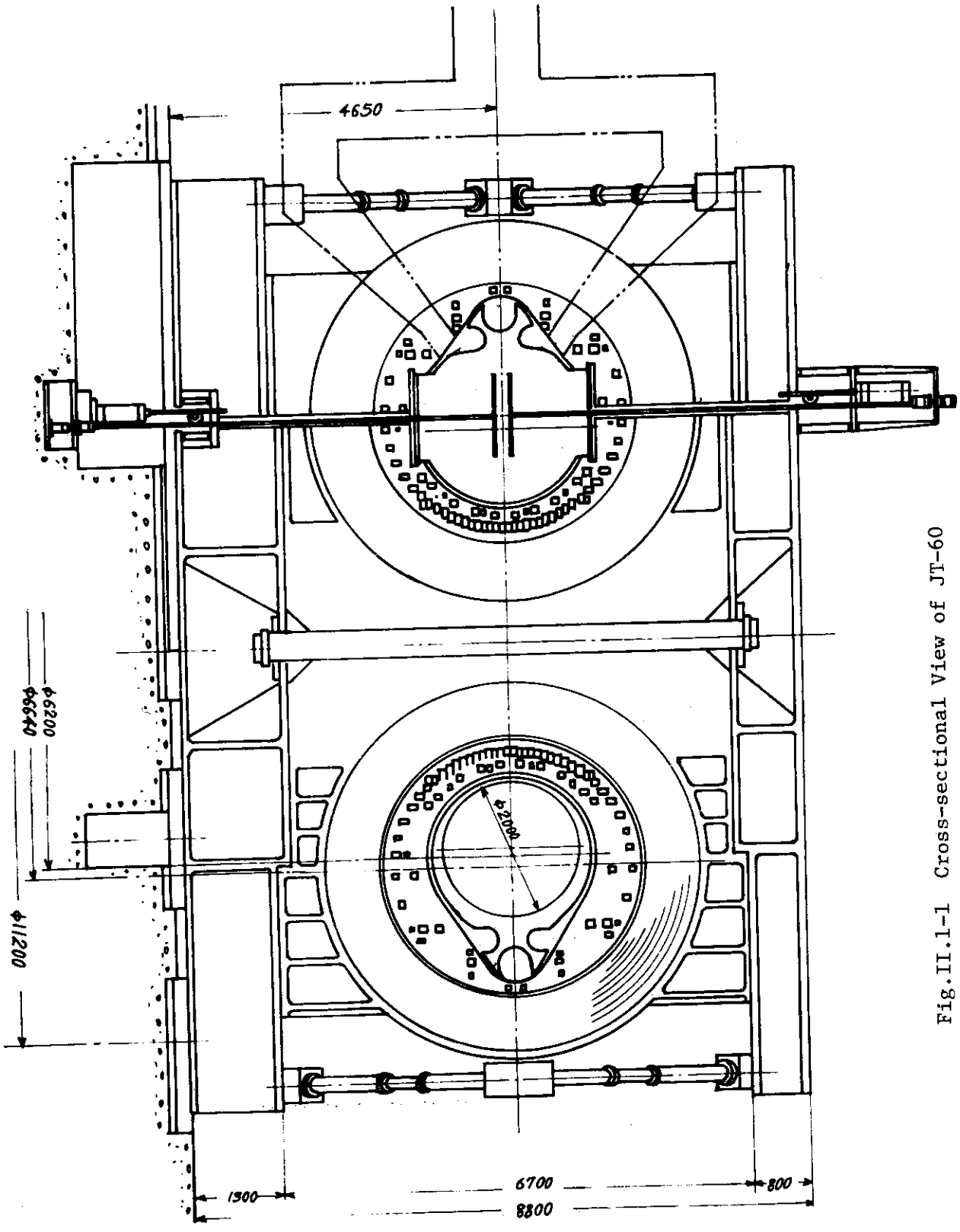

Fig.II.1-1 Cross-sectional View of JT-60

2. Equilibrium, Stability and Control in JT-60

2.1 Introduction

For a large scale tokamak like JT-60, it will be necessary to provice a poloidal magnetic field that is accurately controllable in space and time, because

(1) the poloidal field should be controlled over a wide range of intensity and spatial characteristics, in order to equilibrate the plasma of various poloidal beta's and current distributions.

(2) the field should include a magnetic limiter field to reduce impurity particles,

(3) it is desirable that the space in the vacuum chamber is utilized effectively, as the energy confinement time strongly depends on the radius of a plasma column.

For the design to realize such a poloidal field, we have developed the following procedures[1,2].

1) We calculate the intensity and distribution of a poloidal field required for given plasma parameters. Here the plasma parameters are the total toroidal current I_p, the current density distribution or the plasma internal inductance ℓ_i, the pressure distribution, the poloidal beta β_p, the geometrical position and shape of the plasma and so on. In this calculation, we define a virtual coil which envelops the domain to be occupied by poloidal coils and assume that a distributed current can flow in the virtual coil. Then we search for a current distribution and a poloidal field to be required for the plasma equilibrium[3,4].

2) After the parameter research in the previous procedure, we determine the coil systems needed. The proper location of each coil system and its current are obtained from the field distribution calculated in the first procedure. Various restrictions from technical requirements are taken into consideration at this stage[5,6,7].

3) In the third procedure, we solve the plasma equilibrium equation as a free boundary problem and check the lumping effect of the current in the discrete coils on the plasma equilibrium[8,9].

2.2 Vertical Field and Quadrupole Field

In JT-60, we have chosen a circular plasma cross section as a standard configuration, taking into account the experimental results of tokamaks up to the present time. In order to reduce impurities in the plasma, however, we provide the device with a magnetic limiter basides an axisymmetric limiter.

From the study of the necessary poloidal field in the first procedure, we have decided to provide two coil systems for the device; one is so-called a vertical coil and the other is a quardrupole coil. Each coil system produces a field of simple and clearly defined characteristics.

In Fig. II.2-1 the flux surfaces are illustrated when the magnetic limiter is not provided, where $\beta_p = 1$, $\ell_i = 1$ (parabolic current distribution) and $I_p = 3.3$ MA. The poloidal field required to equilibrate the plasma column is shown in Fig. II.2-1B. Here the poloidal field by the vertical field B_v is that on the horizontal median plane. The field B_v in the figure is well approximated by a linear function of major radius R. n is so-called the n-index, that is $n = -\frac{R}{B_v}\frac{\partial B}{\partial R}$. When a magnetic limiter is used, the flux surfaces become as shown in Fig. II.2-2, where the current I_d flowing in the main magnetic limiter coil is 1 MA, and the current in each of the two auxiliary coils is -0.5 MA. The plasma equilibrium is calculated on the assumption that the plasma surface is bounded by a flux separatrix surface. In Fig. II.2-2B the suffix VL indicates the total value including the magnetic limiter field. The field B_v is well approximated by a linear function of R in this case, too.

From the calculations including other plasma parameters, we concluded that the poloidal field in JT-60 should be produced in a manner as expressed as $B_v(R) = B_{vo} + \frac{R}{R_o} B_{v1}$, where R_o is the radius of the center of plasma region. The parameters B_{vo} and B_{v1} should be changed widely with the variations of plasma parameters, and the linear dependence of the field should be held good in the total region of the vacuum chamber. Such a field is produced by means of the two coil systems mentioned before; One is a vertical coil, the current in which produces the field distribution $B_v(R) = B_{vo}(1 + \alpha\frac{R}{R_o})$, and the other is a quadrupole field coil, the current in which produces a quardupole field $B_q = B_{qo}\frac{R - R_o}{R_o}$ in the vacuum chamber. The relation between B_v and n-index is shown in Fig. II.2-3, where β_p is changed from 0.1 to 1.0, $\ell_i = 0.5$ and 1, and $I_p = 3.3$ MA. As is shown in

the figure, these two coil systems can allow the operation in the hatched region which is required for equilibrium over a wide range of plasma parameters. In cases of a plasma current below 3.3 MA, the B_V value of each in Fig. II.2-3 should be reduced in proportion to the plasma current.

2.3 Magnetic Limiter Field

In the present stage of JT-60 design, the position of the magnetic limiter is to be at the outer side of the plasma column, since in this case we can use the region of the toroidal field of a high intensity and a small ripple for the plasma. This system has also an advantage of reducing the escaping particles and impurities when the magnetic mirror effect is taken into account. But a major disadvantage of this system is that prasma instability may occur owing to the decrease of the magnetic well depth and the deterioration of the positional stability condition. In order to reduce these disadvantages, we use three coils for the magnetic limiter; one is the main coil in which the direct current flows up to 1 MA and the other two are auxiliary coils in which the current flows up to -0.5 MA each. The most preferable location of the auxiliary coils is shown in Fig. II.2-4.

Comparative studies of various magnetic configurations were carried out from the standpoint of stability and diffusion. For each configuration we calculated the distribution of q-value as a function of minor radius $\frac{d\Phi}{d\psi}$, shear parameter $\Phi \frac{d}{d\Phi}(\frac{1}{q})$, magnetic well depth $\frac{dV}{d\Phi}$, the ratio of neoclassical diffusion coefficient $D_{neoclssical}$ to $D_{clssical}$ and the vertical or holozintal stability, where Φ means the toroidal flux and ψ the poroidal flux.

The actual positions of the poloidal coils are determined by employing the linear programming, the non-linear programming or Zakharov's method, depending on the purpose of each coil. If the coil positions interfere with each other or with forbidden regions such as diagnostic ports and injection ports through a graphic display device.

The coil system determined by these processes is verified by the third procedure, solving the equilibrium equation of free boundary problem. An example of plasma configuration is shown in Fig. II.2-4. We assume in this calculation that the plasma surface is defined by a

separatrix flux. The effect of lumping the coil currents on the periphery of the plasma can be estimated from this figure. A small scale poloidal ripples occur on the plasma boundary.

2.4 Equilibrium during the Current Build-up

Impurity influx must be reduced in the start-up phase of a discharge as well as in the steady phase. In the start-up phase a skin current configuration is predicted which brings about a strong kink instability. As a remedy to this, we install a fast movable limiter on the device. In addition to it, an expanding magnetic limiter can be operated by using the coil systems mentioned before. A steady octupole field is established before a discharge. When a discharge is started, a plasma enclosed inside a separatrix flux surface is made to expand with the plasma current. In Fig. II.2-5, an example of thus obtained octupole field is shown. A series of the predicted equilibria in the current build-up phase are shown in Fig. II.2-6 to 9. As a current build-up mechanism in the start-up is not clear, we assumed tentatively $\beta_p + \frac{\ell_i}{2} = 0.75$ in the total phase of current build-up in calculation of these equilibria, and we also assumed that the plasma surface is defined by a separatrix flux surface. We can visualize the behaviour of the surrounding separatrixes and the diverted flux lines during the current build-up from these figures. The characteristics of the expanding process are summarized in Fig. II.2-10, where the behavior of a plasma radius, plasma position, q-value estimated from cylindrical approximation, required vertical field and quadrupole field are shown as functions of the plasma current.

2.5 Control of the Poloidal Field

We have paid attention to the spatial distribution of the poloidal field and now describe the control system of the poloidal field which maintains a plasma in a correct position during the discharge.

From the reasons mentioned in section 2.1, we have to control not only the plasma position but the shape of the cross section. The currents in the vertical field coil, the quadrupole field coil and the horizontal

field coil have to be operated accurately and amenably enough to track the time variations of the plasma parameters. In order to meet these requirements we use a digital computer system to control the phase of the power thyristors that feed currents to the coils. We apply a hierarchical construction in the control system; the higher part provides a pre-programmable current control and the lower part provides a direct feedback control. Fortunately, the experiments in JT-60 will be of a pulse operation in which a short period of the discharge less than 10 sec is followed by a long interval more than 5 min. The computer can make calculations to optimize the time variations of the currents of the coil systems, using the modern control law during this long interval and apply the calculated results to the next discharge. A small unexpected variations of the plasma parameters are controlled by the feedback system.

In order to analyse the efficiency and the stability of the control system, calculations have been undertaken by use of the servo control theory. Though the JT-60 device has not an ideal conductive shell, a lot of elements in the device play a role of a resistive shell; the liner, the vacuum chamber, the cooling plate, the toroidal coils and the poloidal coils. Calculations are under way to derive magnetic coupling relations between the plasma, the three control coils, the magnetic limiter coils and resistive shells. The plasma dynamics under these conditions are computed by an analog or digital computor.

The results of a preliminary analysis are described next, where the interaction between the vertical, horizontal and quadrupole systems are neglected and these three systems are treated independently. Figure II.2-11 shows a functional block diagram of the vertical field control system[1]. This diagram is derived from the equation of the plasma motion and the coupling relations among the components.

The waveforms of typical quantities against a step-wise field disturbance are shown in Figs. II.2-12 and 13, where P control means a method to feedback a proportional amount of the displacement to the coil voltage and PD control means a method to feedback a proportional amount and its time derivative. It is aimed at keeping the displacement less than 2 cm against an external field disturbance whose strength is 5% of the total vertical field. From this analysis shown in the figure we conclude that a 15% forcing voltage is required, and that the P control with 1 ms sampling interval, can suppress the displacement less than the specified value while the PD

control requires a 10 ms sampling interval.

References

1) Suzuki, Y., Kameari, A., Ninomiya, H., Masuzaki, M. and Toyama, H., IAEA Tokyo Conference (1974), CN-33/A11-2.
2) Suzuki, Y., Nucl. Fusion 14 (1974) 345.
3) Kameari, A., Suzuki, Y., and Ninomiya, H., JAERI-M 6027 (in Japanese).
4) Kameari, A., Suzuki, Y., and Ninomiya, H., JAERI-M 6028 (in Japanese).
5) Kobayashi, T., Tamura, S., and Tani, K., JAERI-M 5898 (in Japanese).
6) Toi, K. and Takeda, T., JAERI-M 6018.
7) Kameari, A., Ninomiya, H. and Suzuki, Y., to be published.
8) Ninomiya, H., Suzuki, Y. and Kameari, A., JAERI-M 6025 (in Japanese).
9) Ninomiya, H., Suzuki, Y. and Kameari, A., JAERI-M 6026 (in Japanese).
10) Suzuki, Y., Ninomiya, H. and Kameari, A., JAERI-M 6050 (in Japanese).

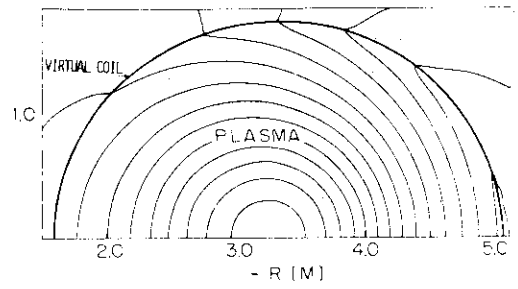

FIG. 1A, TYPICAL MAGNETIC CONFIGURATION OF CIRCULAR CROSS SECTION, CASE A.

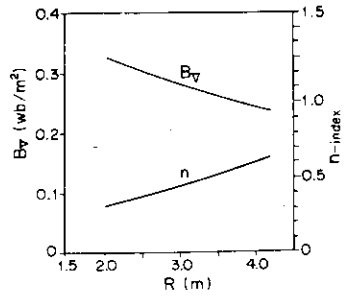

Fig.II.2-1 A typical magnetic configuration without a magnetic limiter (1A), and the radial profile of poloidal magnetic field (B_V) for plasma equilibrium in case of Fig. 1A, where $n = -\frac{R}{B_V}\frac{\partial B_V}{\partial R}$ (1B).

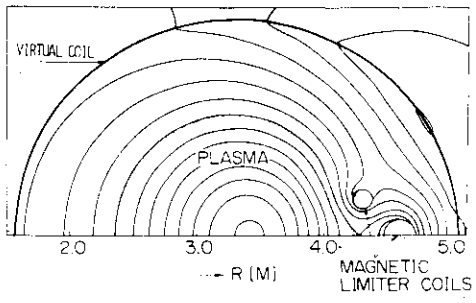

FIG. (2A) TYPICAL MAGNETIC CONFIGURATION WITH MAGNETIC LIMITER, CASE B.

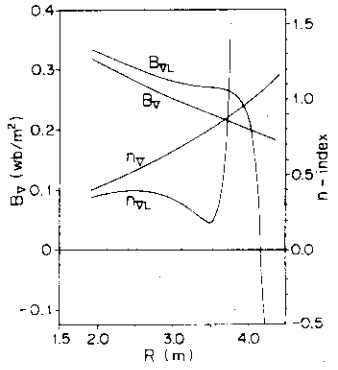

Fig.II.2-2 A typical magnetic configuration with a magnetic limiter (Fig. 2A) and the radial profile of a poloidal magnetic field (B_V) for plasma equilibrium in case of Fig. 2A (Fig. 2B) where $n_V = -\frac{R}{B_V}\frac{\partial B_V}{\partial R}$. A suffix VL means the corresponding values including magnetic limiter field.

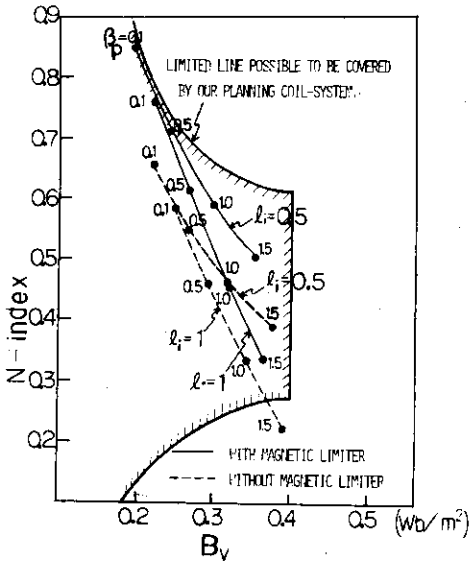

Fig.II.2-3 The relation between vertical magnetic field (B_v) and n required for $\beta_p = 0.1 \sim 1.0$ and $\ell_i = 0.5 \sim 1.0$.

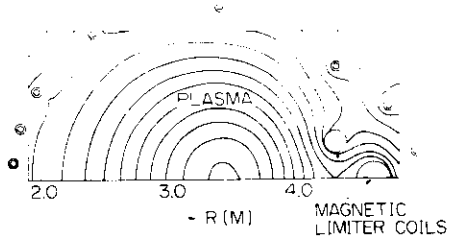

FIG. 13 A. A MAGNETIC CONFIGURATION CALCULATED UNDER THE LUMPED COILS.

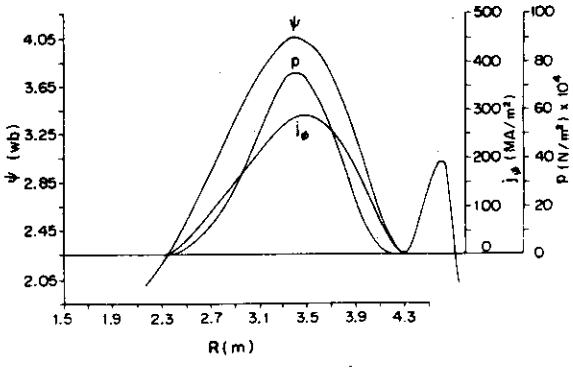

Fig.II.2-4 A plasma equilibrium obtained by lumped coil currents in vertical coils and magnetic limiter coils (Fig. 4A) and the radial profile of a flux-function (ψ), plasma pressure (p) and toroidal current density (j_ϕ) in case of Fig. 13A (Fig. 4B).

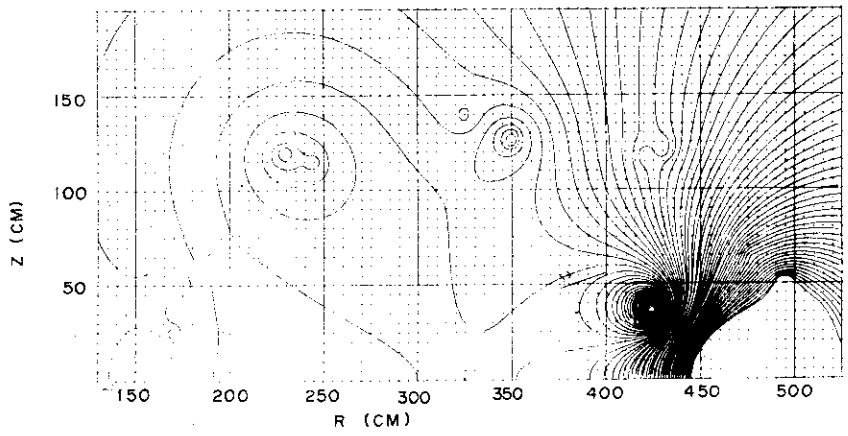

Fig.II.2-5 Octupole field produced by the currents in magnetic limiter coils, vertical field coil and quadrupole field coil.

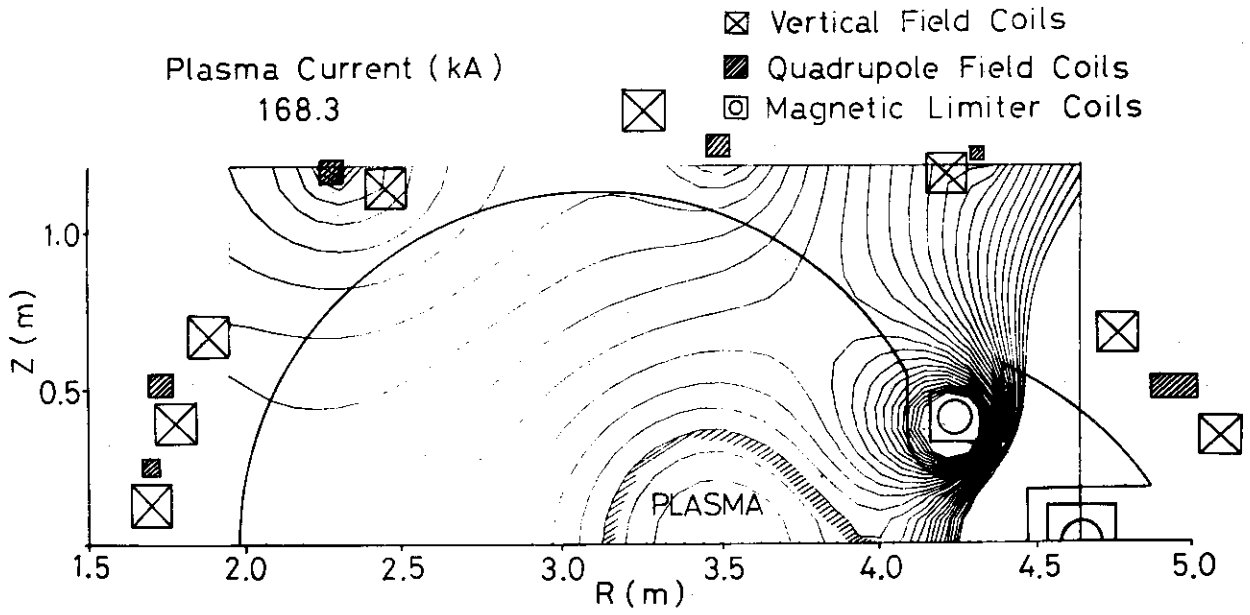

Fig.II.2-6

Fig.II.2-6∿9 Equilibrium configurations at the current build up phase. The plasma currents are indicated in each figure.

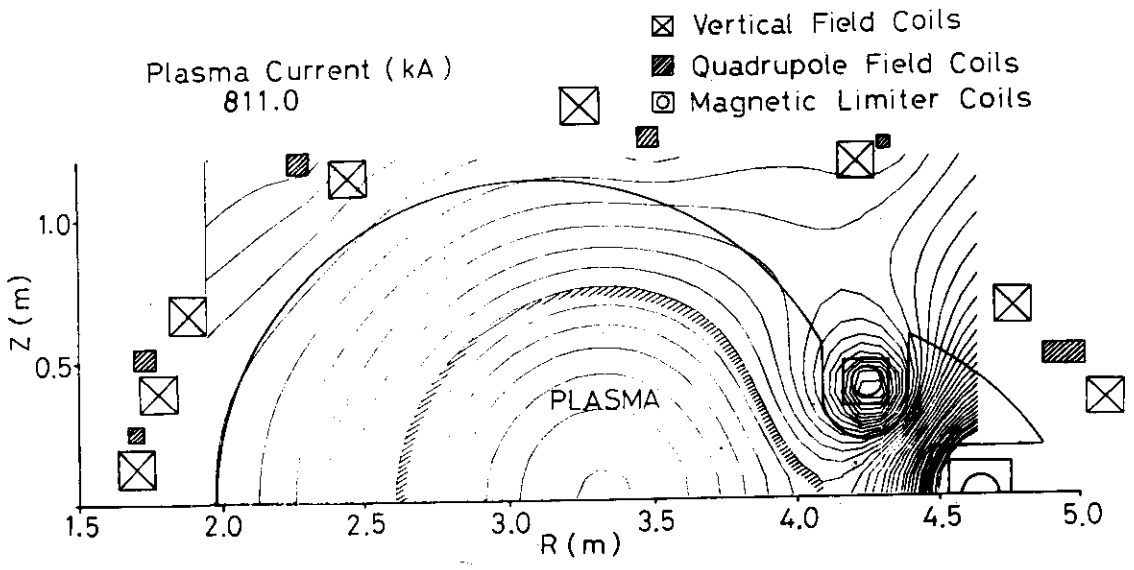

Fig.II.2-7

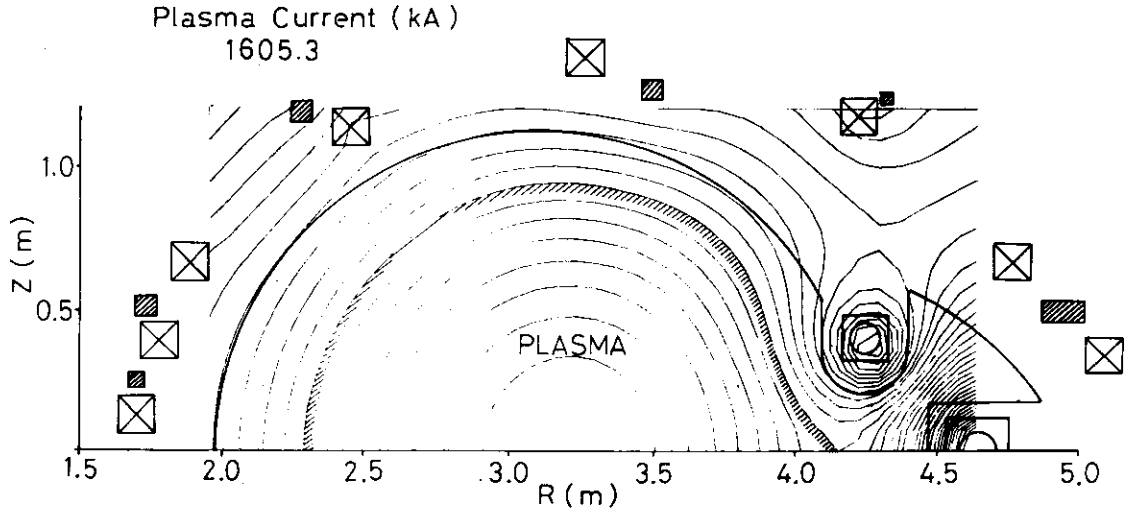

Fig. II.2-8

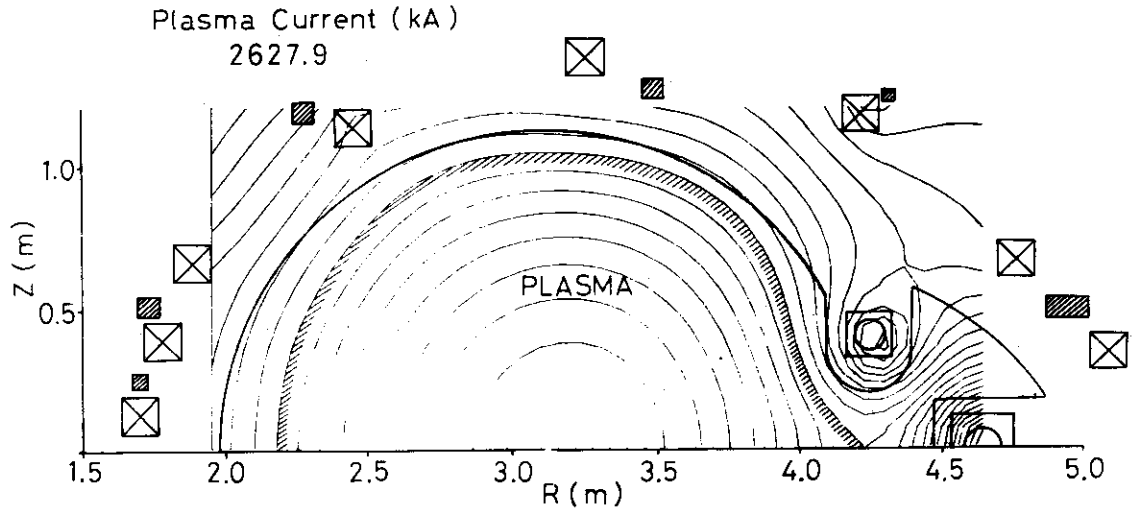

Fig.II.2-9

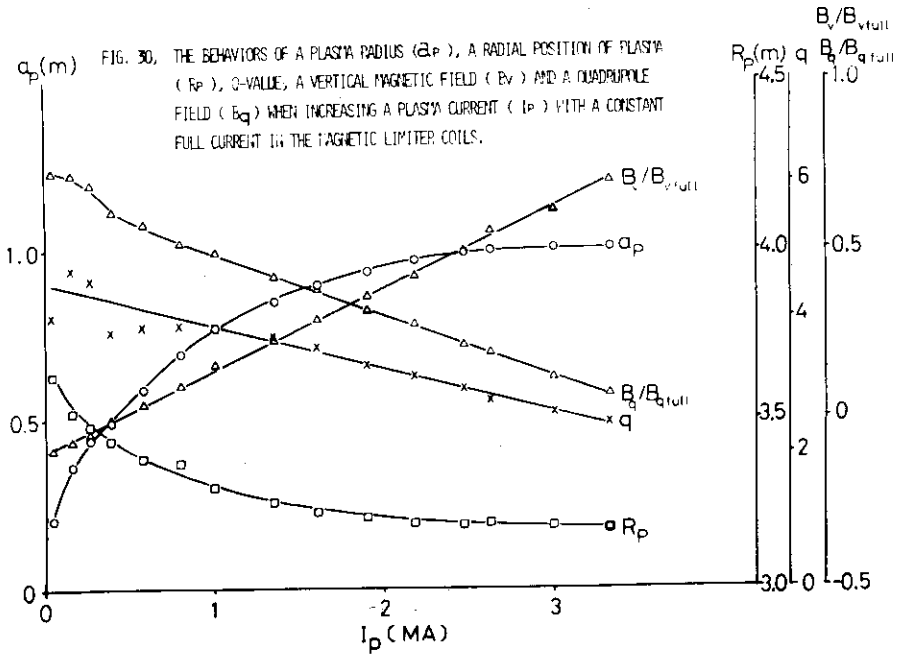

Fig.II.2-10 The behavior of a plasma radius (a_p), a radial position of plasma (R_p), q-value estimated from cylindrical approximation, a vertical magnetic field (B_v) and a quadrupole field (B_p) when a plasma current increases with a constant full current in the magnetic limiter coils.

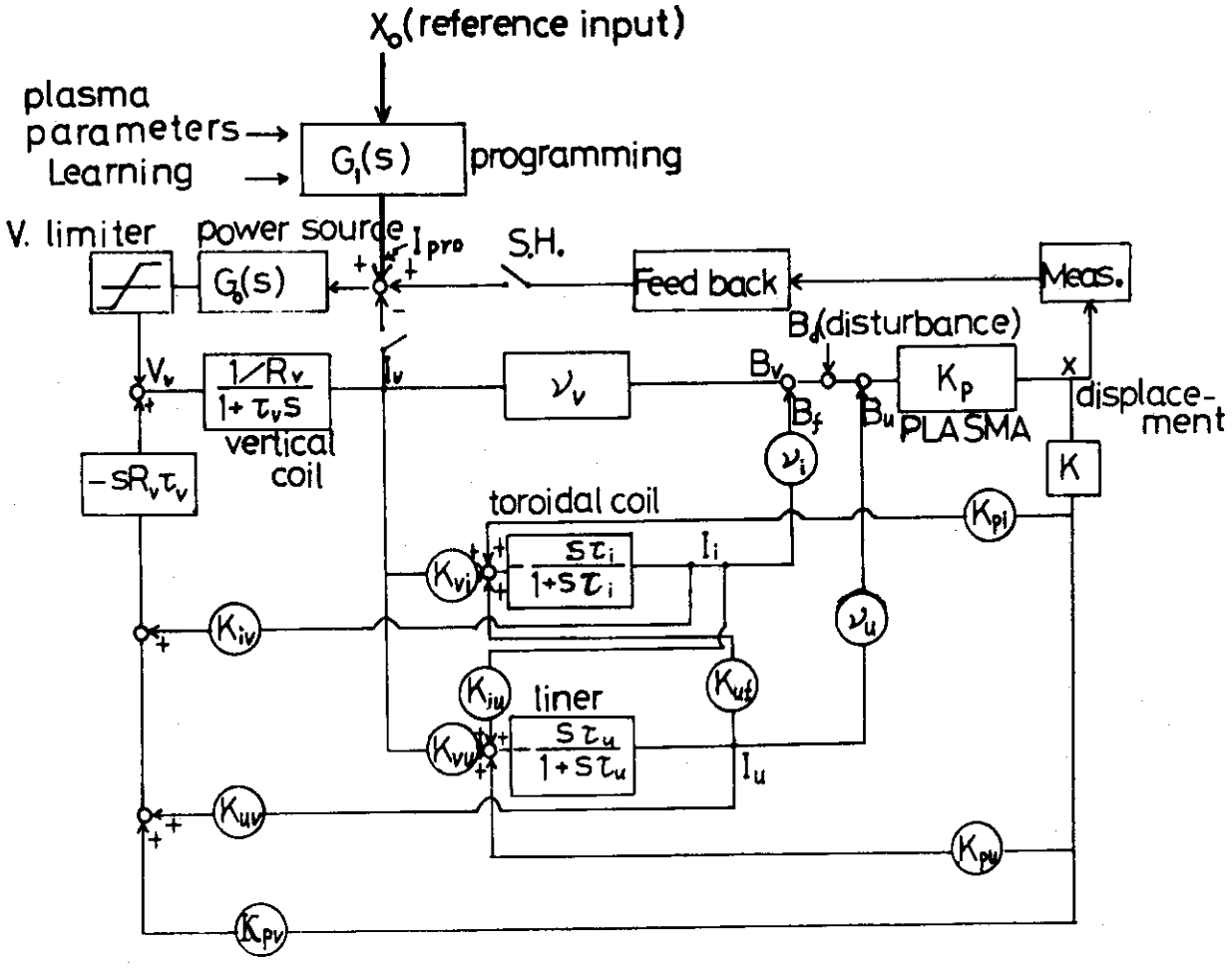

Fig.II.2-11 Block diagram of a simple control system for horizontal displacement.

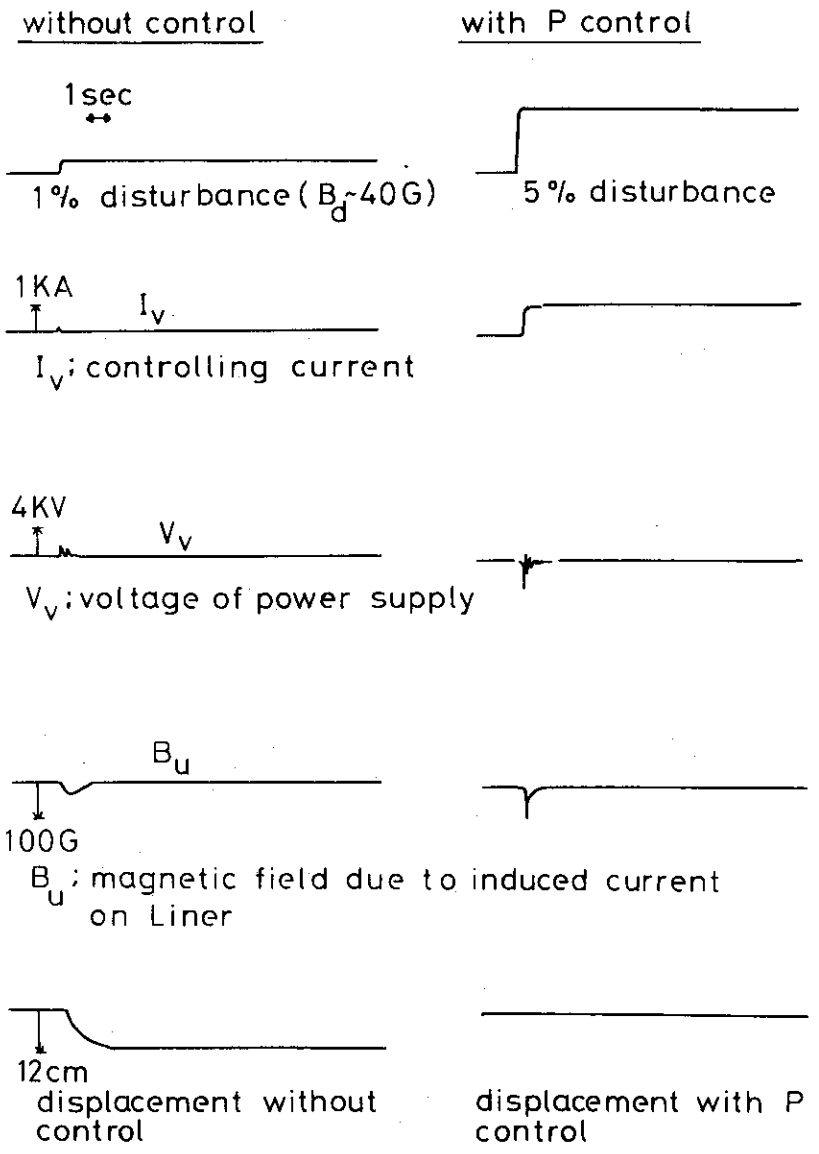

Fig.II.2-12
Responses at the branches of the block diagram when a step field disturbance enters. Without control and with P control.

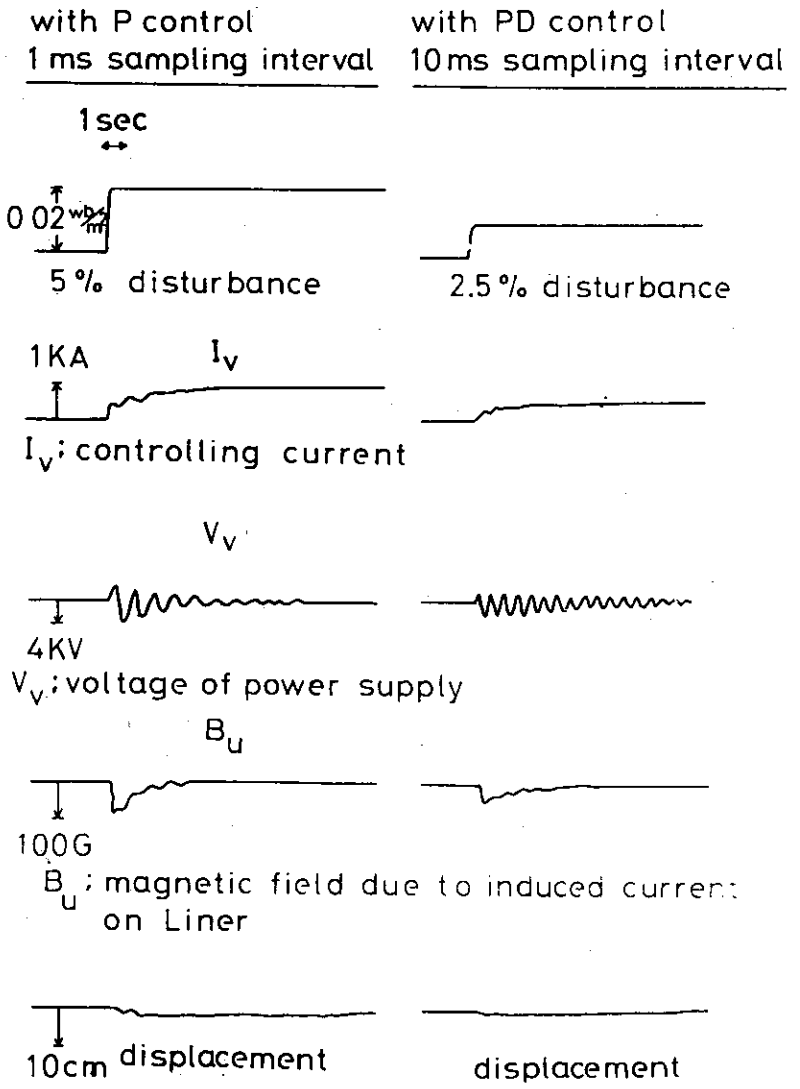

Fig.II.2-13
Responses at the branches of the block diagram when a step field disturbance enters. With P control and 1 ms sampling interval, and with PD control and 10 ms sampling interval.

3. Particle and Energy Balances in JT-60

MKS units are used throughout this subsection, and symbols used are standard.

3.1 Gas Feed

Feeding of gases by fast-acting valves and a wall temperature of 500°C are adopted as standard in JT-60 to provide the plasma with good reproducibility in density and to determine the plasma density in direct relationship with the initial gas pressure in a Joule heating phase.

3.2 Preionization

In order to reduce the initial break down voltage and to widen the stable regimes of tokamak discharges, good preionization is highly recommendable. A fast movable limiter is used as an electrode for preionization by RF power and as a mount of the electron beam sources to preionize the gases.

3.3 Particle Recycling

The re-emission process includes the "self-sputtering" process of hydrogen and the thermal desorption of hydrogen process. The latter process will become more active at high wall temperatures. In Molybdinum, the thermal desorption of incident hydrogen particles may occur within the time of the order of 10 ms at a wall temperature of 500°C, as far as the energy of incident hydrogen particles is below a few keV where the formation of trapping sites is negligibly small. This feature of Molybdinum at high temperatures [1] suggests that the recycling ratio of hydrogen particles can be kept unity at any moment. It allows to maintain the plasma at a constant density during a Joule heating phase and make a straightforward interpretation of experimental results.

The properties of SiC and carbon under particle bombardment and its

thermal desorption characteristic are not well known. The experimental investigation will be made in 1976-1977.

3.4 Preliminary Results of Simulation

In an axisymmetric cylindrical plasma, the MHD equations of the plasma are given as

$$\frac{\partial n}{\partial t} = \frac{1\partial}{r\partial r} r(D\frac{\partial n}{\partial r}) + \alpha_i n n_0 - \beta n^2 + s_{nb}$$

$$\frac{3\partial}{2\partial t} nkT_e = \frac{1\partial}{r\partial r} rn(\chi_e \frac{\partial}{\partial r} kT_e - \frac{5}{2} v_p kT_e) + v_p \frac{\partial}{\partial r} nkT_e - \frac{3}{2} n \frac{k(T_e - T_i)}{\tau_{eq}}$$

$$- P_{br} - P_{cy} + \eta j_z^2 + (p_{nb})_e$$

$$\frac{3\partial}{2\partial r} nkT_i = \frac{1\partial}{r\partial r} rn(\chi_i \frac{\partial}{\partial r} kT_i - \frac{5}{2} v\ kT_i) + v_p \frac{\partial}{\partial r} nkT_i + \frac{3}{2} n \frac{k(T_e - T_i)}{\tau_{eq}}$$

$$- \frac{3}{2} \alpha_c n n_0 k(T_i - T_0) + (p_{nb})_i$$

$$\frac{\partial}{\partial t} j_z = \frac{1}{\mu_0 r} \frac{\partial}{\partial r} r(\frac{\partial}{\partial r} \eta j_z)$$

A pseudoclassical dependence is used for the diffusion coefficient D and the thermal conductivity coefficinet of electron χ_e with empirical anomaly factors, and a classical dependence for the resistivity η with empirical anomaly factors. The neoclassical thermal conductivity coefficient of ion χ_e is employed, and other coefficients are classical. For example, empirical anomaly factors $\gamma_{\chi e}$ for χ_e and γ_η for η determined to fit the experimental results are

$$\gamma_{\chi e} = A(u_e/v_{eth})^2 + 1\ ,\ \bar{\gamma}_{\chi e} = \int \gamma_{\chi e} \chi_e ds / \int \chi_e ds = 10^2 (\bar{u}_e/\bar{v}_{eth})$$

$$\gamma_\eta = B(u_e/v_{eth})^2 + 1\ ,\ \bar{\gamma}_\eta = \int \gamma_\eta \eta ds / \int \gamma_\eta ds = 10\ (\bar{u}_e/\bar{v}_{eth}) \qquad (2)$$

Boundary conditions are $\frac{\partial}{\partial r}$ (n, T_e, T_i, j_z) = 0 at r = 0 (axis) and at r = r_p (surface) n, T_e, and T_i are given a certain value such as $2 \times 10^{12}/cm^3$, 10 eV, 5 eV, respectively, and $\int j_z ds = I_p$.

The density of neutral hydrogen particles at each time is given by a steady-state equation [2] considering ionization and charge-exchange processes, since these processes occur rapidly enough compared with other processes of the plasma such as the diffusion and the thermal conduction. Here the neutrals are assumed to be mono-energetic and a slab model is used. The boundary value of first-generation neutrals $n_1(r_p)$ with a temperature of 5 eV is determined by a relation, $\Gamma_1 = \Gamma_c + \Gamma_p + \Gamma_0$, which implies that the recycling ratio of hydrogen particles is unity.

The particle source term by neutral beam injection s_{nb} in Eq. (1) is described as

$$s_{nb}(r) = \sigma(r)n(r) \oint \frac{d\theta}{2\pi} \oint \frac{d\psi}{2\pi} \left(\frac{R}{R_o}\right) \left(\frac{I_{nb}(\xi,\eta)}{e}\right) \exp\left\{-\int \sigma(r')n(r')ds\right\} \quad (3)$$

neglecting the excursion of ion drift orbits from the magnetic surfaces. And the respective energy source terms of electron and ion by neutral beam injection in Eq. (1) are given as

$$(p_{nb}(r))_e = \frac{2m_e s_{nb}}{m_i} \nu_e kT_e \int_0^\tau t \left(\frac{E_{nb}}{T_e}\right) \exp\left(-\frac{t}{\tau_c}\right) dt$$

$$(p_{nb}(r))_i = \left[\frac{3(\pi)^{1/2}}{4} \left(\frac{m_i}{m_e}\right)^{1/2}\right] \left(\frac{2m_e s_{nb}}{m_i}\right) \nu_e kT_e \int_0^\tau t \left(\frac{T_e}{E_{nb}}\right)^{1/2} \exp\left(-\frac{t}{\tau_c}\right) dt \quad (4)$$

In a case where 10 MW neutral beams with 20 cm diameter are injected parallel into the torus aiming at a point 50 cm to the inner side of the center line of the torus, and $I_p(t)$ is given with a 0.5 sec rise time, Fig. II.3-1 shows four examples of the calculation. In all of the four cases, the plasma density will increase from $2 \times 10^{13}/cm^3$ to $5 \times 10^{13}/cm^3$ within 2-3 secs. In the case where the calculation starts at the very initial stage of Joule heating (at 5 ms), the initial mean temperatures of electron and ion are assumed to be about 10-20 eV. Mean temperatures of electron and ion do not reach 5 keV in Case (1) and (3) as shown in Figs. II.3-2, 3, since the energy confinement time is still as small as 0.1-0.2 sec at the time when the injection starts and the total number of particles rapidly increases by the injection.

In Case (2) where the initial conditions are given as $\bar{T}_e = \bar{T}_i = 1$ keV, $\bar{n} = 2 \times 10^{13}/cm^3$ and the distributions are given as $(1-(r/r_p)^2)$ and $(1-(r/r_p))^4$ respectively, the conduction loss is initially so small that

the temperature increases rapidly to 10 keV. This is because the anomaly factor is small in these initial conditions as seen in Eq. (2). While, in Case (4) where the plasma is heated by Joule power for 2 secs until the energy confinement time becomes as large as about 1 sec, the maximum mean temperatures of electron and ion reach above several keV but soon decrease, since the density and energy losses are increased. Figures II.3-4 ∿ 8 show the computed results for Case (4). The density and ion temperature distributions become rather peaked in the central region of the plasma with the time as shown in Figs. II.3-4, 5, since the sources of particle and energy have the peaked distributions as shown in Fig. II.3-7. Figure II.3-6 shows that the temperature distribution of electron is nearly parabolic.

It is shown in Fig. II.3-8 that a strong skin effect appears in the current density distribution in JT-60, although the code predicts only a weak skin effect in simulating today's tokamak experiments. The Joule heating is not as effective is in cases without the skin effect, since most of the Joule heating power is generated in the skin region where energy loss of the plasma are very large, and it causes the electron temperature nearly equal to the ion temperature. While, the current density distribution does not change much in a keV plasma as shown in Fig. II-3-8 and Fig. II.3-9, since the skin time of the current is long. For this reason, and also from considerations for the disruptive instability and other ordinary MHD instabilities, it is advantageous to generate a parabolic distribution of the current density at the end of Joule heating phase by using a fast movable limiter or an expanding magnetic limiter.

3.5 Energy Losses due to Impurities [3]

To estimate the impurity effect from the standpoint of related energy losses, we calculate the permissible level of impurity concentration in JT-60 by using the following simple model. On the assumption of an axisymmetric cylindrical plasma, a set of MHD equations for the stationary impurity ion densities, taking into account the classical diffusion across the magnetic field and ionization-recombination processes, is given as

$$\frac{1}{r}\frac{d}{dr}\left(D_k \frac{dn_k}{dr}\right) + n_e\left(\alpha_{k-1}n_{k-1} - \alpha_k n_k\right) - n_e\left(\beta_{k-1}n_k - \beta_k n_{k-1}\right) = 0. \qquad (5)$$

$$k = 2, 3, \ldots, M$$

which is solved under the boundary conditions; $dn_k/dr = 0$ at $r = 0$ (axis) and $n_k = 0$ at $r = r_p$ (surface). The Pfirsch-Schlüter diffusion coefficients for impurity ions are defined as $D_k = (1 + q^2)\rho_k^2\nu_k$. neglecting the inward diffusion of impurity ions due to the plasma pressure gradient. The density distribution of impurity neutrals $n_1(r)$ is expressed by a slab model assuming that the neutrals enter the plasma at thermal velocity V_1 at a temperature of 5 eV and is decreased in the passage by ionization process as

$$n_1(r) = n_1(r_p)[\exp(-\frac{1}{V_1}\int_r^{r_p}\alpha_1 n_e dr') + \exp(-\frac{1}{V_1}\int_0^{r_p}\alpha_1 n_e dr' - \frac{1}{V_1}\int_0^{r}\alpha_1 n_e dr')]. \quad (6)$$

Energy losses caused by impurities, i.e. ionization loss $P_i(r)$, Bremsstrahlung loss $P_{br}(r)$, and excitation loss $P_{ex}(r)$ in J/m^3s, are calculated using the stationary distributions of impurity ions obtained. Figure II.3-10 shows the total amount of energy loss; $P_t = P_i + P_{ex} + P_{br}$ in comparison with the total Joule input power P_j for $\bar{n}_i = 5 \times 10^{13}/cm^3$. The total energy loss is rather constant with the temperature, and becomes larger than the Joule input power at about 1 keV in the case of 5 % concentration of carbon or oxygen, and 0.5 % concentration of iron. As we can expect the maximum supplementary heating power of 10-20 MW in JT-60, the permissible levels of impurity concentration are of the order of 1 % for light inpurities and of the order of 0.1 % for heavy impurities.

3.6 Impurity Control

(1) Countermeasures

In order to reduce the concentration of impurities down to the permissible level described in 3.5, the following measures are adopted in JT-60.

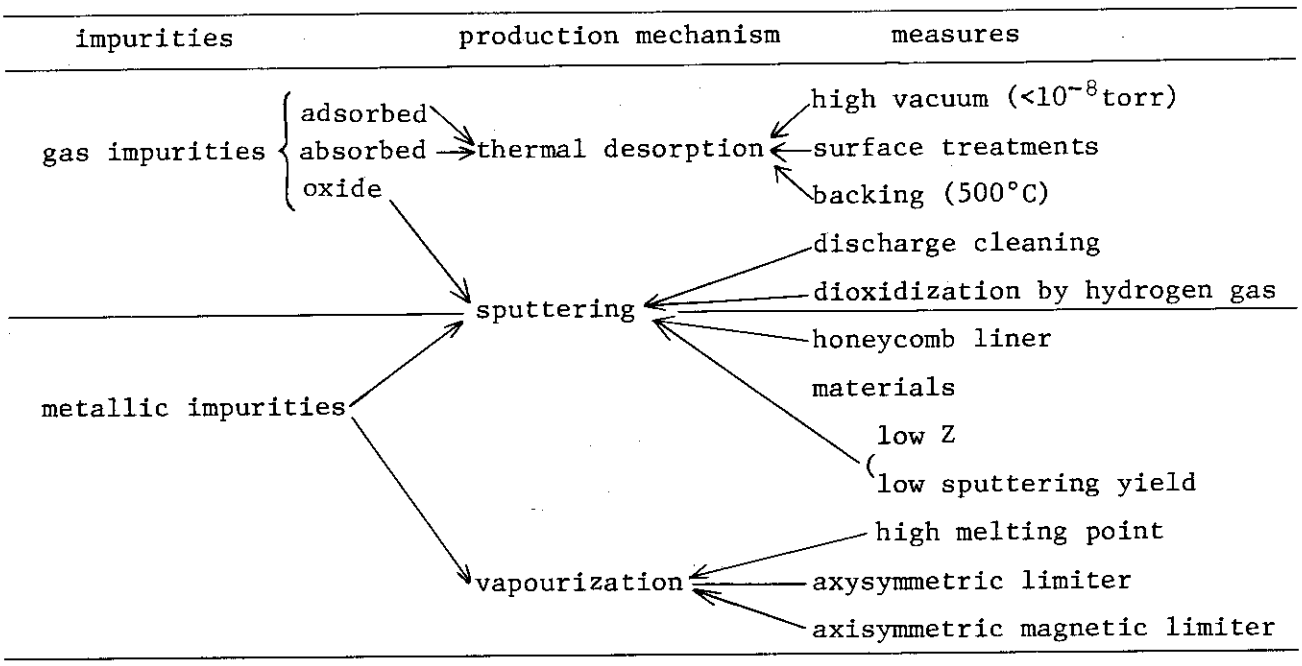

(2) Recycling Processes of Impurities [3]

A simplified model which considers the particle induced desorption due to hydrogen and impurity ions, and hot neutrals generated through charge exchange in the plasma gives the following equation for impurity accumulation

$$\frac{dN_z}{dt} = (1-\zeta_1)\eta_1 \frac{N_p}{\tau_p} + (1-\zeta_1)\,\eta_2 \left(\frac{\gamma}{1-\gamma}\right)\left(\frac{N_p}{\tau} + \frac{dN_p}{dt}\right)$$

$$+ (1-\zeta_1)\eta_3 \frac{N_z}{\tau_z} - \xi_3 \frac{N_z}{\tau_z} \qquad (7)$$

In the case that the plasma density is constant with time, the final impurity concentration is given under the condition $\eta_3 < \zeta_3/(1-\zeta_1)$ as

$$\frac{N_z}{N_p} = \frac{[(1-\zeta_1)\eta_1 + (1-\zeta_2)\eta_2(\frac{\gamma}{1-\gamma})]}{[\zeta_3 - (1-\zeta_1)\eta_3]} \left(\frac{\tau_z}{\tau_p}\right) \qquad (8)$$

Here we assume the ratio of hot neutral particles escaping from the plasma to incident particles γ is 0.1, and the confinement time of impurities τ_z is nearly equal to that of the plasma τ_p.

Assuming that the sputtering yield of hydrogen ion η_1 is nearly equal to that of hydrogen neutrals η_2, the divertor efficiencies are the same; $\zeta_1 \sim \zeta_2$, and the sticking probability of the metallic impurities ζ_3 is unity, the conditions to reduce concentration of the metallic impurities

N_z/N_p to the permissible level of 10^{-3} are: η_1 should be less than 10^{-3}, ζ_1 should be higher than 0.5 (for example by a magnetic limiter), and the self-sputtering yield η_3 should be less than unity. The condition for the gas impurities to reduce N_z/N_p to the permissible level of 10^{-2} assuming that $\eta_1 \sim \eta_2 \sim \eta_3$ $\zeta_1 \sim \zeta_2$, and $\zeta_3 \sim 0.5$, is as follows; η_1 should be less than 10^{-2} without a divertor, which is attainable by reducing the oxide layer on the wall surface with discharge cleaning and deoxidization by hydrogen gas.

References

1) McCracken, G. M., Rep. Proc. Phys. 38 (1975) 241.
2) Dnestrovski, Yu. N., et al., Atomnaya Energia 32 (1972) 301.
3) Tazima, T., et al., Fifth Conference on Plasma Physics and Controlled Nuclear Fusion Research, Tokyo (1974) second part of paper CN-33/A1-2.

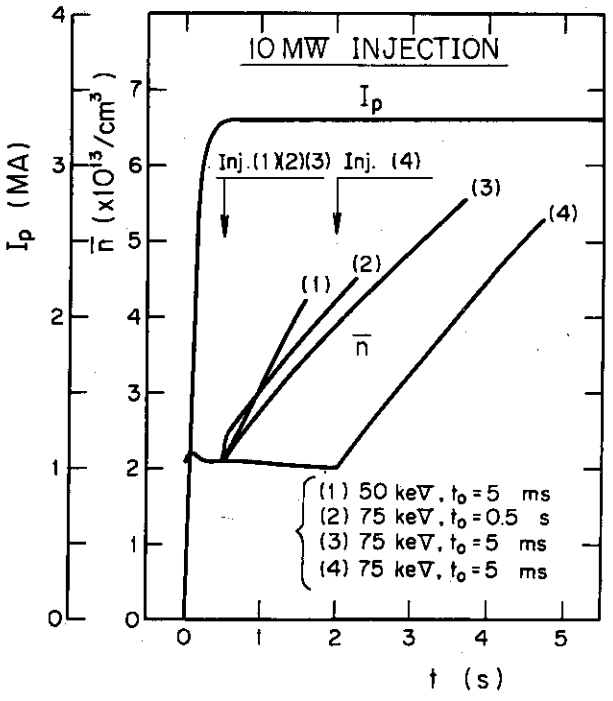

Fig.II.3-1 Four examples of computed mean plasma density $\bar{n}(t)$. The total plasma current $I_p(t)$ is given, and t_0 means the time at which calculation starts.

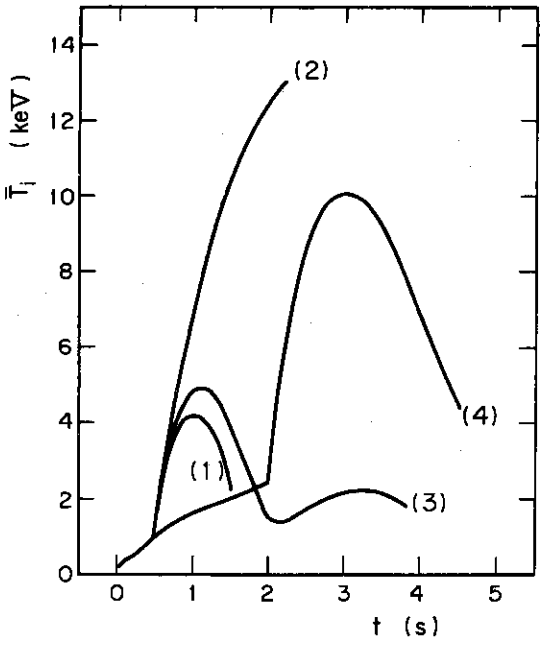

Fig.II.3-2
Computed mean temperature of ion $\bar{T}_i(t)$ and $\bar{T}_e(t)$, respectively.

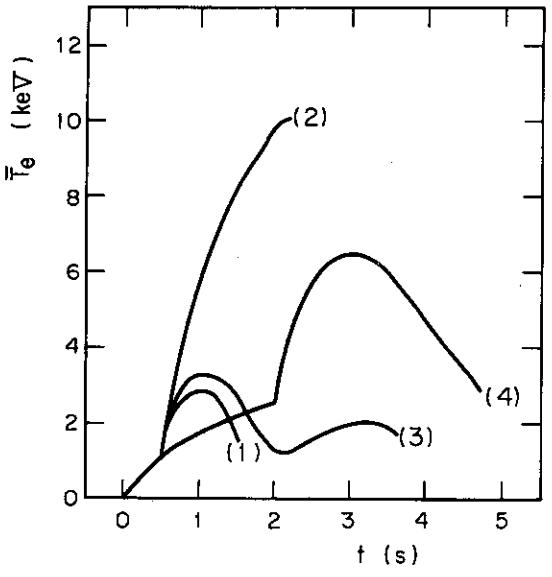

Fig.II.3-3

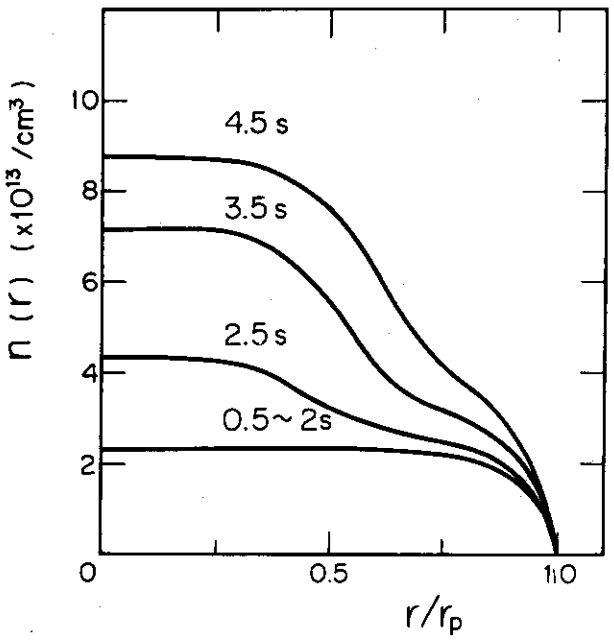

Fig.II.3-4
Time-evolution of radial distributions of plasma density n(t,r), ion temperature $T_i(t,r)$, and electron temperature $T_e(t,r)$, respectively, in Case (4).

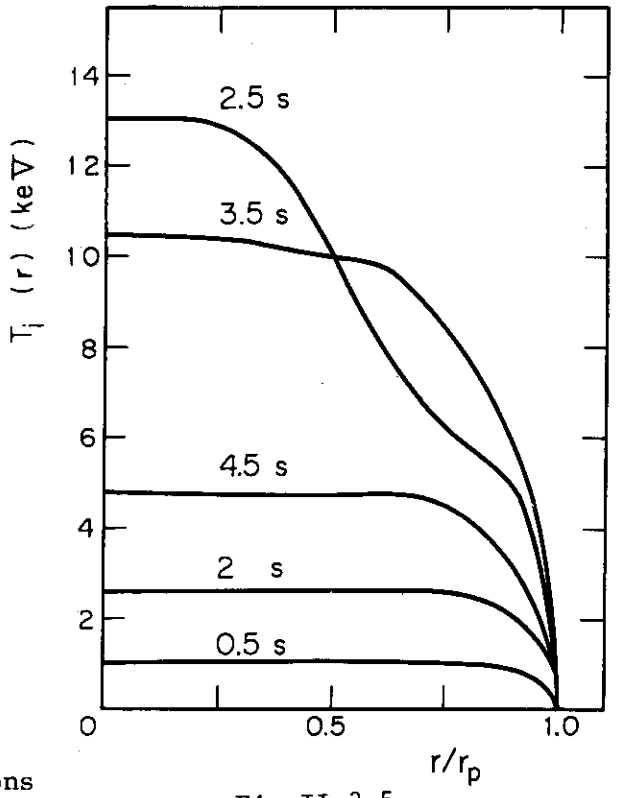

Fig.II.3-5

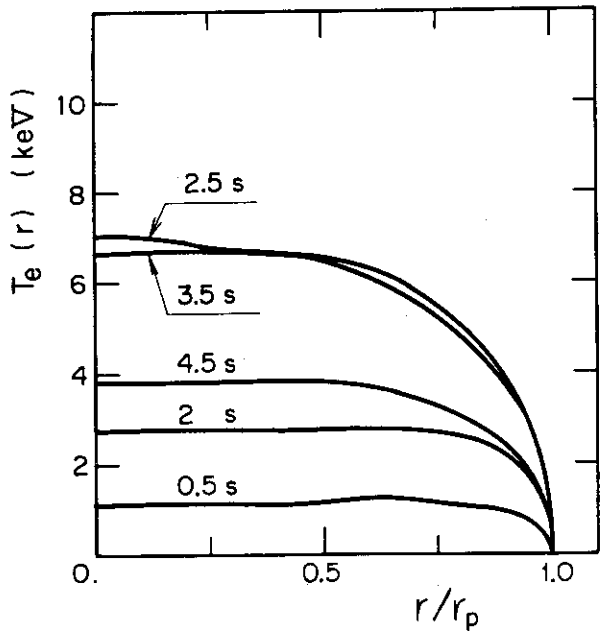

Fig.II.3-6

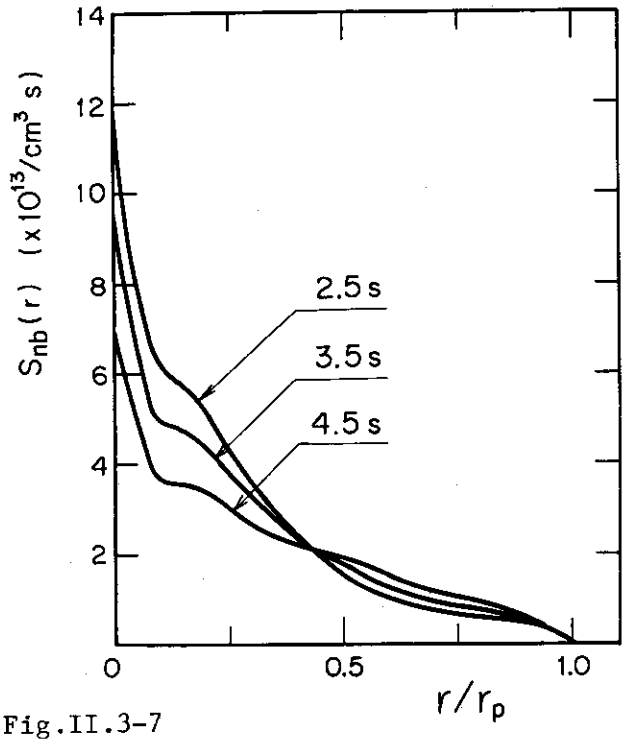

Fig.II.3-7
Radial distributions of the fast ion density by neutral beam injection $s_{nb}(r)$ in Case (4).

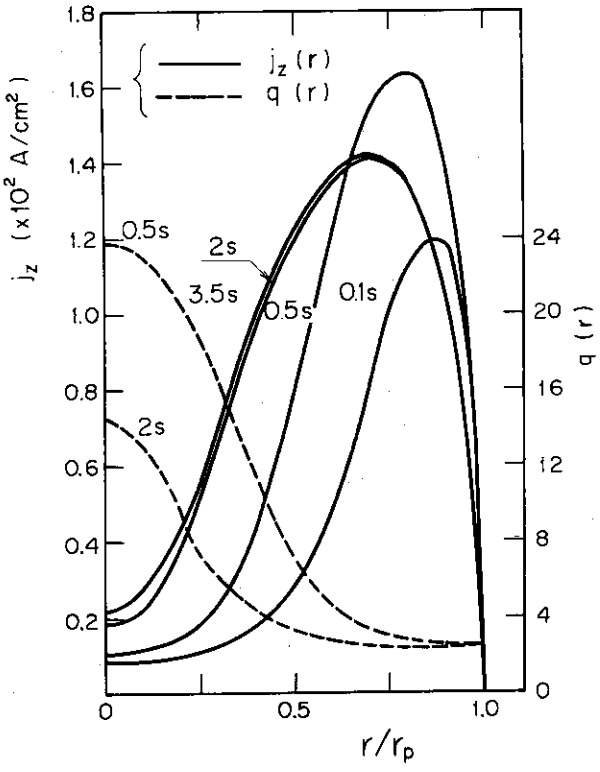

Fig.II.3-8
Time-evolution of radial distributions of plasma current density $j_z(t,r)$ in Case (4) and in Case (2), respectively.

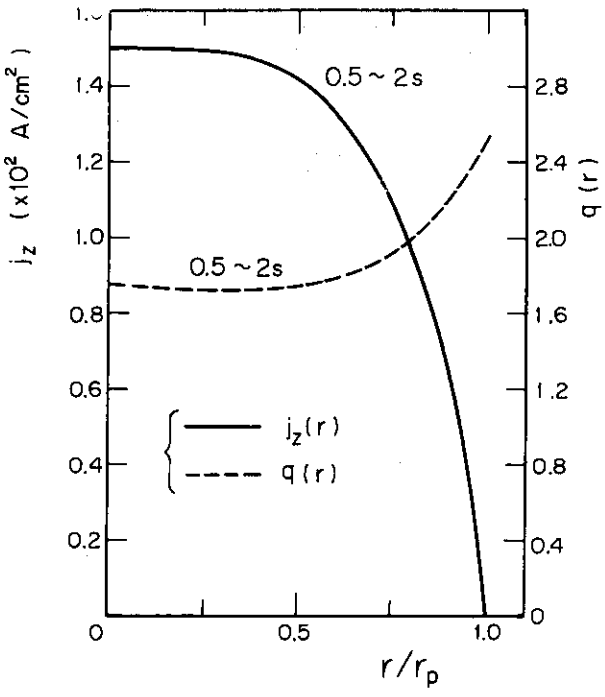

Fig.II.3-9

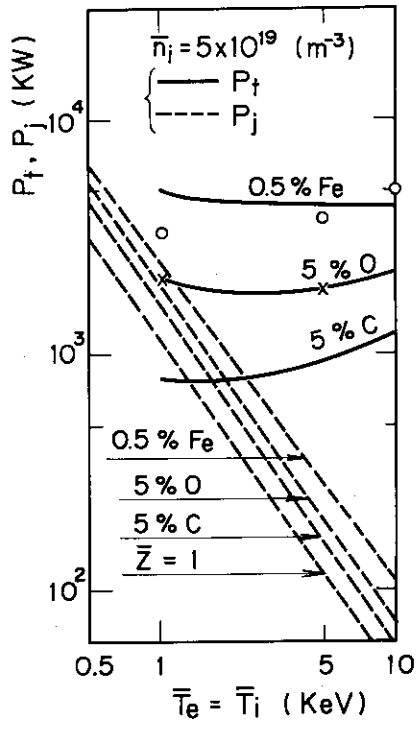

Fig.II.3-10 Total energy loss P_t caused by carbon, oxygen, and iron impurities in comparison with total Joule heating power P_j in JT-60.

4. Design of the Machine

4.1 Vacuum Chamber and Auxiliary Components

1) Vacuum Chamber

Two basic types of vacuum chamber are usually considered in Tokamak devices to obtain sufficiently high electric resistance along a torus. One is a bellows-type and the other a ceramic insulation type. Though the latter is preferable from the viewpoint of mechanical stress and electric resistance, the manufacture of the ceramic section suitable to JT-60 is far beyond the current technological capability. It is especially difficult to manufacture a noncircular cross-section ceramic piece with a large radius and to connect it with a metal ring and vacuum seals. From the above reason we decided to use a bellows-type vacuum chamber.

There are two types of bellows, that is, U-shaped bellows and welded bellows. Though the former is harder to bend into a torus, it is better suited for cleaning of the surface and less likely to have leaks compared to the latter. We calculated mechanical stresses in both cases for the same bellows height, electric resistance and cross-section. The stress in the U-shaped bellows is about 20% lower than that of the welded bellows. On this basis the decision was made to use the U-shaped bellows for the vacuum chamber.

Table II.4-1 and Fig. II.4-1 show the specification and a cross-sectional view of the vacuum chamber, respectively. The material will be selected from Inconel 625, Inconel X-750, Hastelloy X and other non-magnetic steels. Electric resistance of a torus should be higher than 3 mΩ. The helium leak rate, the outgas rate and the ultimate vacuum pressure are lower than 10^{-8} torr l/sec, 10^{-12}torr l/sec cm^2 and 10^{-9} torr, resectively. The baking temperature will be above 500°C for the vacuum chamber and 250°C for the ports. The vacuum chamber is sealed by welding and the ports by metal seals. The vacuum chamber is composed by bellows and thick rings of about the same length around the torus. The vacuum chamber is supported at the thick rings by bars extended from a platform. The chamber is heated by non-magnetic electric heaters and cooled by water pipes wound a round it.

A vacuum chamber is loaded by centripetal forces both toward the major axis and toward the minor axis due to the atmospheric pressure. The centripetal force toward the major axis is about 300 ton and that toward

the minor axis is over 1500 ton. The electromagnetic force produced by the interaction of the chamber current (0.7 MA) with the poloidal field is of about the same magnitude as therefore the atmospheric pressure. The maximum stress caused by the above forces and thermal expansion is about 20 kg/mm^2 when the height, pitch and thickness of the bellows are 70 mm, 20 mm and 2 mm, respectively.

Moreover, another stress is added to the above at the connection with the thick ring. This local stress is caused by the difference of radial deflection between the bellows and the thick rings. It is one of the most serious problems in manufacturing a vacuum chamber to decrease a sum of the above stresses to an allowable value of structural materials.

2) Liner

A liner is attached to the inner surfaces of the vacuum chamber. Liner material is chosen from Molybdenum, Graphite and Silicon Carbide. The applicability of the two latter materials is under examination at present. Molybdenum is considered a good material for a liner because of the high melting temperature and low sputtering yields. It has an advantage in that the oxide film on its surface may be removed by means of deoxidization in the hydrogen gas at high temperatures. A preliminary test shows that the oxide on the Molybdenum is greatly reduced by keeping the surface at 500°C in hydrogen at a pressure of 1 torr. The liner is $2 \sim 5$ mm thick. Though the shape and size of the liner segments are not yet frozen, they are most likely rectangular with a length of $300 \sim 2000$ mm. The baking temperature is 500°C and the outgas rate is expected less than 10^{-12} torr 1/sec cm^2.

3) Fixed limiters

Axisymmetric fixed limiters are placed at the inner surfaces of the liner. Their material is the same as that of the liner. Their number, cross section and positional accuracy are under examination, taking into account the thickness of scrape-off layer the ellipticity of plasma cross section, the rotational speed of the plasma rotation, and the heat load deposited on it.

4) Collector Plates (Magnetic Limiter Plates)

The collector plates are positioned at the outer side of the chamber

as is shown in Fig. II.4-1. Collector plate surface will probably have a honey-comb structure. The thickness of the plate should be more than 2 cm to keep the surface temperature low enough under the design heat load of 10 MW for 10 sec.

It should be recalled that Molybdenum becomes very brittle above the recrystalizing temperature (∿1200°C). A design effort may be required to reduce the heat flux by moving magnetic flux lines or collector plates cyclically.

5) Movable Limiter

A fast-acting removable limiter is installed in JT-60. The limiter is removed during the build-up phase of plasma current. Its driving mechanism consists of an air or oil cylinder with electromagnetic valves and bellows to hold the vacuum. The limiter is removed vertically for a stroke of 1100 mm with a mean velocity of 1100 mm/0.1 sec.

4.2 Toroidal Field (T.F.) Coils

At first we mention the specification of T.F. coils. The toroidal magnetic field is 50 kG at a major radius of 3 m. The maximum magnetic field in the coils is about 110 kG and the magnetomotive force is 75 MAT. The major radius of T.F. coil is 3320 mm and the minor inner radius 1940 mm. The number of unit coils is 24. The field ripple is expected less than 0.05% in the plasma region. The rise of the conductor temperature is over 80°C at the inner side where the cross section is the smallest. In order to cool the coils a hollow conductor pipe is soldered on one side of the flat bar conductor. Since the maximum stress in the conductor is about 10 kg/mm^2, we use high tension copper containing a small amount of silver. We are examining an adequate amount of silver content in the copper. The T.F. coils are wedge-shaped at both inner and outer parts of the torus. The former shaping is done from the necessity of a lower aspect ratio and the latter for making space needed for parallel neutral injectors. The specification of the T.F. coil is listed in Table II.4-2.

Various kinds of electromagnetic forces act on the T.F. coils. A hoop force along the minor axis and a centripetal force toward the torus axis are 3.3×10^5 ton and 1.3×10^5 ton, respectively. The former is withstood by

both copper conductors and the outer stainless steel rings wrapped round the coils.

The latter is supported by a solid column positioned at the torus axis. A twisting moment of about 10^3 ton m is caused by the interaction of coil current with the poloidal fields, which are mainly produced by the transformer coils and the vertical field coils. In an accident of layer shorting in the T.F. coils there occur abnormal forces on the neighboring coils. The above force is about 3000 ton. The error field due to the leads and the return winding is less than 4 G in the plasma region.

4.3 Poloidal Field Coils

The poloidal field coils consist of transformer coils (primary windings), vertical field coils, horizontal field coils, quadrupole field coils positioned between the toroidal field coils and the vacuum chamber, and magnetic limiter coils inside the chamber. The position of each coil is shown in Fig. II.4-1. The specifications of the poloidal field coils are listed in Table II.4-3.

First we describe the design of the transformer coils as an example of coils placed outside the chamber and secondly the magnetic limiter coils installed inside the chamber.

1) Transformer coils

The transformer coils are wound in a small space between the toroidal field coils and the vacuum chamber. The conductor consists of copper, hollow conductor, and high tension alloys or st ainless steel reinforcements which withstand against hoop forces. Coils are divided into two half sectors and connected with each other by bolt-joints. The transformer coils are supported together with other poloidal field coils by 24 or 48 supporting structures. The maximum mechanical stress of the conductor occurs at the middle between two support structures and is about 7 kg/mm^2 when no reinforcements are used.

Cooling is done by flowing water forcibly through hollow conductors. The rise of temperature is about 35 °C in the conductor except bolt-joints. It is not clear at present how much the temperature rises and the mechanical stress increases in bolt-joint sections. A high voltage is applied to the

transformer coils not only at the initial stage of discharges but also during discharges. The insulation material which withstands against a ground voltage of 25 kV is composed of mica and epoxi resin. We are examining the properties and X-ray damage of the above insulation materials.

2) Magnetic limiter coils

The magnetic limiter coil current is steady and is excited long before the discharge. The design allows to reduce the number of turns of the coils and greatly reduces the electrical and mechanical problems in these coils. The detail of magnetic limiter coils is under design. The coils are supported from thick rings of the vacuum chamber. The stresses due to the thermal expansion of the coils and the difference of deflection between the coils and the vacuum chamber are reduced by using the sliding mechanism. Bolt joints are used for the connections of coil sections. The coils are encased in a stainless steel cover which is assembled by welding.

The conductor of magnetic limiter coils is composed of hollow conductors and copper plates. Both are soldered with each other.

4.4 Vacuum Pumping System

Two identical vacuum pumping systems are installed in JT-60. The total pumping speed is 20,000 1/sec for nitrogen at the pumping ports of the vacuum chamber.

If the outgas rate of the vacuum chamber and the liner is less than 10^{-12} torr 1/sec cm^2, the ultimate vacuum pressure will be less than 10^{-9} torr. The allowable Helium leak rate is less than 1×10^{-8} torr 1/sec. The baking temperature of the manifolds and the pumping ports is as high as 250°C though the intakes of turbo-moleculer pumps cannot be baked out above 160°C. The pumping system consists of 6 turbo-molecular pumps (1700 1/sec/pump), 6 sputter ion pumps (4800 1/sec/pump) and 2 Titanium getter pumps (10,000 1/sec/pump).

4.5 Technological Problems

We mention the technological problems of each component of JT-60.

1) The vacuum chamber

Selecting suitable materials of the bellows and the thick rings.
Manufacturing a large böre bellows with a noncircular cross-section.
Local stress in the welded connections between the bellows and the thick rings.
Cleaning the vacuum chamber for the ultra high vacuum.
Vacuum seal of the ports.
Assembling, dismantling and reassembling.

2) The liner, Fixed limiters and Collector plates

Selecting a suitable material of the liner, the fixed limiters and the collector plates.
Cleaning the above surfaces for the ultra high vacuum.
An allowable setting error of the fixed limiters.
A heat removal of the collector plates and the fixed limiters.
Reduction of a thermal stress caused by the difference in the thermal expansion of the vacuum chamber and the liner.
Sputtering yields and evaporation rate of Carbon and Silicon carbide materials.

3) The mobable limiters

Development of a driving mechanism with a stroke of 1100 mm and a mean velocity of 1100 mm/0.1 sec.
Development of long bellows to be contracted at high speeds.
Development of bearings workable at high temperatures in a vacuum.

4) Toroidal field coils

Development of the connection of large conductors with cooling pipes.
Development of the most suitable insulation usable at a temperature of about 150°C under high compression and shear stresses.
Development of a support structure loaded by the centripetal force and the twisting force.
Development of feeder joints.
Wedge shaping technique.

5) Poloidal field coils

Development of connection joints of conductors with cooling pipes.

Development of high voltage insulations used under high stresses.
Development of feeder joints.
Support structure of magnetic limiter coils and its vacuum seal.
Assembling, dismantling and reassembling.

Table II.4-1 Specifications of Vacuum Chamber and its Auxiliary Components

VACUUM CHAMBER

Structure	U-shaped Bellows and Thick Rings
Cross Section	Ref. Fig. 1
Materials	Inconel 625, Inconel X-750. Hasteroy X or Stainless Steel 304L
Magnetic Permeability	<1.02
Electric Resistance	>3 mΩ
Allowable He Leak Rate	$<1 \times 10^{-8}$ torr ℓ /sec
Expected Outgas Rate	$<1 \times 10^{-12}$ torr ℓ /sec cm^2
Expected Ultimate Vacuum	$<10^{-9}$ torr
Baking Temperature	
Vacuum Chamber	500°C
Ports	250°C
Vacuum Seal	
Vacuum Chamber	Welding
Ports	Metal Seal
Earthquake Proof	0.3 G

LINER, FIXED LIMITER AND COLLECTOR PLATE

Material	Molybdenum, Graphite Carbon or Silicon Carbide
Cross section	Ref. Fig. 1
Thickness	
Liner	2-5 mm
Collector Plate	20-30 mm
Baking Temperature	500°C
Expected Outgas Rate	$<10^{-12}$ torr /sec cm^2
Earthquake Proof	0.3 G

MOVABLE LIMITER

Maximum Stroke	1100 mm
Mean Velocity	1100 mm/0.1 sec

Table II.4-2 Specification of Toroidal Field Coils

Magnetic Field at R=3 m	50 kG
Magnetomotive Force	75 MAT
Coil Shape	Sector
Major Radius of T.F. Coils	3320 mm
Minor Outer Radius	2820 mm
Minor Inner Radius	1940 mm
Number of T.F. Coils	24
Azimuthal Length	640 mm
Radial Length	880 mm
Flat-top Time	10 sec
Conductor Material	Copper
Coolant	Water

Table II.4-3 Dimensions of Poloidal Field Coils

1. Position and Current of Poloidal Field Coils

Number	R (m)	Z (m)	Current (kAT)
1	1.521	0.046	240
2	1.525	0.122	"
3	1.534	0.201	"
4	1.548	0.281	"
5	1.567	0.363	"
6	1.592	0.447	"
7	1.622	0.532	"
8	1.660	0.619	"
9	1.706	0.709	"
10	1.763	0.802	"
11	1.831	0.899	"
12	1.914	1.000	"
13	2.038	1.123	320
14	2.170	1.231	160
15	2.280	1.306	"
16	2.493	1.421	320
17	2.769	1.523	160
18	3.021	1.578	"
19	3.349	1.600	"
20	3.790	1.545	"
21	4.376	1.296	"
22	4.969	0.641	"

2. Position and Current of Quadrupole Field Coils 1974.

Number	R (m)	Z (m)	Current (kAT)
1	1.699	0.251	53.41
2	1.733	0.513	80.12
3	2.286	1.189	-106.83
4	3.495	1.270	-106.83
5	4.310	1.220	-53.41
6	4.949	4.920	133.53

3. Position and Current of Horizontal Field Coils

Number	R (m)	Z (m)	Current (kAT)
1	1.933	0.949	30.77
2	3.062	1.296	15.39
3	4.304	1.316	15.39

4. Position and Current of Magnetic Limiter Coils

Number	R (m)	Z (m)	Current (kAT)
1 (main)	4.640	0.000	1.000
2 (sub)	4.240	0.350	0.500
3 (sub)	4.240	0.350	0.500

5. Position and Current of Vertical Field Coils

Number	R (m)	Z (m)	Current (kAT)
1	1.702	0.130	282.11
2	1.776	0.388	"
3	1.889	0.662	"
4	2.449	1.146	"
5	3.257	1.381	-282.11
6	4.216	1.177	"
7	4.760	0.668	"
8	5.094	0.337	"

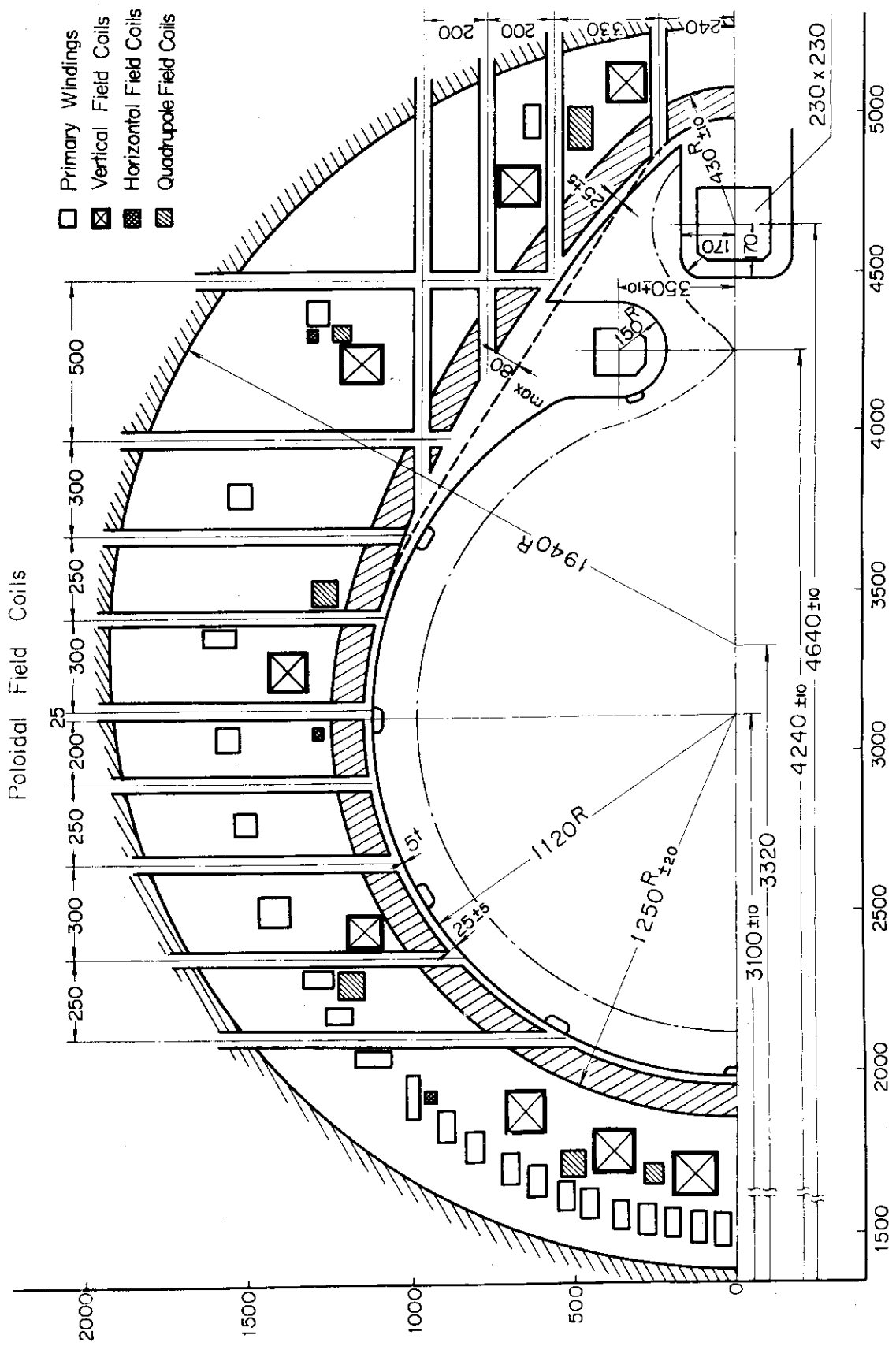

Fig.II.4-1 A cross sectional view of the vacuum chamber and the poloidal field coils

5. Power Supplies

5.1 Power supplies for Plasma Driving System

A preliminary engineering design of the power supplies for the plasma driving system was made in close cooperation with certain companies with which JAERI made a contract in 1974. The idea adopted in the preliminary design is to construct the power supply using a common set of motor-flywheel-generator for the whole plasma driving system, followed by thyristor controlled rectifier stages for respective coils. Some numerical values in this design are: the speed of the set is 3000 r.p.m., the required energy for the flywheel for the air-core transformer is about 400 MJ and the generator rating power is 140 MVA. A detailed engineering design which further incorporates more definite plasma-physical requirements and engineering considerations will be made in 1975.

It has been recognized that technological study and development of high capacity dc circuit breaker is quite essential to develop the JT-60 program. This will be put into practice as a two-years research and development program (1975 - 1976) for two candidates of circuit breakers, a vacuum circuit breaker and a solid-state circuit breaker. The aim of this program is to develop a dc circuit breaker of the type mentioned above which is capable of interrupting a current of 80 kA with 50 kV maximum interrupting voltage with high repetition rates (the numerical values are tentative and fairly conservative for the JT-60 ohmic heating system). The final choice will be made by comparative evaluation of the results.

5.2 Power Supplies for Toroidal Field Coils

An engineering design of the power supply was also made in 1974. Several options were considered primarily for evaluation and selection purposes of a mode of excitation of the power supply. As a result, a certain type of hybrid mode which consists of a set of motor generator with flywheel followed by conventional silicon rectifiers and a direct feeding of the power from the ac power grid was proposed on the basis of consistency of the whole system, relative easiness for control of the system and economic point of view. Some of the related design parameters are: the maximum speed

of the set is 3000 r.p.m., the generator rating power is about 300 MVA, the total GD^2 of the flywheel is about 400 ton-m^2. The 24 phase rectifier is adopted to miminize the voltage fluctuation on the ac power grid and the influences of higher harmonics of the generator to a permissible level. From technological point of view, no particular problem which requires research and development before ordering and construction was found.

III. Theory

M. Azumi, M. Okamoto, M. Tanaka,
T. Tazima, T. Tuda, M. Wakatani

1. Introduction

Theoretical and computational works have continued on tokamak confinement and heating. Emphasis is placed on subjects closely related to the experimental program.

Studies of neutral beam injection heating started at the end of 1973 proceeded as far as the thermalization process of fast ions. Guidelines for the injection heating in the JT-60 device and for the JFT-2 experiment of perpendicular injection were obtained.

A numerical scheme for the time dependent impurity distribution in a tokamak plasma was developed by taking account of the cross-field diffusion and atomic processes, which is incorporated in the tokamak radial transport code. Impurity transport in the mhd regime was reexamined in the presence of a radial electric field. The case of non-axisymmetric systems was also studied yielding similar features as in the axisymmetric one. An impurity drift instability driven by the ion parallel viscosity is found in the mhd regime. Cooperation was made with JT-60 group on the estimate of energy losses due to heavy impurities, modelling of recycling processes etc.

On the basis of neoclassical theory, detailed analysis was made on the relaxation of the radial electric field in a tokamak plasma in the banana regime and reveals the existence of an extremely fast relaxation mechanism due to the ion-ion friction. The influence of the toroidal field ripples was also examined.

Particle transport in the presence of helical magnetic cells due to magnetic perturbations was examined and compared with the Pulsator experiment which uses the helical winding.

Studies of mhd instability have continued. Analysis of kink instability of a high β tokamak was made assuming a skin current. Plasma becomes unstable even when $q(a) > 1$ (mixing of $m = 1$ and large $m = 2$ modes). Positional stability of an elliptic tokamak was also examined. A survey was made in cooperation with JFT-2a group on a tokamak with noncircular cross-section[1].

(M. Tanaka)

2. MHD Stability

2.1 Kink Instabilities in a Tokamak of Large β_p*)

Kink instabilities in high β regime of tokamak, i.e. $\beta_p \sim \varepsilon^{-1/2}$ and $q(a) \sim 1$, were studied in toroidal geometry, where ε is an inverse aspect ratio and q(a) is a safety factor at a plasma surface r = a. The n = 1 kink mode becomes unstable for q(a) above Kruskal Shafranov limit. At marginal stability, the amplitude of m = 2 mode becomes larger than that of m = 1 mode for larger b/a, where b is a position of conducting shell. The stabilizing effect of conducting shell on the n = 1 kink mode can be expected for $b/a < 1.4$.

(M. Wakatani)

2.2 Toroidal Effect of Vertical Displacement of Tokamak Plasma with Elliptic Cross-Section**)

Axisymmetric modes of a free boundary cylindrical tokamak with elliptical cross-section was investigated by Rutherford[2] assuming a flat current profile. He showed that the column becomes unstable against the rigid displacement in the direction of the large axis. We examined the influence of toroidicity on the positional instability, and found that the plasma is stable against axisymmetric modes provided that

$$\frac{\ell-1}{\ell+1} < \frac{3}{8}\left(\frac{a}{R}\right)^2 \left(\ell n \frac{8R}{a} - \frac{17}{12}\right)$$

where $\ell = (a+E_a)/(a-E_a)$. Here the plasma boundary is given by $\rho = a+E_a\cos 2\theta$. The plasma becomes more unstalbe for a peaked current profile, which is due to the larger quadrupole field required to maintain an elongated plasma cross-section.

(M. Wakatani)

---

*) J. Phys. Soc. Japan 38 (1975) 1481.
**) J. Phys. Soc. Japan 38 (1975) 1555.

3. Transport and Impurity

3.1 Decay of Poloidal Rotation in a Tokamak Plasma*)

The decay of poloidal rotation in a tokamak plasma has been studied for the banana regime. A very fast damping mechanism of the order $\delta^{3/2}/\nu_{ii}q^2$ (δ is the inverse aspect ratio, ν_{ii} the ion collision frequency, q the safety factor) is shown to exist. The plasma in a tokamak has a large effective dielectric constant by a factor $(B_T/B_\theta)^2$.

(T. Tuda)

3.2 Ripple Diffusion and Decay of Poloidal Rotation in a Tokamak Plasma**)

The decay of a radial electric field in tokamak systems due to toroidal field ripples was studied. We obtain the characteristic decay time of the radial field.

$$\tau_R = \frac{m_i \nu_{ii} R^2}{9.29\delta^{3/2} G(\alpha) H^2 T_i}$$

where R is the major radius, δ is the depth of the field ripples, $G(\alpha)$ is a geometrical factor given by Connor and Hastie[3] and $H = B_\theta/B_Z$. This characteristic time becomes several tens of milliseconds for typical plasma parameters of a next generation tokamak and seems to be short enough to neutralize the radial electric field generated during the neutral beam heating of the plasma.

(T. Tuda)

3.3 Diffusion in a Tokamak with Helical Magnetic Cells***)

In a tokamak with helical magnetic cells produced by a resonant helical magnetic field, diffusion in the collisional regime was studied. The diffusion is greatly enhanced near the resonant surface even for a weak helical magnetic field. A theoretical model for disruptive instabilities based on the enhanced transport due to helical magnetic cells was examined.

---

*) JAERI-M 5934 (1974), J. Phys. Soc. Japan 38 (1975) 1358-1364.
**) Nuclear Fusion 15 (1975) 541.
***) JAERI-M 6124 (1975), to be published in Nuclear Fusion.

This may explain qualitatively experiments of the tokamak with resonant helical fields.

(M. Wakatani)

3.4 Effect of a Radial Electric Field on the Impurity Transport*)

Impurity transport in a tokamak plasma was examined in the mhd regime[4]. We reconsidered the problem taking account of a radial electric field. Heavy impurity ions do not penetrate into the plasma column when the positive potential of the plasma exceeds a certain value.

(T. Tuda)

3.5 Impurity Transport in Non-Axisymmetric Toroidal System**)

Cross-field impurity diffusion in a non-axisymmetric system (stellarator or tokamak with field ripples) has been studied.

Each ion species was assumed to be collisionless, and the particle trapping due to the field ripples was taken into account. The impurity transport in a non-axisymmetric system was found to be similar to that in the axisymmetric one, i.e. inward diffusion and peaking of the impurity ions are indicated.

(T. Tuda)

3.6 Numerical Study of Impurities in a Tokamak***)

Numerical analysis has been made of the time dependent density profiles of impurities in a tokamak plasma. Diffusion and atomic processes of impurity ions are simultaneously treated. Two different numerical methods were used. The results are in good agreement. Calculations described below are made assuming that a background plasma is constant in time.

Temporal evolution of the impurity distributions in the plasma is described by the following equations.

---

*) JAERI-M 6096 (1975).
**) JAERI-M 6171 (1975).
***) JAERI-M 6143 (1975).

$$\frac{\partial I_k}{\partial t} = -\frac{1}{r}\frac{\partial}{\partial r}(r\Gamma_k) + n_e(\alpha_{k-1}I_{k-1} - \alpha_k I_k) - n_e(\beta_{k-1}I_k - \beta_k I_{k+1}) \quad . \tag{1}$$

$$(k = 1, 2 \ldots\ldots N)$$

Here I_k is the density of impurity ions in the (k-1) stage α_k and β_k are the rate coefficients of ionization and recombination, respectively. We consider the Pfirsch-Schluter regime and thus make use of the following expressions for impurity flux.

$$\Gamma_k = -D_k\frac{\partial I_k}{\partial r} + D_k\frac{k-1}{Z_i}\frac{1}{n_i}\frac{\partial n_i}{\partial r} \quad , \tag{2}$$

$$D_k = (1 + 2q^2)\nu_k\rho_k \quad ,$$

$$\rho_k^2 = \frac{m_{ki}T_i}{(k-1)^2e^2B_z^2} \quad , \tag{2}'$$

$$\nu_k = \frac{4}{3}\frac{\sqrt{2\pi}\,(k-1)^2Z_i^2e^4n\,\ell n\Lambda}{\sqrt{m_{ki}}\,T_i^{3/2}} \quad ,$$

where m_{ki} is the reduced mass of m_k and m_i and other notations are conventional. The second term of eq. (2) represents the "so-called" inward diffusion. Numerical calculations were made both by Hamming's predictor-corrector method and by solving the eigenvalue equation of eq. (1).

The results of the calculation are shown in Fig. III.3-1 --- III.3-6. The boundary condition is that the total impurity flux vanishes at the plasma boundary, i.e. $\Gamma = \sum_k \Gamma_k = 0$, at r = a. Also at r = a corona equilibrium is assumed. Fig.III.3-1, is the profile of background plasma and Fig.III.3-2 the initial density distribution of oxygen impurities. Fig. III.3-6 shows the stationary state, where low-Z ions almost disappeared and concentration of highly ionized ions is noticed.

(M. Okamoto and T. Amano*))

*) Plasma Physics Laboratory, Faculty of Engineering, Osaka University.

3.7 Radial Transport Code for Tokamak Plasma

Further development was made on the simulation code for the time evolution of tokamak plasma. The code is based on the particle and energy balance equations and the Maxwell equations. Effect of neutrals and impurities are also included. Routines for the impurity were developed which treat both atomic and diffusion processes simultaneously.

The code described here includes the following processes i) transport process -- neoclassical, pseudoclassical, and anomalous transport due to trapped electrons or trapped ions, ii) external circuit systems, iii) cold and hot neutrals including recycling, iv) impurity (oxygen ions at present).

The code solves the problem by two steps. The first step neglects the effects of neutrals and impurities and solves the particle and energy balance equations of the plasma together with the Maxwell equations by the difference method of Crank-Nicolson. The second step solves the equation for neutrals, which is the steady state form of the Boltzmann equation, and the equations for impurities, which include the atomic and diffusion processes. Here the plasma profiles given by the first step are used. The change of particle densities Δn_e, Δn_i and of energies ΔE_e, ΔE_i due to the neutrals and impurities were calculated. Then the plasma profiles were corrected through the first step. Numerical results are shown in Figs. III.3-7 ∿ III.3-12.

(M. Okamoto and T. Amano*)

3.8 Impurity Drift Instability of Dissipative Type**)

A new type of impurity drift instability was investigated in the short mean free path limit. This mode is driven by the ion parallel viscosity and is stabilized by the collisional diffusion of impurity ions across the magnetic field when the impurity concentration is lower than a certain value.

(T. Tuda and M. Tanaka)

---

*) Plasma Physics Laboratory, Faculty of Engineering, Osaka University.
**) JAERI-M 6167 (1975).

4. Thermalization Process of Fast Ions

A computer code has been developed to investigate the thermalization of fast ions in a toroidal system. The code simulates the Coulomb interaction of test particles (fast ions) with field particles (electrons, protons and impurity ions) by the Monte Carlo technique, taking account of the ments up to the second order. The test results were compared with analytic solutions of 2D Fokker Planck equation and yielded a good agreement. The code also includes i) charge exchange process with background neutrals, ii) excursion of fast ion orbits from magnetic surfaces, iii) acceleration due to the toroidal electric field driving the plasma current. Plasma parameters are assumed to be constant to save the computing time.

Our code has an advantage that the thermalization process of fast ions can be treated in realistic ways. Namely the spatially dependent characteristics of the slowing down process can be easily taken into account. Some results for the JT-60 parameters are briefly described below.

Loss of fast ions due to charge excharge reactions with background neutrals was estimated. An example for a rather high background neutral density is shown in Fig. III.4-1. Some of the charge exchanged neutrals are re-ionized and thus captured inside the plasma when their mean free path is less than the plasma radius. The successive charge exchange and ionization processes decrease the loss of fast ions (dotted lines in Figs. II.4-1(b) and (c) correspond to no re-ionization in the plasma) and also flatten the spatial distribution of fast ions.

The characteristics of fast ion orbits are taken into account in the loss rate calculation in two ways. It should be noted that the slowing down time of fast ions is considerably longer than the circulating time along their orbits in typical circumstances of injection heating. The energy loss due to loss cone in the velocity space is evaluated by making use of a model orbit, which is a circle for an untrapped particle. For a trapped particle its banana orbit is approximated by a model orbit consisting of two arcs separated by its banana width. Fast ions are randomly scattered at an arbitrary position on their orbits at every time step. The effect of impurity concentration and plasma current on the energy loss in JT-60 heating was evaluated in this way.

More precise treatment of fast ion orbits was made assuming a highly dense plasma, in which the slowing time is comparable to the bounce time.

The guiding center equations are solved by the predictor-corrector method and ions are scattered at every time step. In Fig. III.4-2 the positions o of 100 test particles with the same initial conditions are plotted at a prescribed time step. The initial orbit of test particles (solid lines) is assumed barely untrapped. Particles spread along the orbit and some of them fall into barely trapped orbits, but thereafter they are well confined within the banana width.

(M. Azumi)

References

1) Y. Shimomura, M. Wakatani, A. Kitsunezaki, H. Maeda and M. Tanaka: JAERI-M 6105 (1975).
2) P. H. Rutherford: MATT-976 (1973).
3) J. W. Connor and R. J. Hastie: Nuclear Fusion, 13 (1974) 221.
4) T. Tuda and M. Tanaka: JAERI-M 5376 (1973), J. Phys. Soc. Japan, 38 (1975) 1128.

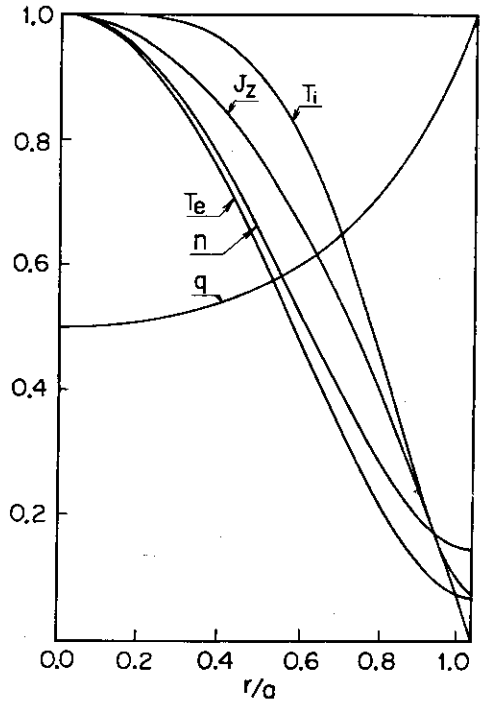

Fig.III.3-1 Radial profiles of background plasma. n_{max}=1.4 10 cm , T_{emax}=300 eV, T_{imax}=200 eV, q=4.46

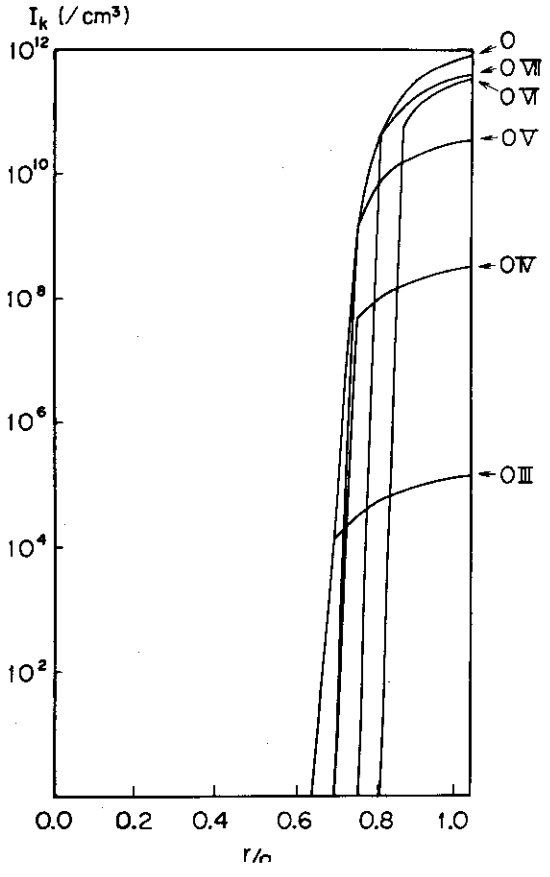

Fig.III.3-2 Initial distributions of oxygen ions.

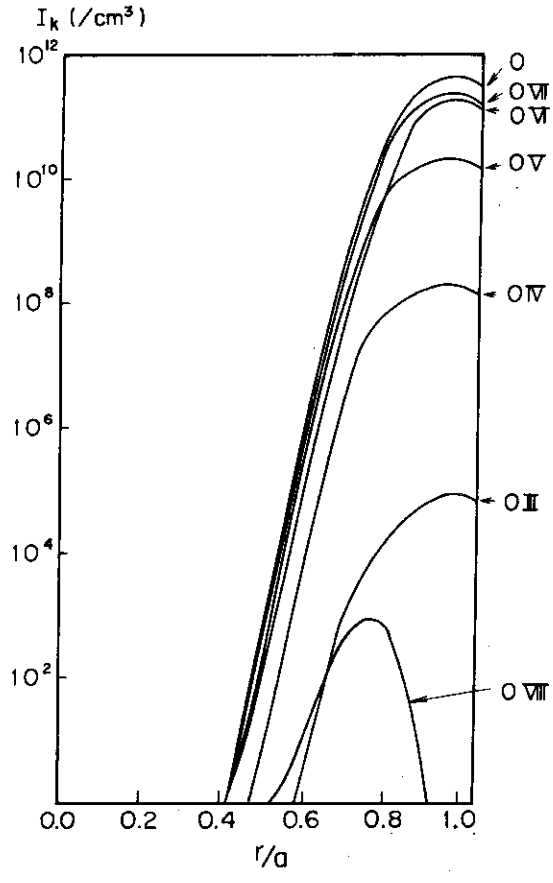

Fig.III.3-3 $t = 10^{-4}$ sec

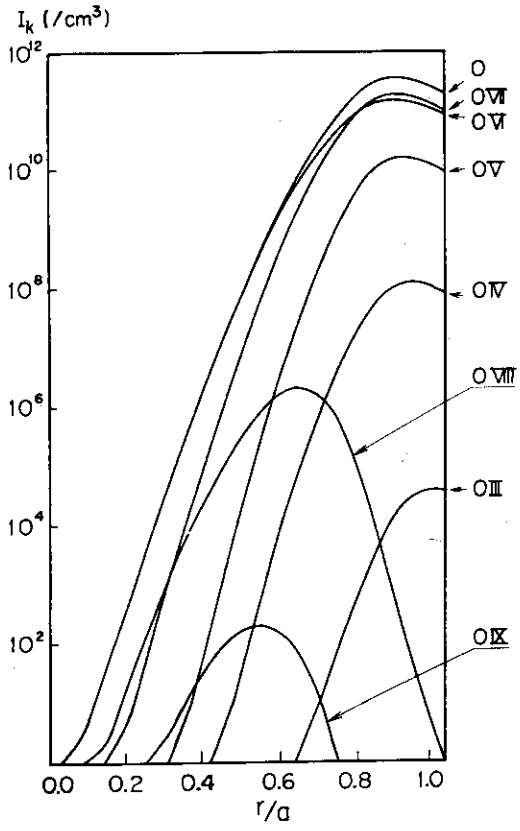

Fig.III.3-4 $t = 10^{-3}$ sec

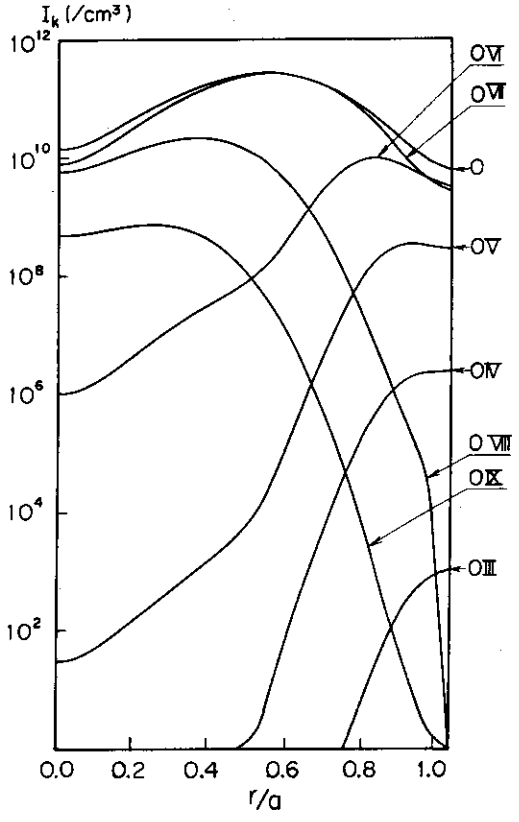

Fig.III.3-5 $t = 10^{-2}$ sec

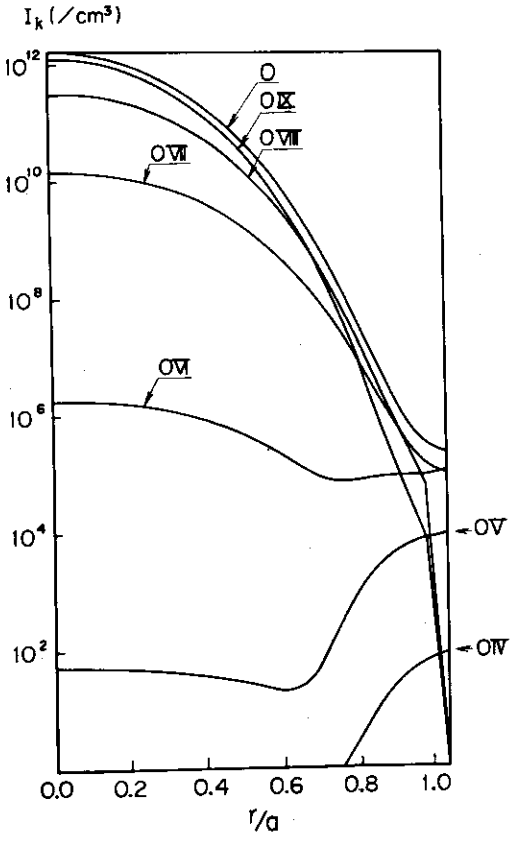

Fig.III.3-6 $t = 0.6$ sec (stationary state)

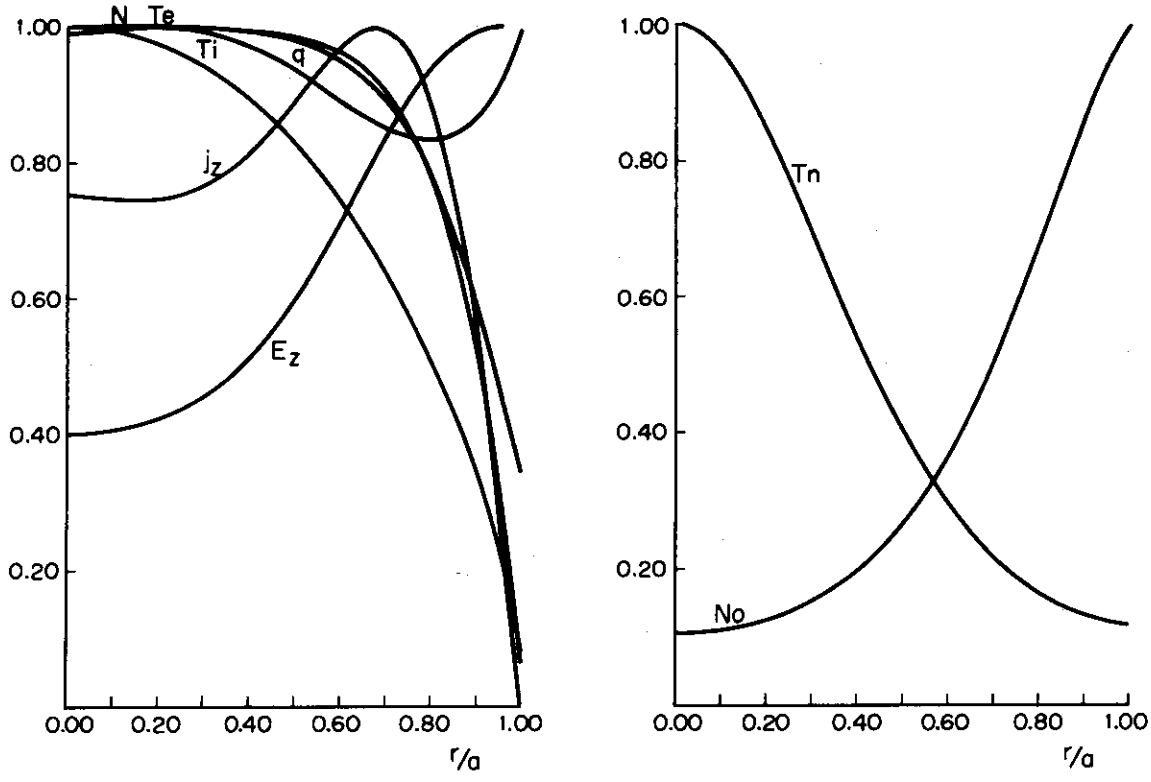

Fig.III.3-11 Pseudoclassical case including neutrals. t=10.39 msec, n (a)=5×10^9 cm^{-3}, T_0(a)=1 eV

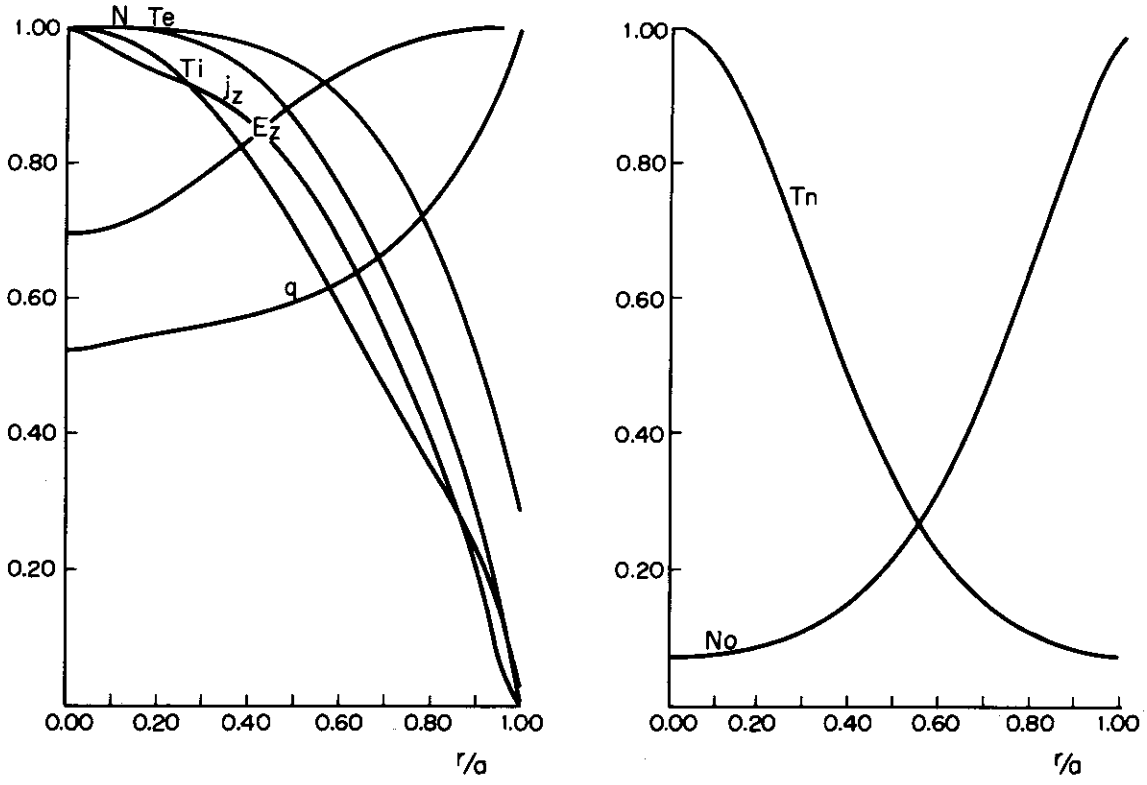

Fig.III.3-12 Pseudoclassical case including neutrals. t=40.39 msec, n_0(a)=5×10^9 cm^{-3}, T_0(a)=1 eV

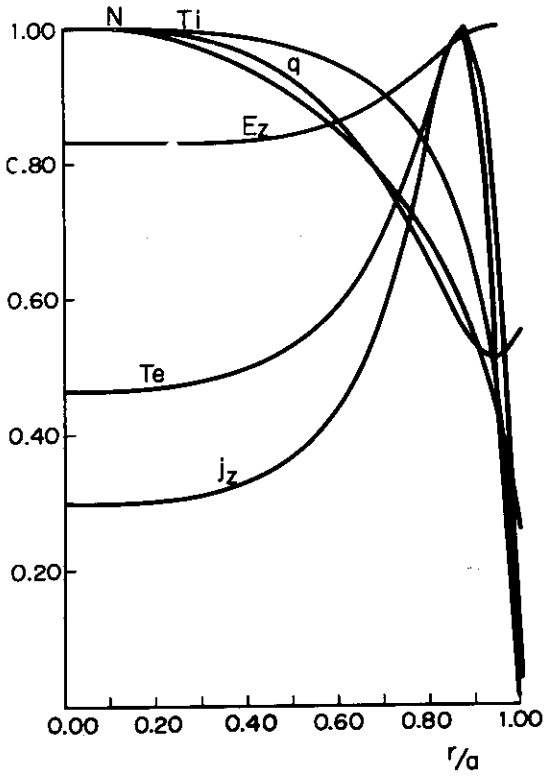

Fig.III.3-7
Simplified neoclassical case.
Only the diagonal terms are retained in transport equations.
$j_z(t=0) \propto 1-(r/a)^2$

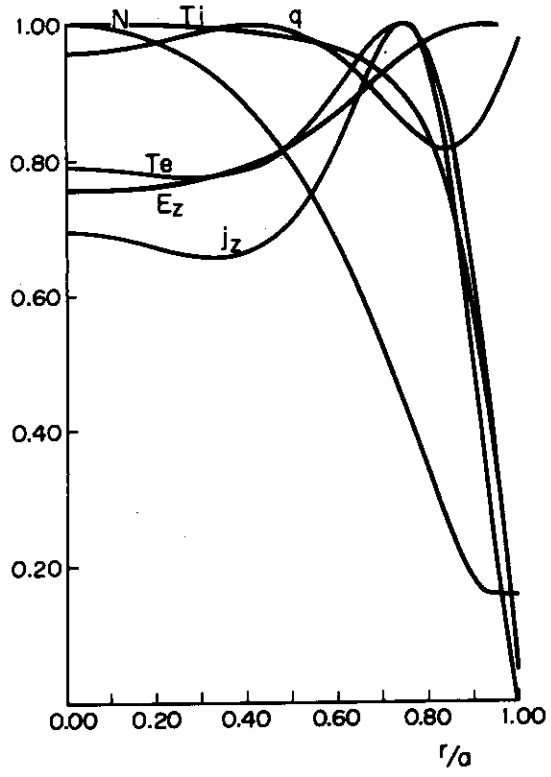

Fig.III.3-8
Complete neoclassical case.
$j_z(t=0) \propto 1-(r/a)^2$

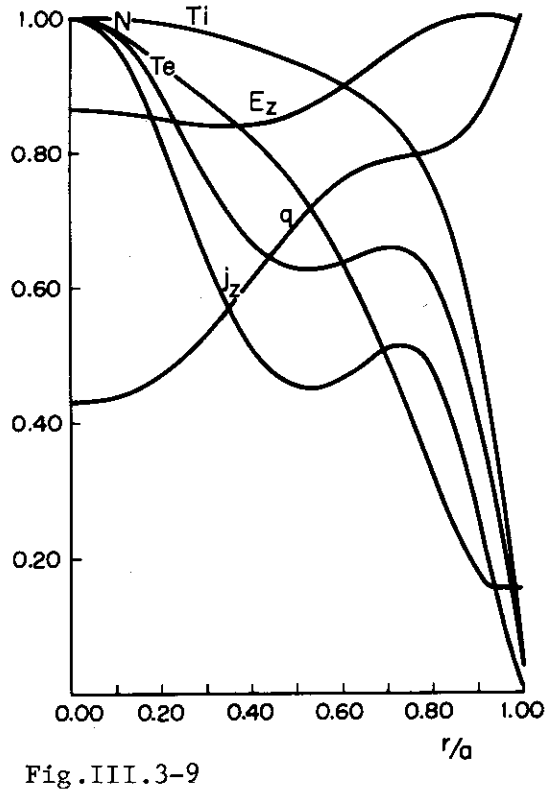

Fig.III.3-9
Complete neoclassical case.
$j_z(t=0) \propto (1-(r/a)^2)^3$
Ipeaked distribution)

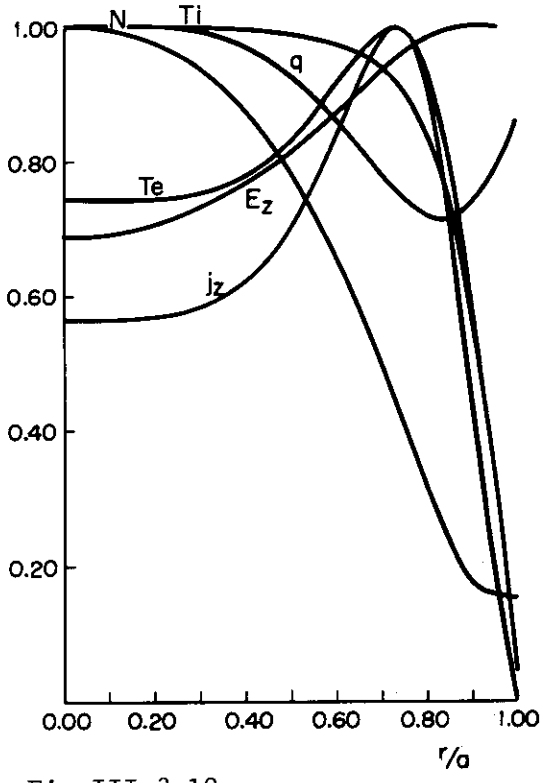

Fig.III.3-10
Complete neoclassical case.
$j_z(t=0) \propto 1-(r/a)^6$ 9
(flat distribution)

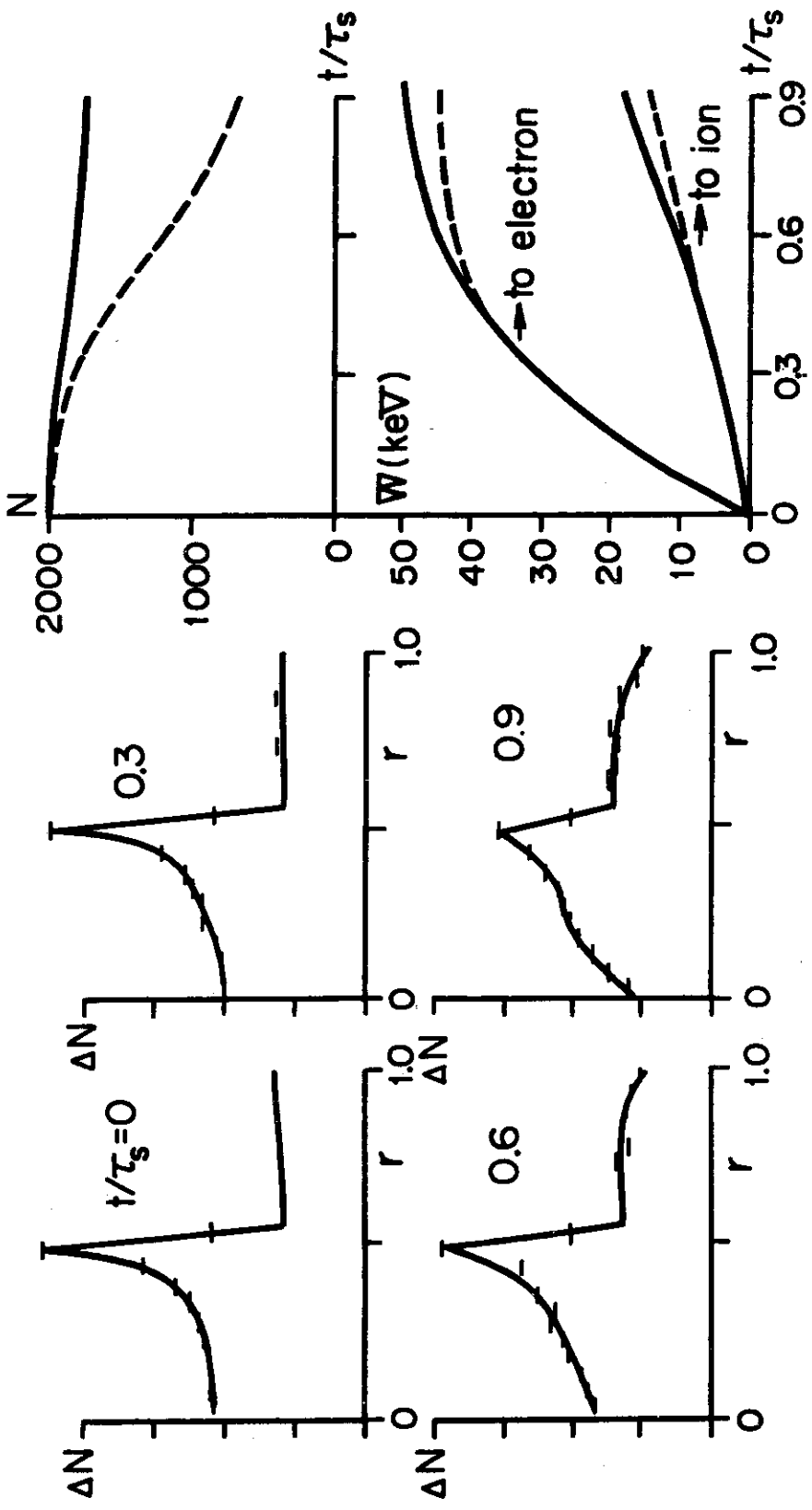

Fig.III.4-1 Effects of the charge exchange process with background neutrals. (a) Density distribution of fast ions, ΔN is the number of particles in the shell. (b) Loss of fast ions, N is the total number of particles. (c) Fractions of the beam energy transfered to electrons and ions, E_{beam}=75 keV, $n_e=2\times10^{13}$ cm^{-3}, T_e=1 keV, $n_0=2\times10^{8}$ cm^{-3}, θ_{inj}=38.7.

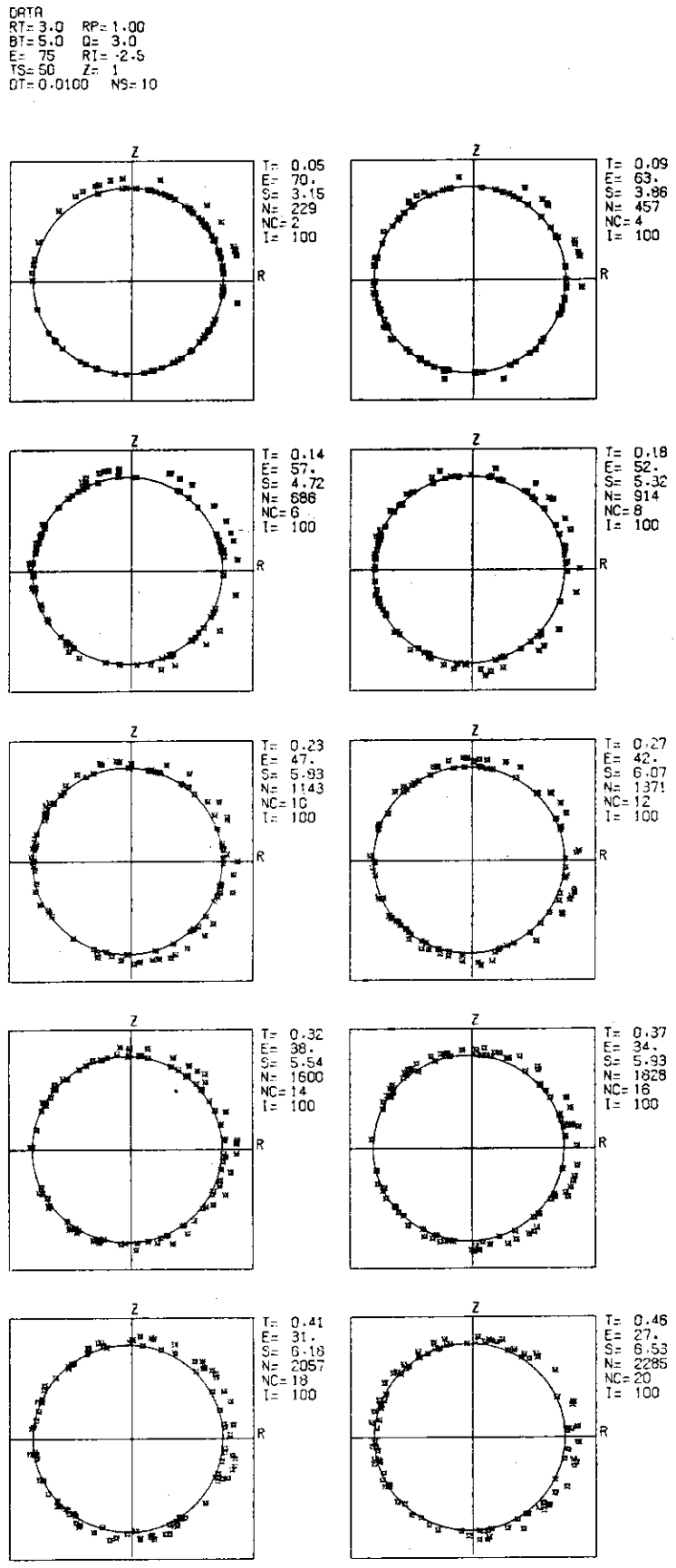

Fig.III.4-2 Motion of test particles during the thermalization process for co-injection (a) and for counter-injection (b).

DATA
RT= 3.0 RP= 1.00
BT= 5.0 Q= 3.0
E= 75 RI= 2.5
TS= 50 Z= 1
DT= 0.0100 NS= 10

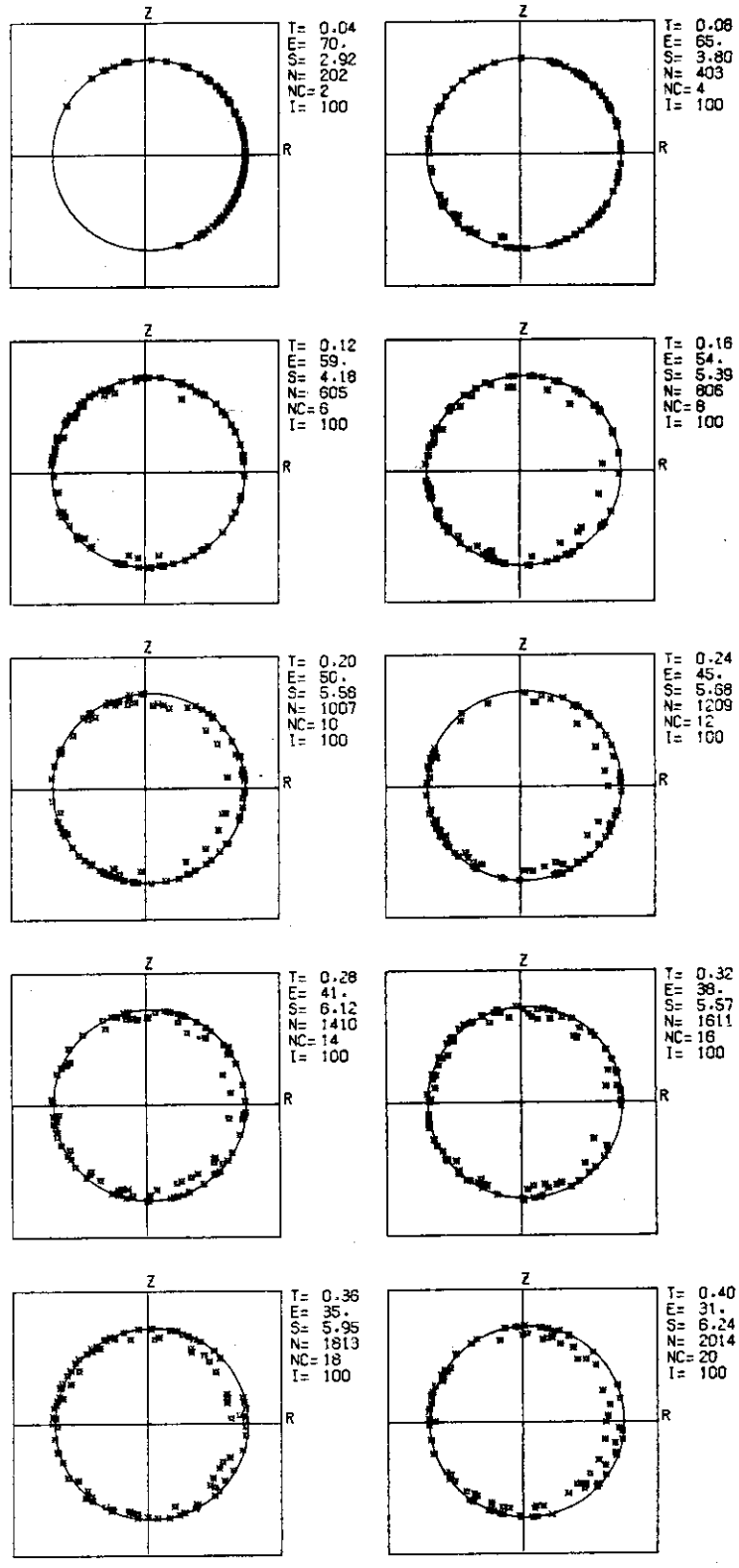

Fig. III.4-2(b)

IV. Reactor Design Study

N. Asami*, Y. Ohkubo**, M. Ohta, K. Sako,
Y. Seki, T. Tone, H. Yamato***

1. Introduction

Design of the 2000 MWt fusion power reactor which started in April, 1973 has been improved to make clear the reactor concept and problem areas for the development. The study covers the design of core plasma, reactor structure, blanket and shield neutronics, superconducting magnet, electrical power supply system, tritium recovery system, reactor cooling system etc.

As the first step for the preliminary design of the experimental power reactor, to be started in April 1975, the reactor concept and the main design criteria have been investigated.

(K. Sako)

2. Design Study of Tokamak Reactor

2.1 General[1)]

The main features of the reactor are as follows; the reactor output 2000 MWt, the first wall loading 2 MW/m^2, the plasma major/minor radius 10/2 m, the toroidal magnetic field on the axis 60 kG and the reactor inlet/outlet coolant helium temperature 400/700°C. Lithium oxide (Li_2O) and molybdenum alloy are used for the blanket fertile material and the first wall material respectively. The detailed design parameters are given in Table IV.2-1, and an overview of the reactor is shown in Fig. IV.2-1.

The two distinct features of the reactor are the utilization of cold gas blanket for fuel supply and suppression of plasma impurities, and the use of Li_2O as the blanket fertile material.

---

*) On leave from Mitsubishi Atomic Power Industries Inc., Omiya, Japan.
**) On leave from Fuji Electric Co. Ltd., Kawasaki, Japan.
***) On leave from Tokyo Shibaura Electric Co. Ltd., Kawasaki, Japan.

2.2 Core Plasma Design

1) Main plasma parameters

Main parameters in a steady operation listed in Table IV.2-1 are determined in the following procedure. a) The poloidal β and the safety factor q are fixed to 2.0 and 1.5 respectively. b) Toroidal magnetic field of 60 kG on the plasma axis is used assuming that Nb_3Sn superconducting material is available. c) The plasma temperature of 15 keV is selected since $\langle\sigma v\rangle/T^2$ or the power density in the plasma is maximum at this temperature. d) As the total power output is fixed, the plasma major radius is determined if the aspect ratio is given.

When the thermal output is 2000 MW, a major radius of 10 m is obtained for an almost minimum possible aspect ratio of 5. If the safety factor is limited to higher values or the toroidal field to lower values, the major radius must be larger to give the same power output and as a result smaller aspect ratio becomes possible. For example, if the safety factor is 2.4, a major radius of 10 m and an aspect ratio of 4 is obtained at the same power and toroidal field.

(H. Yamato and M. Ohta)

2) Power balance calculation

The plasma density is about 10^{14} cm^{-3} when the thermal power output is 2000 MW and energy release per fusion is 22.4 MeV. The following loss processes, that is, the thermal and particle diffusions, the bremsstrahlung and the excitation and recombination radiations of impurities, are taken into account. The simplified equation introduced by G. R. Hopkins is used to estimate the impurity radiations[2]. Amounts of impurities assumed here are 1 % of O_2 and 0.02 % of Mo.

The total power loss and the radiation loss are about 313 MW and 114 MW respectively. The remaining 199 MW is due to the thermal and particle diffusions which correspond to the energy confinement time of 2.9 sec. Confinement times given by the scaling laws of the pseudoclassical diffusion and trapped ion mode are 34.4 sec and 0.81 sec respectively[3,4].

(M. Ohta and H. Yamato)

3) Fuel supply

It is assumed that the fuel is supplied by the cold fuel gas surrounding

the core plasma in the reactor . The radial distributions of density and temperature are calculated numerically from diffusion equations. A result of calculation is shown in Fig. IV.2-2. In this calculation, the neutral temperature is fixed to 10 eV for simplicity, but in reality, various energy components are produced by charge exchange processes at different temperatures, even when the surrounding gas is at a certain fixed temperature. The neutral density to supply fuel to the plasma density of 10^{14} cm^{-3} is about 10^{13} cm^{-3} which corresponds to 3×10^{-4} torr, when the neutral temperature is 0.1 eV.

This neutral gas pressure is not sufficient to stop the fast neutral particles produced by charge exchanges. Sputtering of the wall and influx of impurities, however, may be suppressed since the temperature of the plasma in the mixed region of the plasma and neutral gas can be as low as 10 eV, which is lower than the sputtering threshold. There are some high energy neutral particles produced in the inner hot region after successive charge exchanges. The above mentioned values of impurities are assumed in the calculation. The quantitative evaluation is now under way.

(H. Yamato and M. Ohta)

4) Ignition and Shutdown

The plasma is heated to 1 keV by Joule heating during the initial discharge of 2 sec and then the 30 MW neutral beam injection heating is applied.

The time behavior of plasma after Joule heating is shown in Fig. IV.2-3. The plasma density is initially fixed to 3×10^{13} cm^{-3} until the temperature reaches 6 keV. Then the density increases to a steady state of 10^{14} cm^{-3} with the time constant of 5 sec by diffusing the gas fuel surrounding the plasma. Though the heating power is switched off at T = 10 keV, the plasma is heated to the steady state by α-particle heating.

The plasma is cooled down by the following method that the tritium injection is stopped and the deuterium injection rate is doubled compared with that of steady state.

(M. Ohta and H. Yamato)

2.3 Reactor Structure Design

In this design most of the main components such as blanket structures, coolant pipings, shieldings, evacuation holes, magnets, injectors, etc. are considered. Repair and maintenance schemes of the main components are also taken into account. An overall view of the reactor is shown in Fig. IV.2-1.

The reactor consists of 12 modules which may be withdrawn in the radial direction for repair. A cross section of the module is shown in Fig. IV.2-4. Each module has 188 blanket cells and one blanket cell with a 1 meter hole for the neutral beam injection and evacuation. As proposed in a previous design[6], the Li_2O pebbles are used as blanket fertile material for simplification of the blanket structure and maintenance.

In this design, since most of energy released by fusion reaction is converted to heat on the wall surface, it is essential to minimize the thermal stress induced in the vessel wall. Therefore molybdenum alloy is employed as the structural material, and a cellular type blanket vessel similar to that of the Culham design[7] is selected. A cross section of the blanket cell is shown in Fig. IV.2-5.

(K. Sako)

2.4 Blanket and Shield Neutronics Design

A one-dimensional cylindrical model of blanket, shield and toroidal magnet used in nuclear calculation is shown in Fig. IV.2-6. The effective thickness of Li_2O and graphite region is 65 cm and 26 cm, respectively. The shield for the superconducting magnet consists of 50 cm thick heavy concrete, 20 cm borated water and 5 cm lead in stainless steel structure. From a preliminary calculation it is found that the irradiation level and nuclear heating rate in the magnet are low enough when the above configuration is adopted[8]. Neutron and gamma-ray fluxes in the blanket, shield and magnet are shown in Fig. IV.2-7.

42 energy group, P_5 neutron cross sections are processed from ENDF/B-3 by SUPERTOG[9]. As the molybdenum neutron cross sections for (n,α), (n,p), (n,d) and (n,n'p) reactions are not included in ENDF/B-3, they are evaluated and added[10]. 21 energy group, P_5 gamma-ray cross sections are calculated by GAMLEG-JR[11]. Radiation heating calculations are carried out from the

code system RADHEAT[11]. Neutron and gamma-ray fluxes and various reaction rates are calculated by the ANISN[12], with P_5-S_8 approximation.

Neutron and gamma-ray heating in the blanket per fusion reaction is 11.1 MeV and 3.7 MeV, respectively, giving the total heating of 14.8 MeV. The heating rate distributions are shown in Fig. IV.2-8. The calculated value of the tritium breeding ratio is 1.24. This value is sufficiently large even if the neutron streaming loss through the injection and evacuation holes is taken into account. On the inner surface of the protection wall, the total and 14 MeV neutron fluxes take the largest values of 3.5×10^{14} $n \cdot cm^{-2} \cdot s^{-1}$ and 7.0×10^{13} $n \cdot cm^{-2} \cdot s^{-1}$, respectively. As a result, the production rate of helium at this point is 167 $appm \cdot y^{-1}$ and that of hydrogen is 382 $appm \cdot y^{-1}$ [10].

A method for calculating induced activity in fusion reactor is developed. The induced activity and decay heat in the copper coil of a zero-power critical plasma experimental facility when D-T burning experiment is carried out has been calculated[13].

(Y. Seki)

2.5 Toroidal Field Magnet Design

The design study of the toroidal field magnet is performed by employing the method of parametric study of coil dimensions, arrangement and structure. In consideration of plasma parameters, blanket and the other structures, the minimum inner radius is decided to be 7 m and D-shape coil is selected to reduce the electromagnetic force[14]. Furthermore, we select 24 coils with irregular arrangement in the toroidal direction. The V-type arrangement of two toroidal field coils is employed to make a unit structure. Correlation between the ripple and the open angle of V-type arrangement (V-angle) is shown in Fig. IV.2-9. According to the theoretical consideration, it is estimated that the ripple should be less than 5×10^{-3} [15]. On the basis of this analysis, 17.5 degree is selected for the V-angle. Figure IV.2-9 also illustrates the ripple along the major radial direction. The calculated ripple at the outer edge of the plasma region is 3.66×10^{-3}. A hybrid (Nb_3Sn-NbTi) superconducting magnet is introduced and Nb_3Sn compound type superconductor is selected because the maximum field at the conductor is calculated to be 115 kG. Other design parameters such as electromagnetic forces, stored energy are summarized in Table IV.2-1.

Preliminary design and stress analysis of coil structures are performed. Furthermore, electromagnetic force in case of coil failure is also analyzed to evaluate the structural integrity of magnet.

(N. Asami)

2.6 Air-Core Transformer and Vertical Field Magnet Design

The position of the primary windings of transformer core, which are wound outside the toroidal field coils, is decided by means of nonlinear programming. The magnetic flux change of 420 V·sec is necessary to excite and sustain the plasma current of 8 MA during 6000 sec. The core radius is 3.6 m and the magnetic field is changed from -52 kG to +52 kG.

The vertical field distribution in our reactor is shown in Fig. IV.2-10. Its coil positions are decided in such a way that the difference between the design field and the ideal[16] at the median plane of plasma is minimized under the fixed values of B_v = 3.55 kG and n-index = 0.38 at the plasma axis which are necessary to equilibrate and stabilize the plasma column with β_p = 2 and a circular cross section.

(T. Takeda, M. Ohta and H. Yamato)

2.7 Neutral Beam Injector Design

To further increase the Joule heated plasma temperature beyond an ignition point, it is necessary to inject a net input power of about 30 MW. Twelve injection ports are installed on the blanket wall, one in each sector with 0.8 m^2 in area, through which a couple of deuterium atom beams in injected almost perpendicularly. The beam energy of 120 keV is chosen because of easier handling and higher overall efficiency. For this purpose, a low density plasma (about 3×10^{13} cm^{-3}) is required in the initial heating phase. The positive ion source unit which may be a two stage accel system composed of 23 cm diameter electrodes with 95 and ten times more apertures in the second and the first stage electrode respectively is capable of extracting ion current of 33 A from the 23 cm diameter electrode with a small beam divergence (0.8°) and is mounted at 16 m apart from the plasma surface. The atomic ion beam is converted to the neutral beam with its conversion efficiency of 45% through the normal deuterium gas cell whose line density is 2.4×10^{-3} torr m. The uncharge-exchanged ion beam is

separated by the magnetic field and is led to the charge collector[17].

(S. Matsuda and H. Yamato)

2.8 Electrical Power Supply System Design

The electrical power supply system for the 2000 MW CTR consists of many subsystems such as a plasma driving system, toroidal magnet charging system, power source for the neutral beam injectors, cryogenic system and vacuum system. With the other necessary power systems (the generating or the starting system), they are conceptually shown in Fig. IV.2-11. In order to reduce peak power load, introduction of the superconducting inductive energy storage (SC-IES) to the relevant systems was examined. Detailed design is now underway.

(Y. Ohkubo)

2.9 Reactor Cooling System Design

A Tokamak fusion reactor is operated periodically, so special consideration is required in two aspects of the reactor cooling system. One is to minimize thermal cycle fatigue of the reactor structures and the other to stabilize heat supply to the electric power generating system.

For the purpose, a cooling system with heat reservoirs and reactor coolant bypass circuits was proposed. The simplified reactor cooling system is shown in Fig. IV.2-12. The heat reservoir was designed preliminarily and a parametric study of the performance characteristics was carried out.

It was shown that the two problems in periodical operation of the reactor can be solved by reasonable design of the cooling system[18].

(K. Sako)

References

1) Sako, K., Yamato, H., Ohta, H., Seki, Y., Tanaka, K., Asami, N., Matsuda, S., Ohkubo, Y., Takeda, T. and Mori, S., 5th IAEA Conf. on Plasma Phys. & Controlled Fusion Research (Tokyo, 1974) paper CN-33/G1-5.

2) Hopkins, G. R., Tech. Cont. Thermonuclear Fusion Exp. Eng. Aspects

Fusion Reactions (Proc. Conf. Austin, 1972), USAEC, Oak Ridge (1974) 795.

3) Kadomtsev, B. B., Pogutse, O. P., Nucl. Fusion 11 (1971) 67.

4) Yoshikawa, S., Christofilos, N., Plasma Phys. and Cont. Thermonuclear Fusion Res. (Proc. Conf. Madison, 1971) II, IAEA, Vienna (1972) 357.

5) Yamato, H., Ohta, M., First Topical Meeting on Tech. Cont. Nucl. Fusion (Proc. Conf. San Diego, 1974).

6) Sako, K., Ohta, M., Seki, Y., Yamato, H., Hiraoka, T., Tanaka, K., Asami, N., Mori, S., Proc. IAEA Workshop (Culham, 1974) Nuclear Fusion Special Supplement 1974.

7) Hancox, R., Booth, J. A., CLM-R 116 (1971).

8) Seki, Y., JAERI-M 6046 (1975) (in Japanese)

9) Wright, R. Q., Green, N. M., Lucius, J. L., Craven, C. W. Jr., ORNL-TM-2697 (1974).

10) Iwai, K., Seki, Y., JAERI-M 5855 (1974) (in Japanese).

11) Miyasaka, S. et al., JAERI-M 5794 (1974) (in Japanese).

12) Engle, W. W. Jr., "A User's Manual for ANISN: A One Dimensional Discrete Ordinates Transport Code with Anisotropic Scattering" K-1963 (1967).

13) Seki, Y., Harada, Y. and Asami, N., JAERI-M 5862 (1974) (in Japanese).

14) File, J., Mills, R. G., Sheffield, G. V., IVth Sump. Eng. Prob. Fusion Res. (Proc. Conf. Washington, D.C., 1971) 277, See also MATT-848 (1971).

15) Stringer, T. E., CLM-P 308 (1972).

16) Mukhovatov, V. S., Shafranov, V. D., Nucl. Fusion 11 (1971) 605.

17) Moir, R. W., Barr, W. L., Nucl. Fusion 13 (1973) 35.

18) Sako, K., JAERI-M 6099 (1975) (in Japanese).

Table IV.2-1 Design Parameters

Power	
Reactor thermal output	2000 MW
Electrical output	800 MW
Dimensions	
Major radius	10 m
Plasma radius	2 m
First wall radius	2.3 m
Core Plasma	
Average plasma temperature	15 keV
Average plasma density	1.0×10^{14} cm^{-3}
Energy confinement time	1.8 sec
Operation period	100 min
Toroidal magnetic field	60 kG
Safety factor	1.5
Poloidal value	2.0
Plasma current	8 MA
Effective Z	1.8
Bremsstrahlung loss	29.4 MW
Recombination radiation loss	23.1 MW
Blanket Materials	
Structural material	Mo alloy
Fertile material	Li_2O pebbles
Reflector material	Graphite balls
Neutronics	
Total first wall neutron flux	6.8×10^{14} n·cm^{-2}·sec^{-1}
Tritium breeding ratio	1.24
Neutron heating	11.1 MeV·n^{-1}
Gamma heating	3.7 MeV·n^{-1}
Total heating	14.8 MeV·n^{-1}
Cooling System	
Reactor coolant	He
Reactor inlet/outlet temperature	400/700°C
Secondary system	Steam cycle

Toroidal Field Magnet	
Number of coils	24
Coil major radius	10.5 m
Coil inner/outer radius	7/8.2 m
Maximum magnetic field (mid plane)	115 kG
Magnetomotive force	300 MAT
Stored energy	160 GJ
Coil shape/arrangement	D-shape/V-type
Superconductor(stabilized)	Nb_3Sn-NbTi hybrid
Average current density/overall	10/1.25 kA·cm^{-2}
Electromagnetic force/coil	
Expansion force	182×10^6 kg
Centering force	72×10^6 kg
Force due to irregular arrangement	22×10^6 kg
Rotating moment	76×10^6 kg-m
Air Core Transformer	
Stored energy	7 GJ
Magnetomotive force	70 MAT
Vertical Field Coil	
Stored energy	0.6 GJ
Magnetomotive force	17 MAT
Neutral Beam Injector	
Number of injectors	24 units
Heating power	30 MW
Ion source output	120 keV, 33 A, D^+
Neutralization efficiency	45 %
Overall power efficiency	65 %

JAERI-M 6359

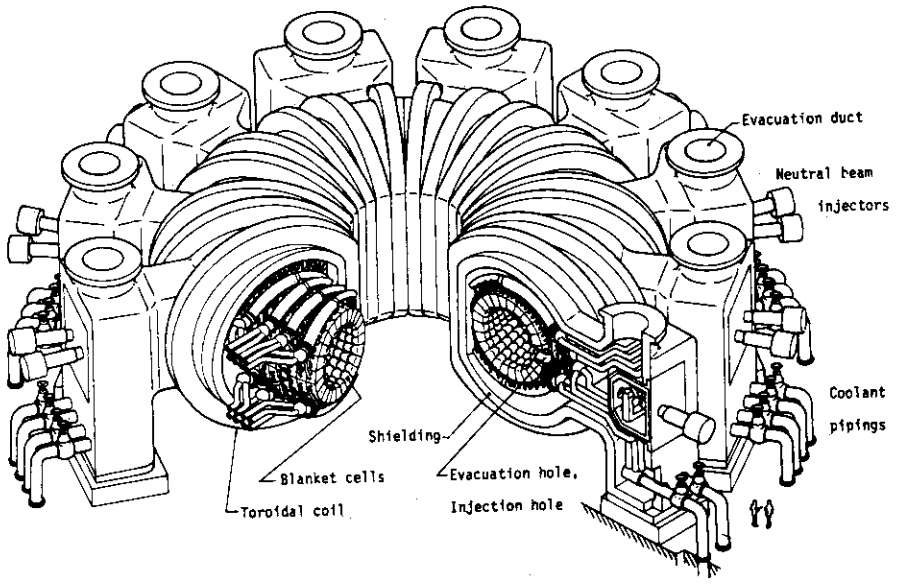

Fig.IV.2-1 Overall view of the reactor

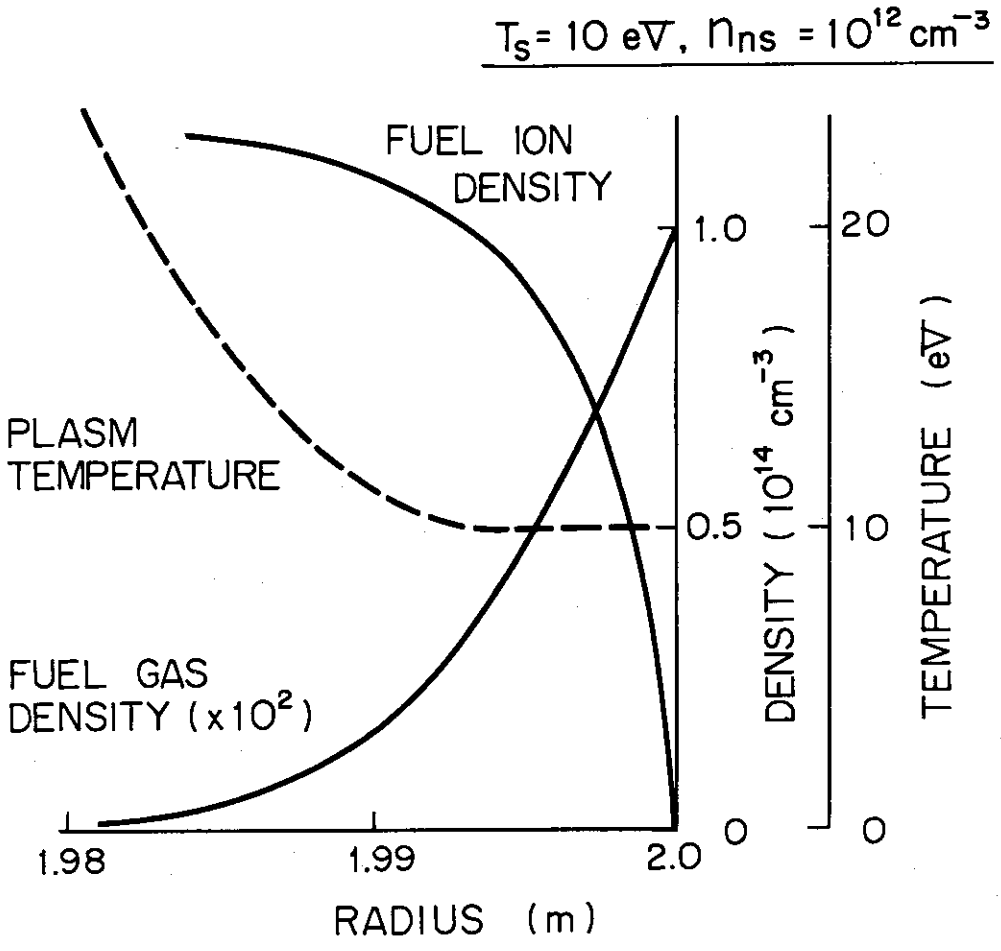

Fig.IV.2-2 Plasma density, temperature and neutral density distributions at the plasma surface.

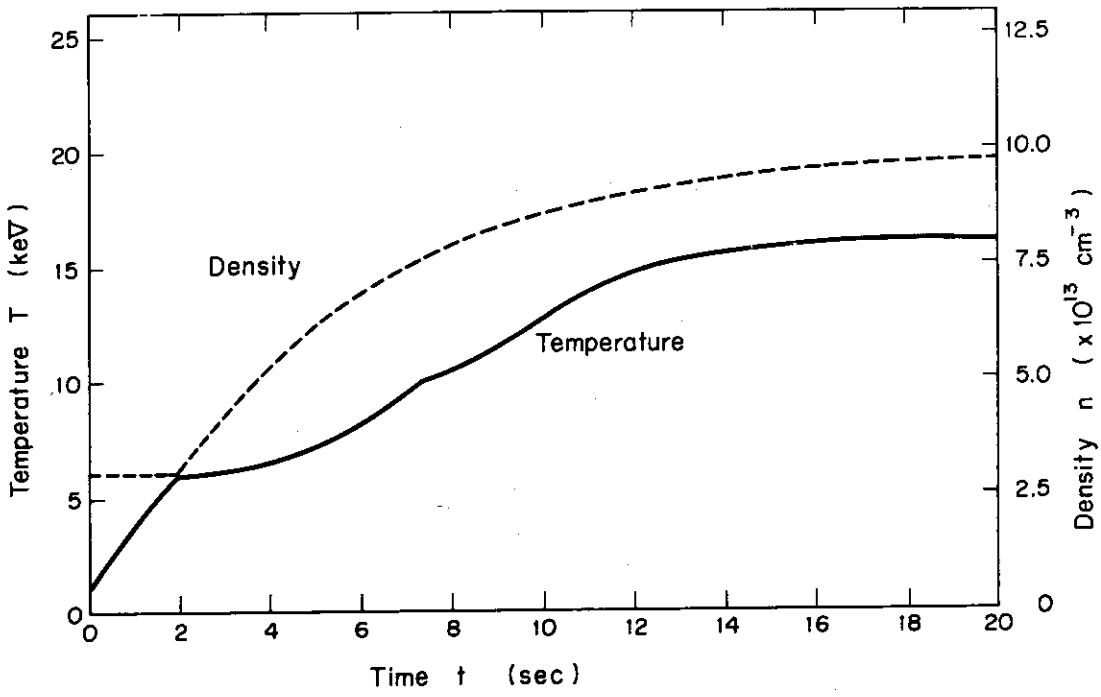

Fig.IV.2-3 Time behavior of plasma density and temperature at the start up.

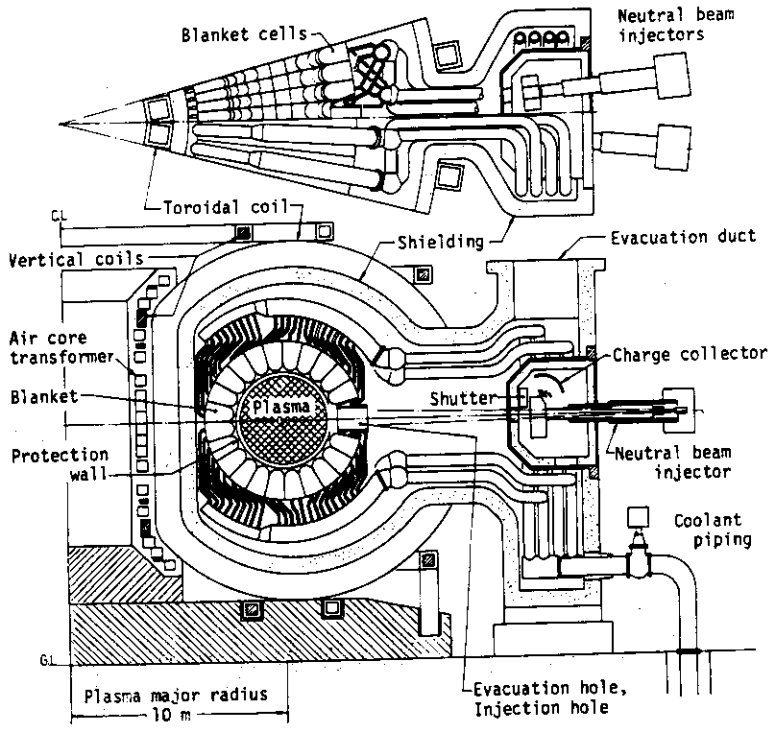

Fig.IV.2-4 Cross section of the reactor module

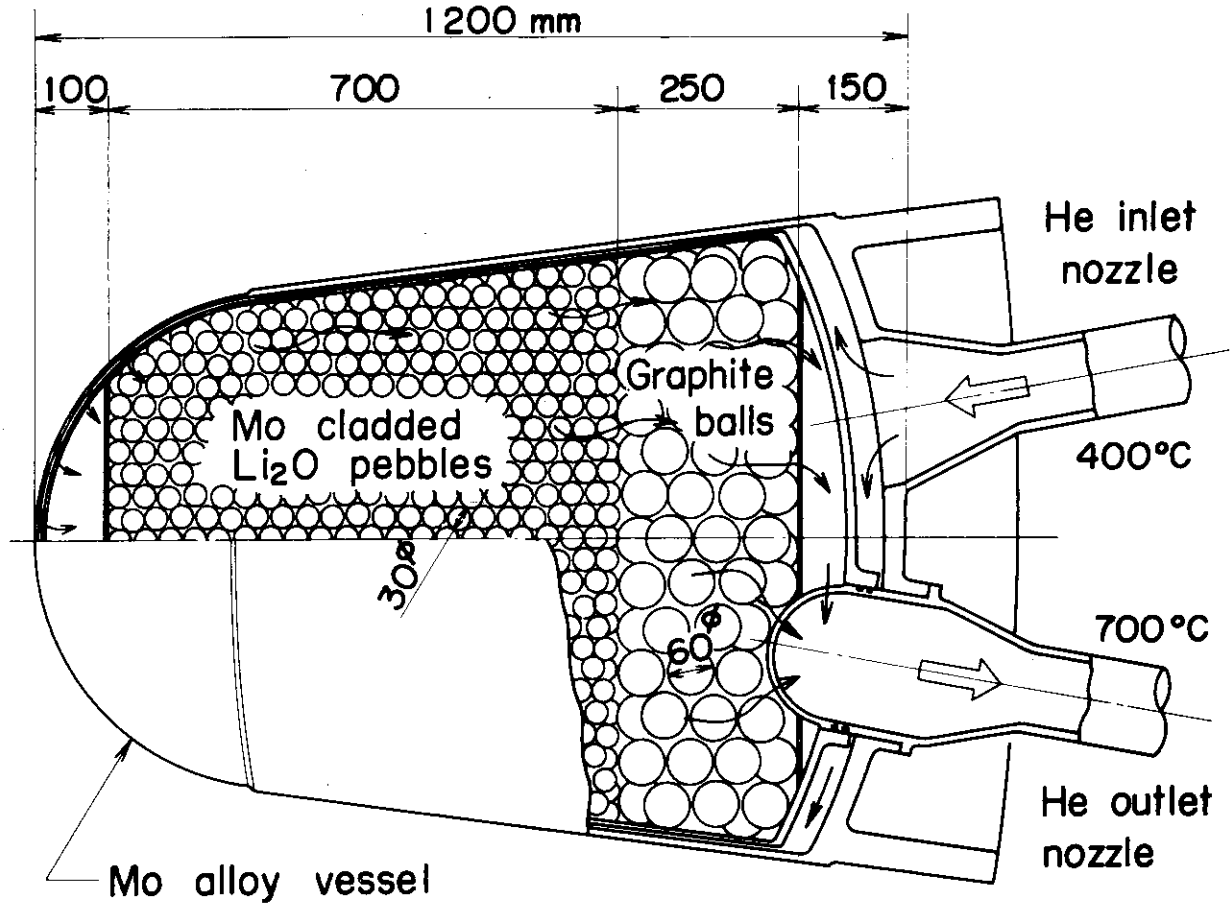

Fig.IV.2-5

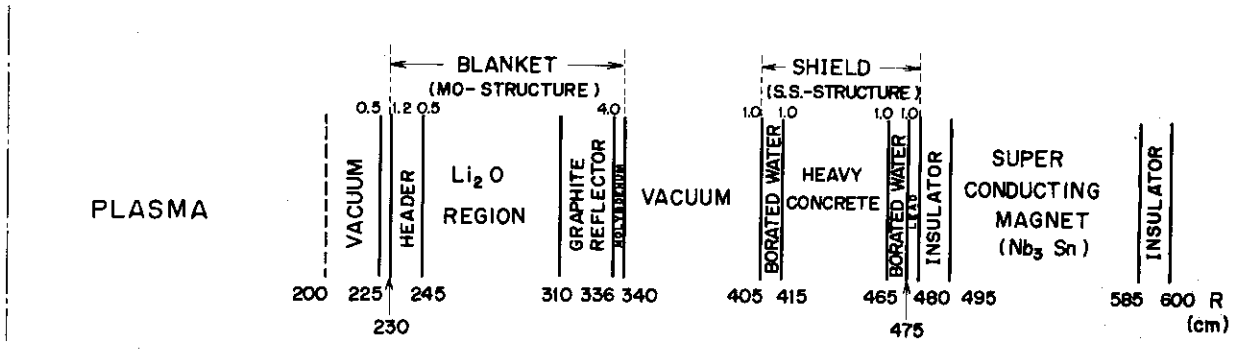

Schematic of Blanket, Shield and Magnet Design

Fig.IV.2-6 Schematic of blanket, shield and magnet design.

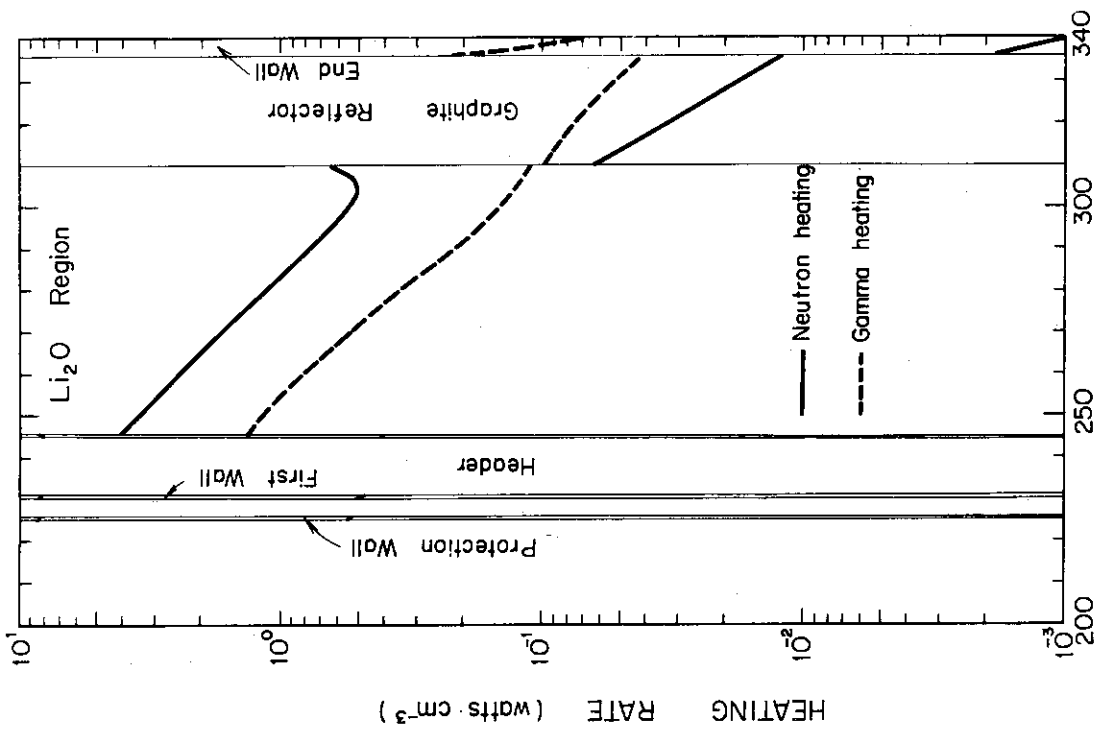

Fig.IV.2-8 The distribution of nuclear heating rate in the blanket

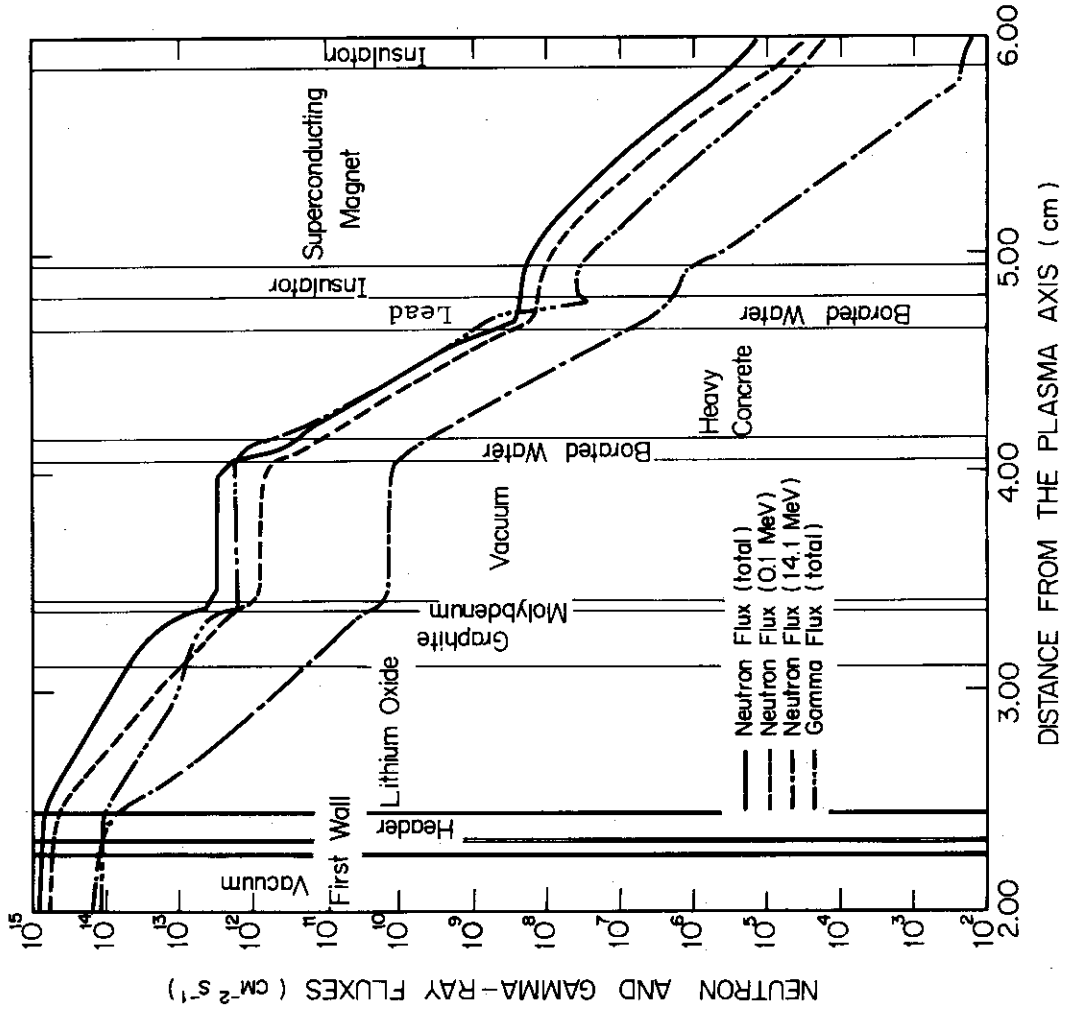

Fig.IV.2-7 Neutron and gamma-ray fluxes in the fusion reactor.

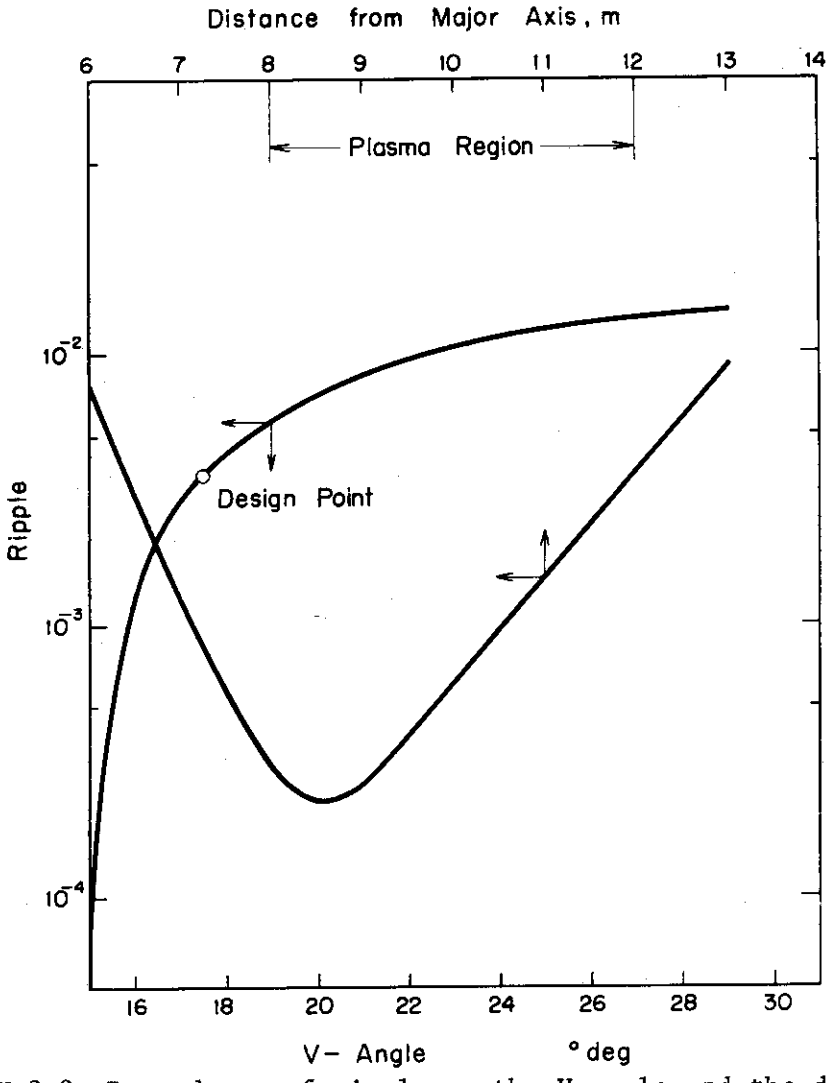

Fig.IV.2-9 Dependence of ripple on the V-angle and the distance

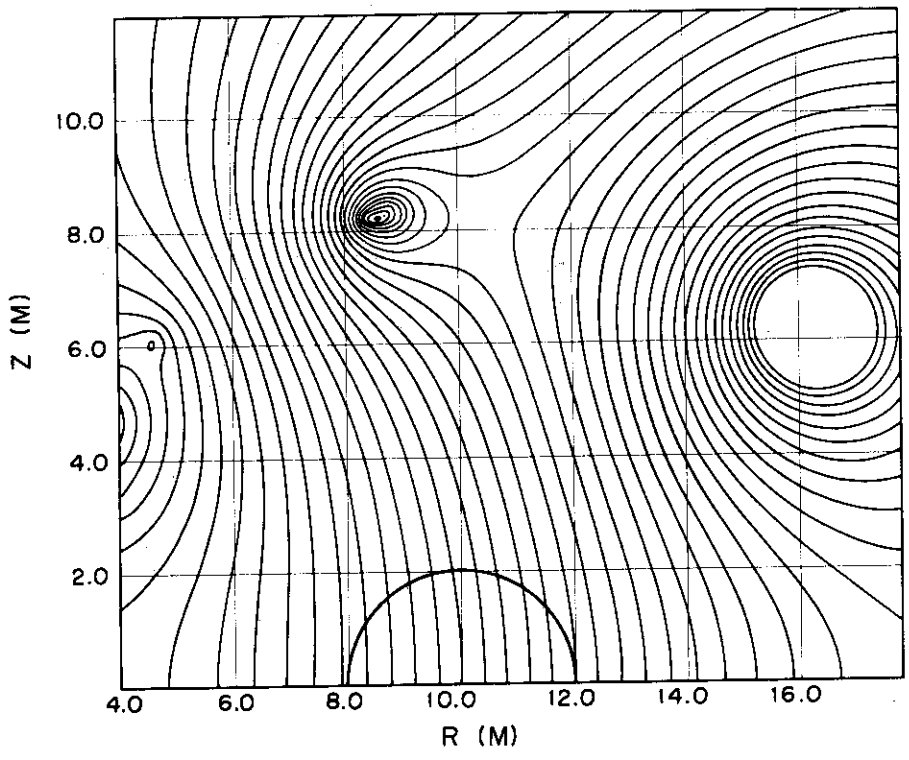

Fig.IV.2-10 Vertical field distributon

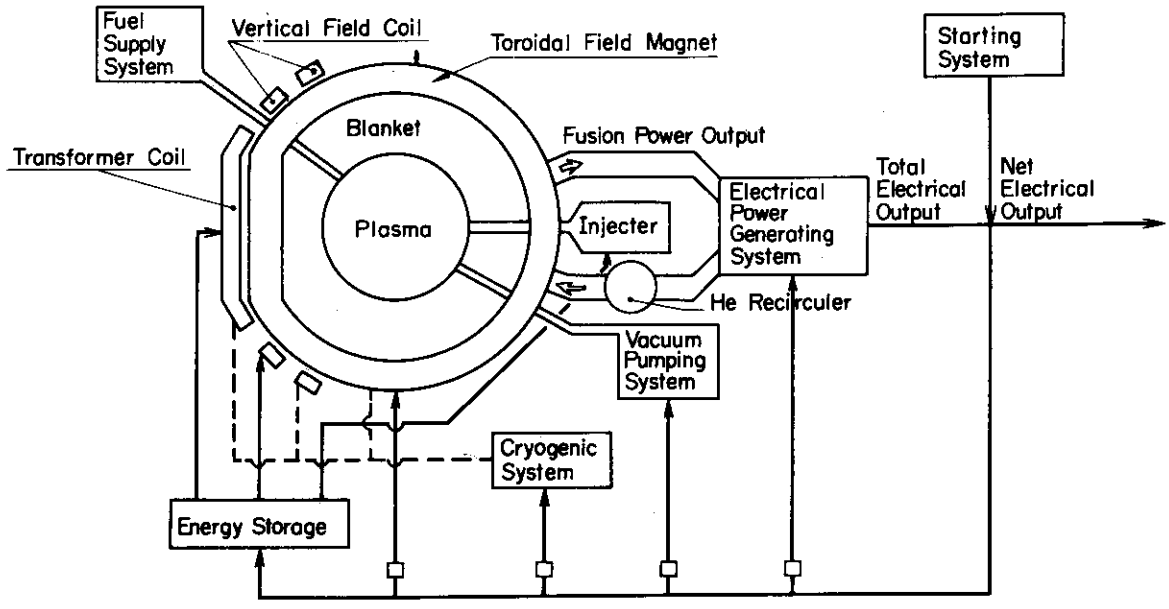

Fig.IV.2-11 Electrical power supply system

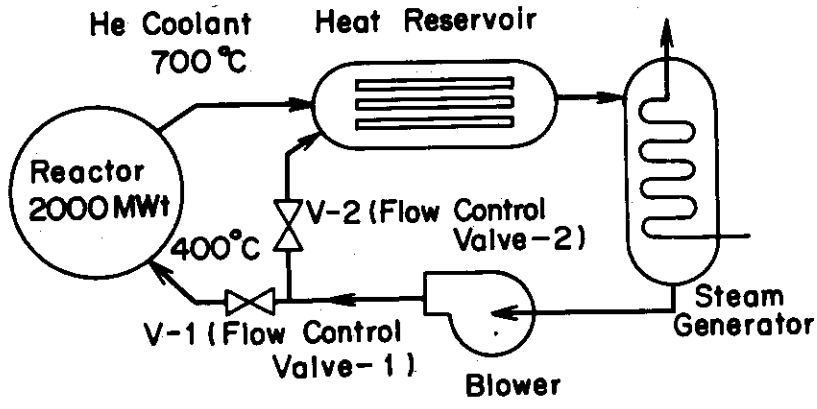

Fig.IV.2-12 Reactor cooling system

APPENDICES

1. Publication List

Seki, Y., Sako, K., Tanaka, K. and Hiraoka, T.: Tritium breeding in ceramic lithium compound blanket, Proc. 1st Topical Meeting on the Technology of Controlled Nuclear Fusion, (San Diego, 1974), CONF-740402-P2, p.77.

Yamato, H*. and Ohta, M.: Ignition, fuelling and shutdown of a D-T fusion plasma, Proc. 1st Topical Meeting on the Technology of Controlled Nuclear Fusion, (San Diego, 1974), CONF 740402-P2, p.309.
(* on leave from Tokyo Shibaura Electric Co., Ltd.)

Fujisawa, N., Funahashi, A., Kunieda, S., Maeno, M., Suzuki, N., Matoba, T., Kasai, S., Itoh, S.*, Takeda, T., Toi, K., Sugawara, T.**, Shoji, T., Kawakami, T., Toyoshima, N., Ohga, T., Arai, T., Yokokura, K., Tani, T., Shiina, T., Ohta, M., Matsuda, S., Yano, S.***, Shirakata, H., Takahashi, K., Tazima, T., Nagami, M., Yoshikawa, M. and Mori, S.: The JFT-2 tokamak experiment, 5th Conf. on Plasma Physics and Controlled Nuclear Fusion Research, (Tokyo, 1974), CN-33/A1-1.
(* Nagoya University, ** on leave from Tokyo Shibaura Electric Co., Ltd., *** Kobe Univ. of Mercantile Marine)

Yoshikawa M., Tazima, T., Shimomura, Y., Kitsunezaki, A., Maeda, H., Inoue, K., Nagashima, T., Tokutake, T., Ohtsuka, H., Nagami, M., Tanaka, M., Kunieda, S., Funahashi, A., Kawakami, T., Takahashi, K., Matoba, T., Azumi, M., Shoji, T., Anno, K., Kumagai, K., Kasai, S., Ohga, T., Takeuchi, H., Tani, T., Arai, T. and Mori, S.: Research on a tokamak with an axisymmetric divertor and impurity problems in tokamak devices, 5th Conf. on Plasma Physcis and Controlled Nuclear Fusion Research, (Tokyo, 1974), CN-33/A1-2.

Sako, K., Yamato H.*, Ohta, M. Seki, Y., Tanaka, K., Asami, N.**, Matsuda, S., Ohkubo, Y.***, Takeda, T. and Mori, S.: Design study of a tokamak reactor, 5th Conf. on Plasma Physics and Controlled Nuclear Fusion Research, (Tokyo, 1974), CN-33/G1-5.
(* on leave from Tokyo Shibaura Electric Co., Ltd., ** on leave from

Mitsubishi Atomic Power Industries Inc., *** on leave from Fuji Electric Co., Ltd.)

Suzuki, Y., Kameari, A.*, Ninomiya, H., Masuzaki, M.** and Toyama, H.***: Free boundary MHD equilibria, 5th Conf. on Plasma Physics and Controlled Fusion Research, (Tokyo, 1974), CN-33/A11-2.
(* on leave from Mitsubishi Atomic Power Industries Inc , ** Nagoya University, *** University of Tokyo)

Hirano, K.*, Kitagawa, S.*, Mimura, M.*, Ohi, S.**, Amano, T.** and Wakatani, M.: Experiment on an axisymmetric fast toroidal pinch with very small aspect ratio 5th Conf. on Plasma Physics and Controlled Nuclear Fusion Research, (Tokyo, 1974), CN-33/E9-5.
(* Nagoya University, ** Osaka University)

Mori, S.: Summary of reactor systems, 5th Conf. on Plasma Physics and Controlled Nuclear Fusion Research, (Tokyo, 1974).

Kitsunezaki, A., Maeda, H. and Shimomura, Y.: Toroidal plasma equilibrium in an open shell with current-carrying conductors, Nuclear Fusion, 14 (1974) 747.

Tazima, T., Tanaka, M., Yoshikawa, M. and Inoue, K.: Behavior of impurity ions in a tokamak plasma, Nuclear Fusion, 14 (1974) 517.

Toi, K. and Takeda, T.: Analysis of tokamak plasma steady state by non-linear programing, Nuclear Fusion, 14 (1974) 577.

Itoh, S., Sugawara, T.*, Suzuki, N., Takeda, T. and Toi, K.: Dynamic limiter experiments in JFT-2 experiment, Nuclear Fusion, 14 (1974) 581.
(* on leave from Tokyo Shibaura Electric Co., Ltd.)

Sugawara, T.*, Itoh, S., Suzuki, N., Takeda, T. and Toi, K.: Stability experiment with dynamic limiter in JFT-2 tokamak, Nuclear Fusion, 14 (1974) 451.
(* on leave from Tokyo Shibaura Electric Co., Ltd.)

Fujisawa, N., Sugawara, T.*, Toi, K., Matoba, T., Kasai, S. and Itoh, S.: Discharge cleaning in JFT-2, Japan J. appl. Phys., 13 (1974) 851.
(* on leave from Tokyo Shibaura Electric Co., Ltd.)

Matsuda, S., Suzuki, N., Ohga, T. and Itoh, S.: Effect of the conducting shell and its gap on generation of the vertical magnetic field in a tokamak device, Japan J. appl. Phys., 13 (1974) 1604.

Matsuda, S.: Effect of the finite size electrode on the beam divergence of an intense ion source for the thermonuclear fusion research, Japan J. appl. Phys., 13 (1974) 1630.

Nagami, M. and Tazima, T.: Numerical simulation of JFT-2a plasma, Kakuyugo Kenkyu, 32, suppl. 2, (1974) 79, (in Japanese).

Momota, H.*, Seki, S.*, Wakatani, M., Tuda, T. and Ikuta, K.**: Review of investigations in low β torus, Kakuyugo Kenkyu, 31 (1974) 1, (in Japanese).
(* Kyoto University, ** Nagoya University)

Gomey, Y.*, Ohta, M. and Yoshikawa, M.: An optimization of plasma feasibility experiment device, Kakuyugo Kenkyu, 32 (1974) 153, (in Japanese).
(* on leave from Tokyo Shibaura Electric Co., Ltd.)

Matsuda, S.: Heating of a plasma by neutral beam injection, J. Atomic Energy Soc. of Japan, 16 (1974) 459, (in Japanese).

Takeda, T. and Itoh, S.*: Numerical simulation of the tokamak plasma with a movable boundary, JAERI-M 5697, (May, 1974), 45 pp.
(* Nagoya University)

Wakatani, M. and Azumi, M.: Feedback stabilization of the high m kink mode, JAERI-M 5703, (May, 1974), 9pp.

Yoshikawa, M.: Effect of multi-hole vacuum walls in fusion devices on reducing effective sputtering yields, JAERI-M 5849, (Sept. 1974), 20pp. (in Japanese).

Seki, Y. and Iwai, K.*: Evaluation of gas production in the molybdenum structure of a fusion reactor, JAERI-M 5855, (Sept. 1974), 31pp. (in Japanese).
(* Osaka University)

Seki, Y., Harada, Y.* and Asami, N.*: Induced activity of the copper coil in D-T burning experiment, JAERI-M 5862, (Oct. 1974) 29pp. (in Japanese).
(* on leave from Mitsubishi Atomic Power Industries Inc.)

Wakatani, M.: Nonlinear effect on the growth rate of internal m=1 kink instability, JAERI-M 5871, (Oct. 1974), 20pp.

Kobayashi, T.*, Tamura, S. and Tani, K.: Optimum design of ohmic heating field coils for an air-core system and equilibrium field coils of a large scale fusion device, JAERI-M 5898, (Nov. 1974), 84pp., (in Japanese).
(* on leave from Hitachi, Ltd.)

Ohara, Y. and Sugawara, T.*: Two-stage acceleration of an ion beam for powerful injectors, JAERI-M 5929, (Dec. 1974), 20pp.
(* on leave from Tokyo Shibaura Electric Co., Ltd.)

Yatsu, K.*, Ariga, S.** and Matoba, T.: Trapping and confinement of a laser produced plasma in a combined mirror-multipole magnetic field, Japan J. appl. Phys., 14 (1975) 163.
(* Tokyo University of Education, ** Kyoto University)

Funahashi, A., Kawai, S., Matoba, T. and Fujisawa, N.: Measurements of impurity-ion lines and particle confinement-times in tokamak plasmas, JAERI-M 5961, (Jan. 1975), 30pp. (in Japanese).

Tuda, T.: Decay of poloidal rotation in a tokamak plasma, JAERI-M 5934, (Dec. 1974), 15pp. (in Japanese).

Matoba, T.: Scattering measurements in tokamak type devices, JAERI-M 6042, (March, 1975), 19pp. (in Japanese).

Takeuchi, H., Takahashi, K., Shirakata, H. and Funahashi, A.: Multi-channel neutral particle energy analyzer for measurements of ion temperature

tokamak plasmas, JAERI-M 6048, (March, 1975), 18pp. (in Japanese).

Toi, K. and Takeda, T.: Numerical Method to obtain an optimum configuration of external magnetic field coils in tokamak device by non-linear programing, JAERI-M 6018, (Feb. 1975) 40pp.

Matsuda, S. and Yoshikawa, M.: Magnetic island formation due to error field in the JFT-2 tokamak, Japan J. appl. Phys. 14 (1975) 87.

Tani, K., Kobayashi, T.* and Tamura, S.: Effect of eddy current in the toroidal field coils of a tokamak with an air-core transformer, JAERI-M 5999, (Feb. 1975), 28pp. (in Japanese).
(* on leave from Hitachi, Ltd.)

Ninomiya, H., Suzuki, Y. and Kameari, A.*: Poloidal magnetic configurations and plasma equilibrium, JAERI-M 6025, (March, 1975), 17pp. (in Japanese).
(* on leave from Mitsubishi Atomic Power Industries Inc.)

Ninomiya, H., Suzuki, Y. and Kameari, A.*: Computational code "NIRVANA" for free boundary equilibrium, JAERI-M 6026, (March, 1975), 26pp.
(in Japanese).
(* on leave from Mitsubishi Atomic Power Industries Inc.)

Kameari, A.*, Suzuki, Y. and Ninomiya, H.: Determination of magnetic configuration for MHD equilibrium in a large tokamak device, JAERI-M 6027, (March, 1975), 16pp. (in Japanese).
(* on leave from Mitsubishi Atomic Power Industries Inc.)

Kameari, A.*, Suzuki, Y. and Ninomiya, H.: "EQUCO" MHD equilibrium code for design of magnetic configuration of toroidal plasma, JAERI-M 6028, (March, 1975), 45pp. (in Japanese).
(* on leave from Mitsubishi Atomic Power Industries Inc.)

Suzuki, Y., Ninomiya, H. and Kameari, A.*: Fundamental block line diagrams for servo control of plasma positions and shape, JAERI-M 6050, (March, 1975), 24pp. (in Japanese).
(* on leave from Mitsubishi Atomic Power Industries Inc.)

Seki, Y.: Evaluation of shielding design of superconducting magnet (I), JAERI-M 6046, (March, 1975), 23pp. (in Japanese).

Yamato, H.*, Ohta, M. and Mori, S.: Numerical analysis of thermal stability in an inhomogeneous D-T fusion plasma, Proc. Texas Symp. Tech. Cont. Thermonuclear Fusion Exp. and Eng. Aspect Fusion React. (Austin, 1972), CONF-721111, USAEC (1974), p.48.
(* on leave from Tokyo Shibaura Electric Co., Ltd.)

Sako, K., Ohta, M., Seki, Y., Yamato, H.*, Hiraoka, T., Tanaka, K., Asami, N.** and Mori, S.: Conceptual design of a gas-cooled tokamak reactor, Proc. IAEA Workshop on Fusion Reactor Design Problems, (Culham, 1974).
(* on leave from Tokyo Shibaura Electric Co., Ltd., ** on leave from Mitsubishi Atomic Power Industries Inc.)

Tazima, T.: Simulation of tokamak plasmas by an MHD model, Kakuyugo Kenkyu, 32, suppl. 2, (1974) 69, (in Japanese).

Wakatani, M., Numerical methods in the tokamak simulation, Kakuyugo Kenkyu, 32, suppl. 2, (1974) 57, (in Japanese).

2. Budget and Personnel

2.1 Budget of the Division

(unit: million yen)

	FY[1] 1974	FY 1969-1974[2] total	FY 1975
Scientific program (excluding staff & administrative costs)	790.2	2,490.1	2,202.1[3] (3,060.2)[4]
Building		299.4	243.8[5] (183.5)[6]

1) From April to March
2) The first phase of the CTR research and development program
3) Including cash of the financial obligation for FY 1975
4) The total financial obligation from FY 1975 to 1976 for the development of the main and critical components of JT-60 and the development of plasma heating systems.
5) Including cash of the financial obligation for FY 1975
6) Financial obligation from FY 1975 to 1976 for the power equipment building for the JFT-2 BNI system

2.2 Number of the staff of the Division

	FY 1974	FY 1975
Regular staff[1]	52	72
Staff on loan	7	15[2]
Guest scientist	3	3[3]
Scholarship fellow	-	10

1) Including scientists, technicians, secretaries.
Numbers in the table are as of the end of each fiscal year.
2) Three from Tokyo Shibaura Electric Co., Ltd.
Two from Hitachi Ltd.
Three from Mitsubishi Atomic Power Industries Inc.
One from Mitsubishi Electric Coporation.
Two from Fuji Electric Co., Ltd.
Two from Sumitomo Shipbuilding & Machinery Co., Ltd.
One from Nisshin Electric Co., Ltd.
One from Kawasaki Heavy Industries Ltd.
3) Two from University of Tokyo.
One from Nihon University.